Changing Graphene's Properties. Etching, Intercalation, and Deuteration.

I n a u g u r a l - D i s s e r t a t i o n

zur

Erlangung des Doktorgrades

der Mathematisch-Naturwissenschaftlichen Fakultät

der Universität zu Köln

vorgelegt von

Ulrike A. Schröder

aus Halle

Köln 2016

Berichterstatter:	Prof. Dr. Thomas Michely
	Prof. Dr. Joachim Krug
Tag der letzten mündlichen Prüfung:	31.10.2016

Et hätt noch immer jot jejange.

Abstract

Graphene is a two-dimensional material consisting of sp^2-hybridized carbon atoms arranged in a honeycomb lattice. It possesses exceptional electronical and mechanical properties, which has sparked intense research in the last years. One goal is to have a broad spectrum of well-understood tools at one's disposal allowing targeted modification of graphene's properties. In this work we explore how the properties of graphene can be selectively changed via different approaches. The approaches described in this work are: etching of graphene by exposing it to molecular oxygen, intercalation of atoms or molecules between graphene and its substrate, and adsorption of atomic hydrogen or deuterium on top of graphene. Graphene on the (111) surface of iridium is prepared and studied *in situ* in ultra-high vacuum to ensure clean and reproducible samples and enable comparison with theoretical work. The experimental methods employed are scanning tunneling microscopy, x-ray photoelectron spectroscopy, temperature programmed desorption, and low energy electron diffraction, providing complementary information about the samples under study.

The application of graphene in devices used at elevated temperatures and ambient pressures poses the question of the stability of graphene. Especially oxygen as a reactive species will be present under ambient conditions. On the other hand, oxygen can be intentionally employed to pattern graphene or change its morphology. The mechanisms for oxygen etching of graphene on Ir(111) are uncovered through a systematic variation of the graphene morphology, ranging from an impermeable graphene layer to graphene nanoflakes. We find a fundamental difference in the onset of etching for an impermeable layer and for graphene flakes. Flakes are etched through dissociative adsorbtion of oxygen on the bare iridium and subsequent attack of graphene edges of mobile atomic oxygen diffusing on the iridium substrate. An impermeable layer is significantly more stable against etching than flakes due to the absence of graphene edges. We identify pentagon-heptagon point defects in the otherwise perfect graphene layer as nucleation sites for large hexagonal etch holes.

Intercalation, i.e., placing a layer of atoms or molecules in between graphene and its substrate, constitutes a nondestructive way to change the electronic properties of graphene. Specifically, doping of graphene can be achieved by intercalation and the doping level depends on the specific intercalant. We measure the x-ray photoelectron C 1s core level shift of graphene in contact with a number of structurally well-defined intercalation layers. By analysis of our own and additional literature data for decoupled graphene, the carbon 1s core level shift is found to be a non-monotonic function of the doping level. For small doping levels the shifts are well described by a rigid band model. However, at larger doping levels, a second effect comes into play that counteracts the rigid band shift and is proportional to the transferred charge per carbon atom. Moreover, not only the position, but also the carbon 1s peak shape displays a unique evolution as a function of the doping level.

Graphene resting on reactive metals has been envisioned as a 2D nanoreactor as the region underneath forms a well-defined reaction space. In this sense intercalation represents a way to perform chemistry underneath graphene. We show for the first time that graphene can actually enable new reaction pathways and demonstrate the formation of a superdense OH-H_2O phase underneath graphene that has never been observed before.

Another interesting aspect of graphene is that it can be viewed as consisting of two surfaces only. The substrate on which graphene is resting may influence the way graphene reacts with chemical species arriving on its other side. We study the interaction of graphene with atomic deuterium and hydrogen. Deuteration of graphene has been widely studied as it introduces a bandgap into graphene but also in the light of a hydrogen storage material for fuel cells. For graphene on Ir(111), we find two distinct binding states of deuterium and can link one them unambiguously to specific adsorption sites on the graphene. The iridium substrate plays a crucial role as graphene binds down towards it in specific regions upon adsorption of atomic deuterium.

Combining deuterium adsorption from the top and deuterium intercalation underneath graphene has been proposed to lead to deuterium bound to both sides of the graphene sheet, resulting in graphane, an insulating material with interesting properties in itself. However, we rule out graphane formation with this particular method by dedicated experiments.

Changing the material in contact with graphene by intercalating several layers of gold, again changes the properties of graphene with respect to binding atomic deuterium. We find surprisingly stable deuterium adsorption although graphene interacts only very weakly with gold.

Kurzzusammenfassung

Graphen ist ein zweidimensionales Material, dass aus sp^2-hybridisiertem Kohlenstoffatomen besteht, die sich bienenwabenförmig anordnen. Es besitzt außergewöhnliche elektronische und mechanische Eigenschaften, die in den letzten Jahren zu intensiver wissenschaftlichen Forschung anregten. In dieser Arbeit wird untersucht, wie die Eigenschaften von Graphen mit unterschiedlichen Methoden gezielt verändert werden können, mit dem Ziel, eine breite Palette verschiedenster, gut verstandener Werkzeuge zur Verfügung zu stellen um Graphen nach Wunsch zu modifizieren. Die Herangehensweisen, die in dieser Arbeit vorgestellt werden umfassen: Ätzen von Graphen mit molekularem Sauerstoff, Interkalation von Atomen oder Molekülen zwischen Graphen und Substrat und die Adsorption von atomarem Wasserstoff oder Deuterium auf Graphen. Die Graphenproben werden *in situ* im Ultrahochvakuum hergestellt und untersucht, um saubere und reproduzierbare Proben und Ergebnisse sicherzustellen, und den Vergleich mit theoretischen Arbeiten zu ermöglichen. Es werden die sich gegenseitig ergänzenden experimentellen Methoden Rastertunnelmikroskopie, Röntgenphotoelektronenspektroskopie, temperaturprogrammierte Desorption und niederenergetische Elektronenbeugung verwendet.

Bei Verwendung von Graphen bei erhöhten Temperaturen und Umgebungsdruck in möglichen Bauelementen stellt sich schnell die Frage nach dessen Stabilität, insbesondere da unter Atmosphärenbedingung stets Sauerstoff als reaktiver Stoff vorhanden ist. Sauerstoff wird indes auch gezielt verwendet um Graphen gezielt zu strukturieren und seine Morphologie zu verändern. Der Sauerstoffätzmechanismus von Graphen auf Ir(111) wird duch eine systematische Veränderung der Graphenmorphologie untersucht, von undurchdringlichen, vollständig geschlossenen Graphenlagen zu kleinen Graphennanoflocken.

Wir konnten einen fundamentalen Unterschied zwischen dem Ätzen einer vollständig geschlossenen Graphenlagen und dem von Graphen-Nanoflocken feststellen. Das Ätzen der Flocken erfolgt über dissoziative Adsorption von Sauerstoff auf der freien Iridiumoberfläche, anschließende Diffusion des atom-

aren Sauerstoffs auf der Iridiumoberfläche an die Graphenkanten und Angriff der Kanten. Eine geschlossene Graphenlagen ist aufgrund der fehlenden Graphenkanten signifikant stabiler. Als Keimbildungsort für hexagonale Ätzlöcher konnten wir Pentagon-Heptagon-Punktdefekte in der ansonsten perfekten Graphenschicht nachweisen.

Interkalation, also das Einlagern von Atomen oder Molekülen zwischen Graphen und dem darunterliegenden Substrat, stellt eine nicht-destruktive Methode dar um die elektronischen Eigenschaften von Graphen zu modifizieren. Insbesondere bewirkt Interkalation eine Dotierung des Graphens wobei das Dotierniveau vom Interkalat abhängig ist. Mit Photoelektronenspektroskopie messen wir die Rumpfniveauverschiebungen des Kohlenstoff-1s-Niveaus von unterschiedlich interkaliertem Graphen. Im Vergleich eigener experimenteller mit zusätzlichen Literaturdaten für entkoppeltes Graphen konnten wir nachweisen, dass die Kohlenstoff-1s-Rumpfniveauverschiebung nicht-monoton vom Dotierniveau abhängt. Für kleine Dotierniveaus ist das Modell der starren Bänder anwendbar. Bei höheren Dotierniveaus wird ein zweiter Effekt wirksam, der der starren-Band-Verschiebung entgegenwirkt und proportional zum Ladungsübertragung pro Kohlenstoffatom ist. Darüber hinaus beeinflusst das Dotierniveau nicht nur die Position des Kohlenstoff-1s-Signals sondern auch dessen Form.

Weiterhin wird Graphen als potentieller 2D-Nanoreaktor in Betracht gezogen, da der Raum zwischen der Graphenschicht und darunterliegenden reaktiven Metallen definierte chemische Reaktionsbedingungen erwarten lässt. Vor diesem Hintergrund können wir erstmals zeigen, dass Graphen tatsächlich völlig neue Reaktionswege ermöglicht, indem wir den Erstnachweis der Bildung einer super-dichten OH-H_2O-Phase unter Graphen erbringen.

Ein anderer interessanter Aspekt von Graphen ist, dass es lediglich aus zwei Oberflächen besteht. Das unter dem Graphen liegende Substrat kann somit die Reaktionsfähigkeit des Graphens mit Substanzen auf der substratabgewandten Seite beeinflussen. In diesem Zusammenhang haben wir die Interaktion von Graphen mit atomaren Deuterium und Wasserstoff untersucht. Deuterierung von Graphen ist von breitem Interesse, nicht nur da dadurch eine Bandlücke im Graphen erzeugt wird sondern auch im Hinblick als Wasserstoffspeichermaterial für Brennstoffzellen.

Bei der Analyse von Graphen auf Ir(111) beobachten wir zwei distinkte Bindungszustände von Deuterium. Einer dieser Zustände konnte eindeutig mit spezifischen Adsorptionsorten auf dem Graphen korreliert werden. Dabei spielt das Iridiumsubstrat eine entscheidende Rolle, indem es Deuterium-Graphen-Iridium-Bindungen in spezifischen Regionen ermöglicht.

Es wurde vorgeschlagen, dass die Kombination von Deuteriumadsorption auf der Oberseite Graphens zum Einen und Deuteriuminterkalation zwischen

Graphen und Iridium zum Anderen dazu führt, dass Deuterium von beiden Seiten an das Graphen bindet. Das entstehende Material wäre Graphan, ein Isolator mit interessanten Eigenschaften. Aufgrund unserer Resultate können wir jedoch die Bildung von Graphan eindeutig ausschließen.

Interkalation von mehreren Goldschichten unter Graphen wird verwendet, um die Reaktionsfähigkeit von Graphen bezüglich atomaren Deuteriums zu verändern. Obwohl Graphen nur sehr schwach mit Gold wechselwirkt, beobachten wir eine erstaunlich starke Bindung des atomaren Deuteriums ans Graphen.

List of symbols

5-7 defect	Heptagon-pentagon defect
Ag	Silver
Al	Aluminum
ARPES	Angle-resolved photoemission spectroscopy
Au	Gold
BE	Binding energy
C	Carbon
CLS	Core level shift
CO	Carbon monoxide
CO_2	Carbon dioxide
Cs	Caesium
Cu	Copper
CVD	Chemical vapor deposition
CVD-Gr	Gr grown by CVD without a TPG step, i.e., the sample was exposed to ethylene while at elevated temperature, typically 1120 K
C 1s	Carbon 1s core level
D	Deuterium
DFT	Density functional theory
DOS	Density of states

E_{F}	Fermi level
Eu	Europium
Gr	Graphene
H	Hydrogen
HOPG	Highly-oriented pyrolytic graphite
HREELS	High resolution electron energy loss spectrometry
Ir(111)	The (111) surface of iridium
L	Langmuir
LEED	Low energy electron diffraction
Li	Lithium
meta	Adsorbate configuration where alternate carbon atoms in the graphene hexagon are occupied
ML	Monolayer
Ni	Nickel
O	Oxygen
ortho	Adsorbate configuration where neighboring carbon atoms in the graphene hexagon are occupied
para	Adsorbate configuration where opposite carbon atoms in the graphene hexagon are occupied
Pt	Platinum
Re	Rhenium
Ru	Ruthenium
SFG	Sum-frequency generation spectroscopy
SiC	Silicon carbide
STM	Scanning tunneling microscopy
STS	Scanning tunneling spectroscopy

TPD	Temperature programmed desorption
TPG	Temperature programmed growth
UHV	Ultra-high vacuum
vdW	van der Waals
XPS	X-ray photoelectron spectroscopy

Contents

Chapter 1

Introduction

Graphene (Gr) is a two-dimensional material consisting of carbon (C) rings in a honeycomb structure. The Nobel prize awarded to Geim and Novoselov in 2010 [1] has sparked immense research in the field. Applications in electronic devices are envisioned, as Gr performs better than widely used silicon in terms of high charge carrier mobility [2], high thermal conductivity [3], and, at least in principle, is cheaper than silicon.

A serious drawback is the missing bandgap of Gr, making its application in standard transistor electronics problematic. Much research, therefore, is directed at introducing a bandgap in Gr, while at the same time keeping its high performance properties. Gr nanoribbons [4] or patterned adsorption of atoms or molecules [5] are promising paths to this end. Hydrogen adsorption has been shown to introduce a bandgap of at least 0.45 eV [6].

Another challenge that remains is the large scale production of high-quality Gr. Industry scale production of Gr has been successfully realized on polycrystalline Cu foils [7], but the quality is of course well below what can be achieved on single crystal transition metal surfaces like Ir(111). However, single crystal transition metals are small and expensive, as well as conducting and as such not of very much use practically. A possible way out of this dilemma is growing Gr on a single crystal and then transferring it to a different substrate that has the desired properties. A viable route towards transfer includes intercalation, i.e., the insertion of a layer of atoms or molecules in between the Gr and its growth substrate. The intercalant decouples the Gr from its substrate and facilitates transfer of the complete Gr film [8]. Moreover, intercalation is of much interest because it allows for doping of the Gr, and by choosing the right intercalant, doping levels between 0.68 eV p-doping [9] and 1.63 eV n-doping [10] can easily be achieved.

Gr is not only thought to enable fascinating new applications, but it is also of great interest when it comes to studying fundamental phenomena

such as Klein tunneling [11], the half-integer quantum Hall effect [12], or massless Dirac fermions [13], just to name a few. Gr has greatly promoted the understanding of these phenomena, for two reasons. For one, it is easy to fabricate experimentally, as essentially blowing anything containing carbon over a hot metal surface will do the trick [14]. On the other hand, its structure - only carbon atoms, in a two-atom basis hexagonal lattice - as well as its reduced dimensionality also greatly facilitates theoretical calculations of situations very close to experimental conditions. A very fruitful exchange between experiment and theory is the result.

Another intriguing property of Gr, at least from a surface scientist's perspective, is that it possesses two surfaces without bulk material in between, opening up new possibilities. By placing material on one side of the Gr sheet, its properties can be tuned with respect to the interaction with materials deposited on the other side. The Gr layer itself does not need to be modified but stays intact. This facilitates the design of reversible changes of its properties.

Also in this view, intercalation plays an important role, as it is the easiest way to change the material in contact with Gr. This is of importance, as Gr-substrate interactions are often a challenge when it comes to describing the behavior of Gr theoretically. A prime example is the interaction of Gr with hydrogen. Although hydrogen is the simplest of atoms, and Gr, in some sense, the simplest of substrates, the combination of the two leads to all but simple physics. As we demonstrate ourselves in Chapters 7 and 8 the substrate seems to play the crucial role in hydrogenation of Gr, although the underlying mechanisms are still not fully understood.

This work is meant to contribute to improving the control of Gr's properties by understanding a variety of processes that are employed to tweak the properties of Gr in one way or the other, including etching of Gr, intercalation under Gr, and adsorption of atomic deuterium and hydrogen on top of Gr. Samples prepared *in situ* in ultra-high vacuum and studied by scanning tunneling microscopy (STM) are used to image Gr in the real space, understand its morphology and follow processes on the surface in real time. Low energy electron diffraction (LEED) gives access to the reciprocal space and is a means to quickly check the quality of samples, and detect ordered structures on the surface or changes thereof. X-ray photoelectron spectroscopy (XPS) easily lets us identify not only the chemical composition of our surface but also subtle changes in the chemical environments of the atoms under concern. Last but not least, temperature programmed desorption (TPD) allows us to study desorption of atoms or molecules from Gr, and thus gives insight into desorption dynamics and reaction products. In most of this work, these four methods are used to complement each other and to further the understanding of the processes under study.

Chapter 4 deals with the process of etching of Gr on Ir(111) with molecular oxygen. The stability of Gr at high temperatures and in the presence of oxygen is of interest when moving towards applications in ambient environments. And although carbon combustion has been studied for over a hundred years [15], fundamental understanding on the atomic level has not been achieved. High-quality Gr as a well-defined system is a perfect model system to study the etching process. This chapter presents an extensive study of the etching in dependence of the Gr morphology, ranging from completely closed Gr films to small Gr nanoflakes. We were able to pinpoint, for the first time, the exact onset of the etching process on a perfectly closed Gr film. Under the experimental conditions used, we were able to image the etching process live in unprecedented resolution employing high temperature STM measurements. For the etching of small Gr flakes, we developed a simple model that allows us to predict the activation energy and the frequency factor of the etching process, where the latter turns out to be surprisingly low.

In Chapter 5 we study core level shifts (CLSs) of the carbon 1 s (C 1s) level, i.e., changes in binding energy of the core level electrons as measured by XPS. CLSs are a powerful tool in surface science because they allow detection of subtle changes in the chemical environment of the atoms under concern, and can even be employed to follow chemical reactions on surfaces (see Chapter 6). Their use as a tool to monitor and control intercalation processes prompted us to further investigate the origin of CLSs, and to link them to the doping level of Gr. We experimentally observe a universal, non-monotonic dependence of the C 1s CLS on the doping level in the case of quasi-freestanding, doped Gr, based on the comparison between our own data and literature. We propose a simple phenomenological model to understand CLSs which can be used as a quick prediction of doping levels solely from XPS measurements. Furthermore, we demonstrate the universality of the CLS dependence on the doping level by intercalation of lithium (Li) which allows for continuous and homogeneous doping of Gr without switching to a different element.

In Chapter 6 we report on the formation of a new superdense OH-H_2O phase underneath Gr/Ir(111) that has not been observed on Ir(111) without Gr as a cover before. This is achieved by simply exposing O-intercalated Gr flakes to H_2. The forming structures are followed by employing XPS CLSs, as well as STM and TPD measurements. The formation of this superdense OH-H_2O phase constitutes a proof-of-principle that Gr can indeed enable new reaction paths and thus act as a 2D-nanoreactor.

In Chapter 7 the adsorption and desorption of atomic deuterium (D) on Gr is studied with TPD, STM and XPS. We calculate the coverage of

D on Gr, explore the two distinct binding states with TPD and STM, and explore the influence of D intercalation. Formation of graphane, a Gr-based insulating material with hydrogen (H) or D attached to both sides of the Gr film, has been recently reported to form on Ir(111) [16, 17], but these results have been challenged [18]. We perform dedicated experiments TPD and XPS experiments and rule out graphane formation.

In Chapter 8, we first study the formation of multiple layers of Au on Ir(111), and observe, to the best of our knowledge for the first time, trigonal strain relief patterns for two and three monolayers of Au/Ir(111) in STM. Intercalation of Au under Gr is studied in dependence of the Gr morphology and the amount of Au intercalated. We move on to study the deuteration of Gr/Au, and find, in contrast to the Gr/Ir case, random adsorption patterns and a more complex desorption signal in TPD.

The following Chapters 2 and 3 provide the reader with some theoretical background and the experimental details, respectively. The work is summarized in Chapter 9, and an Appendix holds additional information.

Chapter 2

Background

2.1 Gr on Ir(111)

Gr is a two-dimensional material consisting of C atoms arranged in a honeycomb lattice, as shown in Figure 2.1. The C atoms are sp^2-hybridized in contrast to, e.g., the sp^3-hybridization in diamond. The three sp^2-bonds form the in-plane σ-bonds. The remaining out-of-plane p_z-orbitals form a delocalized π-system.

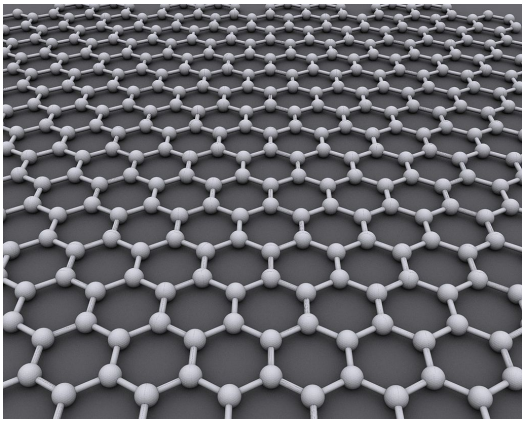

Figure 2.1: Ball-and-stick model of Gr. The spheres represent C atoms, the sticks the sp^2-bonds. From [19].

Its electronic structure is displayed in Figure 2.2. The valence (π-) band and the conduction (π^*-) band touch each other at the six corners, or K-points, of the Brillouin zone. These points are called Dirac points. In the vicinity of the Dirac points, the energy dispersion is linear and forms a Dirac cone (see magnification in Figure 2.2). This means that the charge carri-

ers behave like massless particles, because their velocity is independent of their energy. The electron density of states (DOS) at the Dirac point is zero, making Gr a semiconductor with a zero bandgap.

Gr possesses a variety of fascinating properties, spanning from fundamental quantum electrodynamic phenomena due to its relativistic charge carriers (Klein tunneling, half-integer quantum Hall effect [12]), and also possesses outstanding mechanical properties [20] making it a candidate for a space elevator but also inducing more mundane uses, such as marketing of tennis rackets [21]).

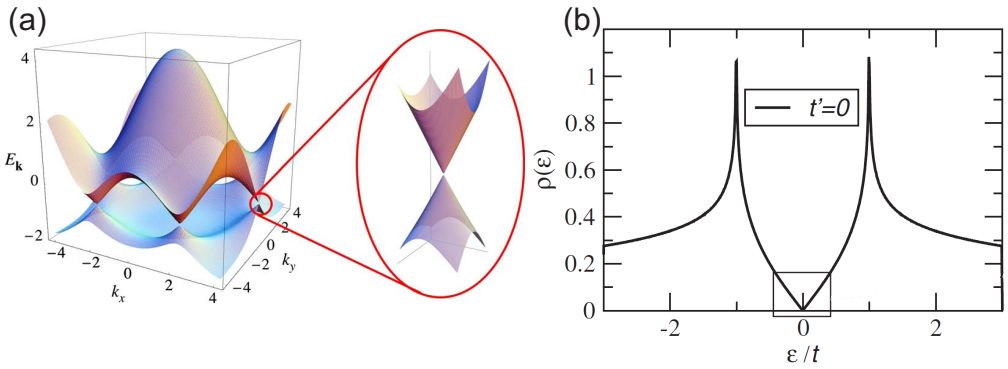

Figure 2.2: (a) Electron dispersion of Gr. Right: zoom in of the energy bands close to one Dirac point. (b) Density of states as a function of the energy neglecting next-nearest neighbor hopping ($t' = 0$). Reprinted figure with permission from [22]. ©2009 American Physical Society.

The (111) surface of the 5d transition metal Ir is widely used as a substrate for epitaxial Gr growth. As the lattice parameters of Ir and Gr are slightly different, an incommensurate 9.32×9.32 superstructure, called a moiré lattice, forms. This is visualized in Figure 2.3. The moiré periodicity is 2.53 nm [23]. Gr is van der Waals (vdW) bound to the Ir. The bond strength varies across the moiré cell, and the Gr is on average 3.38 Å $\pm$ 0.04 Å above the iridium substrate [24]. Ir(111) is a popular substrate because it exhibits enough interaction to enable nearly defect-free, single-domain Gr over several μm [25] but little enough interaction to leave the bandstructure of Gr almost intact, compared to free-standing Gr [26].

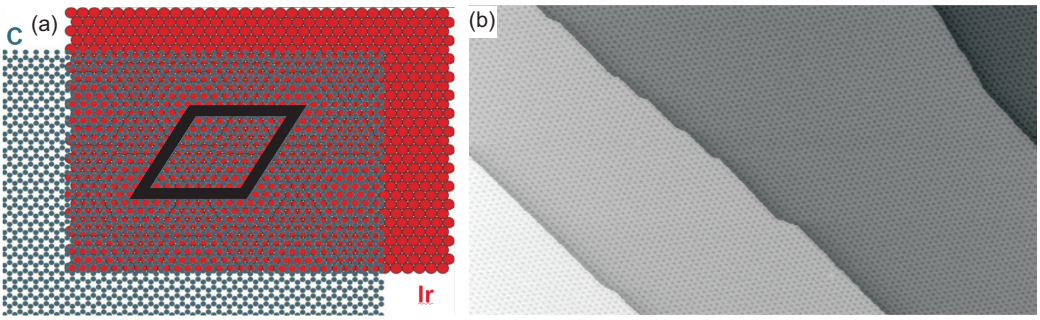

Figure 2.3: (a) Gr lattice (grey) on top of an Ir(111) lattice (red) and the resulting moiré superstructure. The moiré unit cell (2.53 nm) is drawn in black. (b) STM topograph of Gr on Ir(111), crossing several Ir steps. Image size 125 nm × 250 nm. Reprinted with permission from [25]. ©2008 American Chemical Society.

2.2 Metal clusters on Gr/Ir(111): A typical binding mechanism

The moiré of Gr/Ir(111) can be used as a template for patterned growth of metal clusters [27]. An example of a cluster array on Gr/Ir(111) is shown in Figure 2.4. Cluster arrays are of interest for fundamental studies concerning nanomagnetism and catalysis. The mechanism underlying well-ordered

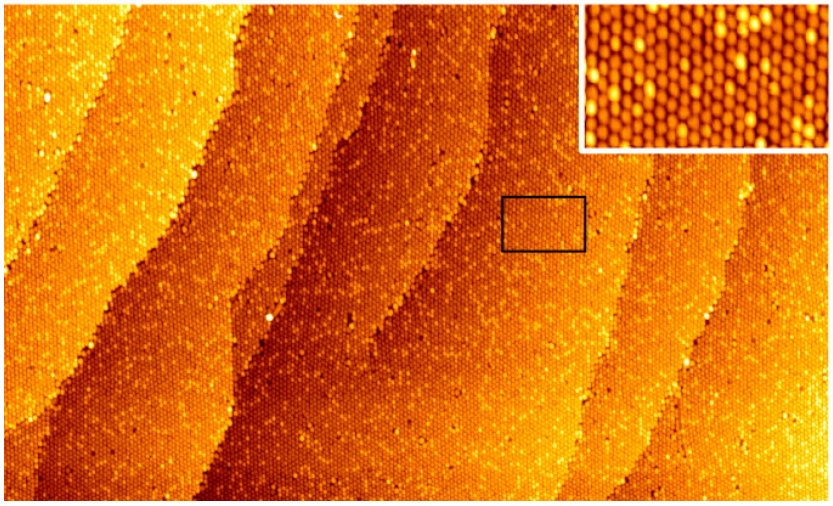

Figure 2.4: Ir cluster superlattice grown on Gr/Ir(111) extending over the entire sample. Image size 0.5 μm × 0.3 μm, inset 50 nm × 50 nm. From [27].

cluster formation on Gr/Ir(111) was illuminated by density functional theory (DFT) calculations [28] and verified experimentally by XPS measurements [29]. Under and near adsorbed clusters, the C layer rehybridizes from sp^2-bonding (characteristic for Gr) to diamondlike sp^3. The sp^3-hybridized C atoms exhibit a fourth bond and are alternately bound to Ir substrate atoms below and metal atoms above the Gr. When taking a closer look at the moiré pattern, three different regions can be distinguished (see Figure 2.5). In atop regions, the C rings are centered on top of an Ir atom. The hcp and fcc regions are named after the adsorption site of the Ir surface on which the rings are centered. sp^2-to-sp^3-rehybridization is only energetically favorable where substrate atoms lie directly below C atoms, and thus occurs only in hcp and fcc regions. In fact, clusters adsorb preferentially on hcp sites, at low temperatures also on fcc but never on atop sites. Through the rehybridization and bond formation to the substrate, the Gr is pinned down locally. DFT calculations show that the distance between C atoms and the Ir plane decreases from $\approx 3.4\,\text{Å}$ to $\approx 2.1\,\text{Å}$.

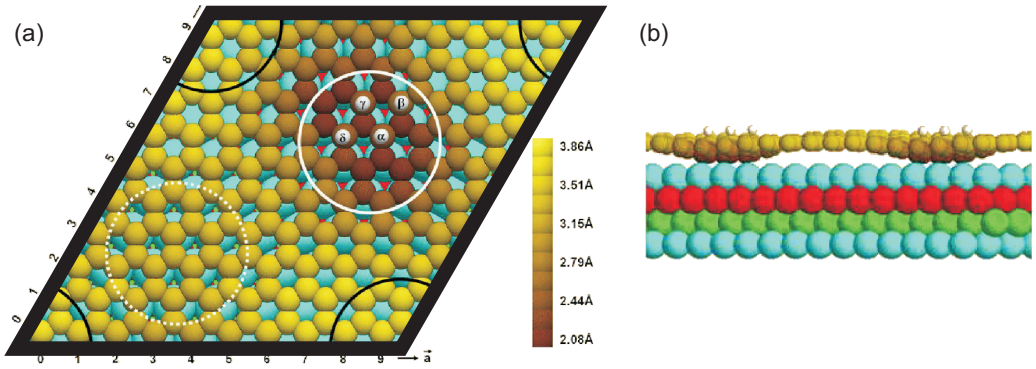

Figure 2.5: (a) Top view of a moiré cell of Gr/Ir(111) obtained by DFT calculations with a 4-atom Ir cluster (small white spheres) in its lowest energy configuration. First, second and third substrate layer Ir atoms are coloured cyan, red, and green, respectively. C atoms are in shades of yellow according to their height. Atop regions are delimited by black arcs. Solid and dotted white circles encompass the hcp and fcc regions, respectively. (b) Side view of (a). Reprinted figure with permission from [28]. ©2008 American Physical Society.

2.3 X-ray photoelectron spectroscopy

X-ray photoelectron spectroscopy (XPS) is a surface-sensitive technique based on the photoelectric effect with which the elemental composition of a surface as well as the concentration and chemical state of the elements can be determined.

X-ray radiation from lab sources like magnesium or aluminum targets bombarded by high-energy electrons or synchrotron radiaton emitted from an accelerated beam of charged particles are used to excite electrons from the core levels, whose kinetic energy E_{K} is measured. Knowing the energy $\hbar\omega$ of the incident photon the kinetic energy amounts to

$$E_{\mathrm{K}} = \hbar\omega - E_{\mathrm{B}} - \phi, \tag{2.3.1}$$

where $\phi = E_{\mathrm{vacuum}} - E_{\mathrm{Fermi}}$ is the work function of the material. In a typical XPS spectrum, the intensity of the detected electrons is plotted against the binding energy E_{B} which is given relative to the Fermi level E_{F}. Since the binding energies (BEs) are characteristic for each element, it is possible to identify which elements a given surface is composed of. By evaluating the peak height it is also possible to determine the concentrations. Depending on the surface material, the kinetic energy of the released electrons is roughly 10 to 1500 eV. The reason for the surface sensitivity of this technique is the low mean free path of the electrons (see Figure 2.6). In this energy region it amounts to only a couple of monolayers which means that an electron detected by the energy analyzer orginated at or close to the surface.

The photoemission spectrum is a fingerprint of the density of occupied states in the probed material. Besides photoemission, other processes occur and contribute to an XPS spectrum. These include the continuous background of inelastic secondary electrons, Auger peaks, and peaks due to plasmon losses found on the low-energy side of each photoemission peak. Moreover, the cross-section for photoionization is different for different electron levels, thus the shape of spectra can vary significantly depending on the used photon energy. In general, photoemission is most probable at photon energies close to the binding energy of the photoelectron and becomes more and more unlikely with increasing photon energy (compare with the cross-section for the Ir 4f signal in Figure 3.5). For this reason, x-rays are most suitable to probe deep core levels.

Figure 2.7 shows XP spectra of Gr completely covering the Ir(111) surface, defined as one monolayer (ML) Gr. In Figure 2.7(a), electrons originating from the C 1s core levels are shown. Pristine Gr can be fitted by single component at (284.09 ± 0.01) eV [32–34]. Figure 2.7(b) shows the Ir $4f_{7/2}$ region of Gr/Ir(111), and (c) shows clean Ir(111). Interestingly, the Ir $4f_{7/2}$

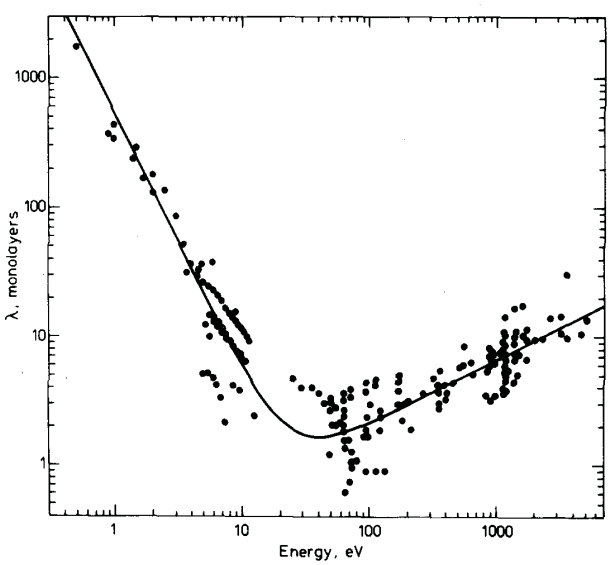

Figure 2.6: Collection of experimental data of the inelastic mean free path of electrons for different materials as a function of the energy. From [31]. ©1979 Heyden & Son Ltd.

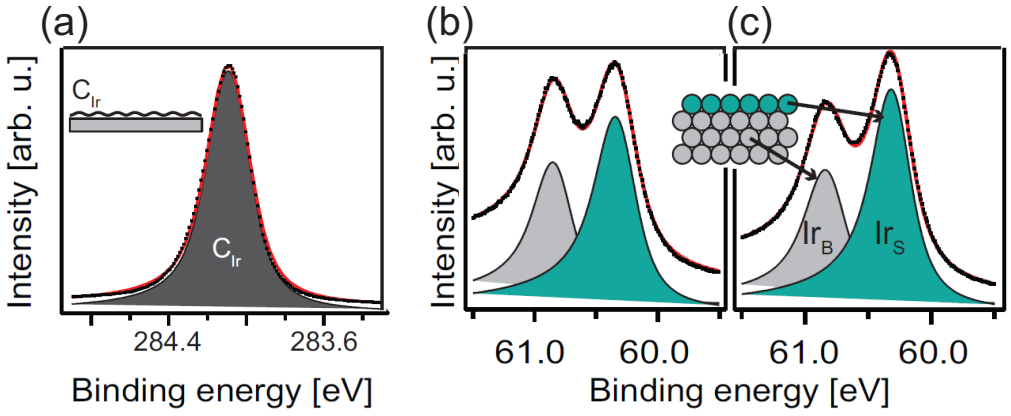

Figure 2.7: XP spectra of (a) the C 1s region of 1 ML Gr/Ir(111), (b) the Ir $4f_{7/2}$ region of 1 ML/Gr/Ir(111) and (c) the Ir $4f_{7/2}$ region of clean Ir(111). Black dots are the data, red lines are fits to the data, filled curves are fit components. Reprinted from [32], ©2016 with permission from Elsevier.

spectrum is the same whether or not Gr is present. This is due to the relatively weak interaction of Gr with the Ir surface that does not affect the Ir 4f core level (although in ARPES there are clear signs for the interaction between Gr and Ir [26]). Two peaks are visible, labeled $\mathrm{Ir_B}$ and $\mathrm{Ir_S}$. $\mathrm{Ir_B}$ at $(60.82 \pm 0.01)\,\mathrm{eV}$ is due to bulk Ir atoms, $\mathrm{Ir_S}$ at $(60.31 \pm 0,01)\,\mathrm{eV}$ is due to Ir atoms sitting at the surface. Bulk and surface peak are shifted in BE due to the different coordination of bulk and surface atoms (for a detailed explanation see ref. [35] and references therein).

Core level shifts in XPS

Core level shifts (CLSs) are shifts in the binding energy of core electrons, as measured by XPS. They are typically used to detect and identify changes in the chemical environment of the atoms or molecules studied. An example is the surface CLS observed of Ir(111) shown in Figure 2.7(b). This surface CLS can be used to distinguish and study adsorption of atoms and molecules, since it usually changes upon adsorption of atoms or molecules (see Figure 2.10). Also in Gr, CLSs play an important role. As we have already seen in Section 2.4, intercalation under Gr leads to a shift of the C 1s BE, just like adsorption on top of Gr (Section 2.7).

The interpretation of CLSs is, however, not always straightforward. A comprehensive description is given by Egelhoff [35] and references therein. In the following, a brief explanation of the main concepts is given, following ref. [35].

Fundamentally, a core-level binding energy ξ is a difference in total energies between the ground and the excited state of a system. A convenient mathematical tool to evaluate this difference is the one-electron eigenvalue. It should be noted that in a multi-electron system, single electrons do not have an energy associated with them in their ground state, and hence one-electron eigenvalues do not describe any real physical property of the system. They are nevertheless useful as an approximation to the difference in total energies between ground and excited states, and because calculations may yield results such as the charge density that do correspond to the real system. Often, XP spectra are compared with the calculated one-electron eigenvalues in the Hartree-Fock approximation. In the Hartree-Fock approximation, kinetic energy, Coulomb, and exchange terms for each electron are calculated assuming all the other electrons form a static background. Koopman's theorem states that under the assumption that the removal of one electron leaves the wavefunctions of all other electrons unchanged the initial-state Hartree-Fock eigenvalue equals the difference between Hartree-Fock total energies of the inital (ground) and final (excited) state. The Hartree-Fock eigenvalue ϵ can

be viewed as a first-order approximation to the measured BE ξ [35]:

$$\xi = -\epsilon + \Delta E^{\mathrm{c}} - \mathrm{E}^{\mathrm{R}}. \tag{2.3.2}$$

ΔE^{c} and E^{R} are corrections to account for the discrepancies between the Hartree-Fock eigenvalues and BEs observed in experiment. ΔE^{c} are the changes in correlation energy in the initial and final state. The correlation energy can be viewed as largely due to the lowered electron-electron repulsion, as electrons tend to avoid each other, in contrast to the static electron background assumed in the Hartree-Fock approximation. E^{R} takes into account the relaxation or redistribution of electrons after the removal of the core electron, thus correcting for the assumption of Koopman's theorem. Hartree-Fock eigenvalues turn out to be successful because the values for ΔE^{c} and E^{R} often tend to cancel, although they can be of the order of several eV. While the eigenvalues ϵ describe the initial state of the sample, the correction terms are often referred to as final-state effects. A typical final-state effect is screening of the photo-hole. Typically, a higher electron charge density leads to better screening, resulting in a higher kinetic energy and hence lower BE of the core electron. It is inherently difficult from experiment alone to decide to what extent a CLS is due to initial or final-state contributions.

In the following, the mechanisms leading to initial state CLSs are reviewed, following Bagus *et al.* [36]. They include charge transfer, electric fields, environmental charge density, and hybridization.

Transfer of charge to or from an atom will lead to a change in the electrostatic potential felt by the electrons, and thus to a change in their BE. In a very simplified view, the charge transfer into the valence band can be estimated as charge transfer onto a sphere, with the nucleus and the core electrons sitting in the center of the sphere. Electrostatics tells us that the change in potential energy is then given by

$$\Delta V = \frac{\Delta Q}{4\pi\epsilon_0 R} \tag{2.3.3}$$

where ΔQ is the charge transfer to or from the sphere and R is the radius of the sphere. Electronic charge transfer to the atom results in a lower BE, and electronic charge transfer away from the atom to an increased BE of the core electron. For a more detailed treatment see ref. [36].

Electric fields arising from charged species external to the core-ionized atoms contribute to CLSs in a similar manner. Again, the potential of the electrons is changed. Shifts due to electric fields are positive when a positive point charge, i.e., a cation, is placed near the atom, and negative for a negative point charge.

Surface CLSs are an example for CLSs caused by environmental charge density changes. The environmental and bonding charge density of valence or conduction bands can contribute to CLSs, due to the large overlap of valence orbitals of neighboring atoms. This overlap, connected to the formation of chemical bonds, leads to accumulation of electronic charge between the atoms, which in turn leads to a change in electrostatic potential felt by the electrons.

Hybridization describes the interference of atomic orbitals so that the resulting hybrid orbitals are directed towards their neighbors, enabling better bond formation [36, 37]. Again, the change in electrostatic potential is responsible for resulting CLSs. As hybridization involves promotion of electrons from a relatively compact to a more diffuse orbital, it typically leads to higher BEs.

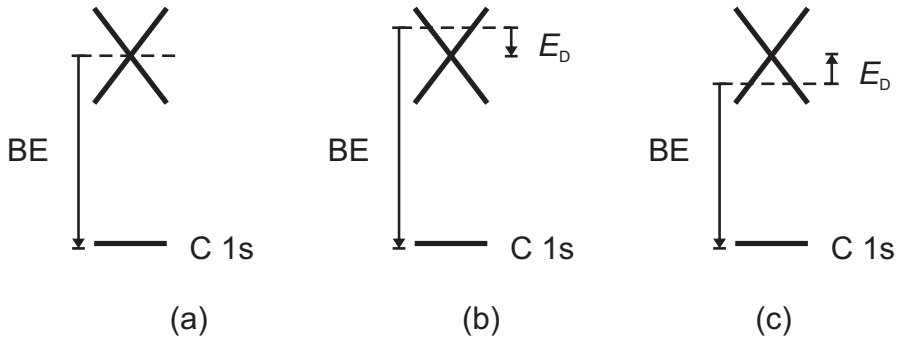

Figure 2.8: Rigid band model explaining the C 1s BE measured in XPS in doped Gr. The Dirac cone and the C 1s level are represented in solid lines, the Fermi level as a dashed line. (a) Undoped Gr, (b) n-doped Gr, (c) p-doped Gr.

For the special case of Gr, CLSs in the C 1s levels are dominated by the rigid band shift, due to Gr's peculiar bandstructure (see Figure 2.2). The density of states (DOS) at the Dirac point is zero, meaning that only very little charge transfer is needed to shift the Fermi level by a significant amount and hence dope the Gr. As visualized in Figure 2.8, the underlying assumption is that the band structure does not change upon charge transfer but stays rigid. Raising or lowering the Fermi level then directly leads to a higher or lower BE of the C 1s electron.

2.4 Intercalation under Gr

Intercalation is the inclusion of atoms or molecules between two other compounds. In the case of Gr, this means the insertion between the Gr layer and the substrate, in our case Ir(111). Intercalation is of interest because intercalates can be used to modify the binding of Gr, to decouple it from its substrate [38–40], to perform or supress chemistry under Gr [41, 42] (see Chapter 6) or to enable exfoliation from the Ir substrate [8, 43].

The substrate on which the Gr is grown influences its electronic structure to some degree. Ir(111) for example induces mini-gaps and slight p-doping in the Gr [44]. Intercalation provides the means to decouple the Gr from its substrate and possibly restore features which are characteristic for free-standing Gr.

Intercalation of a large variety of species under Gr has been studied so far, e.g. metals [45–49], halogens [43, 50], hydrogen [32, 38, 39] and oxygen [9, 33, 40–42].

As part of this thesis, H and O were intercalated. In their molecular form, H_2 and O_2 have a low sticking coefficient on Gr, making adsorption unlikely. Intercalation, however, can occur if adsorption underneath the Gr layer is energetically favourable in the chosen environmental conditions. If the Gr film is not closed or molecules can somehow pass through the film, they can adsorb on or even react with the surface below the Gr.

Oxygen intercalation

The saturation coverage of O on Ir(111) is a (2×1) structure with respect to Ir which appears in three by 60° rotated domains [33, 51, 52]. Under Gr, a $(2\sqrt{3} \times 2\sqrt{3})$R30° phase was recently observed [53] under certain conditions of pressures and temperatures. This phase dominates for relatively high O_2 pressures ($2.4{\cdot}10^{-4}$ mbar). The O_2 pressures used for intercalation throughout this thesis, however, are an order of magnitude smaller and yield a (2×1) saturation structure as for the bare Ir case.

O is of interest because it decouples the Gr and p-dopes it by -0.68 eV [54]. This is shown in the angle-resolved photoemission spectroscopy (ARPES) measurements in Figure 2.9(a,b), where (a) shows pristine Gr/Ir(111) and (b) shows the O-intercalated Gr sample [9]. After O intercalation, the Dirac cone has shifted up as the Gr is p-doped. The minigaps and replica cones visible in (a) – both signs of the interaction of Gr with its substrate – have vanished. XPS measurements of O intercalated Gr/Ir(111) are shown in Figure 2.9(c) [33]. In the C 1s region, O intercalation is signaled by a shift of -0.45 eV relative to the pristine Gr C 1s peak when the saturation coverage is reached

(upper spectrum). For subsaturation coverages, two additional components (C_1 and C_2 in the figure) have to be introduced. For a detailed description of the energetics and kinetics of O intercalation the reader is referred to refs [33,55]. Martínez-Galera *et al.* have shown that dependent on the pressure and also the Gr morphology, O-(2×2), O-$(\sqrt{3} \times \sqrt{3})$R30°, O-$(2 \times 1)$, and O-$(2\sqrt{3} \times 2\sqrt{3})$R30° superstructures with respect to Ir(111) are observed underneath Gr [53]. Possibly, these structures can be linked to the C 1s components observed in XPS measurements [33].

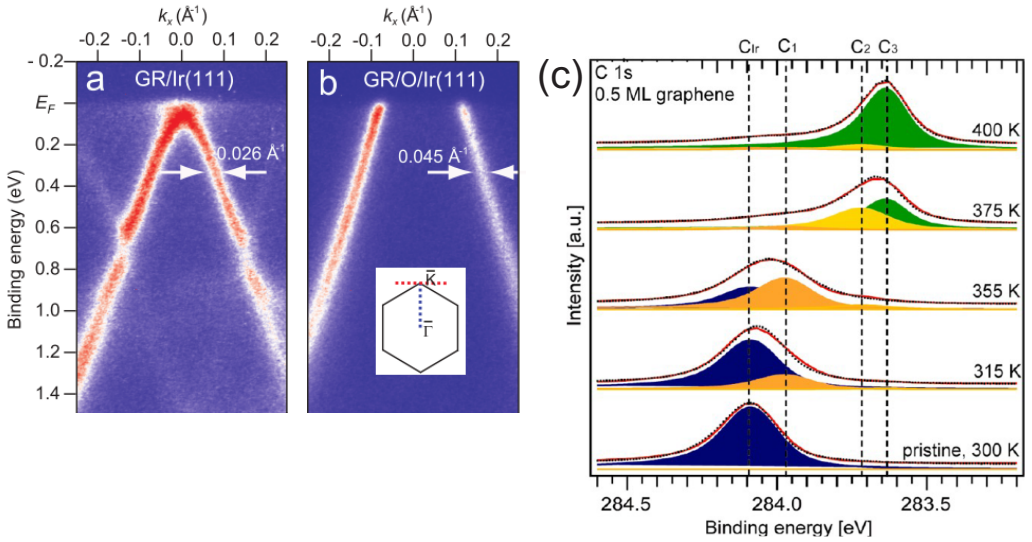

Figure 2.9: ARPES measurements of (a) pristine Gr/Ir(111) and (b) Gr intercalated by O. Adapted with permission from [9]. ©2012 American Chemical Society. (c) C 1s region measured by XPS of pristine Gr (lower spectrum) and Gr exposed to 750 Langmuir (L) O_2 at stepwise increasing temperatures as indicated in the figure. Black dots are the data, red lines are fits to the data, filled curves are fit components. From [33], ©2013 American Chemical Society.

Hydrogen intercalation

Hydrogen intercalation under Gr/Ir(111) is described in detail in ref. [32]. At low temperatures (90-140 K), hydrogen dissociatively adsorbs on bare Ir(111) patches and subsequently diffuses rapidly underneath the Gr flakes. Figure 2.10 shows the C 1s spectrum of H-intercalated Gr. The peak can be fitted by a component C_H (green), shifted by -0.18 eV compared to pristine Gr, and a component C_{Ir} (dark gray) corresponding to unintercalated Gr flakes,

some of which are always present. STM measurements show that it is mostly small flakes that do not grow over Ir step edges that resist intercalation [32]. Next to the C 1s spectrum, the corresponding Ir $4f_{7/2}$ spectrum is shown. It is fitted with four components, Ir_B (light gray) due to bulk Ir atoms, a small component Ir_S (blue) due to Ir surface atoms not covered by H atoms (i.e., underneath the unintercalated Gr flakes), and the main component, Ir_H (purple), due to H-covered Ir. Additionally, a small component Ir_{CO} needs to be included, due to CO contamination. This CO contamination can also be seen in the O 1s region shown in Figure 2.10(b). The different Ir 4f components are visualized in the schematics in Figure 2.10(c).

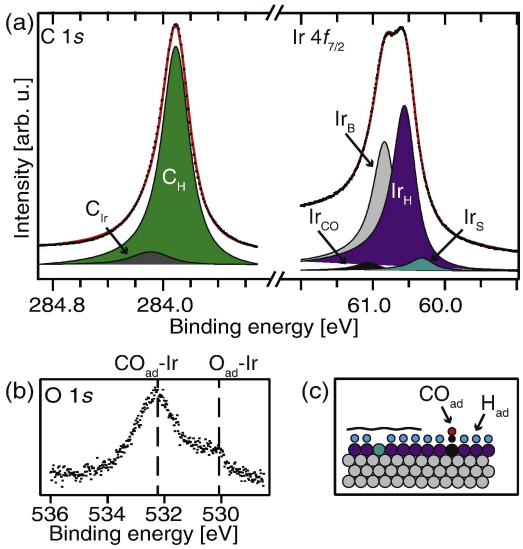

Figure 2.10: XP spectra of H intercalation of 0.5 ML Gr on Ir(111), obtained through exposure to $1 \cdot 10^{-6}$ mbar of H_2 during cool down from 300 K to 120 K, and an additional 5 min H_2 exposure at $5 \cdot 10^{-6}$ mbar at 120 K. (a) C 1s and Ir $4f_{7/2}$ spectra. Black dots are the data, red lines are fits to the data, filled curves are fit components. (b) O 1s spectrum showing contamination of adsorbed CO and O after the prolonged H_2 exposure. (c) Schematic model of the H-intercalated Gr. Black curve is Gr. Colors correspond to the colors of the fitted components in (a). Reprinted from [32], ©2016 with permission from Elsevier.

Europium intercalation

Europium (Eu) intercalates Gr when dosed at elevated temperatures (720 K) [56]. Depending on the coverage, the intercalated Eu forms either a (2×2) or

a $(\sqrt{3}\times\sqrt{3})$R30° superstructures with respect to Gr [57], as shown in Figure 2.11(a,b). It n-dopes the Gr by +1.36 eV in the (2×2) structure and by even +1.43 eV in the $(\sqrt{3}\times\sqrt{3})$R30° structure [57]. The corresponding ARPES measurements are shown in Figure 2.11(c,d).

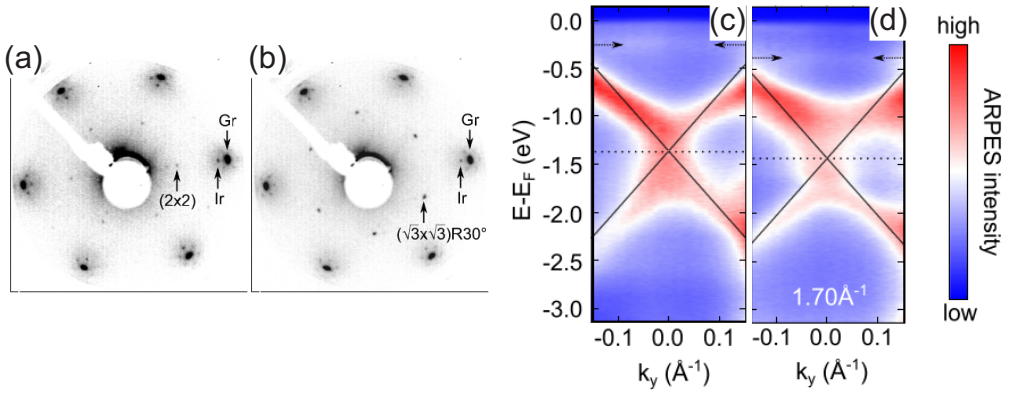

Figure 2.11: Eu intercalated Gr/Ir(111). LEED images of (a) the (2×2) and (b) the $(\sqrt{3}\times\sqrt{3})$R30° Eu intercalation structures under Gr. ARPES around the K point of Gr intercalated by (c) the (2×2) Eu and (d) the $(\sqrt{3}\times\sqrt{3})$R30° Eu structure. Reprinted figure with permission from [57]. ©2014 American Physical Society.

Caesium intercalation

The mechanisms of caesium (Cs) intercalation are described by Petrović *et al.* [58]. Upon deposition of low Cs doses at room temperature, a first phase, denoted α, develops where the Cs atoms sit on top of the Gr, as can be seen on the right-hand side of the STM image in Figure 2.12(a). In LEED [Figure 2.12(b)] the Gr moiré spots vanish due to the disordered adatom structure on top. The α-phase reaches its maxium density at 0.06 ML (1 ML here refers to the $(\sqrt{3}\times\sqrt{3})$R30° Cs saturation coverage, relative to Ir). Upon further Cs deposition, the two-dimensional pressure due to Cs-Cs repulsion overcomes the vdW binding of Gr to Ir and intercalation occurs through defects anchored at wrinkles in the Gr. The intercalated Cs (γ-phase) is visible on the left-hand side of the STM image in Figure 2.12(a). It forms a (2×2) structure relative to Gr and increases at the expense of the α-phase upon further Cs deposition. Once the entire sample has transformed into this structure (at approximately 0.92 ML), the γ-phase becomes even denser upon additional Cs deposition, forming a $(\sqrt{3}\times\sqrt{3})$R30° structure relative

to Ir. At saturation, only this latter structure is present [Figure 2.12(b)]. As visible in STM, no adatoms are present on top of the Cs-intercalated Gr.

Figure 2.12(c-e) show ARPES data of pristine Gr, Gr intercalated by 0.5 ML Cs, and Gr intercalated by 1 ML Cs, respectively. Below saturation, there are two Dirac cones visible due to phase separation. The lightly electron-doped Dirac cone (blue in the inset) corresponds to the α-phase, the heavily electron-doped Dirac cone (red) corresponds to the γ-phase. The saturated Cs intercalated sample in (c) shows only one Dirac cone, corresponding to the $(\sqrt{3}\times\sqrt{3})$R30° saturation structure. The Gr is then n-doped by 1.2 eV.

Lithium intercalation

Lithium (Li) has been used in graphite-intercalation compounds for decades [59, 60]. It intercalates readily under Gr/SiC at room temperature [61]. Recently, its intercalation under Gr/Ir(111) has been studied with DFT and ARPES [10, 58] as well as low-temperature STM [62]. vdW-DFT calculations show that intercalation is energetically favorable even for dilute Li phases [58]. The ARPES measurements displayed in Figure 2.13 show that Li-intercalation continuously shifts the Dirac cone as a function of Li dose, leading to a more and more n-doped Gr film. The fact that a single Dirac cone is observed for all Li coverages means that the system does not exhibit phase separation. Based on the reappearance of the Ir(111) spots in LEED, Pervan *et al.* [10] attribute the saturation Li intercalation coverage to a (1×1) structure relative to Ir.

Low temperature STM measurements of Halle *et al.* [62] – where Li was intercalated at 630 K and subsequently imaged at 6 K – reveal that at low Li coverages (0.037 Li atoms per Gr unit cell) intercalated Li dots appear in the *hcp*-sites of the Gr moiré. These dots grow in size until $\approx$ 7 Li atoms occupy one dot at a coverage of 0.061 Li atoms per Gr unit cell. At higher coverages ($\approx$ 0.167 Li atoms per Gr unit cell) the dots grow into cloverlike intercalation assemblies, or stripes near step edges or defects, attributed to the occupation of *fcc*-moiré lattice site.

Gold intercalation

Gold has been successfully intercalated underneath Gr/Ni(111) [63, 64], Gr/SiC(0001) [48, 65], Gr/Ru(0001) [66] and underneath Gr nanoflakes on Ir(111) [67]. Gr is decoupled from the underlying Au, as visible in ARPES measurements that show an unperturbed Dirac cone. Gr grown on a Au(111) substrate is slightly p-doped [68], for Gr/Au/Ni(111) doping levels of 0 eV

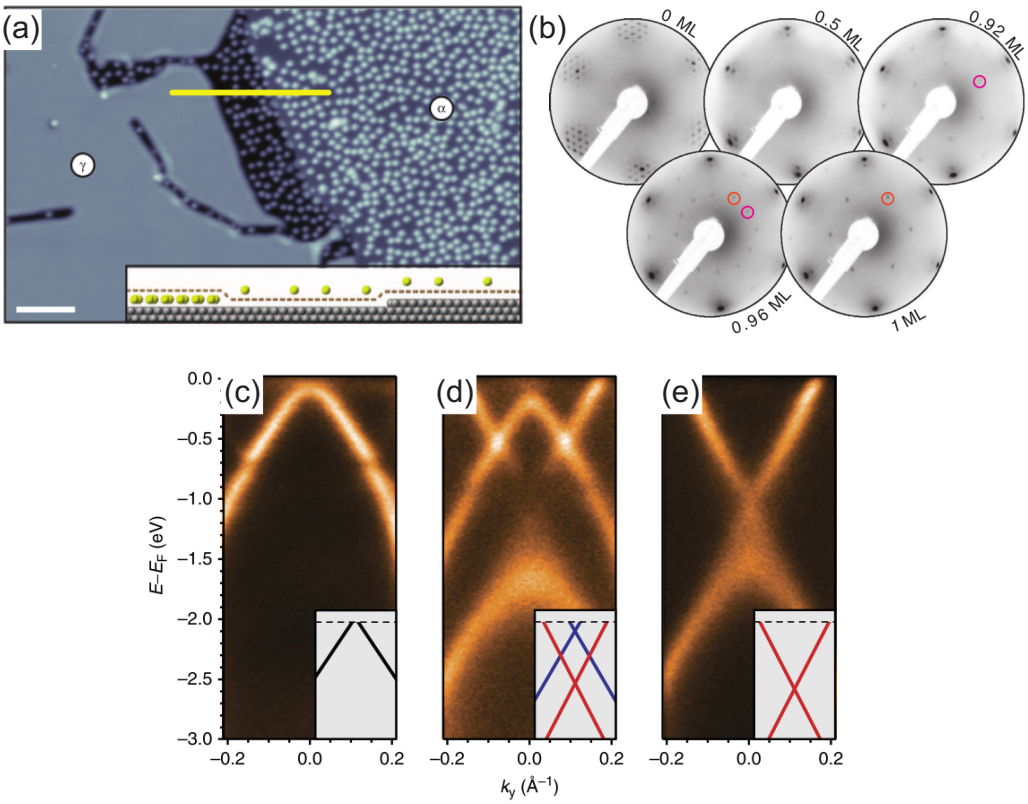

Figure 2.12: (a) STM image of the α- (right-hand side) and γ-phase (left-hand side) of Cs deposited on Gr/Ir(111). As seen in the schematic profile along the yellow line, the α-phase consists of adatoms on top of the Gr layer, whereas the γ-phase consists of intercalated Cs atoms. The white scale bar corresponds to 10 nm. Recorded at 6 K. (b) LEED patterns of Gr/Ir with increasing Cs coverages. First a (2×2) structure relative to Gr develops (magenta circles), upon further dosing a $(\sqrt{3} \times \sqrt{3})$R30° structure relative to Ir appears, which is the saturation structure (orange circles). The coverages given are relative to the Cs saturation coverage. (c-e) ARPES characterization of Cs intercalated Gr, (c) pristine Gr, (d) Gr intercalated by 0.5 ML Cs, (e) Gr intercalated by 1 ML Cs. The insets schematically indicate Dirac cones visible in the ARPES maps, corresponding to pristine (black), light (blue), and heavily (red) electron-doped Dirac cones. Adapted by permission from Macmillan Publishers Ltd [58] ©2013.

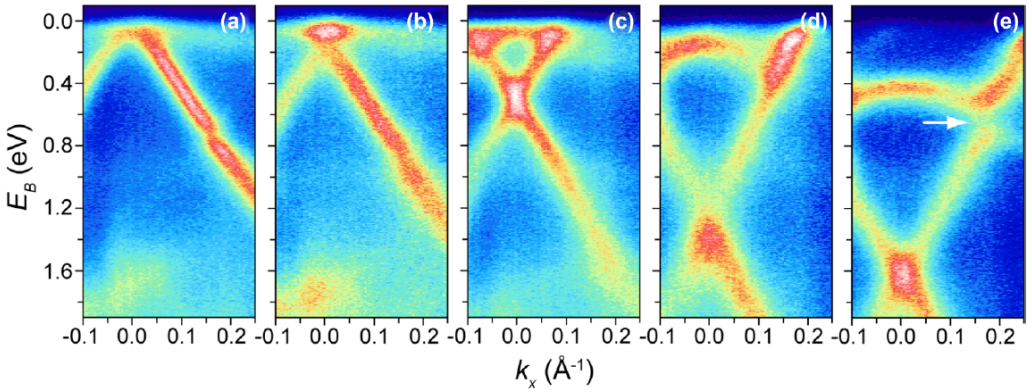

Figure 2.13: ARPES measurements showing the lower part (filled states) of the Gr Dirac cone for (a) pristine Gr/Ir(111), (b-e) increasing amounts of intercalated Li. Reprinted figure with permission from [10]. ©2015 American Physical Society.

[46, 63] and 0.1 eV [69] have been observed, and for Gr/1 ML Au/SiC(0001) also a slight p-doping of 0.1 eV is observed [65].

2.5 Surface reconstruction and strain relief patterns

The top atomic layer of a material is different from the bulk due to the lower coordination of atoms in the surface layer. This leads to tensile surface stress as surface atoms prefer shorter in-plane bond length. Thus, the equilibrium structure of the surface layer is expected to differ from that of bulk layers. When the interlayer distances of the first few layers differ from that of the bulk, this is called relaxation [30]. In some cases, the atomic structure of the top layer is modified, this is then called a reconstruction of the surface. Relaxation and reconstruction are due to the lowering of the Helmholtz free energy of the system. A prominent example is the surface of Au(111), which shows a $(22 \times \sqrt{3})$ reconstruction, called herringbone reconstruction, with a periodicity of 6.3 nm [72, 73]. An STM topograph is shown in Figure 2.14(a). As shown in the schematic in (b), most of the Au surface atoms sit in fcc adsorption sites, and a smaller fraction of surface atoms occupies hcp sites. This leads to an overoccupation and hence compression of the surface layer compared to bulk Au. Bright stripes are visible at the boundaries of fcc and hcp regions.

In epitaxial thin film growth, there are three principal near-equilibrium

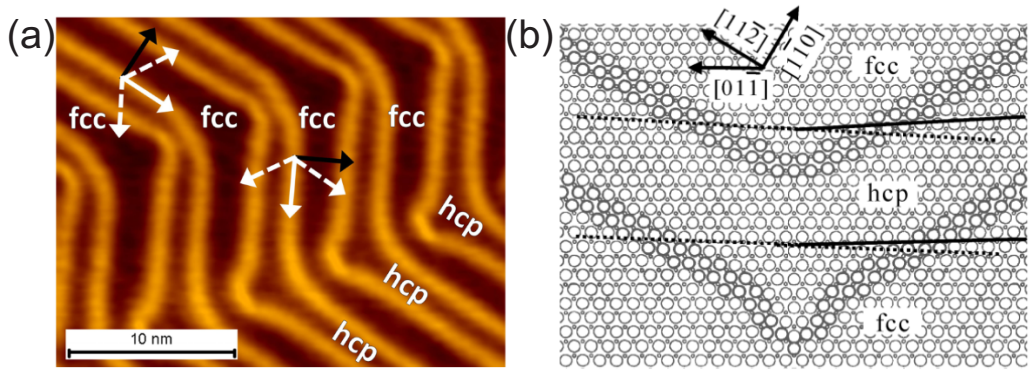

Figure 2.14: (a) STM image of a reconstructed Au(111) surface. Black arrows mark the compressed axis, solid white arrows mark the uncompressed $\sqrt{3}$ axes, dashed white arrows mark the partially compressed $\sqrt{3}$ axes. Reprinted from [70], with the permission of AIP Publishing. (b) Schematic model of the different regions of the $(22\times\sqrt{3})$ reconstructed Au(111) surface. Large circles are surface Au atoms, small circles are second-layer Au atoms. Regions where surface Au atoms adsorb on fcc and hcp adsorption sites are indicated, as well as the crystal directions. Reproduced from [71] with permission of the PCCP Owner Societies.

growth modes [30]. Layer-by-layer (or Frank-van der Merve) growth occurs when the film atoms are bound more strongly to the substrate then to each other. If, on the other hand, the film atoms are bound more strongly to each other than to the substrate, island (or Vollmer-Weber) growth is the result. Layer-plus-island (or Stranski-Krastanov) growth represents the intermediate case, where first a complete 2D layer is formed, followed by 3D-island growth. In the following, we will only consider layer-by-layer growth.

Strain, relaxation and reconstruction occur not only at the interface of a material to the vacuum, but also at the interface of two different materials. As the lattice constants of two materials differ, it is rare that commensurate, lattice-matched growth takes place. Typically, the crystal structure of the guest material differs from the host material. The misfit ϵ is a measure to quantify this difference and is given by [30]

$$\epsilon = \frac{d_{\text{guest}} - \mathrm{d}_{\text{host}}}{d_{\text{guest}}}. \tag{2.5.1}$$

It can also be viewed as the strain under which the guest material would be, if it were to grow lattice-matched. ϵ is positive if the guest material needs to be compressed, and negative if it needs to be stretched to fit commensurately on the host material. Low misfits can be accomodated by elastic

strain in the guest material while it keeps the periodicity of the underlying substrate. This is called pseudomorphic growth. The film is distorted in the perpendicular direction to the surface, due to the Poisson effect. At higher misfits, strain is relieved through dislocations at the film/substrate interface. Which growth mode prevails depends on the energy related to straining the guest film and the energy associated with dislocations. For a given thickness and below a certain critical misfit, a purely strained film is energetically favorable, whereas above this critical misfit, the dislocated film becomes favorable. Additionally, the film thickness also has an influence. As the strain energy increases with film thickness and the dislocation energy remains essentially constant, there is a critical thickness above which the introduction of dislocations is energetically favored.

Hexagonal surfaces are special as they possess two adsorption sites, fcc and hcp, which are very close in energy. Strain relief by dislocations can thus occur through fcc-hcp domain boundaries. The low energy cost for forming these kind of domain walls typically reduces the critical thickness to 0 or just the first monolayer. fcc-hcp domain boundaries can lead to striped or trigonal strain relief patterns [74, 75]. Both stress and strain can be released through the striped or trigonal patterns, depending on whether the boundary is such that it leads to over- or underoccupation in the surface layer compared to the underlying layers.

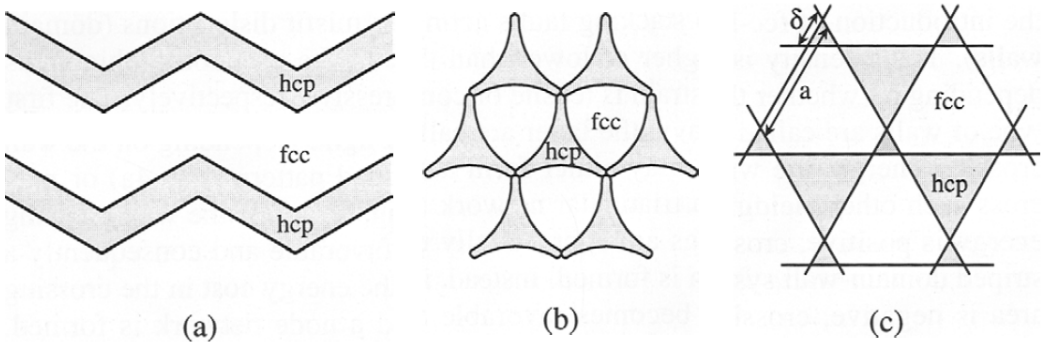

Figure 2.15: Possible domain wall structures on fcc(111) surfaces. (a) Striped phase with mesoscopic bending into a herringbone structure. (b,c) trigonal networks with wall crossings. Reprinted from [76], ©1997, with permission from Elsevier. See also [75].

The energy required for a domain boundary crossing is called crossing energy, it is negative if boundaries are preferred, and positive if not. Positive crossing energies thus lead to striped patterns (herringbone), negative cross-

ing energies to trigonal patterns [76], visualized in Figure 2.15. Boundaries can be shifted with respect to each other, leading to different ratios in fcc-to-hcp area, to alternating small and large triangles, or to an almost hexagonal pattern [Figure 2.15(c)].

Trigonal and striped strain relief patterns have been observed for a variety of hexagonal systems. The resulting patterns depend on the specific systems, and even for one system they depend on the number of layers, as for Cu/Ru(0001) [77, 78] or on the growth or annealing temperature, as for Ag/Pt(111) [74] and Ag/Re(0001) [79]. Systems where striped or trigonal strain relief patterns were observed by STM are summarized in Table 2.1, ranging from positive to negative misfits.

Table 2.1: Comparison of the misfit ϵ of metal epitaxy on hexagonal surfaces from the literature.

guest/host	ϵ (%)	reference
Cr/Re(0001)	32.328	[80]
Fe/Re(0001)	31.894	[80]
Ag/Ru(0001)	6.334	[81–83]
Au/Ru(0001)	6.172	[83]
Au/Ir(111)	5.860	this work
Ag/Re(0001)	4.431	[79]
Ag/Pt(111)	3.946	[74, 84]
Ag/Al(111)	0.900	[85]
Cu/Ru(0001)	-5.869	[77, 78, 86]
Co/Re(0001)	-10.132	[80]
Co/Pt(111)	-10.690	[87]
Ni/Re(0001)	-10.795	[88]

2.6 Hydrogen on Ir(111)

The terms hydrogen and deuterium are often used interchangeably in the literature, as the two are chemically equivalent. For simplicity, in this work the term hydrogen will be used when stating general facts applying to both hydrogen and deuterium. The abbreviation D or H (or D_2, H_2) will be used when we wish to refer to the specific isotope (e.g., when describing experiments).

Hydrogen dissociatively adsorbs on the Ir(111) surface [89] with a $p(1\times1)$ saturation structure [90]. It is highly mobile with a diffusion barrier for atomic H on Ir of only approximately 0.13–0.17 eV [91]. TPD spectra of D_2 on Ir(111) are shown in Figure 2.16. Although D is dosed onto the sample, mass 4 (D_2) is measured, stemming from recombining D atoms. Two desorption peaks can be identified, termed β_1 and β_2. The β_2-peak is present already for low coverages, it appears at 310 K and shifts to 270 K [89] for higher coverages [Figure 2.16(a)]. This downshift with increasing coverage, together with the symmetrical peak shape, is characteristic for second-order recombinative desorption of D_2 [30, 89]. Towards saturation the β_2 peak appears at 190 K. Hagedorn *et al.* [89] attribute the β_2-peak to second-order recombinative desorption of delocalized D atoms and the β_1-peak to desorption of localized D atoms when the coverage is sufficiently high. Moritani *et al.* [92] [Figure 2.16(b)] additionally resolve a peak at 320 K, and their β_1 and β_2 peaks appear at slightly shifted temperatures of $\approx$ 155 K and $\approx$ 220 K, respectively. These differences are probably due to the different heating rate. From Figure 2.16 it can be seen that the sticking coefficient of D on Ir decreases with increasing coverage. To go from $\theta = 0.90$ to 1.00, a factor 10 in dosage is needed (compare to the factor 1.11 in coverage).

2.7 Atomic hydrogen on graphite and Gr

The interaction of Gr with atomic H or D is interesting for a variety of reasons, including the formation of a bandgap in Gr [6], or the formation of graphane [93].

Graphane

Graphane is Gr with a hydrogen attached to every C atom, but sitting alternately on different sides of the Gr sheet, shown in Figure 2.17. Upon complete hydrogenation, every C atom is sp^3-hybridized. As shown by Elias *et al.* [93], subjecting free-standing Gr to atomic hydrogen (the authors use

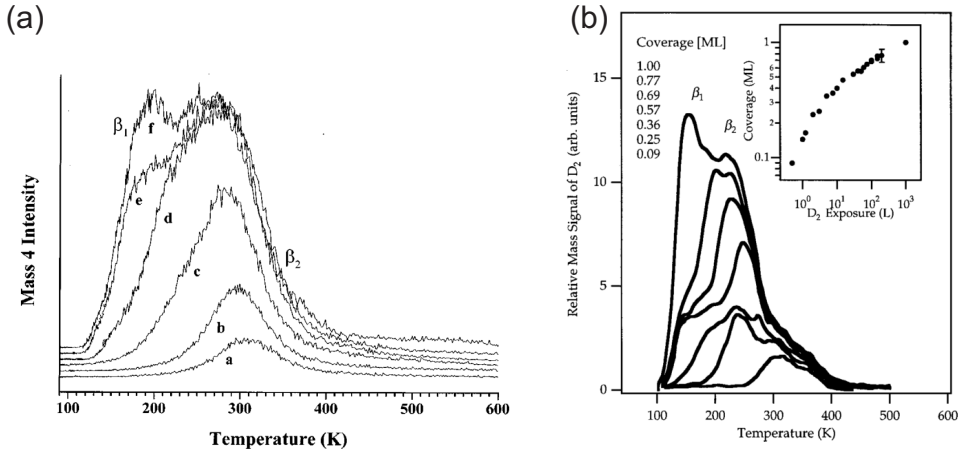

Figure 2.16: (a) TPD spectra of various doses of D_2 to the clean Ir(111) surface at 90 K. Heating rates 20 K/s. The curves lettered a–f correspond to different doses, the resulting relative coverages θ are given in parentheses. a: 1 L ($\theta = 0.09$); b: 2 L ($\theta = 0.18$); c: 5 L ($\theta = 0.44$); d: 20 L ($\theta = 0.77$); e: 100 L ($\theta = 0.90$); f: 1000 L ($\theta = 1.00$). Reprinted figure with permission from [89]. ©1999 American Physical Society. (b) TPD of various doses of D_2 on clean Ir(111) at 100 K. Indicated are the relative coverages, where 1.00 corresponds to a dose of 1000 L. Heating rates 1 K/s. The inset shows the deuterium uptake curve, determined by integrating the TPD spectra. Reprinted from [92], with the permission of AIP Publishing.

a cold hydrogen plasma) leads to the formation of graphane.

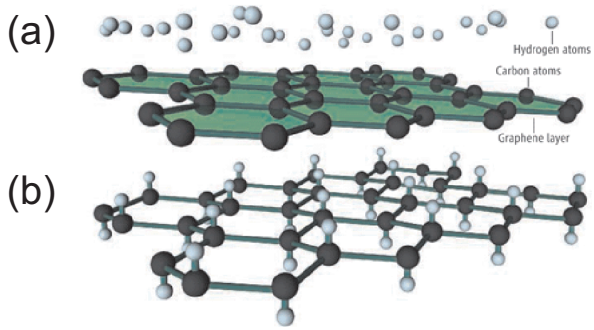

Figure 2.17: (a) A Gr layer (C atoms are black spheres) exposed to a beam of atomic hydrogen atoms (white spheres) leads to formation of (b) graphane, where hydrogen binds alternately to the C atoms. From [94]. Reprinted with permission from AAAS.

Atomic hydrogen on graphite

The adsorption of atomic hydrogen on HOPG has been well-studied [95–100] due to its relevance in interstellar chemistry. Although in certain regions of space, H atoms are dissociated by ultraviolet and cosmic radiation, H_2 is still the most abundant molecule [101]. H_2 formation cannot be explained with a gas-phase mechanism due to the low density of H atoms [102]. Instead, it has been shown that H_2 formation occurs on the surface of carbonaceous dust grains [103], and the (0001) surface of highly-oriented pyrolytic graphite (HOPG) has been successfully used as a model system to study H recombination dynamics [97]. The (0001) surface of highly ordered pyrolytic graphite (HOPG) can be viewed as one layer Gr, stacked onto many others in ABAB-stacking order. It is therefore worthwhile to see how atomic hydrogen behaves on HOPG.

Hornekaer *et al.* [97] found by STM and TPD that at low coverage hydrogen dimers form on graphite, as displayed in Figure 2.18. Dimers are pairs of H atoms bound to the same C ring. From simulated STM pictures, corroborated by DFT calculations, the authors deduce that the most stable dimer formations are those in *ortho* configuration [Figure 2.18(b)], followed by those in *para* configuration [Figure 2.18(c)].

Hydrogen atoms in any dimer configuration are more stable than two monomers would be, because formation of a single H-C bond requires a C=C

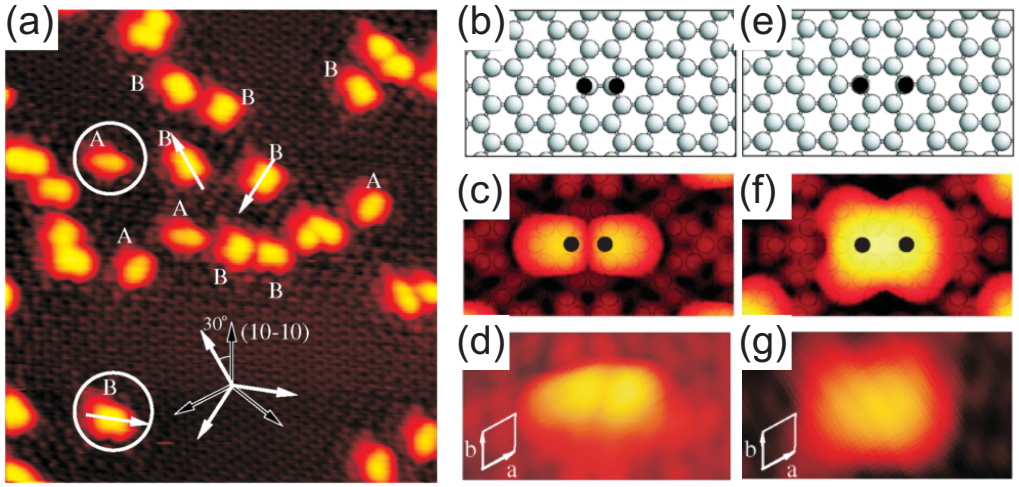

Figure 2.18: (a) STM image of H dimers adsorbed on HOPG. Dimers in the *ortho* configuration are marked with an 'A', those in *para* configuration with a 'B'. Image size 10.3 nm × 11.4 nm. (b-d) show the *ortho* configuration and a simulated and a measured STM image thereof, from top to bottom. (e-g) show the *para* configuration, a simulated and a measured STM image thereof, from top to bottom. Reprinted figure with permission from [97]. ©2006 American Physical Society.

double bond to break and thus leaves an unpaired electron on the neighboring C atom. This configuration is only metastable at room temperature resulting in desorption on a timescale of minutes at room temperature [98] unless joined by a second hydrogen atom, thus forming a dimer. Dimers in the *meta* configuration - that is, sitting on next-nearest neighbor C atoms - have a low barrier of diffusion into either *ortho* or *para* dimers. The desorption path for *ortho* dimers was calculated to be diffusion into the *meta* and subsequently the *para* configuration and desorption from there [97]. According to Hornekaer *et al.* [98] the barrier of adsorption for a second H atom is strongly reduced compared to monomer adsorption, leading to clustering of H atoms on HOPG by preferential sticking.

TPD measurements of D on HOPG were measured by a number of groups [95–97, 99], an example is shown in Figure 2.19. For low coverages a double peak structure is observed, with the main peak at 490 K and a shoulder at 580 K [95]. As shown in 2004 [96], the double-peak structure observed is not defect related but intrinsic for hydrogen desorption from terraces. The two peaks that are resolvable at low coverages were assigned by Hornekaer *et al.* [97] to the aforementioned *para* (490 K) and *ortho* (580 K) dimers, based on STM experiments where, upon heating, only *ortho* dimers were observed on the sample. The process leading to the 580 K peak is not direct desorption of *ortho* dimers but diffusion of *ortho* dimers into the *para* state which at 580 K desorbs immediately [97]. At higher doses, the lower peak shifts to 500 K and a shoulder at 540 K develops [95]. The reason for this is reduced barriers of adsorption for third and fourth adatoms arriving next to *para* dimers, referred to as clustering [98, 100, 104]. Those clusters then desorb via the *para*-type reaction path [99]. When adsorbing H instead of D, an isotopic shift to lower temperatures is observed, by ≈ 40 K for the main peak and shoulder, and by ≈ 20 K for the high temperature peak [95]. This difference in isotopic shift attributed to a different bonding environment of the hydrogen in the two peaks.

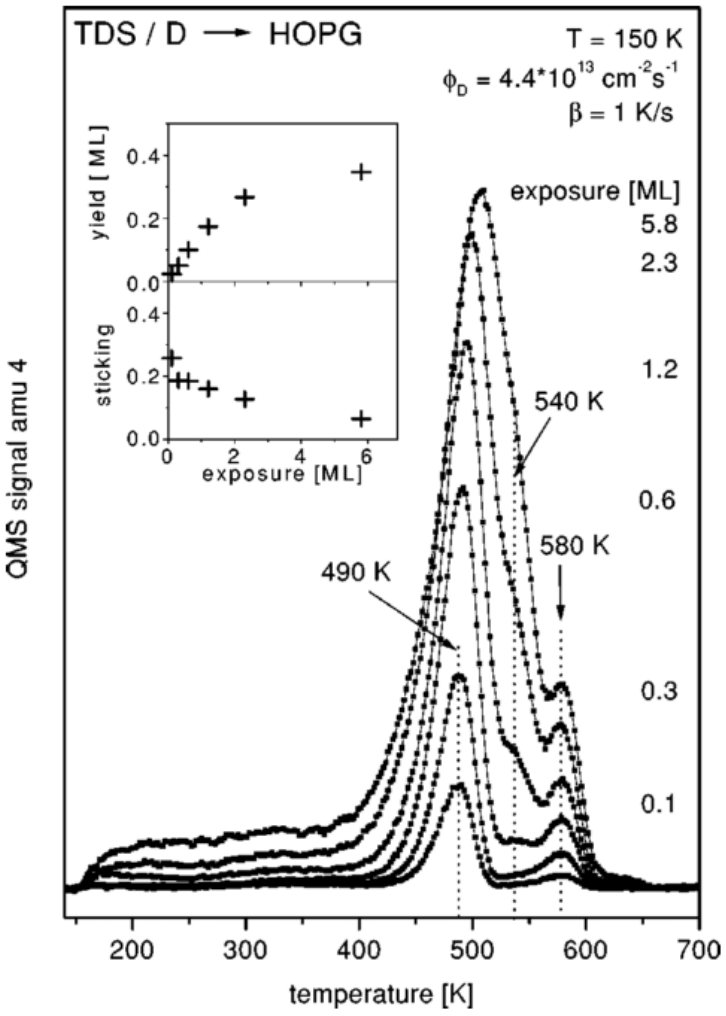

Figure 2.19: TPD spectra for atomic D dosed on HOPG at 150 K. The atom exposures are given in units of graphite monolayers, 1 ML= $3.8 \cdot 10^{15}\,\mathrm{cm}^{-2}$. Heating rate 1 K/s. The inset illustrates the D uptake and the sticking coefficient as a funciton of the D coverage. Reprinted from [95], with the permission of AIP Publishing.

Atomic hydrogen on Gr/Ir(111)

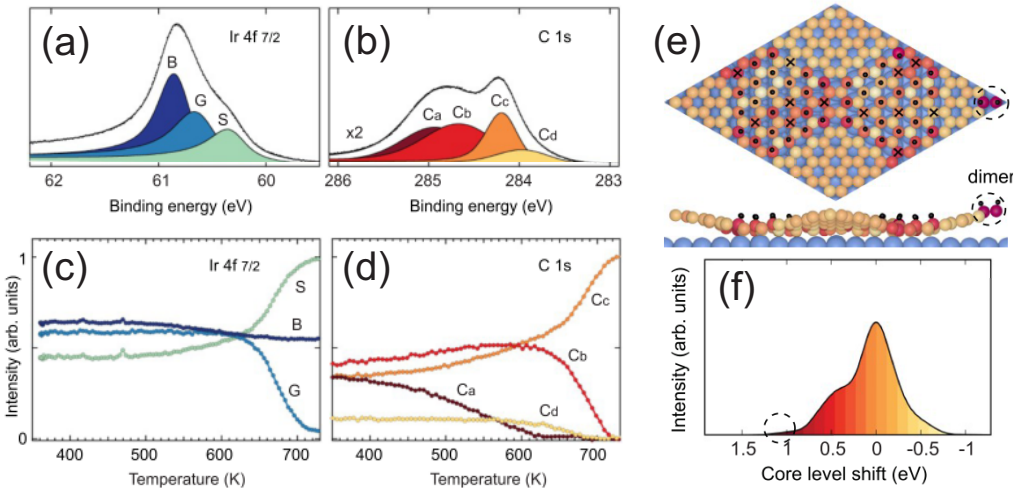

Figure 2.20: Hydrogenated Gr/Ir(111) studied by XPS and DFT. XP spectra of (a) the Ir $4f_{7/2}$ region and (b) the C 1s regions. Black lines are data, the filled colored lines fitting components (see text). (c,d) Evolution of the component intensities when heating the sample. (e) Proposed structure of H atoms on Gr, Gr atoms are sphere colored yellow to red, H atoms are small black spheres, vacancies are indicated by an X, and the Ir substrate atoms are displayed in blue. Encircled is a dimer structure (see text). (f) CLSs calculated by DFT according to the structure displayed in (e), colors correspond to colors of the C atoms. Adapted with permission from [105]. ©2013 American Chemical Society.

The adsorption of atomic hydrogen on Gr/Ir(111) has been studied by various groups by XPS, STM, DFT, high resolution electron energy loss spectrometry (HREELS) and sum-frequency generation spectroscopy (SFG) [6, 16–18, 105–107]. Most authors agree that hydrogen adsorbs in 'graphane-like' patches that follow the moiré periodicity where C atoms alternately bind up to hydrogen atoms and down to the Ir substrate, similar to the cluster binding mechanism described in Section 2.2. This corresponds to hydrogen atoms sitting in *meta* configurations. Hydrogen adsorption was shown to open up a bandgap [6] of at least 0.45 eV due to symmetry breaking [108]. According to Balog *et al.* [6, 105], 'graphane-like' H-islands form in fcc and hcp sites and dimers, similar to what is observed on HOPG, form in the sp^2-hybridized top areas of the Gr. The dimers and also H-vacancies in the H-islands need to be included in order for their DFT calculations, shown

in Figure 2.20(e,f), to, at least approximatively, reproduce the XPS peak shape, shown in Figure 2.20(b). Figure 2.20(a,b) show the Ir $4f_{7/2}$ and C 1s spectra after hydrogenation of Gr. For pristine Gr, the Ir $4f_{7/2}$ signal consists of a bulk component (B) and a surface component (S). Upon hydrogenation, part of the surface component is shifted to lower binding energy (G), due to C atoms binding down to Ir atoms. The C 1s spectrum appears rather complicated and is fitted by four components. C_c corresponds to the pristine Gr component. DFT calculations suggest that C atoms bound to H can possess either negative or positive CLSs, depending on the H-island size and on the exact position. Components C_b and C_d are assigned to originate from 'graphane-like' environments, while the C_a component is attributed to dimers in the atop regions of the moiré. The group of Hasselbrink [16, 17, 107] has performed SFG measurements on hydrogenated Gr/Ir(111) and their results suggest graphane formation. Their work will be discussed in more detail in Section 7.4.

Atomic hydrogen on Gr/Pt(111): STM and TPD

Atomic H dosed on Gr/Pt(111) was studied by Rajasekaran *et al.* [109, 110]. From STM and XPS, it appears to behave similar as H on Gr/Ir(111) [109]. H adsorbs on Gr/Pt(111) in a ring-like manner following the moiré periodicity, visible in Figure 2.21(b), similar to its behavior on Gr/Ir(111) [6]. The authors state that the predominant Gr domain displays a 1.95 nm moiré periodicity, characterized as the $(\sqrt{63} \times \sqrt{63})R19°$ structure [111]. The C 1s spectrum [Figure 2.21(c)] displays a similar shape as H on Gr/Ir(111) [105], and in the Pt $4f_{7/2}$ region [Figure 2.21(e)], the disappearance of the surface peak is visible. It is therefore plausible that, just as proposed for Gr/Ir, H on Gr/Pt forms graphane-like patches where C atoms sp^2-rehybridize and alternately bind up to H atoms and down to the substrate.

A TPD spectrum for D on Gr/Pt(111) was also measured by the same group [110], it is displayed in Figure 2.22 (black curve). It displays a peak at ≈ 640 K with a shoulder at ≈ 690 K. Dinger *et al.* [112] observe the same peak-and-shoulder shape in their TPD (note that the conclusions drawn – hydrogens binding to Gr edges give rise to the TPD signal – are wrong). For saturation doses of D on Gr/Pt(111) they observe the peak at 630 K and the shoulder at 675 K, in line with ref. [110], shown in Figure 2.22(b). They observe an isotope shift when they dose H on Gr/Pt(111), with the peak then at 600 K and a shoulder at 650 K. They find an H-coverage dependence in the main peak, it shifts from ≈ 550 K to ≈ 600 K. The shoulder displays only a very slight dependence of maybe 10 K. Andersen *et al.* find with DFT that graphane-like H-clusters on Gr/Pt(111) show an increase in

binding energy with increasing cluster size. Especially the STM images suggest that graphane-like H- or D-clusters exist, as in the case of Gr/Ir(111). The feature observed in TPD must then be due to desorption from those graphane-like clusters. Whether both peak and shoulder can be attributed to this, or whether one stems from another binding type of hydrogen, has not been studied, and is hard to decide based on the available data.

A further complication enters with the observation by Rajasekaran *et al.* [110] who supposedly grew few-layer Gr on Pt(111), adsorb atomic D on this, and obtain a TPD curve [red curve in Figure 2.22(a)] that is strikingly similar to that obtained from D on 1 ML Gr/Pt(111). The interpretation given by the authors is that the surface adsorption of H induces a sp^2-to-sp^3-rehybridization of the C atoms that propagates through the Gr layers, resulting in interlayer C bond formation that is stabilized through the termination of interfacial sp^3 C atoms by the substrate. Two alternative interpretations come to mind. (i) The authors have not succeeded in growing few-layer Gr, and have misinterpreted their XPS Gr-coverage data, maybe because their 1 ML Gr recipe does not yield a full layer. Unfortunately, no TPD data is shown below 350 K which happens to be the temperature where H desorption from Pt(111) would come to an end. (ii) H on Gr/Pt(111) behaves similarly as H on HOPG and this is why the spectra of 1 ML Gr/Pt and 4 ML Gr/Pt look alike. Indeed, spectra of H on HOPG have the same peak-and-shoulder shape, only shifted to lower temperature. However, above a certain number of Gr layers a shift of the spectral features to lower temperatures should be visible. This is not the case yet in the data displayed, raising the question why and how 4 ML Gr are different from HOPG.

Atomic H on Gr/Ni(111)

H on Gr/Ni(111) was studied with TPD, XPS and DFT by Zhao *et al.* [113]. Gr/Ni(111) grows commensurate [114], and DFT calculations found the most stable adsorption site for H to be on C atoms above fcc-hollow site, at full coverage leading to a *meta* configuration, i.e., every second C atom is occupied by an H atom [113]. Figure 2.23 shows the TPD spectra for low (top), medium (middle) and high (bottom) doses of atomic H on Gr/Ni(111). For low H coverages the main desorption peak lies at ≈ 600 K, but interestingly, this peak decreases in height for high H coverages, at the expense of a desorption peak at ≈ 370 K. With the help of DFT calculations this at first glance strange behavior is explained as follows: the 370 K desorption peak is due to H atoms desorbing from a *meta* state, i.e., H atoms adsorbed on two C atoms that are next-nearest neighbors. At high coverages, a lot of H atoms happen to be adsorbed in this configuration and can desorb directly.

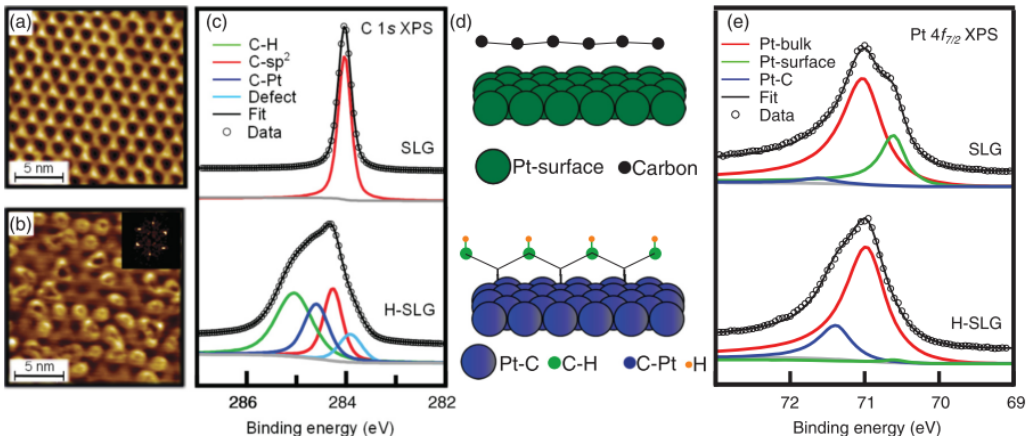

Figure 2.21: H adsorbed on Gr/Pt(111) studied by STM and XPS. STM images of (a) pristine Gr/Pt(111), (b) H on Gr/Pt(111). XP spectra displaying (c) the C 1s region of pristine Gr/Pt(111) (upper spectrum) and H on Gr/Pt(111) (lower spectrum), (e) the Pt $4f_{7/2}$ region of pristine Gr/Pt(111) (upper spectrum) and H on Gr/Pt(111) (lower spectrum). (d) gives a sketch of the proposed bindings in certain parts of the moiré for pristine Gr/Pt(111) (upper sketch) and H on Gr/Pt(111) (lower sketch). In (c,e) black dots are the data, black lines are fits to the data, colored curves are fit components. Reprinted figure with permission from [109]. ©2012 American Physical Society.

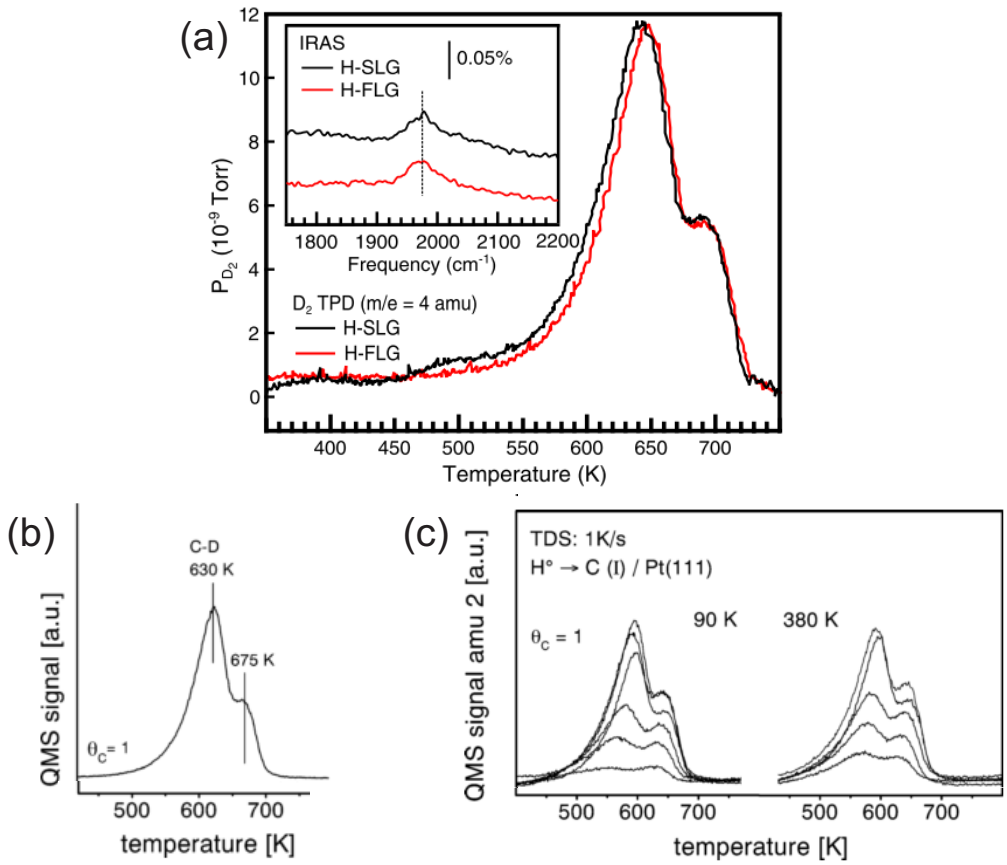

Figure 2.22: (a) TPD spectra of D_2 dosed on single layer Gr/Pt(111) (black curve) and few-layer Gr/Pt(111) (red curve). The inset shows IR absorption spectra of the C-D vibrational mode for both samples. Reprinted figure with permission from [110]. ©2013 American Physical Society. (b) TPD spectrum of a saturated D dose on 1 ML Gr/Pt(111). Reprinted from [112], ©1999, with permission from Elsevier. (c) TPD spectra of various doses of H dosed at 90 K (left spectra) or 380 K (right spectra) on 1 ML Gr/Pt(111). Reprinted from [112], ©1999, with permission from Elsevier.

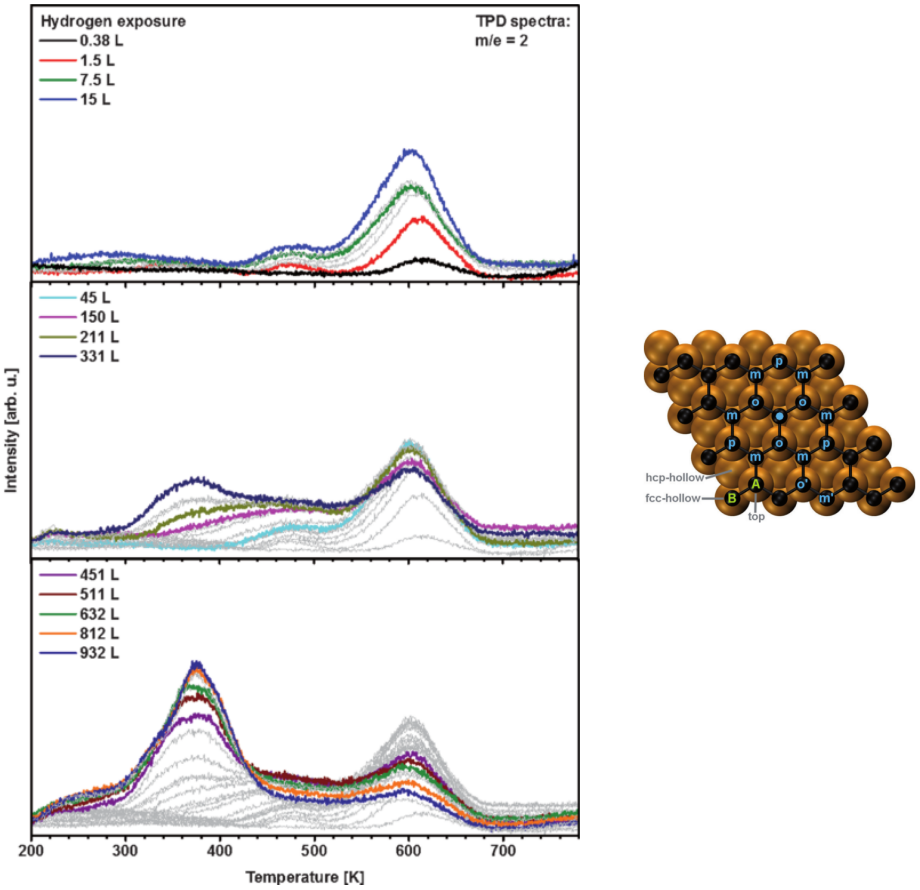

Figure 2.23: TPD spectra of various H doses (indicated in L) onto Gr/Ni(111) at 170 K. Heating rates 3 K/s. On the right a schematic top view of Gr/Ni(111) is with Ni atoms in brown, C atoms in black and H patterns in blue letters. The blue circle marks the reference point, and neighboring sites are denoted *ortho* (o), *meta* (m), and *para* (p). From [113]. ©2015 Wiley-VCH Verlag GmbH & Co. KGaA, Weinheim.

At lower coverages, however, random adsorption and the absence of diffusion at dosing temperature make it improbable that H atoms are adsorbed in the *meta* state. DFT calculations show that direct desorption from other adsorption states or from isolated H atoms is less likely than diffusion into the *meta* state, and thus at low H coverages the desorption process is diffusion limited. A higher energy is needed for diffusion to than for desorption from the *meta* state, leading to a higher desorption temperature.

Atomic hydrogen on Gr/Au

Hydrogenation of Gr on Au was studied for the system Gr/Au/Ni(111) [63, 115, 116]. Note that as intercalation of Au seems to be limited to 1 ML in the Gr/Ni(111) system [64] it is questionable to what extent Gr/1 ML Au/Ni(111) is comparable to Gr on many layers Au.

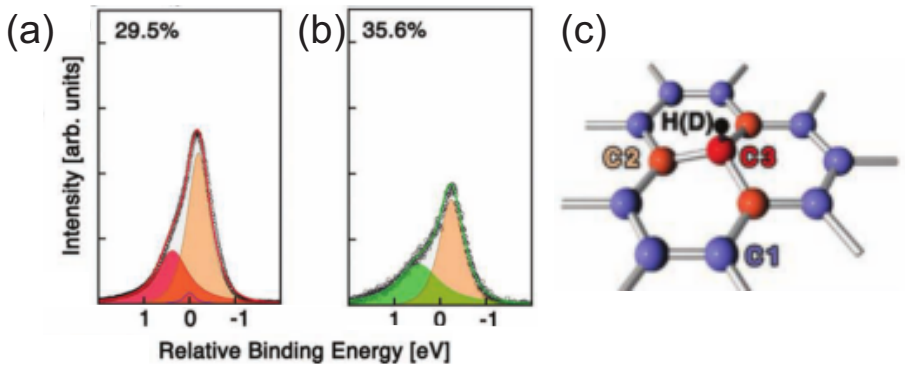

Figure 2.24: XP spectra of the C 1s region of a saturation dose of atomic (a) H and (b) D on Gr/Au/Ni. Red and green lines are fits to the data, orange components represent unhydrogenated C atoms (C_2), and red or green components represent hydrogenated C atoms (C_3). (c) Schematic representation of H or D (black) adsorbed to Gr, C atoms corresponding to the components in (a,b) are labeled. From [116]. ©2013 WILEY-VCH Verlag GmbH & Co. KGaA, Weinheim.

Haberer *et al.* [63] observe signs for partial sp^3-rehybridization of the Gr upon hydrogenation but attribute this only to C atoms binding upwards to H. XP spectra of D and H on Gr/Au/Ni(111) are shown in Figure 2.24. The C 1s spectrum can be fitted with three components corresponding to pristine Gr (C_1, barely visible at saturation coverage), to C atoms that are next-nearest neighbor to a C-H bond (C_2), and to C atoms that are neighbors to a C-H bond (C_3) [63]. The coverages are calculated by $C_3/(C_1 + C_2 + C_3)$ and are obviously based on the assumption that C_3 atoms only bind upwards to H or

D and never down to Au. For details on the kinetic isotope effect resulting in the different saturation coverages for H and D, the interested reader is referred to the publication [116]. Scheffler *et al.* observe with STM for very low H coverages triangular shapes and shapes elongated along the zigzag edges of Gr. They attribute these shapes to single and double C-H sites, respectively. As only the *meta* configuration gives rise to a spatial extension of the charge density along the zigzag edges of Gr they believe their elongated shapes to be H atoms in *meta* configurations.

Chapter 3

Experimental

STM, TPD and LEED experiments were performed at the TuMA III lab in Cologne while XPS experiments were performed at beamline I311 [117] of the MAX IV Laboratory in Lund. In the following, the experimental techniques used within this work are described, and the two setups are briefly described, as well as typical sample preparation methods.

3.1 Scanning tunneling microscopy

Scanning tunneling microscopy (STM) relies on the tunneling effect [118]. An atomically sharp tip is brought very close (in the order of Ångströms) to a conducting surface. A bias voltage is applied to either surface or tip. This leads to a tunneling current I. As the tunneling probability is exponentially damped with the width of the vacuum barrier, I depends sensitively on the distance between tip and sample. Furthermore, I depends on the electron density of states and the work function of both tip and sample. Therefore, the resulting image can be understood as a convolution of the topography and the local electron density of states.

In practice, the tip is attached to a piezo element. By applying a voltage to the piezo element, the height of the tip can be controlled, and it can be scanned laterally over the sample. Our STM is beetle-type, employed in constant-current mode [119]. A bias voltage applied to the sample induced the tunneling current. The tunneling tip was made of an electrochemically etched platinum(0.8)-iridium(0.2) wire with a diameter of 0.25 mm provided by Keysight Technologies.

Unless otherwise noted, STM images were recorded at room temperature. All STM images were processed using WSxM software [120]. The tunneling parameters are indicated in the figure captions.

3.2 Temperature programmed desorption

In temperature programmed desorption (TPD) the sample is placed beneath a mass spectrometer and heated, typically with a linear heating rate. The desorbed species are measured and the desorption signal is plotted against the temperature. The resulting spectra can yield information on the binding energy of the species, its mobility on the surface and its desorption mechanics. A helpful description of the physics involved is given by Standop [121], while spectral analysis is explained clearly by King [122].

We use a quadrupole mass spectrometer (Pfeiffer Vacuum QME-200) equipped with a Feulner cup [123] to reduce desorption signals from the sample holder or chamber surroundings. Chemical species are ionized by a filament in the mass spectrometer and detected based on their mass-to-charge ratio, assuming single ionization.

During the TPD measurements in Chapter 4 (Oxygen etching), the sample holder was cooled with liquid nitrogen to avoid desorption from the sample holder. The desorption of CO and CO_2 was measured simultaneously, enabling the correction of the CO signal for the contribution due to CO fragments of CO_2 created by electron impact ionization.

In Sections 7.1 - 7.5 (Deuteration of Gr/Ir) a polynomial background was subtracted (for details see ref [124]), in Section 7.6 and Chapters 4 (Oxygen etching) and 8 (Au intercalation and deuteration of Gr/Au/Ir) a linear background was subtracted, determined by one point at the beginning of the spectrum and one or more points at the end. The first point was found by looking at the measurement signal against time and determining the intensity value shortly before heating was turned on. The high-temperature end of the fitting regime can be easily identified, there the intensity is approximately linear and slowly decreasing. This is shown in Figure 3.1. No background subtraction was used for the TPD spectrum in Chapter 6 (OH-H_2O phase).

The desorption signal measured is a current, but since the mass spectrometer was not calibrated, a.u. are given as units. To enable comparison between different spectra, the factors by which the measured currents were divided are given in the figures as well, reading for example 'Intensity ($\times 10^{-9}$) a.u.'.

Especially when dosing atomic D on Gr/Ir(111), some inconsistencies in the TPD intensities were noted [124]. A slow decrease in intensities was found over the course of one year. The intensities of different spectra displayed in one graph can be safely compared if not noted otherwise, as they were taken within a single or a few days. Comparing intensities from different experiments, however, should be done with some caution.

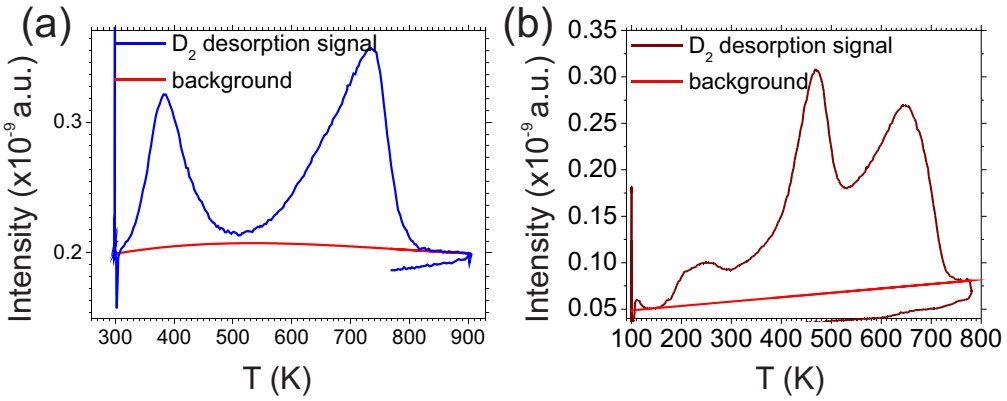

Figure 3.1: TPD background subtraction, blue and brown are measured D_2 adsorption signals, red is the background. (a) Typical background subtraction for deuterated Gr/Ir(111), see Chapter 7. Adapted from [124]. (b) Typical background subtraction for deuterated Gr/Au, see Chapter 8. Heating rate 5 K/s.

3.3 Low energy electron diffraction

Low energy electron diffraction (LEED) allows to observe ordered structures at the sample surface in reciprocal space [30]. We use LEED to confirm the Gr quality after growth, to check intercalation processes as many intercalants form well-ordered structures, and in general to examine if foreign species introduced to the sample arrange in a well-ordered manner. The LEED patterns were documented using a hand-held digital camera. The electron energy is indicated in the figure captions.

3.4 X-ray photoelectron spectroscopy

The details of the X-ray photoelectron spectroscopy (XPS) technique are described in Section 2.3. Here, we describe the details of data aquisition and analysis. All XPS spectra were collected in normal emission with an acceptance angle of $\pm 5°$. Binding energies are calibrated to the Fermi edge. Specifics like photon energy or data analysis vary slightly and are described for each chapter separately in the following.

The XP spectra shown in Chapter 4 (Oxygen etching) were measured with photon energies of 390 eV for C 1s, 190 eV for Ir 4f, and 625 eV for O 1s, unless otherwise indicated. The total energy resolution of the light and analyzer is better than 60 meV, 45 meV, and 200 meV for the respective

core level spectra. Curve fitting was performed with Doniach-Šunjić functions convoluted with Gaussians, together with linear backgrounds. The Gaussian Full Width at Half Maximum (GFWHM) is a measure for the statistical error of the experiment. As far as no changes were made to the experimental setup (e.g., moving the sample, mirror or monochromator) the GFWHM should stay more or less constant during one experiment. The Lorentzian Full Width at Half Maximum (LFWHM) is a value specific for the bound state and depends on the lifetime of the final state. Usually, it is experimentally determined. For the C1s fittings the LFWHM was kept constant for all peaks and all temperature steps. The O 1s spectra were normalized to sweeps and current, and a linear background was subtracted. As a measure of coverage, the spectra were normalized to the background, and the respective peak intensities were integrated to yield the peak area, with a typical relative error of 10%. The direct current heating used for temperature programmed XPS (Figure 4.13) changes the potential of the crystal, leading to a shift of peak positions. Therefore, Fermi edges were measured for each current value after the desorption measurements. The error in binding energy calibration of this method is estimated to be approximately 50 meV.

In Chapter 5 (Core level shifts) C 1s core levels were measured with a photon energy of 390 eV. Ir 4f and Li 1s spectra were measured with a photon energy of 120 eV, if not otherwise indicated, and the O 1s spectra were measured with a photon energy of 625 eV. For the C 1s spectra a third-polynomial background was subtracted, and the specta were normalized to the C 1s peak height. For the Ir 4f spectra a Shirley background was subtracted, for the Li 1s a fourth polynomial, and both were normalized to the Ir $4f_{7/2}$ bulk peak. Fitting of the C 1s and Li 1s spectra was done with one or two Voigt components. BEs are given as the positive difference between a core level and the Fermi edge so that CLSs are positive when the BE increases.

The XP spectra shown in Chapter 7 (Deuteration of Gr/Ir) were measured with photon energies of 120 eV for Ir 4f, 390 eV for C 1s and 850 eV for O 1s-Ir 4p regions.All C 1s spectra were normalized to the peak height. All Ir 4f spectra were normalized to the background, and a Shirley background was subtracted. The O 1s spectra were normalized to the Ir $4p_{3/2}$ peak height.

For XPS measurements in Chapter 6 (OH-H_2O phase) photon energies of 390 eV for C 1s, 120 eV for Ir 4f, and 625 eV for O 1s were used. For Figure 6.4, the O 1s and C 1s regions were monitored simultaneously with a photon energy of 625 eV for both core levels. Curve fitting was performed with Doniach-Šunjić functions convoluted with Gaussians, together with linear backgrounds.

3.5 TuMA III setup

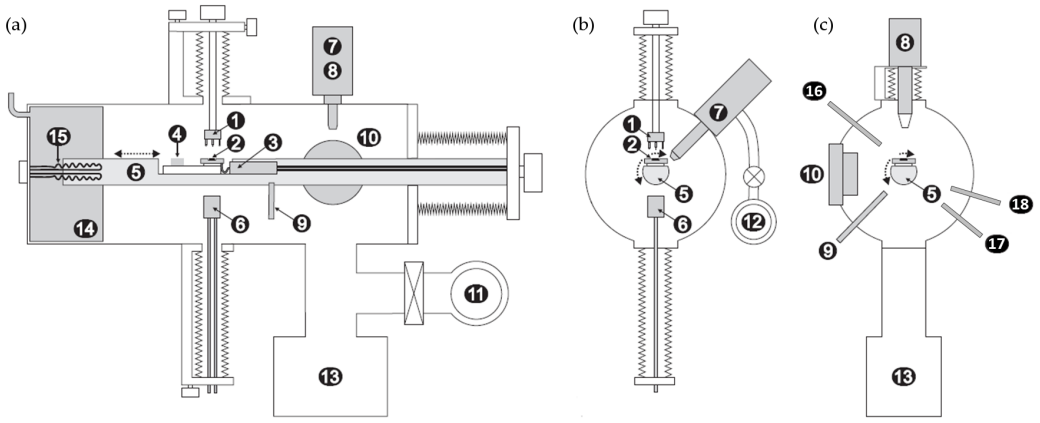

Figure 3.2: Experimental setup of TuMA III showing cross sections (a) along the manipulator axis, and (b),(c) through the manipulator axis. (1) STM, (2) Ir(111) sample, (3) cryostat, (4) Faraday cup, (5) manipulator, (6) e-beam evaporator, (7) ion source, (8) quadrupole mass spectrometer, (9) gas doser, (10) LEED system, (11,12) turbomolecular pumps, (13) sputter ion pump, (14) cold trap, (15) titanium sublimation pump, (16) thermal cracker, (17) Knudsen effusion cell, (18) Cs evaporator. Adapted from [124,125].

STM measurements were carried out in the ultra-high vacuum (UHV) chamber TuMA III in Cologne (Figure 3.2). The base pressure was lower than $1 \cdot 10^{-10}$ mbar. UHV was achieved with the following pumps: two turbomolecular pumps, one (11) in the main chamber and one (12) used for differential pumping at the ion source, a titanium sublimation pump (15), a sputter ion pump (13), and a cold trap (14) that was typically used during STM measurements and after gas exposure.

An Ir(111) single crystal was used as a sample (2) and mounted on a movable and rotatable manipulator (5). It could be cooled by a flow cryostat (3) and heated through electron bombardment with a filament situated below the sample. The temperature at the sample and at the sample holder was measured with two type K (NiCr/Ni) thermocouples.

Xe^+ sputtering was provided for sample cleaning with the ion source (7) that was equipped with a Wien filter. The ion current was measured with a Faraday cup (4).

Gases (ethylene, oxygen, hydrogen, deuterium, carbon monoxide) were usually introduced into the chamber via a gas doser (9). The gas doser consisted of a tube of a slightly larger diameter than the sample diameter which

ended approximately half a centimeter in front of the sample. The local pressure at the sample is estimated to be roughly a factor 80 ± 20 higher than the background pressure measured by the ion gauge. Throughout this work, the factor 80 has been included whenever gases were dosed through the gas doser. A thermal cracker (16) was available for dosing atomic hydrogen or deuterium. A four-pocket e-beam evaporator (6) equipped with a shutter was available for deposition of platinum. A Knudsen effusion cell (17) was used for Au evaporation.

The sample could be analyzed with a LEED system (10), a quadrupole mass spectrometer (9) and an STM (1) [119].

3.6 Beamline I311 at MAX-lab

The XPS measurements were carried out at the beamline I311 at the MAX-lab in Lund, Sweden. The beamline is undulator based for high resolution electron spectroscopy. A schematic setup is shown in Figure 3.3. The pre-mirror (M1) focuses the incoming radiation horizontally. The desired photon energy is selected with a monochromator consisting of a grating (G) and a spherical focusing mirror (M2). The vertically deflecting mirror (M4) focuses the exit slit onto the sample while the horizontally deflecting mirror (M5) images the focus of the pre-mirror (M1) onto the sample position. The resolving power of the grating is shown in Figure 3.4. The slit size is chosen as to find a compromise between energy resolution and intensity. A smaller slit size increases the energy resolution but as less light comes through, the measured signal intensity decreases.

The photon energy selected has to be optimized with respect to several factors. The monochromator energy resolution is generally better for low photon energies (Figure 3.4). The cross-section for the photoionization process, (examplified for the Ir 4f peak in Figure 3.5) has to be taken into account. Finally, for maximum surface sensitivity, the photoelectrons should have a low mean free path which is the case for energies between 10 and 100 eV (see Figure 2.6).

The experimental station consists of a preparation chamber mounted on top of an analysis chamber. The two chambers can be separated by a gate-valve. The sample is mounted on a long, vertical manipulator and can be cooled with liquid nitrogen. The sample was heated via direct current heating. Temperatures were measured with a chromel-alumel thermocouple spot-welded to the back of the crystal. The preparation chamber includes an ion sputtering gun, a LEED and a gas inlet system. A SCIENTA-SES200 electron energy analyzer [128] is mounted at the analysis chamber for high resolution

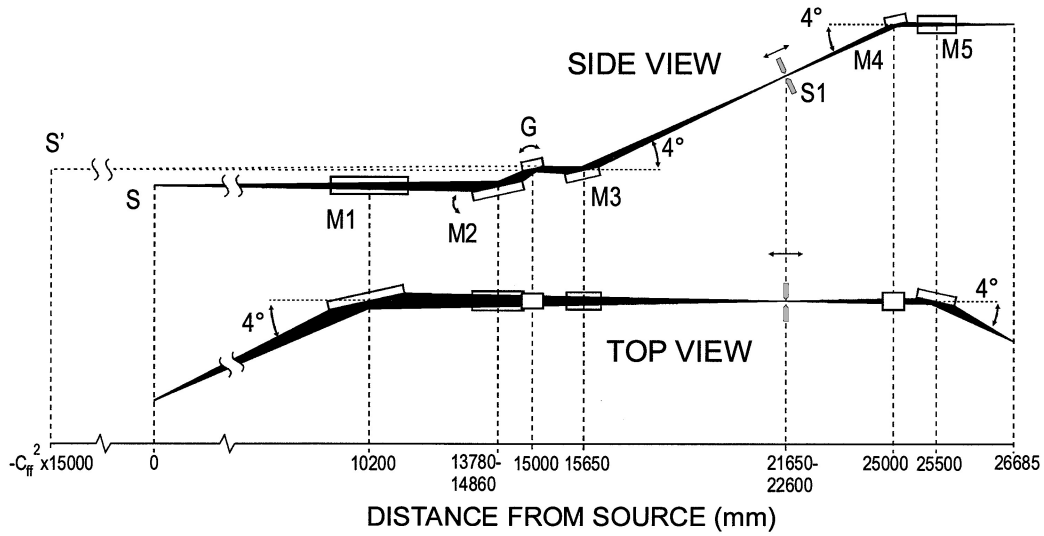

Figure 3.3: Schematic layout of the I311 beamline. The optical elements consist of a horizontally focusing pre-mirror (M1), a rotatable plane mirror (M2), a plane grating (G), a spherical focusing mirror (M3), and spherical re-focusing mirrors (M4,M5). (S1) is a movable exit slit. The real source is at S and the virtual monochromatic source at S'. Reprinted from [117], ©2001, with permission from Elsevier.

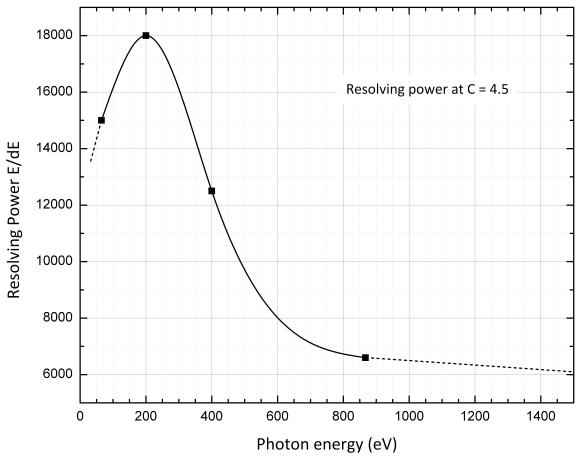

Figure 3.4: Resolving power of the 1220 lines/mm monochromator grating over the entire photon energy region. From [126].

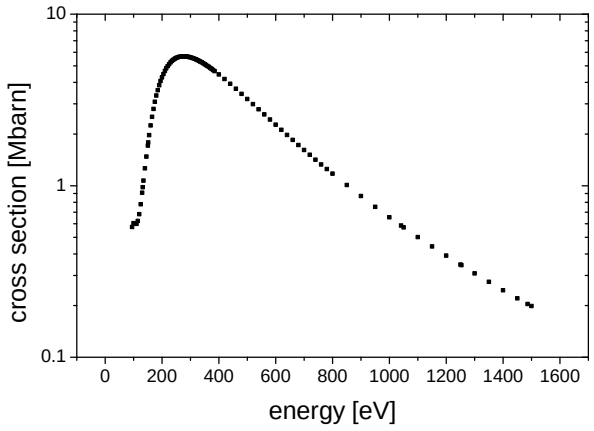

Figure 3.5: Atomic calculation of photoionization cross-section for the Ir 4f signal. From [127].

XPS. The base pressure in the preparation and analysis chamber was lower than $1 \cdot 10^{-10}$ mbar.

3.7 Sample preparation

For the STM measurements, the sample was sputtered by 1.5–4 keV Xe^+ bombardment for 60–120 min. Sputtering with lower energies (1.5 keV) is recommended to minimize the implanted noble gas [129]. Oxygen treatment ($8 \cdot 10^{-8}$ mbar, 5–10 min, 1170 K) was used sporadically to remove carbon impurities from the crystal. High temperature sputtering (1120 K, 30 min) was used occasionally to prepare large terraces. In general, high temperatures during sample preparation were minimized as far as possible to avoid adsorbates on the sample. The cleaning procedure was completed by a flash to 1520 K.

For the XPS measurements the Ir(111) crystal was cleaned by cycles of Ar^+ sputtering at room temperature for 15 min, and subsequent oxygen treatment at 1200 K for 10 min with a partial oxygen pressure of $1 \cdot 10^{-7}$ mbar in order to remove residual carbon impurities. Cleaning was completed by a flash to above 1400 K, the sample being heated by direct current. The cleanliness of the sample was checked by XPS.

Gr was grown by temperature programmed growth (TPG) [130], chemical vapor deposition (CVD) [130], or a TPG step followed by CVD [131]. A TPG step consists of saturating the Ir surface with ethylene at room temperature, typically by exposing the sample for 30 s to a pressure of $p_{\mathrm{TPG}} = 8 \cdot 10^{-7}$ mbar,

followed by a flash anneal to $T_{\mathrm{TPG}} = 1450\,\mathrm{K}$, if not noted otherwise. One TPG step results in ≈ 0.2 ML of the bare Ir surface to be covered by Gr [26]. CVD consists of dosing ethylene at a pressure p_{CVD} at elevated temperatures, typically T_{CVD} =1120–1200 K for a certain time. Gr growth on Ir(111) by ethylene exposure is self-limited to 1 ML, as the Ir(111) acts as a catalyst for ethylene dissociation and has a low solubility for carbon [132].

In Chapter 4 (Oxygen etching), a fully closed ML was prepared by one TPG step ($T_{\mathrm{TPG}} = 1400\,\mathrm{K}$) and subsequent CVD at an ethylene pressure of $p_{\mathrm{CVD}} = 8 \cdot 10^{-7}$ mbar at 1170 K for 40 min. This CVD time at the given temperature is sufficient for achieving a perfectly closed layer of graphene, indicated by its inability to intercalate oxygen at 450 K [33]. 0.5 ML Gr was grown by three TPG cycles, and consists of flakes and coalesced flakes with a broad size distribution and circle-equivalent diameters of 10–100 nm. In both cases, Gr displays only the well-known incommensurate (9.32×9.32) moiré superstructure with the dense-packed rows of Gr and Ir(111) in parallel, with a scatter of less than $\pm 0.5°$ [23]. Graphene nanoflakes with a nominal coverage of 0.2 ML were grown by one TPG cycle using lower values of T_{TPG} [130].

Oxygen exposure was conducted in an O_2 pressure of $1 \cdot 10^{-5}$ mbar for 100 s, if not specified otherwise. The resulting dose of 750 L is more than an order of magnitude larger than what is necessary to reach saturation coverage on Ir(111) [133, 134].

High purity platinum was evaporated from an Oxford Applied Research EGN4 Mini e-Beam Evaporator with a typical evaporation rate of $1{\cdot}10^{-2}$ ML/s. During evaporation the sample was held at room temperature. The platinum evaporator was calibrated by determination of the fractional area of monolayer platinum islands deposited onto clean Ir(111).

In Chapter 5 (Core level shifts) a percolated Gr layer ($\theta \approx 0.9$ ML) was grown by 10 TPG steps for Eu and O intercalation. A full Gr layer ($T_{\mathrm{TPG}} = 1300 - 1400\,\mathrm{K}$, $T_{\mathrm{CVD}} = 1120 - 1170\,\mathrm{K}$, $p_{\mathrm{CVD}} = 1 \cdot 10^{-7}$ mbar) was used for Cs and Li intercalation. For H intercalation – both in Chapter 5 and 7 (Deuteration of Gr/Ir) – a partial Gr layer($\theta = 0.5$ ML) was grown by three TPG steps (XPS: $T_{\mathrm{TPG}} = 1400\,\mathrm{K}$, STM, TPD: $T_{\mathrm{TPG}} = 1450\,\mathrm{K}$) Europium was evaporated from a Knudsen effusion cell. Intercalation took place during deposition at a sample temperature of 720 K. The structure of the intercalated layer was checked with LEED. Molecular oxygen exposure was conducted in an oxygen pressure of $p = 1 \cdot 10^{-5}$ mbar for 100 s (750 L). Caesium and Lithium were evaporated by running a current through SAES Getters Alkali Metal Dispensers in home-built evaporators. Saturated Cs intercalation was confirmed by checking for only a $(\sqrt{3}\times\sqrt{3})$R30° being present in LEED. Saturated Li intercalation was reached when the Li 1s peak characteristic for bulk Li [135], located between 55.4 and 55.1 eV, did not increase

in intensity anymore (see Chapter 5 for more details). Hydrogen was intercalated by exposing Gr to $p = 1 \cdot 10^{-6}$ mbar H_2 during cooldown from 300 K until 125 K, followed by additional 5 min H_2 at $5 \cdot 10^{-6}$ mbar (1125 L), leading to a H intercalation coverage of more than 90% [32].

In Chapter 6 (OH-H_2O phase), 0.5 ML Gr was grown by three TPG steps $T_{\mathrm{TPG}} = 1400$ K. Oxygen exposure onto Gr was conducted using an O_2 pressure of $5 \cdot 10^{-6}$ mbar (200 L), if not specified otherwise. H_2 exposure was conducted at $5 \cdot 10^{-7}$ mbar (100 L), if not specified otherwise. No further change in the C 1s spectrum was seen at higher hydrogen doses.

Deuterium was used for TPD measurements in Chapters 7 (Deuteration of Gr/Ir) and 8 (Au intercalation and deuteration of Gr/Au/Ir) because hydrogen is one of the main constituents of the residual gas in UHV systems, resulting in a high background signal. Large doses of molecular deuterium were exposed to the sample from the gas doser, allowing large doses such as 3600 L to be administered in a reasonable period of time. Smaller D_2 doses (e.g. 15 L) were dosed through the cracker with the cracker turned off. This allowed experimental consistency when comparing to cracked, atomic deuterium doses. The local pressure of atomic deuterium at the sample surface is not known, so all doses are always calculated based on the background pressure. Due the proximity of the capillary to the sample and it being directed towards the sample the local pressure is probably significantly higher than the reading of the ion gauge. These doses therefore should not be compared to gas doses administered through the gas doser or to doses from literature.

Atomic deuterium and hydrogen in Cologne were produced by using an Oxford Applied Research TC-50 thermal gas cracker. D_2 is fed through an iridium capillary, once the desired pressure is reached, the capillary is e-beam heated to temperatures of ≈ 1300 K, sufficient for dissociating D_2. Unless stated otherwise, the cracker was operated at 65 W and at a pressure of $8 \cdot 10^{-8}$ mbar, and varying exposure times to change the dose. Doses were calculated based on the chamber pressure read by an ion gauge. Again, the true atomic D pressure at the sample surface is unknown, but will undoubtedly be higher than what is measured by the ion gauge. Thus, our figures given for dosage should in fact read $4x$ L or $15x$ L, with x being an unknown factor accounting for the higher D dose at the sample. Based on the saturated D/Ir TPD spectrum obtained after dosing 15 L D through the cracker, x could be as high as 70. Regardless of its precise value, x is consistent throughout our experiments. Given doses thus serve as reliable references against each other, but comparison with doses found in literature should be made with caution.

Atomic hydrogen in Lund was produced using a Scienta Omicron EFM-H electron beam evaporator with a tungsten capillary and a cracking efficiency close to 100%. Unless noted otherwise, the cracker was operated for 4 min 30 s

at 700 V and 25 mA, a H_2 pressure of $5 \cdot 10^{-6}$ mbar, as this was found sufficient for saturation.

Gold was evaporated from a pyrolytic boron nitride crucible mounted in a standard effusion (SF) cell by Dr. Eberl MBE-Komponenten, equipped with a thermocouple to read the crucible temperature. It was operated at 1400 K for evaporation, which yields an evaporation rate of ≈ 0.014 ML/s for Au deposition on Ir(111) at room temperature. Gold was intercalated under Gr with the sample at 780 K. The sticking coefficient of gold on Ir should not change significantly compared to room temperature, however, we believe that Au at least partly re-evaporates from the Gr (see Chapter 8 for details). All Au coverages are given with respect to evaporation at room temperature on Ir(111), but true coverages on Au-intercalated Gr might differ.

Chapter 4

Etching of graphene on Ir(111) with molecular oxygen

This chapter is based on the manuscript published in Carbon 96, 320 (2016), reprinted from [136], ©2015, with permission from Elsevier. It contains contributions from: E. Grånas, T. Gerber, M. A. Arman, A. J. Martínez-Galera, K. Schulte, J. N. Andersen, J. Knudsen, and T. Michely. I was responsible for the design of the experiments, performed all STM and TPD measurements and analyses, was involved in all XPS measurements, developed the etching model for the nanoflakes, prepared Figures 4.1(c),4.5 - 4.12, 4.14(d), 4.15 and wrote the first draft of the manuscript.

Etching of Gr through molecular oxygen has become a topic of intense research in the past years [9, 41, 49, 137–147], not only because it is a long-standing scientific problem, but also due to the interest in using Gr for future applications. The stability of Gr in an oxidizing atmosphere will be a key issue during processing of graphene devices. Specifically, through dissociative chemisorption of oxygen on metal electrodes or metallic particles, through release from surface oxides or from the metal bulk, atomic oxygen may be provided, which etches Gr efficiently [148–152]. High duty cycles in chemical vapor deposition (CVD) Gr growth require the withdrawal of Gr from the CVD furnace at the maximum possible temperature, that still assures the absence of etching [146]. This temperature is likely to depend on the nature and concentration of defects in Gr [144], making it desirable to understand the mechanism of etching at defects. Understanding how structural defects

affect Gr etching would also open possibilities to shape and structure Gr at the nanoscale.

Introducing suitable point defects in defined areas of the Gr sample, e.g., by a He ion microscope lithographic system followed by a subsequent oxygen etch that removes defected areas in a controllable fashion, could be an efficient structuring procedure and result in patterns with rather perfect edges. Moreover, the proposed use of Gr as a protective coating [47, 153–156] crucially relies on knowing the limits of stability of Gr as a function of its morphology and defect structure.

In this chapter, a combined scanning tunneling microscopy (STM), x-ray photoemission spectroscopy (XPS), and temperature programmed desorption (TPD) study is conducted. We carefully investigate how morphology and defects in Gr supported by Ir(111) affect Gr's stability against etching by molecular oxygen. Our work is embedded in a context of intense scientific research investigating oxygen etching of Gr on metals [9,41,137,138,140–147].

If present, defects are considered to be the starting points for etching of Gr. For Gr etching on transition metals, point defects [138], domain (grain) boundaries [9,143,144,146], flake edges [41] and wrinkles [142,145] were found to be starting locations of etch attack. Here, we shed some light on the role of defects in etching and, for the first time, identify and describe in atomic detail a point defect being the location of etch attack, in the case of Gr edges being absent.

Only in a few recent studies have the defect concentration in Gr or the Gr morphology been purposely varied to explore their effect on etching. At 300° C, Zhang *et al.* [145] found wrinkles in a closed Gr layer on Ru(0001) to be more stable against oxidation than those in Gr islands. Gotterbarm *et al.* [144] found the scatter in orientation – and thus the grain boundary concentration in a closed layer – to significantly affect the onset temperature of etching. Despite these insights, the field still lacks a systematic analysis of how etching depends on graphene morphology. In the present work, we investigate the etching behavior of a closed monolayer, flakes partially covering the surface, and nanoflakes of Gr on Ir(111) when introducing molecular oxygen. Of specific interest is the etching mechanism for the case of the closed monolayer [138, 144, 157, 158], as understanding this might also give insights into the well-known problem of graphite etching [15, 159, 160] from a new perspective.

Intercalation of oxygen underneath Gr was frequently observed [9, 33, 41, 142, 158, 161] to take place already below the onset temperature of etching. To date, it appears unclear whether intercalation is a necessary precondition of Gr etching on a metal or just an incidental byproduct. Here, we will demonstrate that the latter is the case and that etching may proceed without

simultaneous intercalation.

Related to this issue is the question of whether adsorbed oxygen is combusted entirely or whether it may partly desorb without reacting to CO or CO_2 [9, 41, 140]. In addition, besides the single study of Yang and Hrbek from 1995 [137] for Gr oxidation on Ru(0001), no information is available on how the conditions of etching determine the ratio of CO to CO_2 as reaction products. Using TPD, we demonstrate that no oxygen desorbs as long as Gr is present on the surface, clarifying the conditions that determine the extent of combustion.

Finally, we extract the activation energy and the attempt frequency for etching of Gr flake edges on Ir(111). We compare these findings to previous results for graphene [41, 141] and graphite [160, 162] and analyze factors (morphology, temperature, pressure) that may modify these fundamental parameters.

The results are presented in four parts. First, as an introduction, we contrast the etching behavior of a closed Gr layer (in the following referred to as 1 monolayer, or ML) with that of Gr consisting of large flakes with a coverage of 0.5 ML. These two cases are analyzed in greater detail in the following two subsections, while a fourth subsection investigates the etching behavior as a function of Gr flake size.

4.1 Etching for full versus partial Gr coverage

Depending on the coverage, etching of Gr on Ir(111) takes place along fundamentally different pathways. In the introductory paragraphs we discuss these differences through a comparative XPS sequence, and oppose 1 ML to 0.5 ML coverage in Figure 4.1(a) and (b), respectively.

Figure 4.1(a) displays the C 1s spectra of 1 ML Gr/Ir(111) before (lowest spectrum) and after successive exposures to 750 L O_2 at stepwise increasing temperatures, as indicated in the figure. The sample was heated up and cooled down in ultra-high vacuum, and oxygen was only present when the sample was at the indicated temperature. At all temperatures the spectra are dominated by the C_{Ir} component at a binding energy (BE) of 284.10 eV [gray in Figure 4.1(a)]. Within the limits of error, the integrated C 1s peak intensity remains constant up to 700 K [Figure 4.1(c)]. Apparently, exposure to molecular oxygen does neither induce Gr etching nor changes in the chemical environment of the C atoms in Gr. The absence of oxygen on the sample up to 700 K is underpinned by the XP spectra of the O 1s and Ir $4f_{7/2}$ levels (see Figure 4.2 and discussion thereof). As visible from Figure 4.1(a) and (c), after O_2 exposure above 700 K, the amount of Gr on the sample

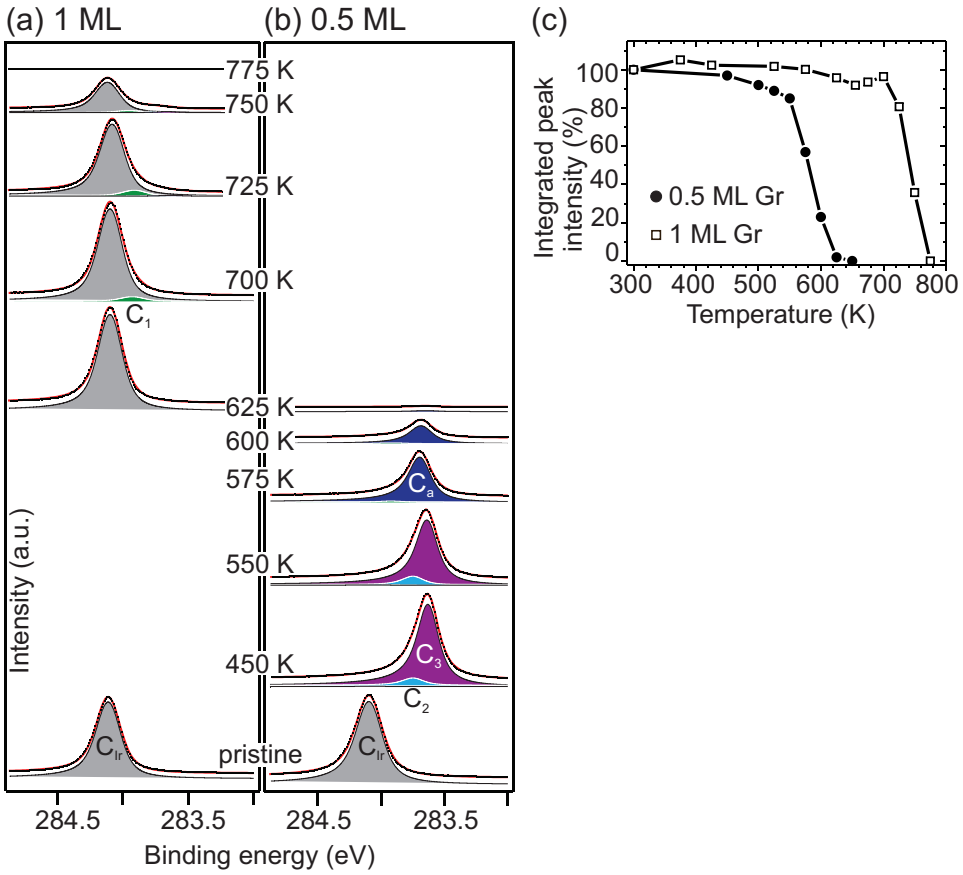

Figure 4.1: XP spectra of the C 1s region of (a) 1 ML Gr/Ir(111) and (b) 0.5 ML Gr/Ir(111), each exposed to 750 L O_2 at stepwise increasing temperatures as indicated in the figure, recorded at room temperature. The spectrum of pristine Gr prior to O_2 exposure is shown at the bottom of (a) and (b). Experimental data are shown as black dots, fitted spectra as solid red lines, and fitted components as filled curves. Consistent with previous work [33,34], fitting parameters are (a) C_{Ir} (gray): binding energy (BE) = 284.10 eV, Gaussian full width at half-maximum (GFWHM) = 0.17 eV, Lorentzian full width at half-maximum (LFWHM) = 0.12 eV; C_1 (green): BE = 283.93 eV, GFWHM = 0.17 eV LFWHM = 0.12 eV. (b) C_{Ir} (gray): BE = 284.10 eV, GWFHM = 0.17 eV, LFWHM = 0.16 eV; C_2 (light blue): BE = 283.72 eV, GFWHM = 0.10 eV, LFWHM = 0.15 eV. C_3 (magenta): BE = 283.63 eV, GFWHM = 0.10 eV, LFWHM = 0.16 eV. C_a (dark blue): BE = 283.70 eV, GFWHM = 0.11 eV, LFWHM = 0.16 eV. (c) Integrated C 1s peak intensities as a function of temperature for the spectra shown in (a) (open squares) and (b) (dots). Lines to guide the eye. Reprinted from [136], ©2015, with permission from Elsevier.

decreases noticeably, and after exposure at 775 K, no carbon is left on the surface. For exposure temperatures at or above 700 K a few % of the spectral weight in the C 1s spectra are shifted to component C_1 [green in Figure 4.1(a)], at −0.17 eV from C_{Ir}. This component has been identified previously by Grånäs *et al.* [33] to originate from Gr in contact with a dilute oxygen adatom lattice gas. Thus, while most of the remaining Gr is chemically unaffected during etching, a small fraction of Gr appears to be intercalated by an oxygen adatom lattice gas.

Figure 4.1(b) displays the C 1s spectra of 0.5 ML Gr/Ir(111) before (lowest spectrum) and after successive exposures to molecular oxygen at stepwise increasing temperatures. Already exposure at 450 K gives rise to a significant shift of the C 1s spectral weight towards lower binding energies and a loss of the C_{Ir} component. As described in ref. 33, this is a result from the intercalation of graphene by dense oxygen adatom phases. Quantitatively, it can be fitted with the C_2 and C_3 components (light blue and magenta in Figure 4.1), that correspond to Gr intercalated by p(2×2)-O and p(2×1)-O structures, respectively. This interpretation is consistent with the corresponding O 1s and Ir $4f_{7/2}$ spectra (see Figure 4.3 and discussion thereof). Up to 550 K exposure temperature the C 1s peak area remains constant within the limits of error (compare to Figure 4.1(c)), and the peak can be fitted with the C_2 and C_3 components, corresponding to the p(2x2) and p(2x1) phases. At 575 K etching has set in, and at 625 K no Gr is left. At the temperatures where etching occurs, a small shift of the C 1s spectral weight to a new position C_a [dark blue in Figure 4.1(b)] is observed. This shift can not be accounted for by the C_2 and C_3 components but has a peak position in between, at 283.70 eV. This BE is in between that of the p(2x2) and p(2x1)-O structures. Martínez-Galera *et al.* [53] observed a $p(\sqrt{3} \times \sqrt{3})R30°$ oxygen adatom phase that exists exclusively underneath Gr. As the coverage of this phase (0.33 ML) is in between that of the p(2x2) and p(2x1) phase (0.25 and 0.5 ML, respectively), we tentatively attribute the C_a component to a $p(\sqrt{3} \times \sqrt{3})R30°$ phase.

Figure 4.2 shows the O 1s and Ir $4f_{7/2}$ spectra of 1 ML Gr/Ir(111) before (lowest spectrum) and after successive exposures to molecular oxygen at stepwise increasing temperatures, corresponding to Figure 4.1(a). Below 700 K, no oxygen is is present on the surface, as shown by the absence of an O 1s peak. This is consistent with the full coverage with Gr, and the absence of bare Ir(111) that would enable dissociative adsorption of oxygen. Accordingly, the Ir 4f signal only shows the bulk (Ir_B) and surface (Ir_0) component. At 700 K, an Ir_1 component, corresponding to Ir surface atoms bound to one adsorbed O atom, starts to appear. It is accompanied by an O 1s peak at 529.9 eV. At 725 K, when etching has already uncovered bare Ir(111), the oxy-

gen coverage increases, and at 750 K, an Ir_2 component appears additionally, corresponding to Ir surface atoms bound to two O atoms. In line with Gråsäs *et al.* [33], we calculated the O coverage based on the relative amounts of Ir_0, Ir_1, and Ir_2, and determine a dilute oxygen phase to be present at 700 K, which turns into a denser p(2x2), and eventually p(2x1) phase for increasing O coverages. We attribute the dense oxygen adatom phases to be present on the Ir areas uncovered by etching, as the C 1s spectra (Figure 4.1) do not indicate a dense intercalation layer.

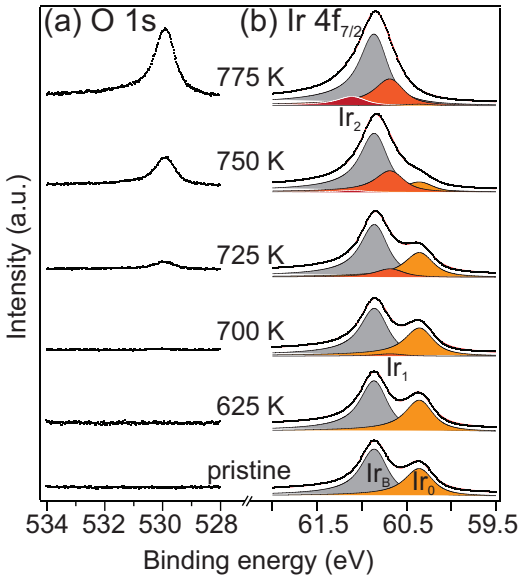

Figure 4.2: (a) O 1s region and (b) Ir 4f region XP spectra of 1 ML Gr/Ir(111) exposed to 750 L O_2 at stepwise increasing temperatures, as indicated. The spectra of Gr prior to oxygen exposure are shown at the bottom. The experimental spectra are shown as black dots, the fitted spectra as solid red lines, and the fitted components as filled curves. A linear background was used. All spectra were recorded at room temperature. Fitting parameters are (b) Ir_B (grey): BE = 60.8 eV, GWFHM = 0.18 eV, LFWHM = 0.27 eV; Ir_0 (light orange): BE = 60.3 eV, GWFHM = 0.20 eV, LFWHM = 0.27 eV; Ir_1 (dark orange): BE = 60.6 eV, GWFHM = 0.20 eV, LFWHM = 0.27 eV; Ir_2 (red): BE = 61.1 eV, GWFHM = 0.20 eV, LFWHM = 0.27 eV. Reprinted from [136], ©2015, with permission from Elsevier.

Figure 4.3 displays the O 1s and Ir $4f_{7/2}$ spectra of 0.5 ML Gr (lowest spectrum) and after successive exposures to molecular oxygen at stepwise increasing temperatures, corresponding to Figure 4.1(b). After oxygen exposure at 450 K, the Gr is fully intercalated. The O 1s signal shows a peak at

529.9 eV, and the Ir surface component Ir_0 has nearly vanished, in favor of the Ir_1 and Ir_2 components, according to an almost perfect p(2x1) oxygen phase underneath Gr and on the uncovered Ir terraces. The C 1s peak area is constant up to 550 K. At 575 K, both the Ir_1 and Ir_2 intensities have decreased, and Ir_0 has increased, with respect to the bulk intensity. This shows that there is less oxygen on the surface, due to consumption by Gr etching. At 600 K, roughly half of the Gr is gone, and the Ir_2 component increases again, when the dense p(2x1) O phase forms on the Ir surface uncovered by Gr. At 625 K, all of the Gr is removed and the Ir surface is covered with a p(2x1) phase of adsorbed oxygen.

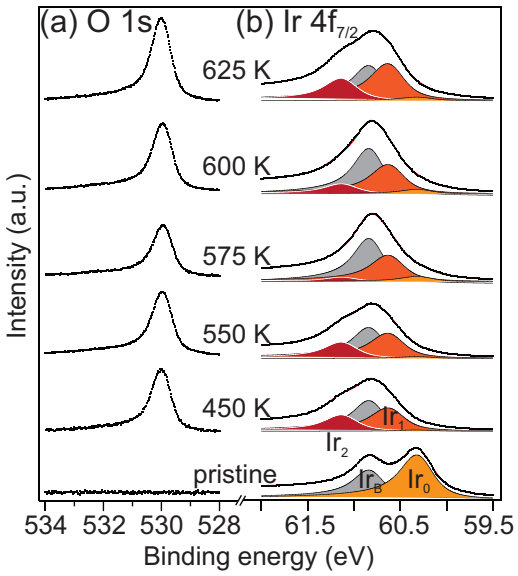

Figure 4.3: XP spectra of (a) O 1s and (b) Ir $4f_{7/2}$ regions of 0.5 ML Gr exposed to 750 L O_2 at stepwise increasing temperatures, as indicated. The spectra of Gr prior to oxygen exposure are shown at the bottom. The experimental spectra are shown as black dots, the fitted spectra as solid red lines, and the fitted components as filled curves. A linear background was used. All spectra were recorded at room temperature. Here, the Ir 4f spectra were obtained with a photon energy of 120 eV. Fitting parameters are (b) Ir_B (grey): BE = 60.8 eV, GWFHM = 0.21 eV, LFWHM = 0.27 eV; Ir_0 (light orange): BE = 60.3 eV, GWFHM = 0.26 eV, LFWHM = 0.27 eV; Ir_1 (dark orange): BE = 60.6 eV, GWFHM = 0.26 eV, LFWHM = 0.27 eV; Ir_2 (red): BE = 61.1 eV, GWFHM = 0.26 eV, LFWHM = 0.27 eV. Reprinted from [136], ©2015, with permission from Elsevier.

We also note that the onset temperature of Gr etching depends sensitively

on the Gr preparation conditions and the perfection with which the Gr layer is closed. Figure 4.4 displays the C 1s, O1s, and Ir $4f_{7/2}$ spectra of Gr grown by 1 TPG cycle followed by only 1200 s (instead of 2400 s) CVD at 1170 K resulting in a nearly closed layer (approximately 0.99 ML) before (lowest spectrum) and after successive exposures to molecular oxygen at stepwise increasing temperatures. At 550 K and below, the C 1s signal can be fitted with a single component, corresponding to $C_{Ir} = 284.10$ eV, and the Ir 4f signal consists of the bulk and surface components Ir_B and Ir_0, respectively. Thus, 0.99 ML Gr is not intercalated at 550 K. We explain this by the small amount of free Gr edges where oxygen can attack. The oxygen adsorbed on the remaining 0.01 ML bare Ir substrate is below the resolution of our XP spectra. At 700 K, a dilute intercalated oxygen phase is present (as inferred from the C_b and Ir_1 components), and the Gr is etched significantly. The larger amount of oxygen seen in the O 1s spectra is attributed to oxygen adsorbed on bare Ir terraces without graphene. Thus, 0.99 ML Gr show a lower etching onset than a full layer, but a higher onset temperature than 0.5 ML Gr. When the CVD growth step is significantly shorter, under the conditions of pressure and temperature as given in the Methods section, the Gr film will not be completely closed, causing a substantially lower onset temperature of Gr etching. Similarly, Gr grown by iterative TPG cycles, without additional CVD growth, does not result in a completely closed Gr layer [26] and the onset of Gr etching will be lower.

To summarize, for a 1 ML, hole-free Gr layer our XPS measurements do not show the presence of any oxygen on the sample after large exposures at increasingly higher temperatures up to the onset of combustion, which occurs around 700 K. In contrast, for a partial Gr coverage with bare metal present, molecular oxygen adsorbs dissociatively on Ir(111) [133], intercalates the Gr layer [33] and etching starts at a markedly lower temperature, around 550 K.

4.2 Etching of the closed Gr layer on Ir(111)

To obtain additional insight into the etching mechanism of the 1 ML, we now use STM to analyze two situations around the onset of etching. Figure 4.5(a) displays the sample morphology after exposure to 750 L O_2 at 700 K. According to Figure 4.1(a), we would expect no etching at this temperature. The STM topograph displays an almost intact Gr layer, however, a few tiny holes in the Gr layer are present. Two of these are highlighted by arrows. We interpret these tiny holes to result from oxygen etching, as no such holes were observed at lower temperatures. The decrease in Gr coverage associated with the hole formation ($< 1\%$ ML) is well below what could be detected by

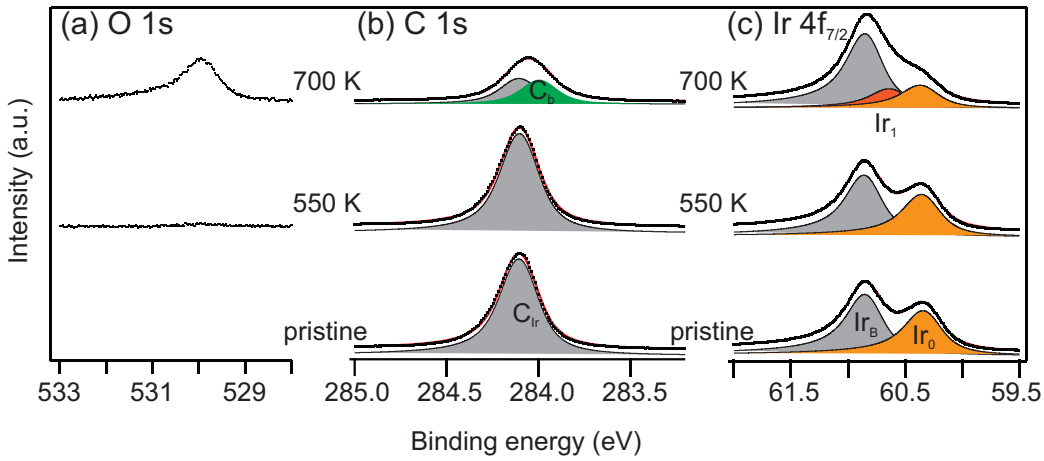

Figure 4.4: XP spectra the (a) O 1s, (b) C 1s, and (c) Ir 4f regions of 0.99 ML Gr exposed to 750 L O_2 at stepwise increasing temperatures, as indicated. The spectra of Gr prior to oxygen exposure are shown at the bottom. The experimental spectra are shown as black dots, the fitted spectra as solid red lines, and the fitted components as filled curves. A linear background was used. All spectra were recorded at room temperature. Fitting parameters are (b) C_{Ir} (grey): BE = 284.10eV, GWFHM=0.17 eV, LFWHM=0.16 eV; C_b (green): BE= 283.99, GWFHM=0.16 eV, LFWHM=0.16 eV; (c) Ir_B (grey): BE = 60.8 eV, GWFHM = 0.21 eV, LFWHM = 0.27 eV; Ir_0 (light orange): BE = 60.3 eV, GWFHM = 0.23 eV, LFWHM = 0.27 eV; Ir_1 (dark orange): BE = 60.6 eV, GWFHM = 0.23 eV, LFWHM = 0.27 eV. Reprinted from [136], ©2015, with permission from Elsevier.

XPS.

The inset of Figure 4.5(a) shows the sample after room temperature post-deposition of 0.3 ML Pt. The Pt forms a regular cluster array on the Gr moiré [27, 163], with clusters being 1 or 2 ML high. Cluster formation relies on chemical bond formation between Ir-C *and* C-Pt, through local sp^2-to-sp^3-rehybridization of the Gr π-electronic system with the substrate Ir($5d_{3z^2-r^2}$) and the Pt($5d_{3z^2-r^2}$) orbitals [164]. If oxygen had been intercalated to any substantial amount it would prevent Ir-C bond formation, and thus inhibit rehybridization. The Pt cluster array would not have been formed, as we have shown in previous work [33]. On the other hand, the presence of etch holes could explain the small fraction of Gr being intercalated by a dilute oxygen adatom lattice gas, as indicated by the small C_1 component in Figure 4.1(a). Thus, our STM observations are consistent with the corresponding XP spectrum of Figure 4.1(a) after 700 K O_2 exposure, and capture, with some luck, a very early stage of oxygen etching.

Figure 4.5(b) displays the sample morphology after a 750 L O_2 exposure at 745 K. According to the XP spectra of Figure 4.1(a) for O_2 exposure at 725 K and 750 K, we now expect a significant part of the Gr to be combusted. Indeed, the STM topograph displays large hexagonal etch holes with a diameter of the order of 100 nm. The separation distance of the hexagonal etch holes is in the same range as the separation distance of the small holes in Figure 4.5(a). Based on the crystallography of Gr on Ir(111) [23], the predominant edges of the holes are zig-zag edges. The orientation of the hole edges can also be seen directly from the Ir cluster positions in the inset of Figure 4.5(b). The more elongated Gr hole, on the right of Figure 4.5(b), may be understood as the result of a coalescence of two hexagonal holes that nucleated in a separation of less than 100 nm. All holes in the Gr layer on other STM topographs are either hexagonal or appear to result from coalescence of hexagonal Gr holes during their lateral expansion by continued etching.

According to the principles of growth and etch shape formation [165], the hexagonal etch holes bounded by zig-zag edges imply that these edges are etched slowest by oxygen, i.e., are the most stable edges. The same preference for zig-zag edge bound holes was observed by Nemes-Incze *et al.* [149] for etching of exfoliated Gr through atomic oxygen provided from the decomposition of the SiO_2 substrate. No anisotropy was identified by the same group as well as by Liu *et al.* [138] for etching of exfoliated Gr on SiO_2 in molecular oxygen. Etching of graphite in molecular oxygen invariably results in the formation of hexagonal etch pits bound by armchair edges, as shown, e.g., by Hughes *et al.* [159] or Dobrik *et al.* [166]. Not unexpectedly, these differences indicate that edge etching of graphite compared to etching of Gr

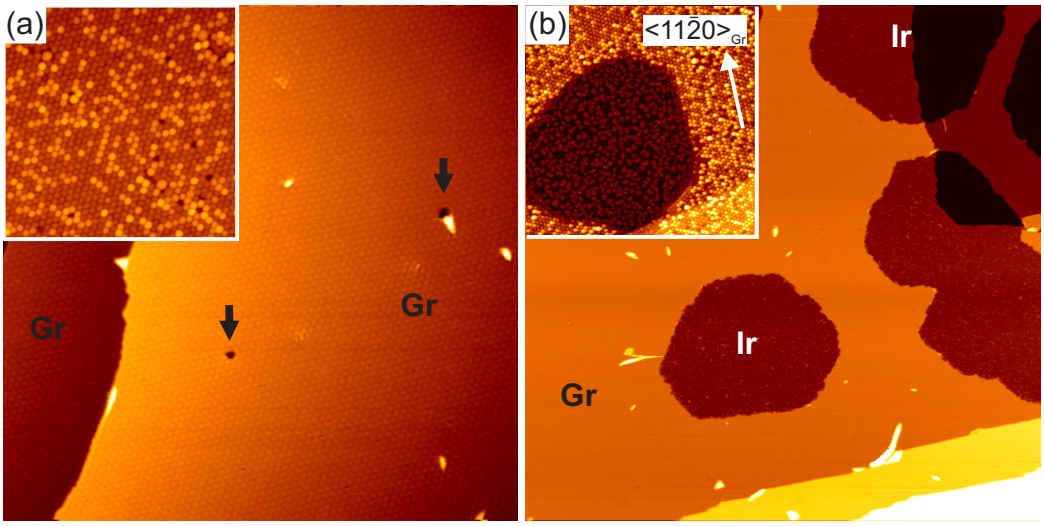

Figure 4.5: (a) STM topograph of 1 ML Gr/Ir(111) after exposure to 750 L O_2 at 700 K. Tiny etch holes are visible in the otherwise fully Gr-covered sample. Two of these are highlighted by black arrows. Image size 160 nm × 160 nm. Tunneling parameters $U_s = 1$ V, $I_t = 0.2$ nA. Inset: Same sample after deposition of 0.3 ML Pt at 300 K. An array of Pt clusters with 1 or 2 atomic layers height covers the sample. Image size 80 nm × 80 nm. Tunneling parameters $U_s = 0.9$ V, $I_t = 0.5$ nA. (b) STM topograph of 1 ML Gr/Ir(111) after exposure to 750 L O_2 at 745 K. Large, partly coalesced etch holes are visible in the otherwise Gr-covered sample. Image size 265 nm × 265 nm. Tunneling parameters $U_s = -1$ V, $I_t = 0.2$ nA. Inset: Same sample after post-deposition of 0.3 ML Pt at 300 K. A Pt cluster array formed on the Gr-covered area, while within the etch hole small scale Pt aggregates of monolayer height are visible. The dense packed $\langle 11\bar{2}0 \rangle$ Gr direction is indicated. Image size 140 nm × 140 nm. Tunneling parameters $U_s = -1$ V and $I_t = 0.2$ nA. Reprinted from [136], ©2015, with permission from Elsevier.

on a substrate, that provides the atomic oxygen, must be assumed to follow different reaction pathways. A similar distribution of holes and trenches (coalesced holes) as observed by us was found by Dobrik *et al.* [166] for graphite etching with molecular oxygen and associated to preferential etching of point defects and grain boundaries. This similarity will be discussed below.

The inset of Figure 4.5(b) shows the sample after room temperature post-deposition of 0.3 ML Pt. As before, the formation of a Pt cluster array in the Gr areas provides evidence for the absence of substantial oxygen intercalation. The array is slightly less perfect than after deposition at 700 K, specifically, close to the rim of the Gr etch hole quite a few moiré sites are unoccupied, consistent with the small C_1 component in Figure 4.1(a) after oxygen exposure. Within the etch hole, the Pt forms a high density of small compact islands with a spacing of the order of 5 nm, as is typical for Pt deposition on Ir(111) with adsorbed oxygen (compare to Figure 4(d) in ref. 33). For clean Ir(111), the deposited Pt would have formed well developed dendrites of threefold symmetry and much lower number density (compare to Figure 6(a) in ref. 33).

Based on the information presented up to now, it appears that once the etch holes have nucleated, etching proceeds by dissociative chemisorption of oxygen on the exposed metal, followed by diffusion to the Gr edge, subsequent reaction at the Gr edge and desorption of the reaction product. Reaction at the rim of the Gr vacancy island is facile, as the Gr edge atoms form chemical bonds to the substrate, and thereby come close to the oxygens adsorbed to it. Edge atom binding to the substrate has been first demonstrated experimentally by Lacovig *et al.* [167] and subsequently substantiated by additional experiments and simulations [168, 169]. As edge Gr C-atoms are close to the adsorbed mobile O atoms, the activation energy to initiate carbon - oxygen bond formation has a minimum. The loss of oxygen through the edge reaction is large enough to prevent the build-up of a two dimensional pressure which is necessary for delamination and subsequent intercalation of a dense oxygen phase [33]. Only close to the edges, signs of a dilute oxygen gas are found after cool down. Most likely, it results from the dense oxygen adlayer on bare Ir(111) in the etch holes, leaking under Gr during the cool down, when the etching reaction has ceased. This interpretation is consistent with *in situ* XPS etching experiments where 1 ML Gr was exposed to $1 \cdot 10^{-7}$ mbar O_2 at 750 K in front of the analyzer, and no additional components are visible during etching (see Figure 10.1 in the Appendix). Thus, there is no indication that intercalation is a necessary condition for etching.

We do not find a direct-attack mechanism of Gr through intercalated oxygen under any of the etching conditions used by us, irrespective of whether we consider etching of full or partial Gr layers. Such a mechanism was pro-

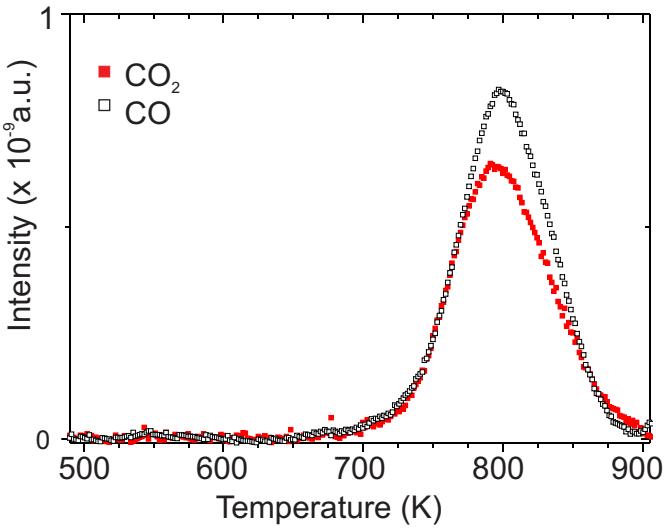

Figure 4.6: TPD spectra of CO_2 (filled red squares) and CO (open black squares) during O_2 exposure of 1 ML Gr layer to a pressure of $3 \cdot 10^{-6}$ mbar. Heating rate 1 K/s. Reprinted from [136], ©2015, with permission from Elsevier.

posed by Starodub *et al.* [142] based on their LEEM observations for oxygen etching of Gr on Ir(111) and Ru(0001).

The efficient oxygen depletion by the edge reaction is consistent with our TPD spectra for CO and CO_2 shown in Figure 4.6. Upon ramping the sample temperature up from room temperature in an oxygen pressure of $3 \cdot 10^{-6}$ mbar, CO and CO_2 desorb as reactions products starting around 700 K. Apparently, due to efficient CO formation at the Gr edge, O is depleted in the initially small etch holes and only a part of the CO molecules formed have the chance to react further to CO_2. As the temperature increases further, more and more Ir is uncovered and one could expect the combustion to become more oxygen rich, i.e., the CO_2 signal to supersede that of CO. This is not the case, but the CO_2 signal starts to decrease even before the CO signal. There are a number of factors that might limit CO_2 production: (i) The Gr-oxygen reaction rate increases exponentially with temperature. (ii) The CO desorption rate increases exponentially with temperature. (iii) Oxygen desorption sets in at 730 K on the time scale of the experiment [see discussion below and Figure 4.13(a)]. The first two factors favor production and direct desorption of CO and factor (iii) may limit the CO oxidation, despite the larger uncovered Ir areas at increasing temperature.

Finally, we take a closer look to the nucleation of holes in the Gr layer, the critical step that initiates etching. Figure 4.7(a) is a moiré resolution STM topograph after exposure to 750 L O_2 at 700 K and displays in its left part a point defect in the moiré lattice and in its right part an etch hole. The line construction in Figure 4.7(a) around the point defect makes plain that it is the dislocation core for two partial edge dislocations (blue lines) with a Burgers vector $\mathbf{a}_{\mathrm{m}}$ corresponding to a primitive translation of the moiré lattice. A similar line construction for the surrounding of the etch hole demonstrates that also in the center of the etch hole a point defect had been located. The constructions in Figure 4.7(b) and (c) visualize that the point defect in the *moiré lattice* is associated with a pentagon-heptagon (5-7) defect in the *graphene lattice* [red atoms in Figure 4.7(b)], i.e., the moiré lattice magnifies the underlying atomic defect, as has been pointed out already by Cosma *et al.* [170]. The 5-7 defect is the dislocation core for two partial edge dislocations (blue lines) with a Burgers vector $\mathbf{a}_{\mathrm{Gr}}$ corresponding to a primitive translation in the graphene lattice. Such 5-7 defects are always present in some concentration in the Gr layer, as they form small angle grain boundaries arising from coalescence of Gr grains during the formation of the closed layer [25]. In an extended analysis of small etch holes we always found that at least one 5-7 defect had been located in an etch hole. In conclusion, etching of a closed Gr layer is initiated by nucleation of etch holes at 5-7 defects. The reactivity of 5-7 defects is also plausible based on their geometry. The σ bond angles deviate substantially from the 120° characteristic for sp^2 bonds and the π electronic system is disturbed. The elastic deformations introduced by 5-7 defects give also rise to out-of-plane bending of the Gr, as was described by Yazyev *et al.* [171] and Lehtinen *et al.* [172]. Consistent with this elastic deformation and the disturbance of the Gr electronic structure, 5-7 defects in Gr on Ir(111) are well recognized by the extended STM contrast change in their surrounding (compare to Figure 4.7(a) and ref. 25).

Having identified the reactive site for the onset of Gr etching in an otherwise perfect Gr monolayer, still the reaction pathway is undetermined. We can envision two fundamentally different mechanisms. (A) First, an oxygen molecule impinges from the vacuum onto graphene. It migrates in its short lifetime on Gr to the 5-7 defect or hits it directly, where it is trapped, dissociates, and forms chemical bonds. The product (CO or CO_2) desorbs and the initial hole is formed. (B) Second, despite the nominally closed, 1 ML Gr layer prepared, some small holes may be present in mesoscopic separations. For instance, cracks in wrinkles [58] might enable rare events of direct impingement of O_2 molecules onto Ir(111), where the molecules dissociatively adsorb. At 700 K, O atoms are highly mobile on Ir(111) under the Gr cover and when they encounter C atoms close to the substrate, as at 5-7 defects,

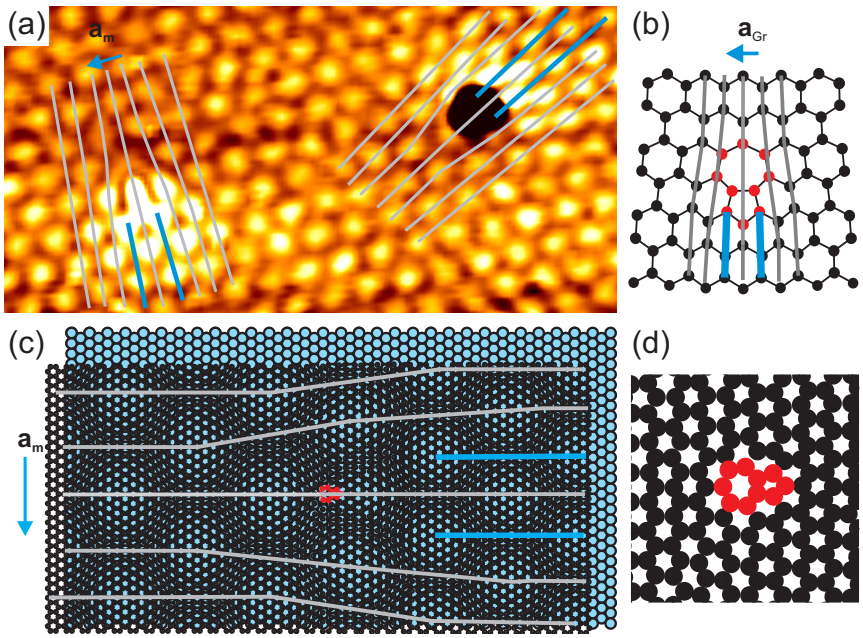

Figure 4.7: (a) Moiré resolution STM topograph of an initially closed 1 ML Gr layer after exposure to 750 L O_2 at 700 K. On the left of topograph a point defect in the moiré lattice is visible that gives rise to two parallel, partial edge dislocations in the *moiré lattice*. Rows of moiré maxima in a direction normal to the dense packed rows in the moiré lattice are connected by thin gray lines. The inserted extra rows of the partial edge dislocations are highlighted by thick blue lines. The Burgers vector of the summed partial dislocations is identical to a primitive translation $\mathbf{a}_m$ in the moiré. On the right in the topograph, a small etch hole in the Gr layer is visible. Connecting again moiré maxima in the vicinity of the etch hole makes plain that prior to etching a defect in the moiré was located at the position of the hole. It is obvious that its topology was identical to that of the moiré defect to the left in the topograph. Image size 40 nm × 20 nm. Tunneling parameters $U_s = 1.0$ V, $I_t = 0.2$ nA. (b) Ball-and-stick model of Gr with a pentagon-heptagon (5-7) defect. The 5-7 defect is colored in red. It gives rise to two inserted partial edge dislocations in the *Gr lattice* along the direction normal to the dense packed rows of Gr. The partial edge dislocations are highlighted by thick blue lines, and rows of carbon ring centers along the same direction by thin gray lines. The summed Burgers vector of the two partial dislocations is identical to a primitive translation $\mathbf{a}_{Gr}$ of the graphene lattice and indicated by a blue arrow. (c) Graphene lattice (black spheres) containing a 5-7 defect (red) overlaid on a hexagonal surface lattice of blue spheres, e.g., Ir(111). The 5-7 defect induces partial edge dislocations in the moiré lattice with Burgers vector $\mathbf{a}_m$, as observed in (a), and thereby amplifies the Burgers vector $\mathbf{a}_{Gr}$ by a factor $\frac{\mathbf{a}_m}{\mathbf{a}_{Gr}} = 10.3$. (d) Zoom of the 5-7 defect and the surrounding Gr lattice from (c). Reprinted from [136], ©2015, with permission from Elsevier.

the reaction is initiated. A very low concentration of intercalated atomic oxygen, well below the detection limit of XPS or STM, would be sufficient. The brief alternative is: oxygen attack from (A) above or (B) below the Gr layer.

To distinguish between these two possibilities we devised the following experiment: Three cycles of 550 K exposure to O_2 with our standard conditions (750 L, $1 \cdot 10^{-5}$ mbar) and subsequent heating to 800 K in a background pressure below $2 \cdot 10^{-10}$ mbar were performed for a complete Gr layer. If possibility (B) were the case, intercalation at 550 K and subsequent reaction at temperatures above 700 K would have taken place, resulting in etch holes which become widened through subsequent cycles. If case (A) is realized, no etch holes are expected. We did not find etch holes, but a perfectly intact Gr layer, as shown in the STM topographs Figure 4.8. Thus, we propose mechanism (A) as the simplest explanation for our observations. Additional *ab initio* calculations might help to clarify the details of the reaction path.

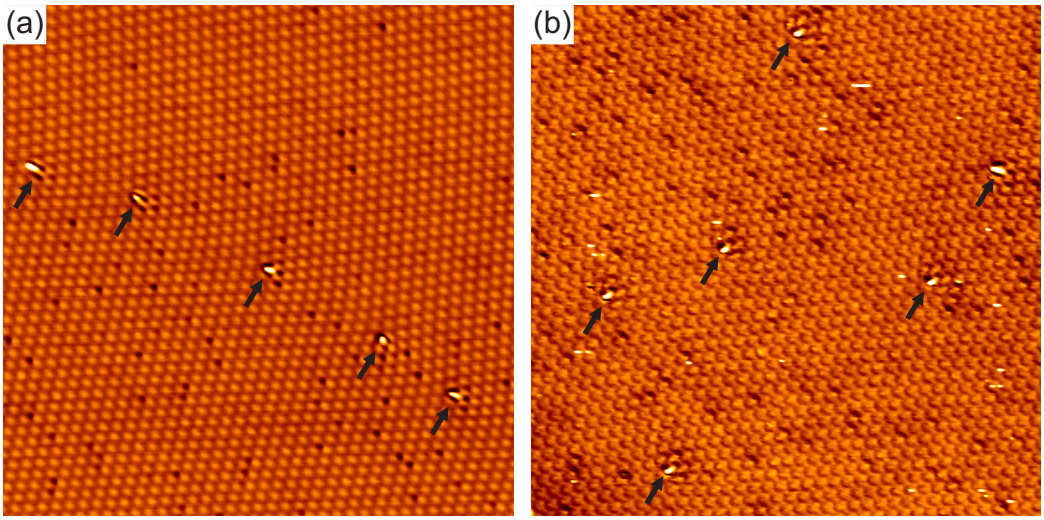

Figure 4.8: STM topographs showing 1 ML Gr/Ir(111) (a) before and (b) after three exposures of 750 L O_2 at 550 K, each followed by annealing to 800 K for 100 s in UHV. Black arrows indicate 5-7 defects that are intact in both cases. Image sizes 100 nm × 100 nm. Tunneling parameters (a) $U_s = -2.0$ V and $I_t = 6.5$ nA; (b) $U_s = -0.9$ V, $I_t = 3.3$ nA. Reprinted from [136], ©2015, with permission from Elsevier.

Larciprete *et al.* [9] and Ulstrup *et al.* [158] observed intercalation of oxygen under a Gr layer on Ir(111) with a nominal coverage of 1 ML already at 520 K. Larciprete *et al.* [9] assumed the penetration of the entire O_2 molecule through point defects or grain boundaries in the Gr layer, while Ulstrup *et al.* [158] propose intercalation through wrinkles. Based on the absence of in-

tercalation up to 700 K and for pressures up to $1 \cdot 10^{-5}$ mbar [1]in our 1 ML Gr layers on Ir(111), we rule out this scenario for our experiments.

Our finding that etching of 1 ML Gr starts at 5-7 defects substantiates a number of previous observations. First we note that not only small angle grain boundaries - as present in our well oriented Gr layers - are formed by a combination of pentagon and heptagon rings [25], but that also large angle grain boundaries are formed through an arrangement of these elements [45, 171, 173]. The difference between a small angle and a large angle grain boundary is the separation of these defects, ranging from hundreds of nm to immediate neighborhood. Gotterbarm *et al.*'s [144] finding that the time needed for etching of a nominally closed Gr layer on Rh(111) decreases with an increasing amount of grain boundaries is fully consistent with our results that 5-7 defects are the nucleation centers for Gr etch holes: more and larger-angle grain boundaries display more 5-7 defects, giving rise to etch holes, and thus to faster etching. Vlassiouk *et al.* [146] observed upon air exposure of Gr on Cu at elevated temperatures a preferential etching of Gr grain boundaries, fully consistent with our finding of the 5-7 defect being the site of etch hole formation. The observation of Dobrik *et al.* [166] that etching of graphite results in sparse hexagonal etch holes together with etched trenches can be rationalized as well by our finding: occasional 5-7 defects in terraces give rise to the hexagonal etch holes, while their dense arrangement in grain boundaries creates the trenches, resulting from densely nucleated holes that coalesce very early.

4.3 Etching of a partial Gr layer on Ir(111)

A partial Gr layer is distinct from a full Gr layer through the presence of Gr flake edges. It is therefore plausible that the much lower onset temperature of etching for a partial layer results from the absence of the nucleation problem. Oxygen dissociates on the bare Ir and can then attack at the Gr edges. To confirm this assumption and to obtain additional insight into the etching mechanism of the 0.5 ML Gr, we continuously imaged a sample by STM at 585 K, while it was exposed to O_2. Figure 4.9(a)-(d) display selected STM topographs during increasing oxygen exposure time, and Figure 4.9(e)-(h) show schematically the cross-sections along the blue lines in Figure 4.9(a)-(d). To visualize the amount of Gr that has been etched, the edges of the holes in the Gr layer prior to oxygen exposure are shown in white in Figure

[1]We tested our Gr layer for impermeability against oxygen also for higher pressures. Up to 520 K and pressures up to $5 \cdot 10^{-4}$ mbar we do not observe oxygen intercalation underneath 1 ML Gr.

4.9(a)-(d). Note that partial Gr layers display substantial variations of the local coverage around their mean (0.5 ML) on the mesoscopic scale. These variations do not influence the processes described here to any significant extent.

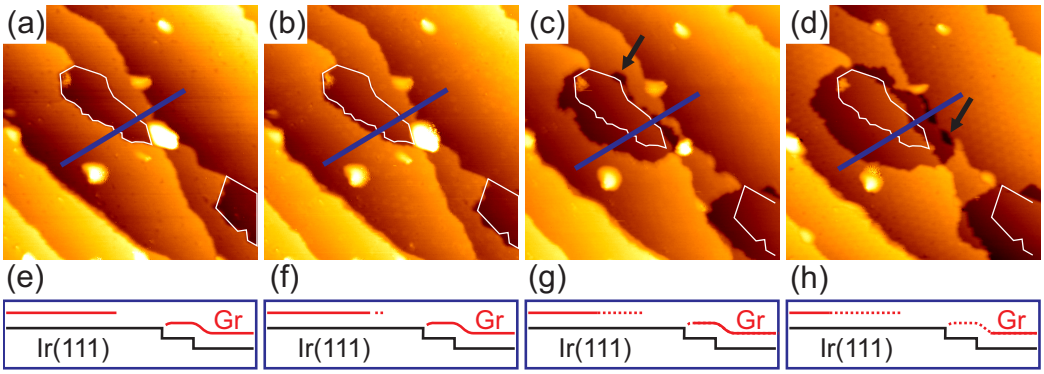

Figure 4.9: Etching of 0.5 ML Gr/Ir(111) exposed to $1.4 \cdot 10^{-7}$ mbar O_2 at 585 K. (a)-(d) STM topographs taken during exposure after (a) 30 L, (b) 80 L, (c) 320 L, and (d) 670 L, showing 6 Gr-covered Ir terraces and two holes in the Gr layer with the contours prior to oxygen exposure encircled in white. Black arrows highlight two of the slot-like holes at a down-step. Image size 50 nm × 50 nm. Tunneling parameters $U_s = 1$ V, $I_t = 0.06$ nA. (e)-(h) are schematic cross-sections along the blues lines in the corresponding STM topographs (a)-(d). The full movie is available online in the Supplementary Data of ref. [136]. Reprinted from [136], ©2015, with permission from Elsevier.

It is apparent in Figure 4.9 that Gr is removed exclusively from the edges of the flakes. In all etching experiments conducted with 0.5 ML Gr, we never observed the nucleation of an etch hole within the Gr layer, consistent with the much higher onset temperature of 700 K for etch hole nucleation in the closed Gr layer, as found above. At 585 K, etching proceeds in all directions and does not give rise to well-defined Gr edge orientations. The etch rate perpendicular to a free Gr edge is roughly 4 nm/h. Whenever the receding Gr flake passes over a down-step of the substrate (forming an up-step for the Gr on the lower terrace), the Gr flake is pinned there for a while. Gradually, small, slot-like etch holes form (black arrows in Figure 4.9), elongated along the substrate step direction. Only when neighboring slot-like holes coalesce, the Gr flake detaches from the step and retracts further onto the substrate terrace.

This phenomenon of Gr flake pinning at up-steps of the substrate is illuminated in more detail in Figure 4.10. Figure 4.10(a) is a larger scale STM topograph after exposure to 750 L O_2 at 410 K and subsequent heating to

900 K. After O_2 exposure at 410 K, Ir is covered by a dense O adlayer, both under the graphene and on the uncovered terraces. As we will see below, during heating to 900 K the entire oxygen is used up to combust Gr to CO_2 and CO. As a result of etching, typical, slot like holes in the Gr are observed downhill of an uncovered substrate step [black arrows in Figure 4.10(a)]. Uphill of an uncovered Ir step the Gr flake edges are curved and found at arbitrary locations on the Ir terrace, typically further away from the substrate step. The situation is clarified by the schematic cross-section in Figure 4.10(b), which is taken along the blue line in Figure 4.10(a). If the up-step is well aligned, parallel to a dense packed $\langle 1\bar{1}0\rangle$ direction, the holes next to the up-step are often rather uniformly spaced with the moiré periodicity, as visible in Figure 4.10(c). We note that the formation of the slot-like holes at up-steps does not depend on the details of oxygen supply, i.e., on whether it is provided at the etching temperature or prior to heating.

To explain our observations, we distinguish edges of a Gr flake freely located on an Ir(111) terrace and edges in contact with an Ir(111) up-step. Carbon atoms of free Gr edges bend down to the substrate, as discussed above. Carbon atoms of Gr edges in contact with an up-step bind to the Ir up-step atoms. Less deformation of the Gr flake is necessary for chemical bond formation with Ir up-step atoms, as they are 2.2 Å closer to the height level of the edge C-atoms. Therefore, these bonds are stronger [132]. Assuming for simplicity – similar to the situation in Figure 4.10(c) – a perfect alignment of up-step and Gr flake, with the $\langle 1\bar{1}0\rangle$ Ir step orientation in parallel with a dense packed zig-zag Gr edge, the C atom positions will vary with moiré periodicity with respect to the up-step atom positions. This will imply a variation of bond strength between C atoms and Ir up-step. The least favorable C-Ir bonds of the free flake edges are most reactive to oxygen and carbon is combusted there. The stronger bonds of Gr flakes in contact with an up-step are less reactive and initially resist etching. Once etching of these steps sets in, etch holes and pinned locations may alternate with moiré periodicity as shown in Figure 4.10, since the bond strength between the Gr flake edge atoms and the up-step Ir atoms varies along the step with this periodicity. As the Gr edge between two pinning points at the up-step becomes more concave with a decreasing magnitude of the radius of curvature during continued etching, the chemical potential of the C edge atoms increases more and more, easing the progress of etching. At the same time the total edge length and thus the related energy increases, making the situation more and more unstable. Through fluctuations or coalescence of neighboring holes, eventually pinning points will be released, thereby lowering the energy of the configuration, and etching progresses.

Next we turn to the analysis of the reaction products of the partial Gr

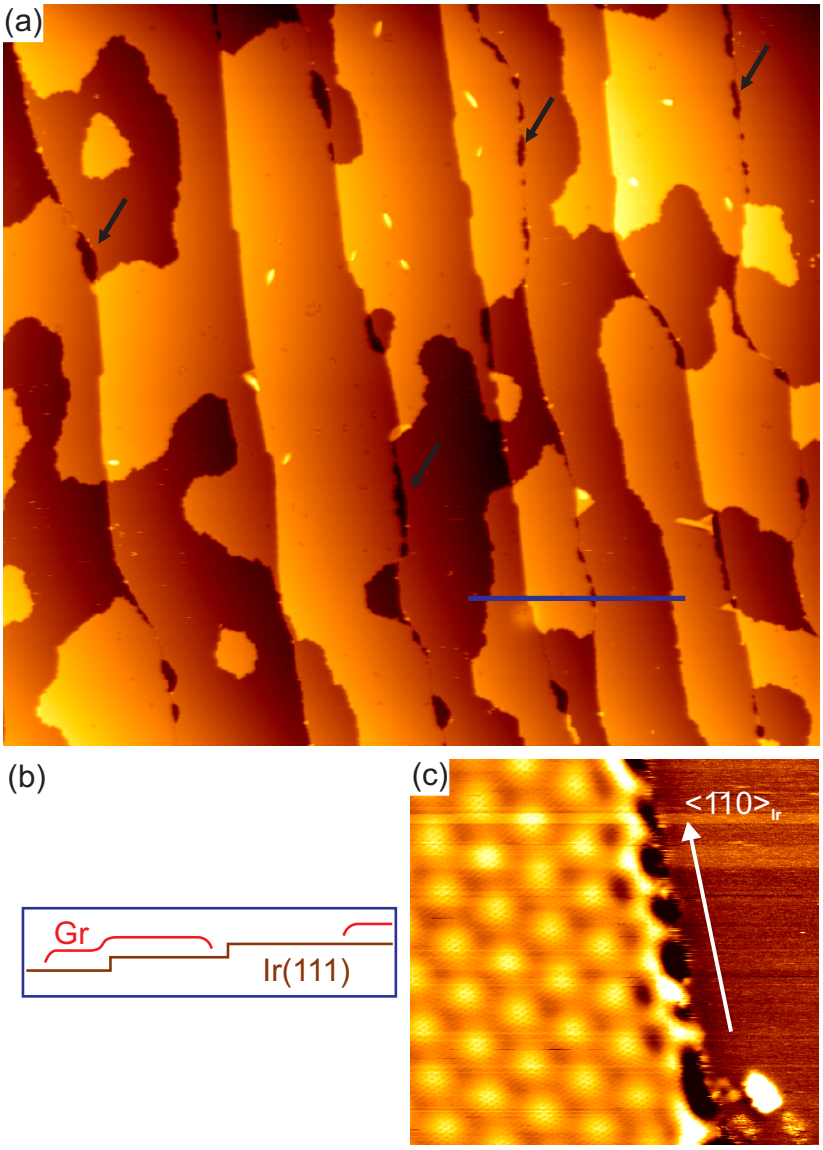

Figure 4.10: (a) STM topograph after 750 L O_2 at 410 K and subsequent heating to 900 K. Black arrows highlight slot-like holes at a down-step, as in Figure 4.9. (b) Schematic cross-section for morphology along blue line in (a). (c) High resolution STM topograph of a Gr flake attached to an Ir step edge after oxygen etching. The Ir step is oriented along a dense packed $\langle 1\bar{1}0 \rangle$ direction. Image size (a) 285 nm × 255 nm; (b) 17 nm × 16 nm. Tunneling parameters (a) $U_s = -2$ V, $I_t = 0.4$ nA; (b) $U_s = 0.8$ V, $I_t = 3.1$ nA. Reprinted from [136], ©2015, with permission from Elsevier.

layer upon O_2 etching as provided by the TPD spectra in Figure 4.11. For these spectra the same oxygen pressure and heating rate as for the spectra of the full monolayer shown in Figure 4.6 were used. As visible in Figure 4.11, etching of 0.5 ML Gr results predominantly in CO_2 production (filled red circles) with an onset temperature of approximately 580 K. This is somewhat higher than concluded from our XPS data presented in Figure 4.1, but still much lower than the onset temperature of 700 K inferred from Figure 4.6 for the 1 ML Gr layer. When the O_2 is provided prior to, and not during heating, the onset temperature of CO_2 production is slightly lower, around 530 K (Figure 4.12). This latter experimental situation is closer to that of the XPS experiments of Figure 4.1(b), where the first O_2 exposure leads to intercalation, and subsequent exposures take place on an already intercalated sample. Consequently, also the onset temperature for Gr combustion is closer to the temperature obtained from the XP spectra. Compared to the TP spectra of the full Gr layer (Figure 4.6), CO production for the partial layer is remarkably reduced. While for the full Gr layer the CO signal was slightly stronger than that of CO_2, for the partial Gr layer the CO production is minor and superseded with a factor of 10 by CO_2 production. As shown in Figure 4.12, during heating of an oxygen intercalated 0.5 ML Gr film, the TPD spectra display no desorption of oxygen.

The higher CO_2 production during combustion of the partial Gr layer may be understood within the same framework outlined already during the discussion of the TPD spectra of the full monolayer. (i) Due to the lower temperature of combustion, the Gr-oxygen reaction rate is exponentially slowed down. (ii) For the same reason, the CO residence time on Ir(111) is higher. (iii) Oxygen desorption from the bare Ir(111) is absent. All three factors tend to favor the CO oxidation to CO_2 prior to desorption. For the partial Gr coverage – in contrast to the closed Gr layer – already at the onset of etching a large reservoir of oxygen is present on the sample, an additional factor in favor of CO_2 formation.

Figure 4.13(a) displays the temperature dependent intensity of the O 1s core level during heating of a 0.5 ML Gr sample. It had been exposed to 750 L O_2 at 380 K, resulting in a saturation with atomic oxygen through adsorption and intercalation, prior to ramping the temperature. The oxygen concentration starts to diminish at 560 K and reaches zero at 720 K [red line in Figure 4.13(a)]. At the same temperature, according to our TPD spectra (Figure 4.11), the Gr combustion ceases. For comparison, in Figure 4.13(a) also the temperature dependent O 1s signal after saturation of the bare Ir(111) sample with oxygen at room temperature is plotted (blue line). Oxygen desorption from bare Ir(111) sets in at 730 K. The comparison of the two O 1s spectra together with the absence of O_2 desorption in our TPD

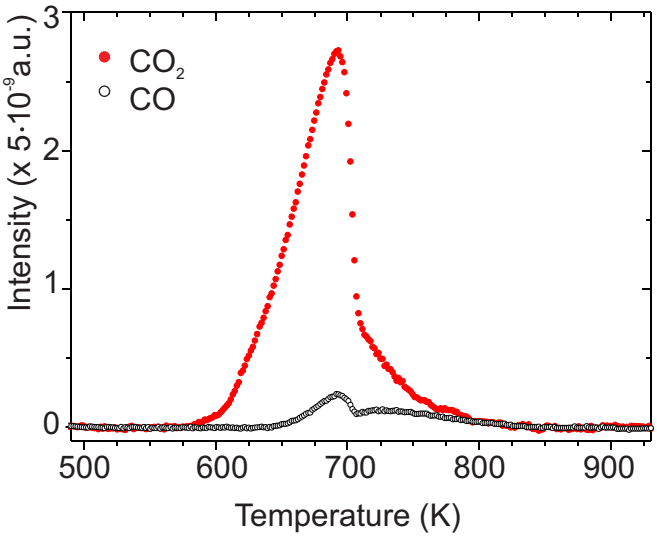

Figure 4.11: TPD spectra of CO_2 (filled red circles) and CO (open black circles) during O_2 exposure of a partial, 0.5 ML Gr layer to a pressure of $3 \cdot 10^{-6}$ mbar. Heating rate 1 K/s. Reprinted from [136], ©2015, with permission from Elsevier.

spectra (compare to Figure 4.12) make plain that in the presence of a partial Gr layer the entire adsorbed and intercalated oxygen is reacted to CO or CO_2.

Finally, in Figure 4.13(b) we follow the peak position of the C 1s signal for a 0.5 ML Gr sample prepared and heated under identical conditions as for the measurements of Figure 4.13(a). Most pronounced, between 600 K and 670 K a rather abrupt shift from 283.72 eV (C_2), characteristic for p(2x1)-O intercalated Gr, to 284.10 eV (C_{Ir}), signaling non-intercalated Gr, is observed. At the same time, the intensity of the C 1s component drops as apparent from the color change from to dark blue to light blue at the position of the maximum intensity. Based on our inferences above, we must interpret the C 1s shift as a transition of Gr intercalated by a still dense oxygen ad-layer to non-intercalated Gr. The drop of the C 1s intensity in this temperature interval is consistent with substantial Gr etching, which is the reason for the oxygen loss. The temperature interval from 600 K to 670 K, where the C 1s peak shifts abruptly, is the same interval as where the O 1s signal in Figure 4.13(a) changes with the highest rate. Note that complete combustion of the pre-adsorbed and intercalated oxygen is only sufficient to burn approximately 1/3 of the initial 0.5 ML Gr coverage.

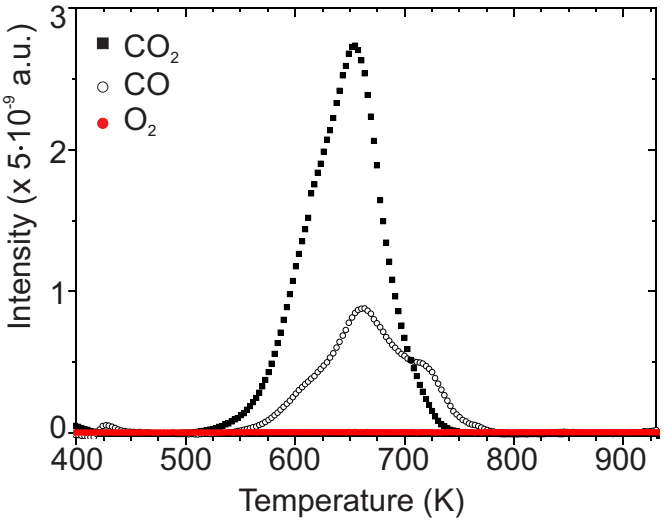

Figure 4.12: TPD spectra of CO_2 (filled circles), CO (open black circles), and O_2 (filled blue circles) after exposure of 0.5 ML Gr to 750 L O_2 at 410 K, leading to completely intercalated Gr flakes. Heating rate 5 K/s. Reprinted from [136], ©2015, with permission from Elsevier.

Sutter *et al.* [41] noted that "the presence of graphene affects the binding of oxygen on Ru(0001), weakening the coupling so desorption can occur at temperatures at which O remains strongly bound on the free metal surface." In the presence of a sufficient amount of Gr we only observe desorption of CO and CO_2, but no desorption of O_2 at any temperature. We therefore conclude that the presence of Gr on Ir(111) does not affect the binding of oxygen to Ir(111) to any significant extent. Transition metal surfaces enabling dissociative adsorption of molecular oxygen catalyze Gr combustion at temperatures well below the desorption temperature of oxygen.

4.4 Etching of graphene nanoflakes

In this section we analyze how the initial size of Gr flakes affects their etching behavior. The size variation was realized by TPG growth temperatures of 970 K, 1020 K, and 1320 K resulting in 0.2 ML flakes with average radii r_0 of 0.8 nm, 5.2 nm, and 11.5 nm, respectively [130]. The XPS etching experiments are represented in Figure 4.14(a)-(c). Similar to Figure 4.1(a) and (b), Figure 4.14(a)-(c) display the C 1s spectra before (lowest spectrum) and

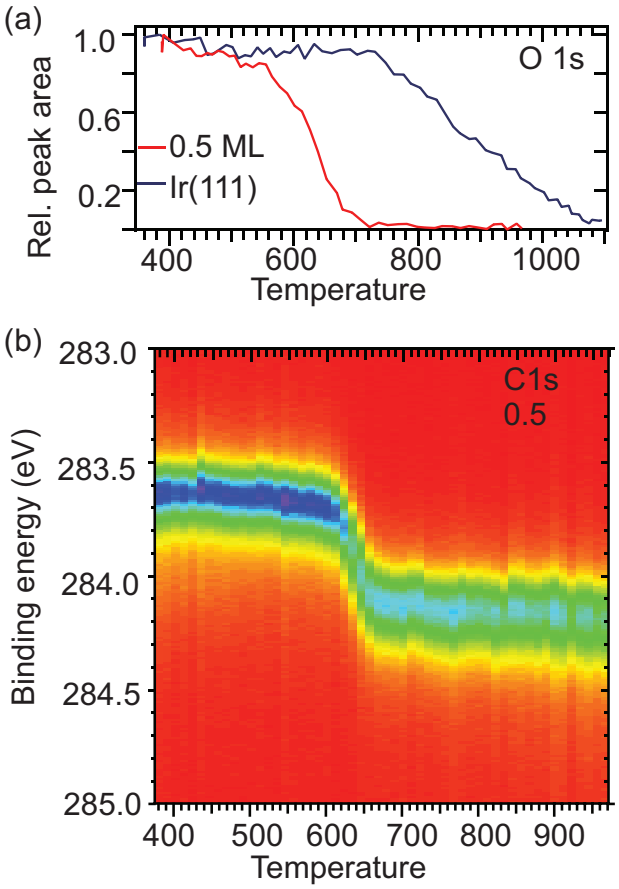

Figure 4.13: (a) Peak area of the O 1s XPS signal as a function of temperature. The red line signal was derived from iteratively recorded spectra *during* heating of 0.5 ML Gr/Ir(111). Prior to ramping the temperature, the 0.5 ML Gr/Ir(111) sample had been exposed to 750 L oxygen at 380 K. For comparison, the relative peak area of the O 1s XPS during heating of Ir(111) is shown as a blue line. Prior to ramping the temperature, the Ir(111) sample had been exposed to 40 L oxygen at 380 K. (b) C 1s spectra recorded iteratively during heating of oxygen 0.5 ML Gr/Ir(111) after the sample had been exposed to 750 L oxygen at 380 K prior to ramping the temperature. Each vertical line represents one C 1s spectrum, dark blue corresponds to high, red to low intensities. Reprinted from [136], ©2015, with permission from Elsevier.

after successive exposures to 750 L of O_2 at stepwise increasing temperatures, as indicated in the figure. Figure 4.14(d) shows the integrated peak intensity (filled squares) of Figure 4.14(a)-(c).

The pristine Gr spectrum of the smallest flakes [bottom spectrum of Figure 4.14(a)] differs from that of large flakes (compare with Figure 4.1) in that it is both shifted and broadened towards lower binding energies. This C 1s peak shape is well known from the work of Lacovig *et al.* [167], who attributed the shift to a modified doping of Gr due to the smaller average height of the nanoflakes, and the broadening to additional components resulting from the large number of edge and near-edge atoms. Surprisingly, upon successive exposures to oxygen at increasing temperatures the C 1s peak maximum for the nanoflakes shifts just by approximately -0.04 eV towards the low binding energy side, compared with the -0.17 eV shift (C_1 component) related to the intercalated dilute adatom gas, and the -0.47 eV shift (C_3 component) expected for the p(2×1)-O adsorbate layer. We have to conclude that there is either none or only a very low concentration of atomic oxygen underneath the nanoflakes. A second remarkable observation is the onset temperature of etching around 400 K [see Figure 4.14(d)], roughly 150 K lower than what we observed for large Gr flakes.

For larger nanoflakes grown at 1070 K, shown in Figure 4.14(b), the typical peak position and shape of pristine Gr is almost recovered, and, as for large flakes, intercalation precedes etching. The onset temperature of etching for the 1070 K flakes around 480 K is higher than that for the 970 K flakes (400 K), but clearly lower than what we know for large Gr flakes (575 K). For Gr flakes grown at 1320 K a similar behavior is observed, the onset temperature, roughly 515 K, is still reduced, but approaches the reference value of the large Gr flakes.

The energetic penalty for delamination of a Gr flake consists of an areal contribution (Gr has to be detached from the Ir substrate) and an edge contribution (Gr edge bonds have to be lifted to raise the flake height). For small flakes the edge contribution becomes substantial, thereby impeding delamination of Gr flakes and thus intercalation by a dense oxygen phase. The fact that even a dilute adatom gas is absent, or that it is much more dilute than usual, can be rationalized by the lower average flake height, as was pointed out by Lacovig *et al.* [167]. Due to the larger deformation necessary to host oxygen adatoms under flakes of reduced height, the adsorption energy of an O adatom underneath such a Gr flake is lower in magnitude (penalty for Gr deformation) than on the terrace. This energy difference will reduce the concentration of a dilute adatom gas compared to large flakes with nominal height.

Two possible explanations for the size dependence of the onset temper-

ature of Gr flake etching can be formulated: (A) Due to the large number of edge atoms, for small flakes the rate of etching is much higher at a given temperature. (B) Due to a stronger binding of small Gr flakes (lower average height) the transition state for the rate limiting step of etching, consisting presumably in the formation of a carbon-oxygen bond, is changed, lowered in activation energy or increased in prefactor or both. We will first analyze hypothesis (A) with the help of a simple analytical model for etching.

In agreement with the experimental results of Cui *et al.* [141] and Sutter *et al.* [41], we assume a linear decrease of the flake radius with time. During the i-th O_2 exposure, flakes approximated as circular with an initial average radius r_i experience a decrease of their radius by Δr_i:

$$\Delta r_i = \Delta r(T_i) = a \cdot \Delta t \cdot \nu(T_i), \tag{4.4.1}$$

with $\nu(T_i)$ being the rate of elementary etching events at the temperature of oxygen exposure T_i and per edge site, Δt the exposure time, and a the decrease in radius after an elementary etching event. We assume an Arrhenius behavior for the elementary etch events

$$\nu(T_i) = \nu_0 \cdot e^{-E_a/(k_B T_i)}, \tag{4.4.2}$$

with E_a being the activation energy and ν_0 the prefactor. The open circles in Figure 4.14(d) show the calculated Gr area according to our model for the three flake sizes resulting from the three different TPG temperatures. E_a and ν_0 were left free as fit parameters, while all other quantities entering the model (T_i, r_0, Δt, $a = 0.213\,\mathrm{nm}$) are fixed by the experimental situation. The fits based on just two free parameters for the three data sets reproduce the experiments surprisingly well, the shifts in etch temperature as well as the overall decay of the Gr coverage with increasing temperature. We obtain $E_a = 0.44\,\mathrm{eV}$ and $\nu_0 = 500\,\mathrm{s}^{-1}$. The quality of the fit seems to be a striking confirmation of the assumption that the variation in edge length is responsible for the differences measured for the three flake sizes.

Given the experimental uncertainties, a more sophisticated fit with additional free parameters seems not to be justified. However, in order to obtain additional insight, we fitted each etching curve separately with its own set of E_a and ν_0 [Figure 4.15(a)]. We obtain a moderate increase of E_a and ν_0 with flake size ranging from $E_a = 0.355\,\mathrm{eV}$ and $\nu_0 = 50\,\mathrm{s}^{-1}$ for the TPG temperature of 970 K to $E_a = 0.56\,\mathrm{eV}$ and $\nu_0 = 5000\,\mathrm{s}^{-1}$ for the TPG temperature of 1320 K. Based on these numbers we conclude that although there may be a slight change in the transition state with flake size, the dominant effect for the shift in the onset temperature of etching with flake size is the change in perimeter length. We note that it is impossible to fit any of the curves with a

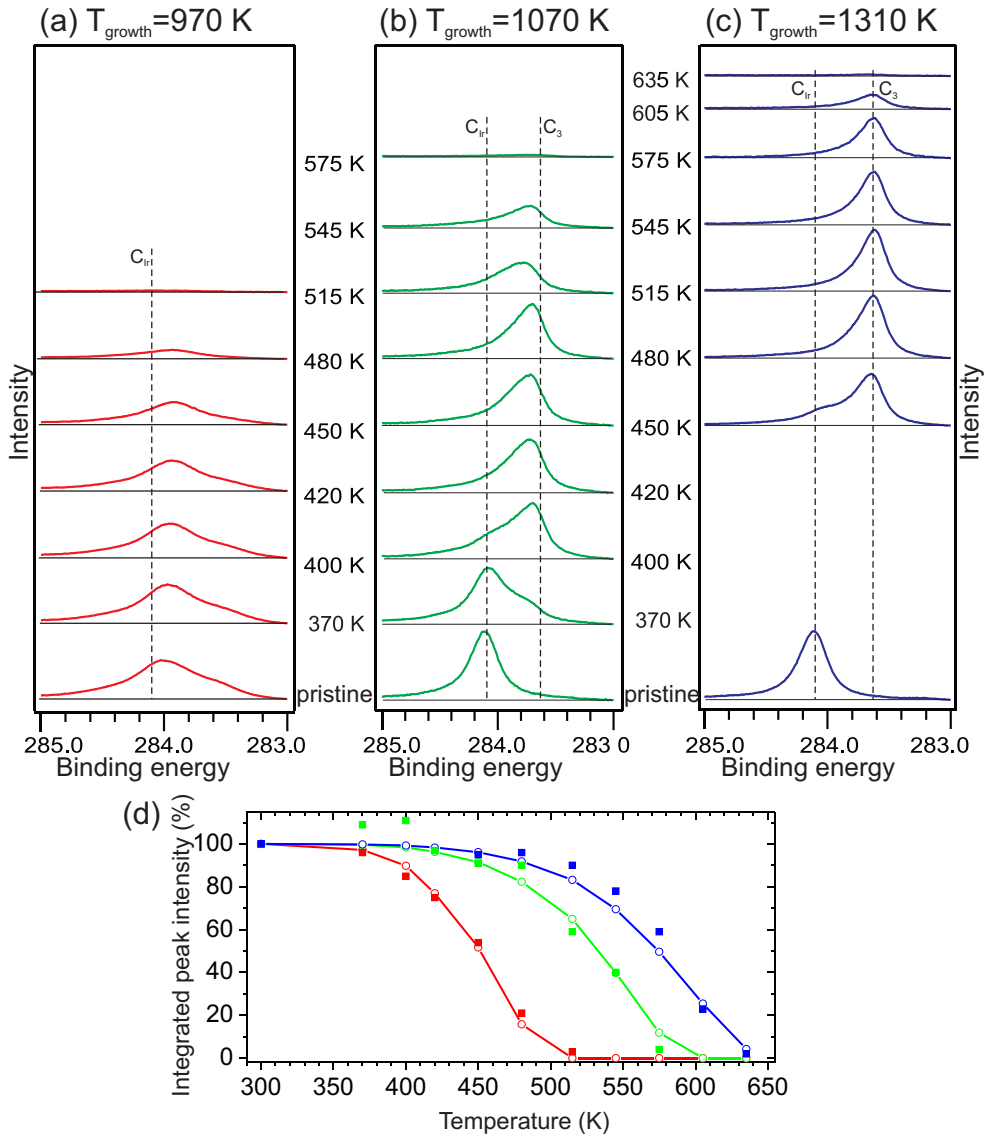

Figure 4.14: XP spectra of the C 1s region of 0.2 ML Gr nanoflakes grown by one TPG cycle at (a) 970 K (b) 1070 K and (c) 1320 K, after exposure to 750 L O_2 at stepwise increasing temperatures, as indicated. The spectra were recorded at room temperature. Dashed lines mark the positions of C 1s components as specified in Figure 4.1 for large, pristine Gr flakes (C_{Ir}) and large Gr flakes intercalated by a dense p(2×1)-O adsorbate layer (C_3). (d) Integrated C 1s intensities as a function of temperature for the spectra of (a) [filled red squares],(b) [filled green squares], and (c) [filled blue squares]. The value of 100 % integrated C 1s intensity was set for the pristine flakes at room temperature. Open circles, connected by lines to guide the eye, are fits to the data assuming $E_a = 0.44\,\text{eV}$ and $\nu_0 = 500\,\text{s}^{-1}$. Reprinted from [136], ©2015, with permission from Elsevier.

prefactor in the standard range between $10^{12} - 10^{14}\,\mathrm{s}^{-1}$ [see Figure 4.15(b)]. The low prefactors of the order of $10^{2} - 10^{3}\,\mathrm{s}^{-1}$ indicate a complex transition state involving several degrees of freedom. Table 1 compares the two etch

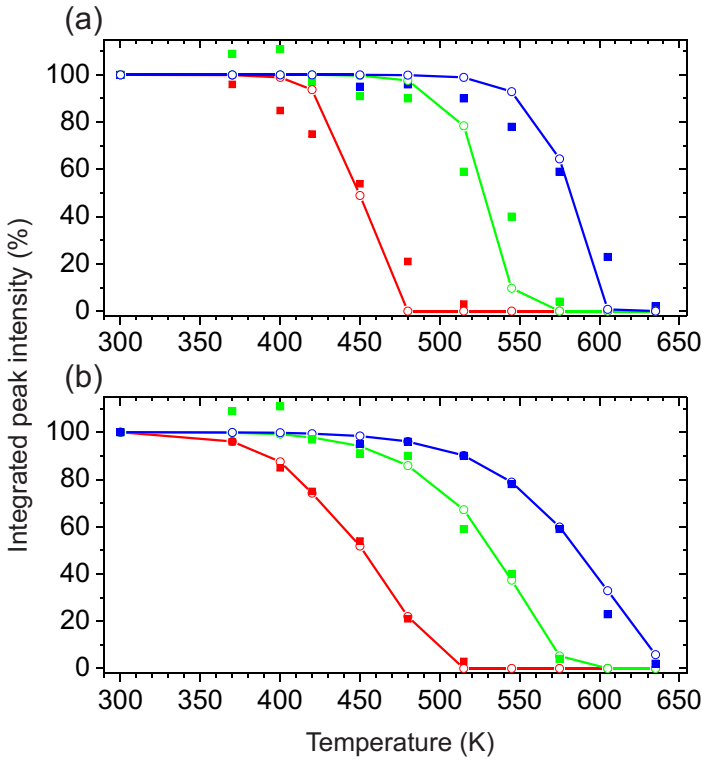

Figure 4.15: Remaining Gr area after etching steps at different temperatures. Experimental data are filled squares, calculated areas are open circles connected by lines that are guides to the eye, $T_{\mathrm{growth}} = 970\,\mathrm{K}$ in red, $T_{\mathrm{growth}} = 1070\,\mathrm{K}$ in green, $T_{\mathrm{growth}} = 1310\,\mathrm{K}$ in blue. (a) Best fit with 6 free parameters. red: $E_a = 0.355\,\mathrm{eV}$, $\nu_0 = 50\,\mathrm{s}^{-1}$; green: $E_a = 0.54\,\mathrm{eV}$, $\nu_0 = 5000\,\mathrm{s}^{-1}$; blue $E_a = 0.56\,\mathrm{eV}$, $\nu_0 = 5000\,\mathrm{s}^{-1}$. (b) red: $E_a = 1.25\,\mathrm{eV}$, green: $E_a = 1.39\,\mathrm{eV}$, blue $E_a = 1.49\,\mathrm{eV}$, and $\nu_0 = 1 \cdot 10^{12}\,\mathrm{s}^{-1}$ for all curves. Reprinted from [136], ©2015, with permission from Elsevier.

parameters obtained by us with literature data. The set of our data agrees reasonable well with the set obtained by Cui *et al.* [141] for etching of Gr on Ru(0001). While lateral etching of graphite displays a similar low ν_0 as obtained by us, the activation energy for etching is substantially higher. Indeed, we consider the metal as a catalyst for Gr etching by providing atomic oxygen at the reaction front. In absence of the catalyst, the activation energy for the rate limiting step is expected to be considerably higher, as observed.

Difficult to reconcile with our results are the data of Sutter *et al.* [41], which are also inconsistent with the results of Cui *et al.* [141].

Table 4.1: Activation energies and prefactors for etching by molecular oxygen. Reprinted from [136], ©2015, with permission from Elsevier.

E_{act} (eV)	ν_0 (s^{-1})	material	reference
0.45	$5 \cdot 10^2$	Gr/Ir(111)	this work
0.28	$5 \cdot 10^4$	Gr/Ru(0001)	ν_0 extrapolated from Fig. 6 of Cui *et al.* [141]
0.99 ± 0.08	$1 \cdot 10^4 - 1 \cdot 10^5$	graphite	Hahn *et al.* [162]
1.1 ± 0.1	$3 \cdot 10^{15}$	Gr/Ru(0001)	Sutter *et al.* [41]

4.5 Summary

For the 1 ML Gr layer on Ir(111) – which contains no defects except small angle grain boundaries – we found the 5-7 defect to be the site of nucleation for hexagonal etch holes. These holes are bound predominantly by zig-zag edges. For the oxygen pressure applied, nucleation takes place at 5-7 defects around 700 K, apparently through dissociation of O_2 approaching from the gas phase. Once the Gr layer has been opened, Gr combustion proceeds by dissociative adsorption of molecular oxygen, diffusion to the Gr edge, reaction with Gr edge atoms and finally desorption of the products. The lower onset temperature of around 550 K for etching of a partial Gr layer with large flakes is based on the fact that no nucleation process is involved. Gr flake edges, the locations where etching proceeds, are already present.

The apparent dependence of the onset temperature for etching on the Gr flake size, ranging down to 410 K for nanoflakes, turns out to result predominantly from geometry: only edge atoms can be etched, of which the concentration strongly depends on the average flake size. The elementary etch process may be described as a thermally activated process at the Gr flake edge with an activation energy of the order of $E_a = 0.44\,\mathrm{eV}$ and a prefactor of $\nu_0 = 500\,\mathrm{s}^{-1}$, irrespective of the flake size. The low prefactor indicates a complex transition state, consistent with the apparent inefficiency of etching: there is an extended temperature range where etching proceeds, but only few of the oxygen atoms supplied actually react with Gr.

Transition metal surfaces providing atomic oxygen through dissociative adsorption of molecular oxygen efficiently catalyze Gr combustion, as can be

inferred from the higher rate of the elementary etch process for a given temperature as compared to graphite. A low temperature of reaction favors CO_2 production. Upon heating, no desorption of molecular oxygen from partially Gr-covered Ir(111) is observed.

Depending on the Gr morphology, temperature and applied pressure of molecular oxygen, intercalation may or may not accompany etching of Gr on a transition metal surface. Based on our results it is not a necessary condition and largely irrelevant for etching: Gr nanoflakes with radii of the order of 1 nm as well as the full monolayer are etched without oxygen intercalation under the conditions of our experiments.

We believe that similar experiments as shown here for the impermeable Gr layer might enable the identification of the nucleation site for etching in graphite, and speculate that this site could be the pentagon-heptagon defect also. Moreover, future density functional theory calculations might provide additional insight into the atomistic details of pentagon-heptagon defect attack by oxygen, as well as into the reaction of chemisorbed oxygen with Gr C atoms binding to the substrate.

Chapter 5

Core level shifts of doped graphene

This chapter is based on a manuscript being prepared for submission and contains contributions from: M. Petrović, T. Gerber, A. J. Martínez-Galera, E. Gråsäs, M. A. Arman, C. Herbig, J. Schnadt, M. Kralj, J. Knudsen, and T. Michely. I was involved in all XPS measurements, analyzed the data, prepared Figures 5.1, 5.2, 5.5 - 5.10, and wrote the draft for the manuscript.

Shifts in the binding energy of core electrons are used in XPS to identify changes in the chemical environment of the atoms under concern. In Gr research, the CLSs of the C 1s photoelectrons are frequently monitored to investigate adsorption and intercalation [9, 33, 34, 174–185]. They can be used with great benefit to follow chemical reactions under Gr [186–188] and may even be the key to uncover new reaction pathways [189]. A quantitative understanding of their magnitude and of changes in the spectral shape associated with CLSs is not only desirable from the scientific point of view, but would make application and analysis in practical graphene work far more beneficial. For instance, a quick estimate for the Gr doping level on the basis of the CLS and spectral shape could be such a benefit. This chapter is intended to contribute to the experimental basis for such an improved understanding of the intercalation core level shifts of Gr.

By investigating K graphite intercalation compounds, DiCenzo *et al.* [190] noted already in 1981 that the main effect of intercalation is to shift E_{F} relative to the bands (compare also with Fig. 2 of [190]). Already a very

small charge transfer arising from intercalation gives rise to a substantial shift of E_F due to the small density of states in graphite around the charge neutrality point. Since CLSs are referenced to the fermi level E_F, its shift implies a corresponding shift of the C 1s core level. The importance of this rigid band shift for the explanation of the C 1s CLS or valence band shifts upon K doping was confirmed subsequently for adsorption *on* graphite by Bennich *et al.* [191] as well as Kilgren *et al.* [192], for intercalation of C onions by Montalti *et al.* [193], and for K_3C_{60} thin films by Schiessling *et al.* [194], to name a few. Since Gr and graphite share the property of a very low density of states near the charge neutrality point (the Dirac point E_D in the case of Gr), it is plausible to invoke this effect also to explain the C 1s CLSs in Gr. Dahal *et al.* [195] presume the rigidity of the Gr band structure (i.e., the identity of CLS and Dirac point shift) for doping levels in magnitude up to 0.5 eV in their model of charge doping of Gr by dielectrics. Also Fedorov *et al.* [185] implicitly invoke the rigid band model to explain the C 1s CLS caused by adsorption of alkali and earth alkali metals to Gr on Au/Ni/W(110). However, the authors note that the C 1s CLS is smaller than the valence band shift, i.e., the shift of the Dirac point, and attribute this observation to core hole screening. Based on *ab initio* calculations for intercalated alkali metals, halogens, O, H, and CO, Andersen *et al.* [184] find a linear correlation between the C 1s CLS and the Gr doping level, except for the highest doping levels. However, the shift of the C 1s core level amounts to only approximately 0.7 of the Dirac point shift, which is not consistent with a rigid band model.

In addition to a CLS, a characteristic C 1s line shape was observed for K adsorption on or intercalation into graphite [190, 191], for Li intercalation into graphite [60, 196], and for alkali-metals intercalated under Gr [183,185,197,198]. Upon deposition or intercalation, the initial, rather narrow and almost symmetric C 1s line shape is asymmetrically broadened towards higher binding energies (BEs) and develops an additional broad shoulder towards higher BEs.

Bennich *et al.* [191] attributed the asymmetric broadening of the C 1s peak to electron-hole pair formation fostered by an increased phase space for such excitations with doping level. The shoulder on the high energy BE side for large deposited amounts of alkali metal was attributed to shake-up loss processes enabled by the formation of the metallic adsorbate layer [191]. Recently, Sernelius [199] pointed out the relevance of 2D plasmons for the characteristic line shape of Gr C 1s spectra upon doping.

Here, we will show that the C 1s CLS is not a monotonous function of doping as predicted by the rigid band model. Although for small doping levels the C 1s shift may, to a reasonable approximation, be considered to

result from a mere rigid band shift, for large doping levels the C 1s CLS is a superposition of the rigid band shift with an opposing shift being proportional to the transferred charge. Further, we demonstrate that the C 1s line shape is characteristic for the doping level.

5.1 CLSs of doped Gr systems

Figure 5.1 displays a sequence of high resolution C 1s core level spectra for different intercalating species that exhibit homogeneous intercalation phases and span a wide range of doping levels. The spectra are, from right to left, of Gr/Cs-p($\sqrt{3}\times\sqrt{3}$)R30°/Ir(111) (magenta), of Gr/Eu-p(2×2)/Ir(111) (orange), of Gr/Eu-p($\sqrt{3}\times\sqrt{3}$)R30°/Ir(111) (blue), of Gr/Ir(111) (black), of Gr/H-p(1×1)/Ir(111) (red) and of Gr/O-p(2×1)/Ir(111) (green). The superstructures for Eu are with respect to Gr [57], whereas the superstructures for H, O, and Cs are with respect to Ir(111) [32, 33, 58].

In order to obtain the main peak position in a systematic manner, the spectra were fitted with Voigt functions. Pristine Gr and Gr/O were fitted with one component. In the case of H, a small fraction of the Gr stays unintercalated [32], this was taken into account by using a two-component fit. The Cs and Eu structures were also fitted with two components to account for the high BE shoulder. The second components of the Gr/Cs, Gr/Eu-p(2×2), and Gr/Eu-p($\sqrt{3}\times\sqrt{3}$) peaks are shifted by 0.59, 0.51, and 0.44 eV, respectively. The fitted C 1s spectra are shown in Figure 5.2 together with the corresponding Ir 4f spectra.

Referenced to Gr/Ir(111), positive CLSs of 0.60 eV, 0.70 eV, and 0.79 eV are observed for the main components of the p($\sqrt{3}\times\sqrt{3}$)R30°-Eu, the p(2×2)-Eu, and the Cs intercalation structures, respectively, whereas a negative CLS of -0.45 eV is found for the O, and a small negative CLS of -0.18 eV is measured for the H intercalation structures.

Additionally, a characteristic change in peak shape is observed in Figure 5.1 for positive CLS. With increasing shift the C 1s peak becomes asymmetric and a shoulder towards the high BE side develops and becomes more and more pronounced. A shoulder towards the high BE side develops as the main peak shifts to higher BE. STM and LEED measurements [57,58] rule out that the high BE shoulder component results from a chemical inhomogeneity or a phase separation: The intercalation layers possess a well-defined structure, are homogeneous, defect-free, and display no adsorbates on top of the Gr layer.

The Dirac point binding energies E_{D} as obtained by ARPES are 1.43 eV for the Eu-p($\sqrt{3}\times\sqrt{3}$)R30° [200], 1.36 eV for Eu-p(2×2) [200], and 1.20 eV for

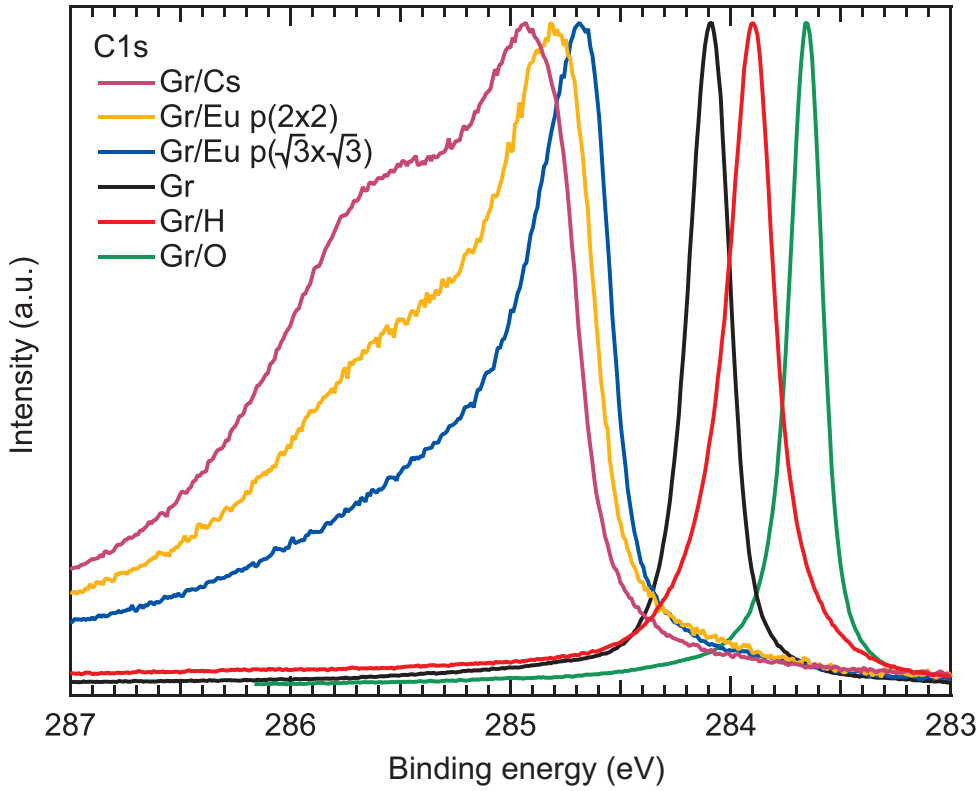

Figure 5.1: XP spectra of the C 1s region from right to left of Gr/Cs-p($\sqrt{3}\times\sqrt{3}$)R30°/Ir(111) (magenta), Gr/Eu-p(2×2)/Ir(111) (orange), Gr/Eu-p($\sqrt{3}\times\sqrt{3}$)R30°/Ir(111) (blue), Gr/Ir(111) (black), Gr/H/Ir(111) (red), and Gr/O-(2×1)/Ir(111) (green). Gr coverage was 1 ML for Cs, 0.9 ML for O and Eu, and 0.5 ML for H intercalation. Adapted and updated from [163]

.

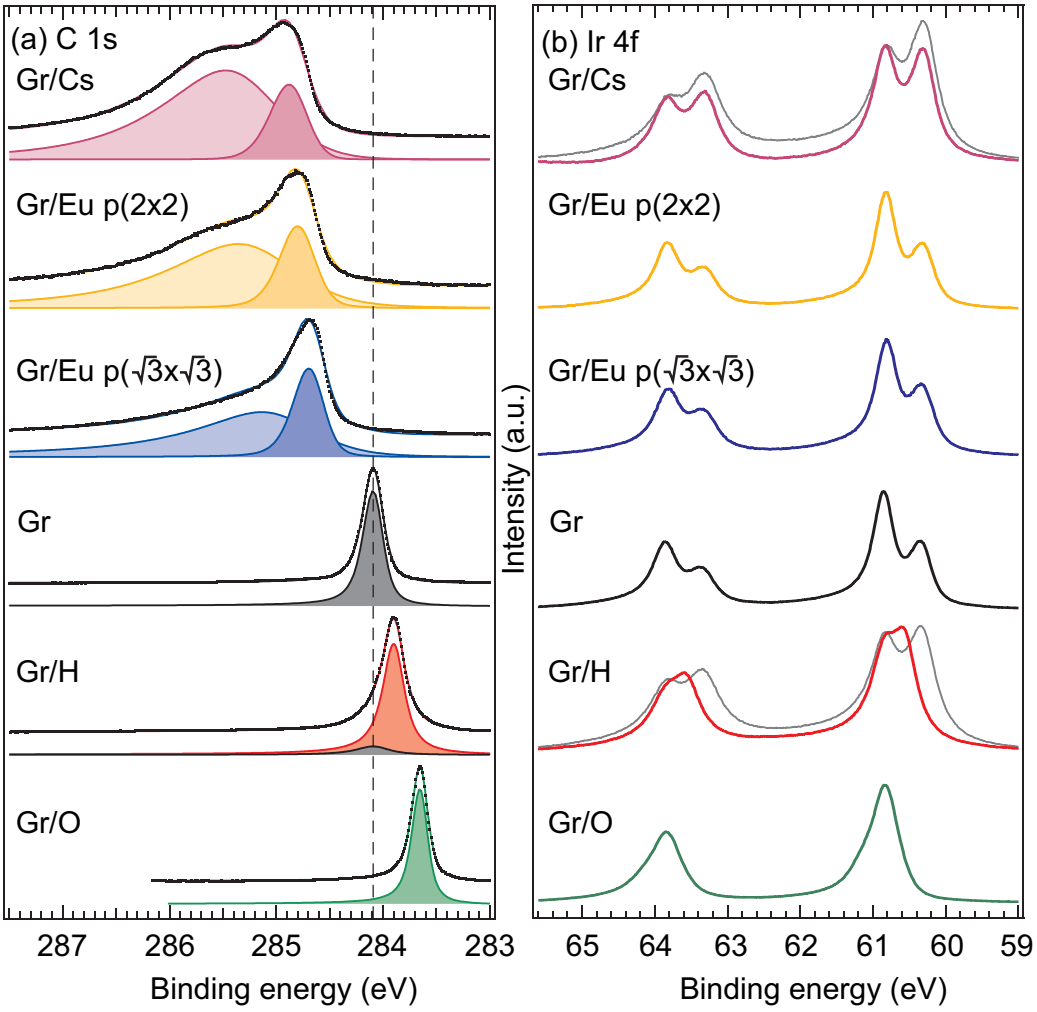

Figure 5.2: XP spectra of (a) the C 1s region and (b) the Ir 4f region from top to bottom of Gr/Cs-p($\sqrt{3} \times \sqrt{3}$)R30°/Ir(111) (magenta), Gr/Eu-p(2×2)/Ir(111) (yellow), Gr/Eu-p($\sqrt{3} \times \sqrt{3}$)R30°/Ir(111) (blue), Gr/Ir(111) (black), Gr/H/Ir(111) (red), and Gr/O-(2×1)/Ir(111) (green). In (a) the experimental spectra are shown as black dots, the fits as solid colored lines, and the filled curves represent the components of each fit. The dashed line indicates the position of pristine Gr. In (b) the experimental data are solid colored lines. All Ir 4f spectrum were measured with a photon energy of 190 eV, except for Gr/Cs (125 eV) and Gr/H (120 eV). In the latter two cases the spectra for pristine Gr/Ir measured at the same photon energy are displayed in gray for better comparison. Gr coverage was 1 ML for Cs as well as Eu, 0.95 ML for O, and 0.5 ML for H intercalation.

the Cs-p($\sqrt{3}$x$\sqrt{3}$)R30° [58] intercalation structures. E_D is defined here as the Dirac point *binding energy* referenced to the Fermi level E_F. Therefore, E_D is positive when E_F is above the Dirac point (n-doping) and negative when E_F is below the Dirac point (p-doping), consistent with the usual notions in XPS. The Dirac point energies E_D for Eu and Cs obtained are thus consistent with strong n-doping. For the intercalated O-p(2×1) structure significant p-doping with $E_\mathrm{D} = -0.68\,\mathrm{eV}$ is observed [54] for the same sample preparation as ours. This is in good agreement with the value $E_\mathrm{D} = -0.64\,\mathrm{eV}$ measured by Larciprete *et al.* [9]. Note that Ulstrup *et al.* observe doping levels of $E_\mathrm{D} = -0.80\,\mathrm{eV}$ and $-0.75\,\mathrm{eV}$ [158,201]. The authors suggest a larger amount of intercalated oxygen due to a higher O_2 pressure applied.

Table 5.1 summarizes our results. In addition, results from the literature for at most weakly hybridized graphene on a dense packed metal surface without and with intercalation layer were added, when a pair of E_D obtained from ARPES and C 1s BEs measured by XPS were available. We also added the C 1s position of graphite because its first layer can be viewed as undoped Gr showing only weak interaction with the graphite substrate.

To better visualize the relation between BE and doping level E_D, the data of Table 5.1 is presented in Figure 5.3, with the BE as a function of E_D. The error due to different apparatuses can be estimated by comparing identical systems measured by different groups, e.g., for Gr/Ir(111) it amounts to around 0.05 eV for the BE and 0.03 eV for E_D. Further systematic errors may be introduced due to varying sample preparations, as in the case of Gr/O, or because for some systems E_D and BE were measured by the different groups.

It can be seen that whenever the Gr is n-doped, the C 1s CLS is positive, whereas for p-doping it is negative, in line with the rigid band model depicted in the inset.

The black line gives the core level binding energy as predicted by the rigid band model:

$$BE_\mathrm{rb} = BE_0 + E_\mathrm{D}, \tag{5.1.1}$$

where BE_0 is the core level binding energy for undoped graphene. As there is no XPS data for truly freestanding, high-quality Gr available, BE_0 was chosen as 284.23 eV, the BE for graphite.

From the data and their comparison to the black line in Figure 5.3 it is immediately clear that the magnitude of CLS deviates from the rigid band model prediction the more, the higher the doping level caused by the intercalant. Moreover, the relation between CLS and doping level is not monotonic. As visible in Figure 5.1, the maximum CLS is obtained for Gr/Cs. For higher doping levels, i.e., the two Eu structures, the C 1s peak shifts back to lower BE.

Table 5.1: C 1s core level binding energy (BE) and Dirac point energy E_D for Gr/Pt(111), Gr/Ir(111) and several intercalation systems with fcc(111) substrates. For reference also the values for graphite are listed. The values in the upper part were measured by us or in collaboration. Updated from [163].

system	E_D (eV)	C 1s BE (eV)
Gr/Eu-p($\sqrt{3} \times \sqrt{3}$)R30°/Ir(111)	1.43 [57]	284.69
Gr/Eu-p(2×2)/Ir(111)	1.36 [57]	284.80
Gr/Cs-p($\sqrt{3} \times \sqrt{3}$)R30°/Ir(111)	1.20 [58, 200]	284.88
Gr/Ir(111)	- 0.1 [44]	284.09 [34]
Gr/H/Ir(111)		283.91 [32]
Gr/O-(2×1)/Ir(111)	- 0.68 [54]	283.64 [33]
Gr/Al/Ni(111)	0.64 [176]	284.65 [176]
Gr/Au/Ni(111)	0.0 [46, 63]	284.2 [63]
	0.1 eV [69]	
graphite	0.0	284.23 [179]
Gr/Ir(111)	- 0.07 [9]	284.14 [9]
		284.16 [179]
Gr/Pt(111)	- 0.3 [202]	283.97 [179]
Gr/O/Ir(111)	- 0.64 [9]	283.60 [9]
Gr/Cl/Ir(111)	- 0.7 [175]	283.8 [175]

As doping involves charge transfer to or from the Gr, one could speculate that this charge transfer is responsible for the observed deviations. We calculated the charge transfer ΔQ per C atom of Gr as a function of the Dirac point binding energy E_{D}, by utilizing the equation

$$\Delta Q = \frac{A_{\mathrm{F}} \mathrm{A}_{\mathrm{u}}}{2\pi^2}, \tag{5.1.2}$$

where A_{F} is the area of the Fermi contour in the reciprocal space and A_{u} is the area of a graphene unit cell in the real space [203]. The area A_{F} is determined for each required doping level (i.e., various E_{D} values) by integrating the area enclosed within one of the six pockets of the tight-binding Fermi surface of the doped graphene [26, 204]. The use of tight-binding bands in the calculation of A_{F} is sufficient for the level of approximation we are working with here.

The deviation ΔE from the rigid band model is the difference between the measured BE and the BE predicted by the rigid band model, i.e., $\Delta E = BE - BE_{\mathrm{rb}}$. It is displayed as a function of ΔQ in Figure 5.4. To first approximation, ΔE is proportional to ΔQ with $\Delta E = -(18.2 \pm 0.9)\,\mathrm{V} \cdot \Delta Q$. Using this fit for ΔE yields the blue curve in Figure 5.3, which is a reasonable representation of the measured data.

Up to now we found (i) a non-monotonic dependence of the C 1s CLS on the Gr doping level, which can be understood as the superposition of a rigid band shift and a counteracting shift proportional to the transferred charge, and (ii) the C 1s peak to become strongly asymmetric and to develop a pronounced shoulder with increasing positive CLS. We believe that (i) and (ii) hold universally for Gr on weakly interacting substrates. A critical reader might argue against the universality of statements (i,ii) by pointing out that they largely rely on only a few spectra, specifically those of the Cs- and the two Eu-intercalation structures. To rule out chemical effects on the CLS and substantiate our claims we conducted additional Li intercalation experiments, as Li allows for continuous tuning of the doping level without switching to a different element.

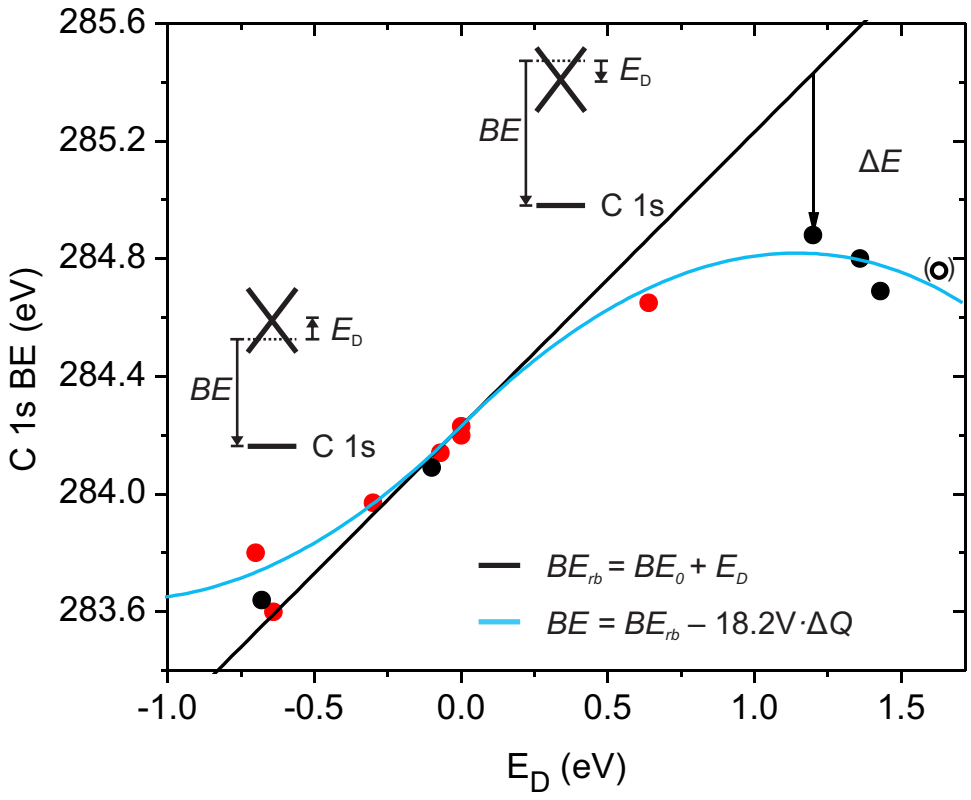

Figure 5.3: Plot of the C 1s BE as a function of E_{D} for the data of Tab. 1. Black dots are data measured by us or in collaboration, red dots are taken from literature. The additional open black circle in brackets corresponds to saturated Li intercalation (see text). Straight black line: prediction of the rigid band model [Equation (5.1.1)]. Blue line: $BE = BE_{rb} - 18.2\,\mathrm{V} \cdot \Delta\mathrm{Q}$ as obtained from Figure 5.4. The insets depict the energetics of the rigid band model for p-doped Gr (lower left) and n-doped Gr (upper middle).

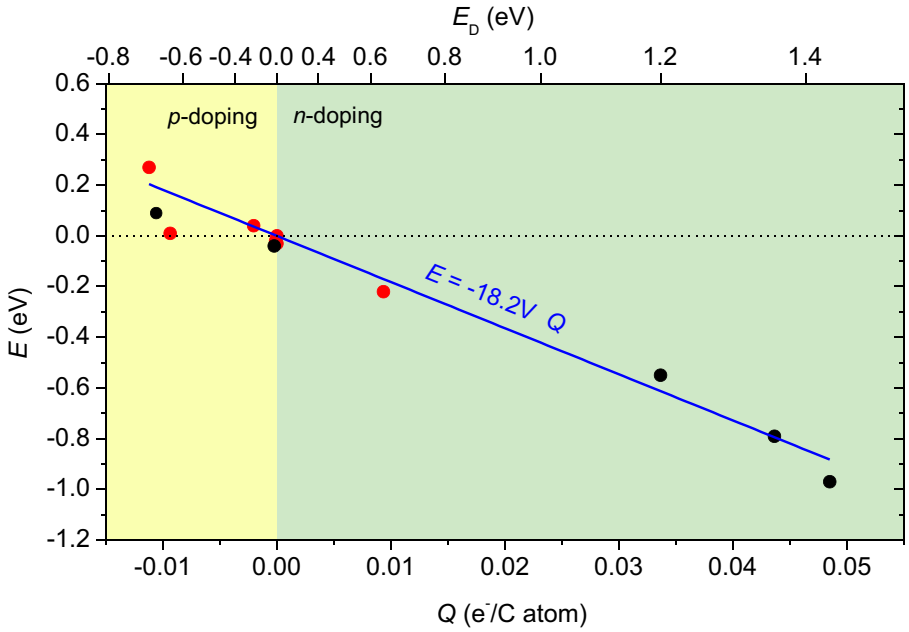

Figure 5.4: Deviation ΔE from the rigid band model versus the charge transfer per C atom ΔQ (lower x-axis). The corresponding doping levels are given on the upper x-axis. The straight blue line is a fit to the data.

5.2 Li intercalated Gr/Ir(111)

We hypothesize the data in Figure 5.3 to represent a universal relationship between doping level and CLS in quasi-freestanding Gr. It follows that the same universal behavior should be observable, were we to solely change the doping level of Gr, without for example also switching to another element. The intercalant of choice is Li, as it does not show phase separation regardless of coverage, leaves the Gr band structure intact, and, with increasing coverage, causes a monotonic shift of the doping level to more and more positive values of E_D [10, 58]. Thus, by intercalating Li, we can continuously shift the doping level of Gr over a wide range while always ending up with a homogeneous, quasi-freestanding Gr sample. Note that, due to phase separation, varying the coverage for Eu or Cs would not result in uniform intercalation phases and thus to not well-defined values of E_D, except for those coverages used in Figure 5.1.

Figure 5.5(a) displays three (out of many) XPS spectra with increasing amounts of Li intercalated. The spectra are normalized to the Ir $4f_{7/2}$ bulk peak at 61.2 eV. Upon Li intercalation the Li 1s peak appears at 55.1 eV (Li_1). With increasing coverage it grows in intensity, slightly shifts, first to higher BEs, but eventually to 54.4 eV, consistent with previous observations for Li-graphite compounds [205] (see Figures 5.8 and 5.9 for additional spectra of different Li intercalation coverages). When depositing larger amounts of Li beyond what is shown in Figure 5.5(a), the Li peak height does not grow any further, but a second component at 56 eV (Li_2) appears, accompanied by a peak at $\approx$ 530.3 eV in the O 1s signal, shown in Figure 5.6. We attribute the saturation of the Li_1 peak height to the saturation of the Li intercalation layer. Consequently, the integrated peak intensity of the cyan spectrum Figure 5.5(a) is set to 1 ML and the other coverages are attributed accordingly, neglecting damping of the Ir 4f bulk peak by the intercalated Li layer. While the precise structure of the intercalation layer is irrelevant for our arguments, based on the data of Pervan *et al.* [10] it is plausible to assume a Li-p(1×1) structure with respect to Ir(111). The Li component growing beyond saturation of the intercalation layer is attributed to Li adsorption *on* Gr, which readily oxidizes, thereby giving rise to the associated O 1s signal. This interpretation is backed up by matching Li 1s and O 1s peak positions for Li_2O in previous work [135, 206, 207], the observation of Li adsorption on top of Gr/Li/Ir(111) near step edges by STM [62], and facile Li oxidation on top of Gr/Cu(111) [208].

For the same experiments as represented by the spectra in Figure 5.5(a), the corresponding C 1s region of Li-intercalated Gr is shown in Figure 5.5(b). For comparison, also the spectrum for non-intercalated Gr/Ir(111) is dis-

played in black. Consistent with statement (i), upon dosing of Li, we observe that the C 1s peak first shifts to higher BE, and then displays a shift back to lower BE for higher Li coverages. In detail, the C 1s spectra of Figure 5.5(b) were fitted with two Voigt components in order to obtain the main peak positions (see Figures 5.8 and 5.9). Upon intercalating 0.06 and 0.19 ML Li, the C 1s main peak shifts to higher BE by 0.30 eV and 0.80 eV, respectively. Intercalating 1 ML Li leads to a back-shift, with a CLS of 0.67 eV, all with respect to the pristine Gr/Ir(111) peak. Figure 5.7 summarizes the C 1s CLS as a function of Li coverage. The colored points correspond to the spectra shown in Figure 5.5, accompanied by data from additional experiments.

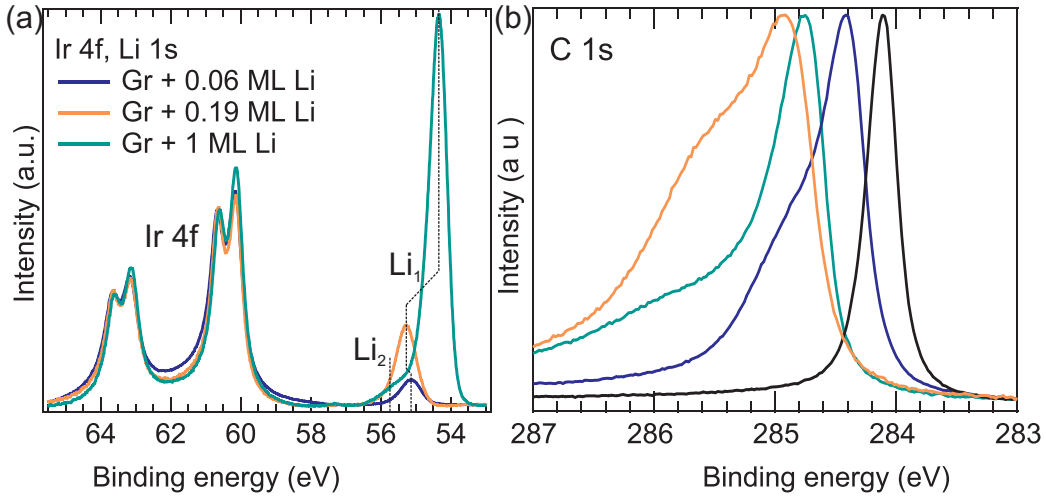

Figure 5.5: XP spectra of (a) the Ir 4f-Li 1s region, (b) the C 1s region of pristine Gr (black) and Li intercalated Gr with Li coverages of 0.06 ML (blue), 0.19 ML (orange), and 1 ML (cyan). The Gr coverage was 1 ML in all cases.

These additional experiments are shown in Figures 5.8 and 5.9. The C 1s, and Ir 4f-Li 1s region of two different experiments of intercalating Gr with different amounts of Li can be seen. The lowest spectra in both figures show the clean Gr case, for comparison. For Figure 5.8, Gr was intercalated by a saturated Li layer (second spectrum from the bottom). Then the sample was annealed to stepwise increasing temperatures, indicated in the Figure. Around 580 K, deintercalation sets in, as evidenced by the decrease of the Li_1 component in (b). The C 1s peak consequently shifts to higher BE, as the Li coverage is between 1 and 0.2 ML. Both the C 1s and the Li 1s spectra were fitted with one or two Voigt functions. For the C 1s spectra, the 2nd components display a CLS of 0.78 eV (saturated), 0.72 eV (583 K), 0.77 eV

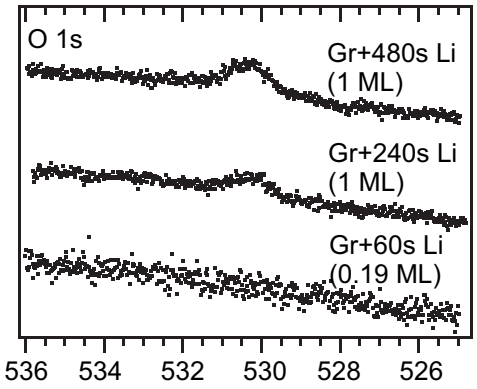

Figure 5.6: XP spectra of the O 1s region for different amounts of Li deposited onto Gr/Ir(111) (compare with Figure 5.9). Coverages given in parentheses correspond to the amount of intercalated Li.

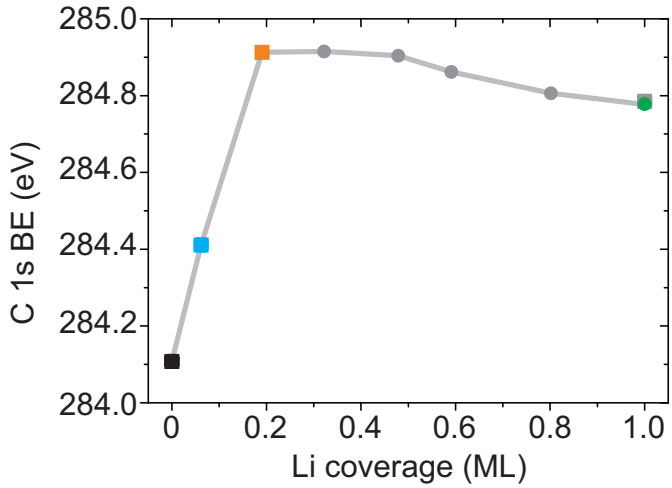

Figure 5.7: Binding energy of the main C 1s component of Li intercalated Gr plotted against the Li intercalation coverage. Different Li coverages were obtained either by intercalating more and more Li (filled squares) or by annealing a fully Li intercalated sample to higher and higher temperatures (filled circles). The coloured squares or dots correspond to the spectra shown in Figure 5.5. Line to guide the eye.

(673 K), 0.77 eV (773 K), and 0.70 eV (873 K). We observe that the Li_1 component shifts to lower BE with higher Li coverages. This is similar to what has been observed for Li-graphite compounds. A likely explanation for this phenomenon is that the charge transfer to the Gr *per Li atom* decreases for increasing Li coverages [205]. According to the electrostatic initial state effect, this leads to a negative CLS.

For Figure 5.9, stepwise more and more Li was evaporated onto the Gr, starting at a very low dose (total evaporation times are indicated in the figure). For the C 1s spectra, the 2nd component displays a CLS of 0.44 eV (15 s), 0.65 eV (60 s), 0.67 eV (240 s), and 0.67 eV (480 s). Upon increasing the Li coverage, the Li 1s peak increases in intensity and shifts to higher BE, as observed before. After 120 s of Li evaporation, the Li_1 peak at ≈ 54.4 eV (Li_1) does not significantly increase in height anymore, but a second component at ≈ 55.75 eV (Li_2) develops. Whenever the Li_2 component is visible, we also observe a non-vanishing oxygen signal at $\approx$ 530.3 eV in the O 1s spectra (Figure 5.6).

Pervan *et al.* [10] find for Li saturation of Gr on Ir(111) a value of $E_D = 1.63$ eV. Using this value of E_D and our C 1s BE resulting from the saturated (1 ML) Li intercalation layer yields the open symbol depicted in Figure 5.3. It fits very well to the other data and the blue fit curve, supporting again our statement (i). However, the data point was not used in Figure 5.4 to establish the relation between ΔE and ΔQ, since the proper choice of E_D (and thus ΔQ) has some uncertainty. As we found Li to continue to accumulate *on* Gr after intercalation has ceased, $E_D = 1.63$ eV as derived by Pervan *et al.* [10] might correspond to a situation with a saturated intercalation layer and some additional Li adsorbed on Gr. In this case, E_D corresponding to our C 1s BE after Li intercalation till saturation could be slightly smaller than $E_D = 1.63$ eV.

Finally, considering the shape of the C 1s spectra represented in Figure 5.5(b), they display the same characteristics of evolution with C 1s BE or doping level as those displayed in Figure 5.1: Upon doping, the C 1s peak broadens asymmetrically, and a pronounced shoulder towards higher BEs evolves which diminishes upon the C 1s backshift by continued doping to saturation. The identical evolution of the peak shape with n-doping for Li intercalation underlines the validity of our statement (ii).

5.3 Discussion

A key finding of our experiments is that the C 1s CLS of intercalated Gr may be described as a superposition of a rigid band shift and a counteracting shift

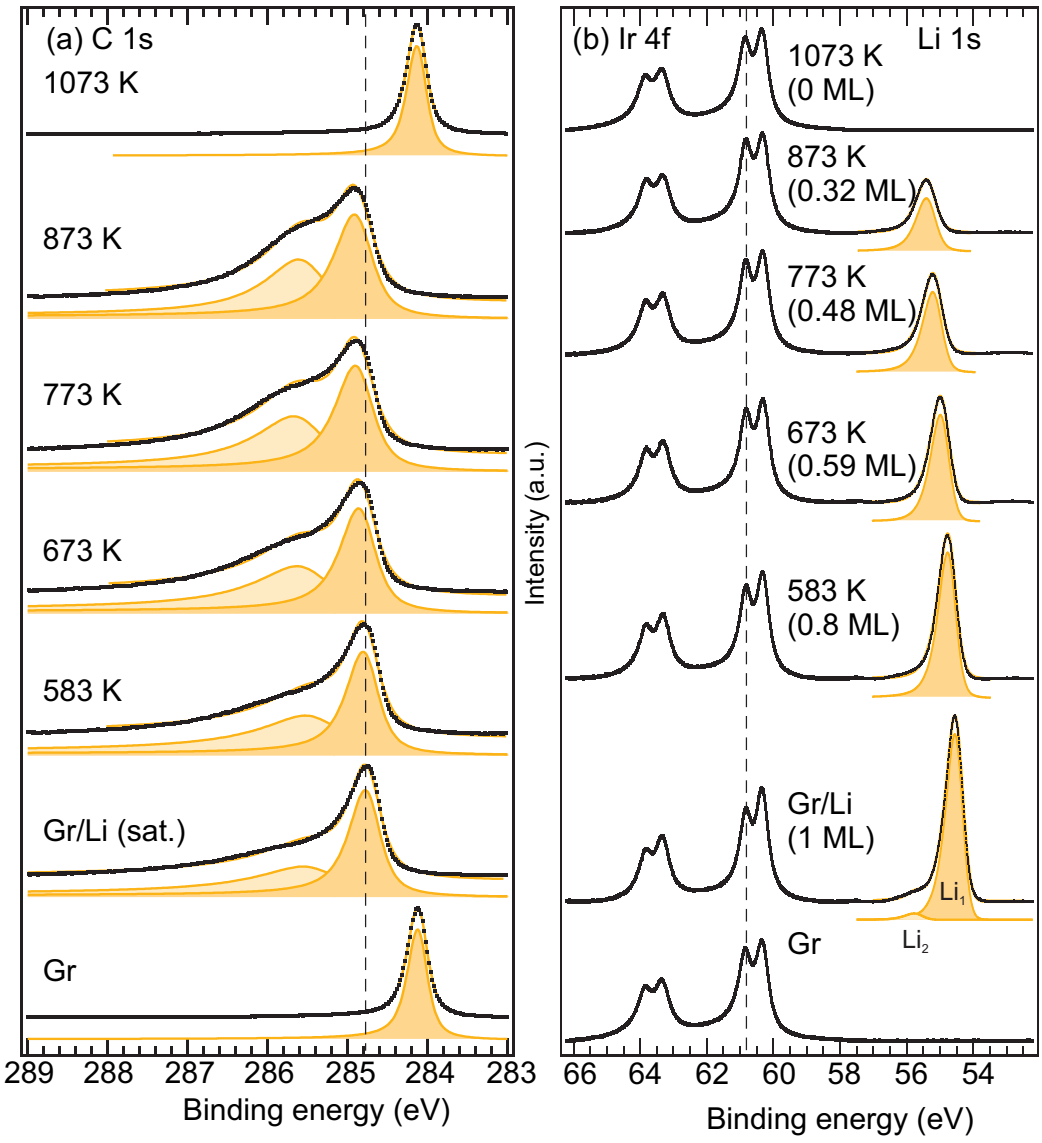

Figure 5.8: XP spectra of (a) the C 1s region and (b) the Ir 4f-Li 1s region of pristine Gr (bottom), Gr with a saturated Li intercalation layer (second from the bottom), and the Gr/Li sample subsequently annealed to the temperatures indicated in the figure. The amount of intercalated Li is given in parentheses in (b). Spectra were recorded at room temperature. The experimental spectra are shown as black dots, the fits as solid yellow lines, and the filled curves represent the components of each fit. The dashed line in (a) indicates the position of the main C 1s component of the saturated Li intercalated Gr film. The spectra in (b) were normalized to the Ir $4f_{7/2}$ bulk peak, indicated by a dashed line.

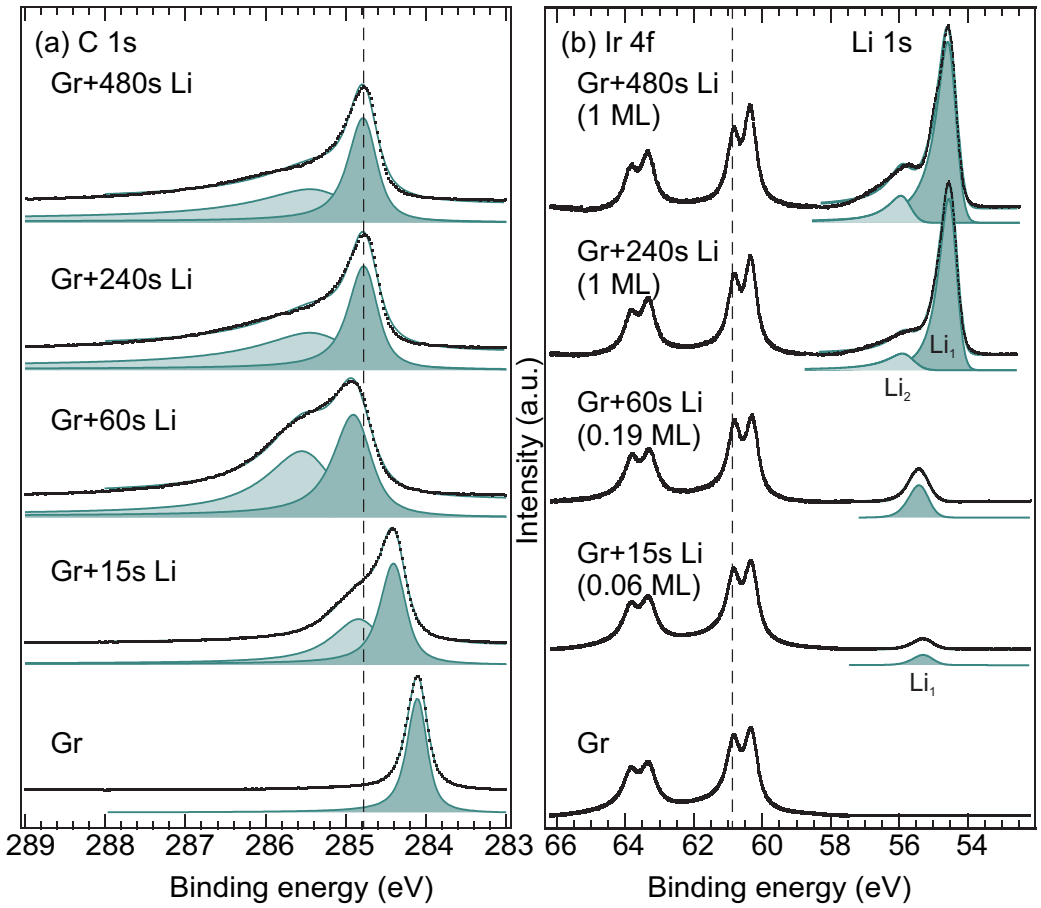

Figure 5.9: XP spectra of (a) the C 1s region and (b) the Ir 4f and Li 1s region of pristine Gr (bottom), and Gr with increasing amounts of intercalated Li. The total evaporation time is indicated in the spectra. The experimental spectra are shown as black dots, the fits as solid green lines, and the filled curves represent the components of each fit. The dashed line in (a) indicates the position of the main C 1s component of the saturated Li intercalated Gr film. The spectra in (b) were normalized to the Ir $4f_{7/2}$ bulk peak, indicated by a dashed line.

proportional to the transferred charge ΔQ.

It is instructive to first take a closer look as to why the rigid band model correctly predicts CLSs when E_{D} is close to zero. The answer lies in the peculiar band structure of Gr, in combination with assuming that charge transfer is in fact responsible for the deviation of the rigid band shift. At the Dirac point, the density of states is zero. When moving away in energy from this point to either side the density of states increases linearly until close to the van Hove singularity of the π or π^* bands, where it rapidly rises [22, 209]. This implies that if the Fermi level is close to the Dirac point very little charge transfer induces a strong increase in the magnitude of E_{D}, justifying the neglect of effects related to charge transfer. As the Fermi level moves further away from the Dirac point the density of states increases and more and more charge transfer is needed for the same increment in the magnitude of E_{D}. Thereby, the charge transfer effect ΔE counteracts the shift of the entire Gr band structure with respect to E_F more and more effectively, until the entire CLS decreases again, as visible in Figure 5.3 for large n-doping beyond 1.2 eV.

The physical origin of the effect counteracting the rigid band shift for larger ΔQ can only be clarified by dedicated calculations, which would be beyond the scope of the present work. Here we can only offer speculations. One effect of transferred valence electron charge is to change the electrostatic potential at the core electron location [35,36]. The additional electronic charge decreases the electrostatic potential in the core of the atom, analog to (and intuitively more accessible) an increased electron-electron repulsion. In consequence, the energy necessary to remove the core electron is lowered (see, e.g., ref. [36] for an explanation strictly in terms of the electrostatic potential). Electronic charge transfer away from the Gr will, conversely, lead to an increased BE of the core electron. The sign of these changes matches with the sign of ΔE, the deviation of our measured CLS from the rigid band model expectation.

In an oversimplified approach, the valence electrons can be approximated as a charged, conducting sphere surrounding the nucleus and the C 1s electrons situated at the center of this sphere. A change in charge, ΔQ, results in a change in the potential energy ΔV felt by the core level electron, with

$$\Delta V = \frac{\Delta Q}{4\pi\epsilon_0 R}, \tag{5.3.1}$$

R being the radius of the sphere, and ϵ_0 the vacuum permittivity. In this picture, the experimental proportionality between ΔE and ΔQ translates to a radius of a charged sphere closely matching the covalent radius of C. Though this estimate shows that an initial state effect could be relevant to

our observations, it has to be noted that extra or deficit valence charge in the π-electron system is not located on a sphere around the nuclei but to better approximation on planes enclosing the sheet of C nuclei, that the charge may be distributed asymmetrically with respect to the Gr plane, and that it may effect also the electrostatic potential of the π electron system itself.

Transferred charge can also affect core hole screening and thus the BE of the outgoing photoelectron. For extra charge in the π electronic system one would expect more complete core hole screening, consistent with our data. However, the sharpness of the C 1s peak of pristine Gr on Ir(111) and the absence of final-state features towards higher BE indicate full screening of the core already without extra valence charge. This assumption is fully consistent with explicit calculations by Sernelius that indicate the C 1s peak of undoped Gr to be close to adiabatic [199].

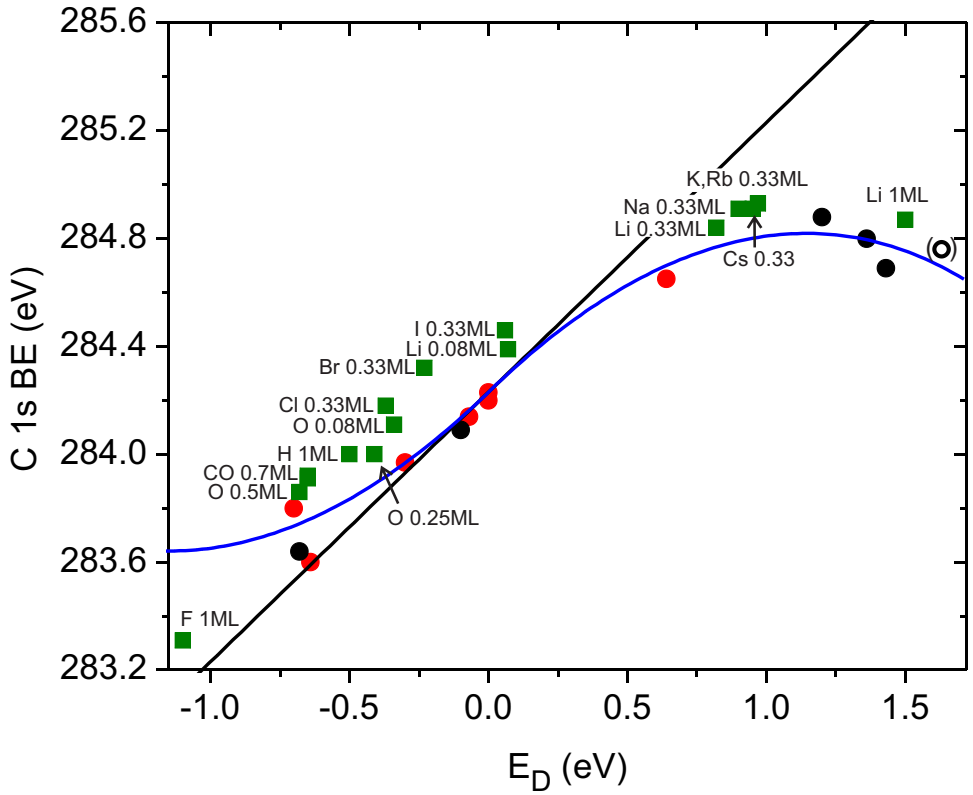

Figure 5.10: Same as Figure 5.3, the additional green dots are calculated doping levels and CLSs from [184]. The coverages indicated after element names refer to the coverages of the calculated structures.

It should be noted that dedicated *ab initio* CLS and E_{D} calculations were

conducted by Andersen *et al.* [184] for Gr intercalation systems on Ir(111). The green dots in Figure 5.10 were obtained by adding the theoretically obtained CLSs to the C 1s BE of Gr/Ir(111) measured by us. Remarkably, the signs of the calculated CLSs matches those experimentally observed here for O, H, Cs, and Li. Also, the magnitude of the calculated CLS agrees reasonably well, but with a tendency to be smaller by 0.1 eV to 0.2 eV compared to the experimental values. The authors remark that the correlation between calculated doping levels and CLSs for intercalated graphene indicates that the doping level is a main factor determining the CLS. This statement is fully consistent with the fact that the low density of states near E_{F} makes rigid band shifts dominant for low and moderate doping levels. Moreover, the calculated Dirac point energy E_{D} is generally larger in magnitude than the CLS, consistent with an effect counteracting the rigid band shift. However, the characteristic signature of a non-monotonic dependence of CLS on E_{D} is missed in the calculations: For successively increasing amounts of intercalated Li, the CLS is monotonically increasing in the calculations, contrary to our findings.

Lastly in this section, a discussion about the characteristic shape of the C 1s peak is in order. First, we consider the asymmetric broadening and tailing to higher BE developing upon n-doping. Such a broadening is in general attributed to electron-hole pair excitations [35, 210] that are more probable for higher doping levels due to an increased phase space for low energy electron-hole pair excitations as E_{F} moves away from E_{D}. In recent calculations Sernelius [199] reproduced the proper asymmetric broadening of the C 1s peak with doping and pointed out that not only electron-hole pair formation, but also 2D plasmon losses contribute to it. Contrary to the 3D cases, 2D plasmons do not give rise to plasmon replicas at higher BEs, but yield losses starting from zero energy and thereby contribute to the observed tailing.

As second observation we noticed the evolution of a shoulder towards the higher BEs, shifted approximately 0.5 eV-0.7 eV with respect to the main component and most pronounced at maximum CLS. For various intercalated Gr and graphite systems with intercalated or adsorbed alkali-metals a similar shoulder has been observed in the past [60, 61, 183, 185, 190, 191, 197, 198].

Wertheim *et al.* observed a broad shoulder, shifted by approximately 1.4 eV from the main peak, for Li intercalated graphite (LiC_6), and tentatively attributed it to surface C atoms which do not have the full Li neighbor environment [60]. Nagashami *et al.* observed a similar shoulder, displaced by approximately 0.8 eV, for Cs, K, and Na intercalated into the Gr/Ni(111) system, and remarked that a structural explanation as in [60] is not applicable here because of the monolayer thickness of the graphite overlayer [197]. They

also discarded the possibility that more charge is donated to C atoms closer to alkali-metal atoms, as this would introduce an asymmetry to lower BE. Instead, they proposed an intrinsic energy loss process due to many-body effects involving plasmon or interband transition, involving the *s* electrons of the alkali-metal atoms. Also Johansson *et al.* [196] found the same loss feature as observed by us after Li intercalation under Gr on the C-face of SiC. Bennich *et al.* [191] observed a pronounced shoulder shifted by roughly 0.7 eV for the (2x2) K phase adsorption layer on graphite and suggested it to be due to a combination of shake-up loss processes enabled by the formation of the metallic adsorbate layer. The characteristic loss energy was linked to a broad loss feature between 0.5 eV and 1.2 eV below the elastic peak in electron energy loss spectroscopy of the same system [211, 212]. Taking this view, it appears difficult to understand why the loss is most pronounced for a specific doping level, i.e., why the loss feature diminishes again towards the highest achievable doping levels. In the light of our data, we rule out different chemical environments of the C atoms as the origin of the shoulder, as proposed by some authors. Instead, the phenomenon seems to be a universal effect that occurs whenever Gr is n-doped. The shoulder reaches its maximum intensity at a doping level of 1.2 eV, and decreases in intensity for both smaller and larger doping levels. We thus propose an intrinsic loss process that does not depend on the specific system but is linked to the electronic structure of Gr. Considering the universality of the C 1s shoulder evolution upon n-doping of Gr or graphite, it would be timely and rewarding to solve this problem and to unambiguously determine its origin by a thorough theoretical analyis.

5.4 Summary

As long as the Dirac cone is left largely intact by the species in contact with Gr on one of its two sides, the associated C 1s CLS shift appears to obey a universal, non-monotonic dependence on the doping level of Gr. The dominating effect at small and moderate doping levels is a rigid shift of the band structure. Due to the small density of states near the Dirac point, substantial rigid band shifts arise for small amounts of transferred charge. The rigid band shift is counteracted by an effect proportional to the transferred charge per C atom, such that for n-doping levels beyond 1.2 eV the CLS decreases in magnitude. While the physical origin of this counteracting effect can only be determined through thorough theoretical analysis, possible explanations include an electrostatic initial state effect or modified core hole screening due to the transferred charge.

The C 1s peak shape displays another universal dependence on the n-

doping level: For small doping levels the peak first broadens asymmetrically towards higher binding energies, most probably due to the enhanced phase space for electron-hole pair excitations. Then, for $E_D \approx 1.2\,eV$, a pronounced shoulder evolves which is shifted by 0.5 eV - 0.7 eV towards higher energy with respect to the main component. Upon continued doping this shoulder diminishes again. A similar broadening and shoulder evolution has been observed in the literature for a variety of n-doped graphene or graphite adsorption or intercalation systems. Different chemical environments can be ruled out for our data, and so this feature is most likely due to a loss process of the photo electron.

We hope that our experimental work will stimulate theoretical efforts to uncover the origin of the non-monotonic CLS and the peak shape evolution of Gr with doping level, as due to the universality of the phenomenon work in this direction will be useful and rewarding.

Finally, based on the dependence of C 1s CLS and peak shape on doping level, a quick estimate of the doping level is possible on the basis of C 1s XPS data. As an example and based on our data, we predict the yet unmeasured Dirac point energy in H-intercalated Gr on Ir(111) to be $E_D \approx -0.2\,eV$.

Chapter 6

A superdense OH-H_2O phase under graphene on Ir(111)

This chapter is based on a manuscript being prepared for submission, which has been published in the Ph. D. thesis of E. Grånas [213], and contains contributions from: E. Grånas, M. A. Arman, M. Andersen, T. Gerber, K. Schulte, J. N. Andersen, B. Hammer, T. Michely, and J. Knudsen. I took part in the design of the experiments, was involved in the XPS, and STM measurements, performed the TPD and LEED measurements, analyzed the STM, TPD and LEED data, prepared Figures 6.3, 6.5, 6.6, 6.7(b), and contributed to the manuscript.

Here, we present the formation of a dense OH-H_2O phase underneath Gr/Ir(111) when exposing oxygen intercalated Gr to molecular H_2. Intercalation of atoms and molecules under Gr and BN has been studied extensively before. Focusing on the intercalation under Gr, it has been studied in such diverse contexts as: Gr as a coating material that enables atomic force microscopy studies of adlayers [214, 215], oxide formation below Gr [216], and CO oxidation under Gr [145, 217]. These studies and more fundamental studies on O-intercalation [9, 33, 41], CO-intercalation [217–219], and H-intercalation [38] have given a profound understanding of intercalation of atoms and molecules under Gr and the phases they form. Further, these studies have shown that Gr intercalation can be controlled by gas pressure, temperature, the morphology of the epitaxial Gr on its substrate [58], and by attachment of atoms to Gr flake edges [220]. The few studies on reaction under Gr [145, 188, 217] and oxide formation [216] just show that Gr

affects the reaction rate (for example due to a lower CO-Pt binding energy), but the reaction proceeds along the same reaction path, resulting in the same products. In contrast, our work demonstrates a new Gr-induced reaction path. The H_2 oxidation under Gr leads to the formation of a new super-dense mixed OH-H_2O structure which has been never observed before. Under comparable conditions of pressure and temperature, on bare Ir(111) just formation of immediately desorbing water molecules takes place. While water films and clusters above [221–224] and below [214, 225–227] Gr and BN have been studied before, the use of Gr to catalyze the formation of a stable water/hydroxyl phase has not yet been explored.

6.1 Formation of a OH-H_2O phase by subsequent oxygen and hydrogen intercalation

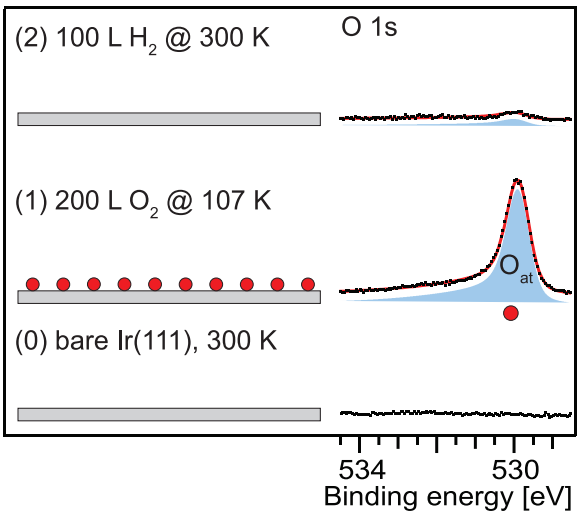

Figure 6.1: XP spectra after subsequently exposing Ir(111) to oxygen and hydrogen. O 1s spectra from (0) bare Ir(111), (1) after exposure to 200 L O_2 at 107 K, (2) after subsequent exposure to 100 L H_2 at 300 K. The experimental spectra are shown as black dots, the fits as red lines and the filled curves represent the components of the fit. To the left of the spectra, schematic representations of the situation on the sample are given, gray is the Ir substrate, and red circles are O atoms. From [213].

Before H_2 oxidation under Gr is discussed, we briefly describe H_2 oxidation by H_2 exposure on Ir(111) without Gr at room temperature. Figure

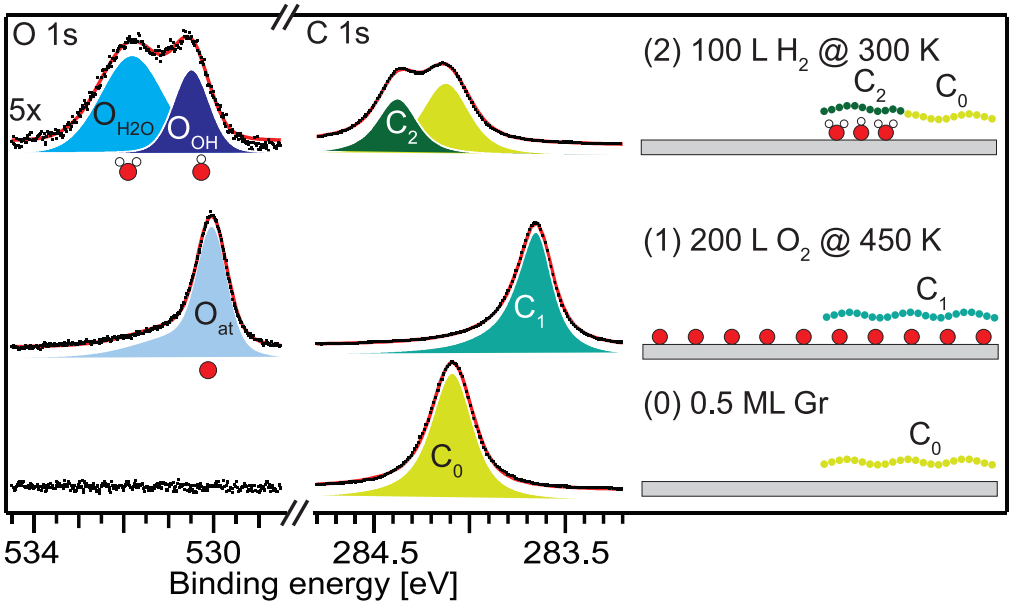

Figure 6.2: XP spectra after subsequently exposing 0.5 ML Gr/Ir(111) to oxygen and hydrogen. O 1s and C 1s spectra from (0) pristine 0.5 ML Gr, (1) after exposure to 200 L O_2 at 450 K, (2) after subsequent exposure to 100 L H_2 at 300 K. The experimental spectra are shown as black dots, the fits as red lines and the filled curves represent the components of the fit. Next to the spectra, schematic representations of the situation on the sample are given, gray is the Ir substrate, red circles are O atoms, white circles are H atoms, small green or blue circles are C atoms in the Gr, colored according to the component visible in XPS. From [213].

6.1 shows the O 1s spectra of Ir(111), from bottom to top: (0) after in-vacuum cleaning, (1) after oxygen exposure until saturation which results in a p(2 × 1)-O structure with O-atoms adsorbed in the 3-fold hollow sites [33], and (2) after subsequent hydrogen exposure reacting the adsorbed oxygen to water, which instantaneously desorbs. Due to the rapid desorption of the water molecules at the reaction temperature of 300 K, atomic oxygen (with a O 1s binding energy of 530.0 ± 0.05 eV) is the only oxygen containing species we observed.

The process is dramatically different when the Ir(111) surface is half covered by Gr flakes (0.5 ML), as shown in Figure 6.2. The O 1s and C 1s spectra prior to any gas dosing is shown in the lowest spectrum (0). The sample was then saturated with oxygen by dosing 200 L of O_2 at 450 K (1). As established in our previous work [33], atomic oxygen, resulting from dissociative adsorption, is mobile at 450 K and pushed under the Gr flakes. A p(2 × 1)-O structure forms on the entire sample, both on the bare Ir(111) and under the flakes. The delamination of the Gr flakes is signaled by a C 1s peak shifted -0.47 eV compared to pristine graphene, called C_1, in agreement with our previous work and the work of Laciprete *et al.* [9, 33]. Upon H_2 exposure, the molecular hydrogen adsorbs dissociatively on the areas not covered by Gr. The H-atoms can now follow two different reaction paths in which they react with atomic O. They either (i) react with O on Ir(111) patches not covered by Gr or they (ii) react with O-atoms under Gr. For reaction path (i) we already demonstrated that water will form and desorb directly. Reaction path (ii) would lead to OH and H_2O molecules being formed, and possibly trapped, under Gr. Comparing the spectra in Figure 6.2, before (1) and after (2) H_2 exposure, it is obvious that the O_{at} and C_1 components disappear, giving evidence that the p(2 × 1)-O structure is fully removed. At the same time, new oxygen components at 530.4 ± 0.1 eV (O_{OH}) and at 531.9 ± 0.1 eV (O_{H_2O}) develop. Similar O 1s components at 530.5 eV and 531.5 eV were observed previously by Shavorskiy *et al.* [228] during low temperature water adsorption and desorption on oxygen covered Ir(111) and attributed to a mixed phase of OH and H_2O. Based on the simultaneous appearance of a new C_2 component 284.37 eV (41 %), the C_0 component (59 %) characteristic for non-intercalated Gr, and the O_{OH} and O_{H_2O} components of the mixed phase, we conclude that trapped OH and H_2O had formed under 41 % of the graphene flakes via reaction path (ii) and caused the new C_2 component. Evidence for H-atoms following reaction path (i) comes from the finding that H_2 dosing leads to a reduction of the O 1s intensity to $35 \pm 10\%$ of the initial coverage of the p(2 × 1)-O structure.

Independent support for the formation of OH and H_2O under Gr comes from a TPD experiment in which 0.8 ML Gr (grown by 8 TPG steps) on

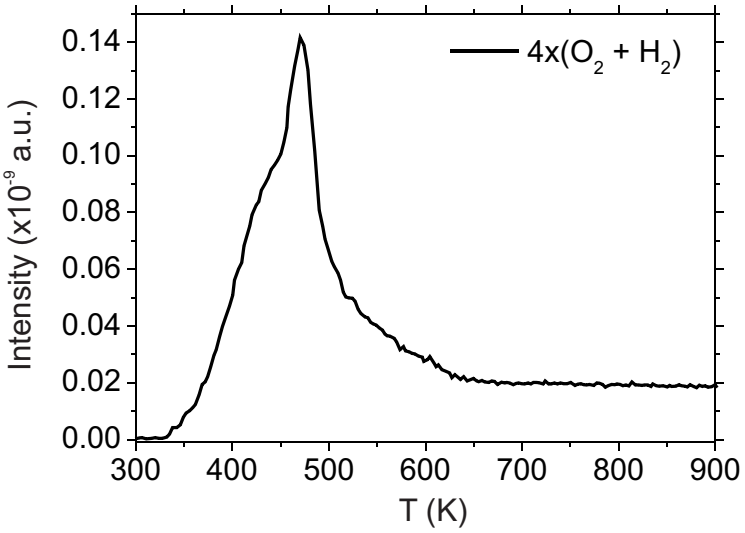

Figure 6.3: TPD spectrum of mass 18 u (H_2O) after 0.8 ML Gr was exposed to 4 cycles of (O_2 + H_2). Heating rate 5 K/s, no background subtracted.

Ir(111) was exposed sequentially to 4 cycles of 750 L (100 s at $1 \cdot 10^{-5}$ mbar) O_2 and 100 L (166 s at $8 \cdot 10^{-7}$ mbar) H_2, the first O_2 exposure was done at 520 K, all subsequent H_2 and O_2 exposures at room temperature. This was done to increase the amount of OH-H_2O under the Gr (see Section 6.4). The Gr coverage was increased so as to increase the amount of OH-H_2O trapped and thus the TPD signal. The resulting spectrum is shown in Figure 6.3. The H_2O desorption peak temperature of 440 K is significantly higher than the desorption peak temperature of the pure H_2O bilayer (170 K) [168, 228, 229] or a mixed OH/H_2O phase (210-235 K) [228, 229] observed on Ir(111).

6.2 Determination of the local OH-H_2O coverage

The local coverage of the mixed OH-H_2O phase causing the C_2 component can be deduced from the absolute intensities of the O_{OH} and O_{H_2O} components and the relative intensity of the C_2 component. The comparison of absolute intensities of XPS components often introduces large errors since small deviations of the photon flux at the sample position and the precise alignment of the electron analyzer, the light, and the sample directly affect the measured intensities. To minimize these errors we dosed hydrogen onto O-intercalated Gr flakes without moving the sample and while measuring

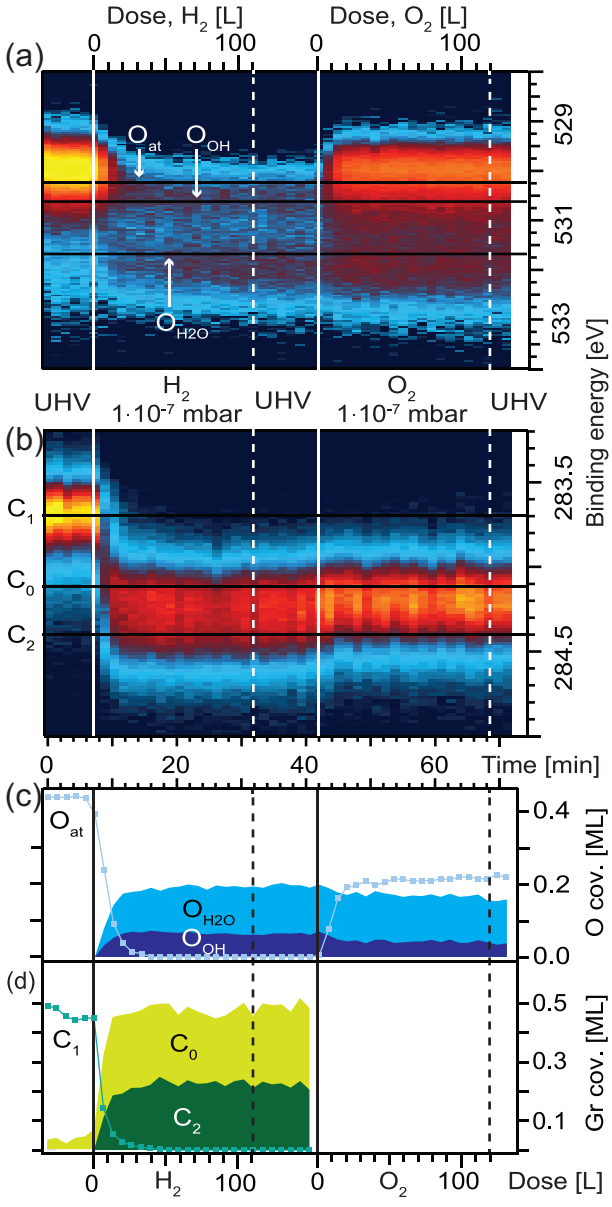

Figure 6.4: Evolution of the O 1s (a) and C 1s (b) regions measured during exposure to $1 \cdot 10^{-7}$ mbar of H_2 and subsequently $1 \cdot 10^{-7}$ mbar of O_2. The BE is given on the y-axis, the intensity is color-coded, dark blue corresponding to low, yellow to high intensity. Horizontal black lines indicate the positions of the fitted peaks in Figure 6.2. The upper horizontal axes display the dose of the respective gas, while the lower axes show the time duration from the first spectrum. Filled vertical lines indicate the time when H_2 and O_2 exposures began, dashed vertical lines indicate the end of the respective gas exposure. Initially (i.e., time = 0 s) the sample consists of 0.5 ML Gr/Ir(111) intercalated by a p(2 × 1)-O structure, corresponding to step (1) in Figure 6.2. The intensity of the fitted O 1s and C 1s components are shown in panel (c) and (d), respectively. The fit components are the same as in Figure 6.2, except for a larger GFWHM of the C 1s spectra due to the worse resolution at the photon energy used. Peak areas are normalized to the average total area of the spectra before gas exposure (average of the first five spectra).

the C 1s and O 1s regions simultaneously. This is shown in Figure 6.4, (a,b) show the evolution of the O 1s and C 1s spectra, respectively, while H_2 and O_2 are dosed subsequently. For Figure 6.4(c,d) each O 1s and C 1s spectrum was fitted with the components introduced in Figure 6.2, and the evolution of these components during dosing is shown. At time $t = 0\,\mathrm{min}$, the sample consists of 0.5 ML Gr intercalated by oxygen. From the O 1s components we obtain the ratio of OH to H_2O molecules of roughly 1:2, leading to an H:O ratio of 5:3 in our observed phase. This leads to a surprisingly high local coverage of 0.79 molecules (H_2O or OH) per Ir surface atom. This coverage is almost the double of the experimentally determined coverage for the p(2 × 1)-O structure (0.44 ML). The high coverage implies that O-atoms trapped under Gr condense into a mixed OH-H_2O phase upon reaction with hydrogen with a density much higher then what has been reported up to now. The reappearance of the C_0 component in panel (2) of Figure 6.2 is a necessary consequence of the higher oxygen coverage of the super-dense OH-H_2O phase.

6.3 Structure of the dense OH-H_2O phase

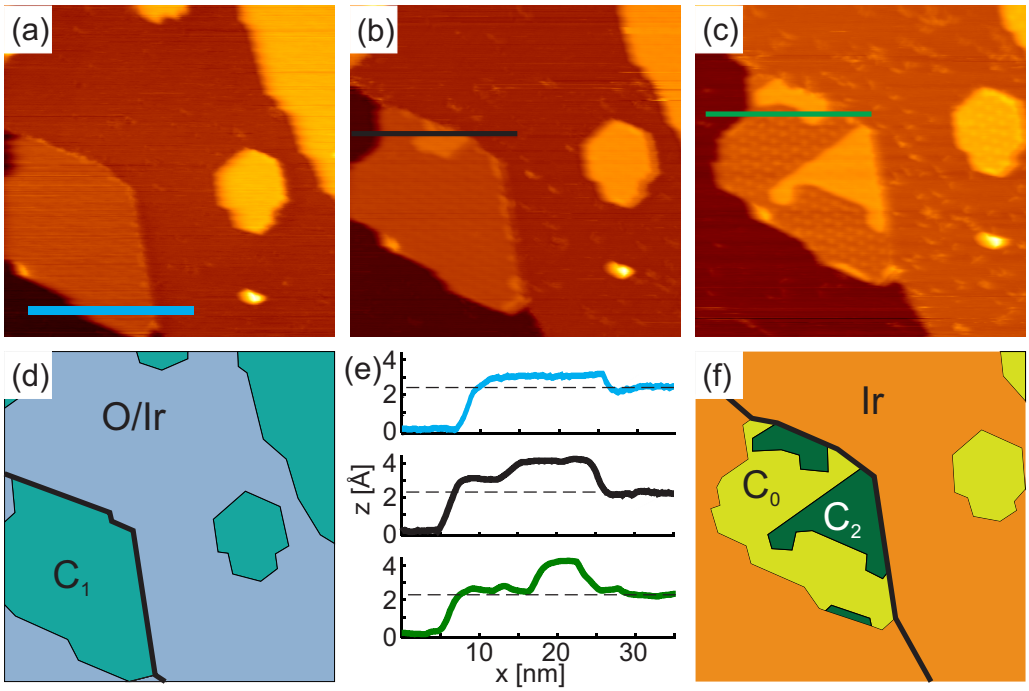

Figure 6.5: Snapshots from an STM movie acquired while O-intercalated Gr flakes are exposed to hydrogen. (a-c) Images from an STM movie showing three O-intercalated Gr flakes while they are exposed to $5 \cdot 10^{-9}$ mbar of H_2. (d and f) Schematic representation of (a) and (c), respectively. Colors analog to the colors used for the XPS components, orange is bare Ir, and black lines show Ir step edges. (e) Line scans along the lines marked in (a-c). Image size 71 nm × 71 nm. Tunneling parameters $I = 5.5$ nA, $U = -1$ V. From [213].

The formation of the super-dense OH-H_2O phase under oxygen intercalated Gr can be followed in real time by acquiring scanning tunneling microscopy (STM) movies during H_2 exposure. Figure 6.5 shows snapshots from such a movie taken during exposure to $5 \cdot 10^{-9}$ mbar of H_2 at room temperature. Upon H_2 exposure the formation of OH-H_2O islands beneath Gr is visible as bright areas. When the formation of the dense OH-H_2O phase has terminated and all O is converted or desorbed, these areas raise by 1.5 Å above the areas of Gr, that are now no more intercalated and thus relaminated to the Ir substrate. The phase boundary between the OH-H_2O phase is sharp and follows the moiré pattern, as visible in Figure 6.5(c). Apparently, the chemical inhomogeneity of the graphene binding to Ir(111) affects the

shape of the OH-H_2O phase formed beneath. The edges of OH-H_2O phase in STM are mobile at room temperature and thus the atomic structure of the phase could not be imaged. We performed LEED measurements of the OH-H_2O phase. Figure 6.6 shows bare Ir (a), 0.8 ML Gr grown by 8 TPG steps with the Ir, C and moiré spots visible (b), 0.8 ML intercalated by 750 L O_2 at 520 K (c), 0.8 ML Gr after 4 cycles of (O_2 + H_2) (d), and the same situation as in (d) but at 100 K (e). Afterwards, the TPD measurements shown in Figure 6.3 were performed with this sample. Upon oxygen intercalation, the intensity of the moiré is significantly reduced, and a (2×2) superstructure is visible that is due to the three, rotated by 60°, (2×1) domains formed by O/Ir [52]. After 4 cycles of (O_2 + H_2) the (2×2) spots have disappeared, no additional spots are seen which is to be expected as the molecules in OH-H_2O phase are mobile at room temperature. However, cooling the sample to 100 K also did not result in the appearance of any additional superstructures. Especially no $(\sqrt{3} \times \sqrt{3})$ superstructure was observed, as would be expected for a water layer on Pt(111) [230]. Note that the electron energy has been slightly varied for each image so as to get the best contrast for each case, all energies were carefully checked but no additional superstructures were found. Low temperature STM measurements could add additional insight.

Based on our XPS, TPD, STM, and LEED results we conclude that room temperature hydrogen dosing onto O-intercalated Gr flakes gives rise to the formation of a super-dense mixed OH-H_2O phase that remains trapped up to a temperature of 440 K. In contrast, upon room temperature H_2 exposure of oxygen adsorbed to bare Ir(111) the reaction products desorb instantaneously. The super-dense OH-H_2O phase on Ir(111) has to the best of our knowledge never been predicted before. Its main difference with respect to adsorbed honeycomb structures of mixed OH (0.33 ML) and H_2O (0.33 ML) on Pt(111) [230] is the higher H:O ratio of 5:3 in our case (compared to 3:2 for the honeycomb structure). One might expect the honeycomb structure to condense into the super-dense OH-H_2O structure, enabling more adsorption. We speculate, however, that the energy barrier associated with the significant reconstruction necessary for converting the meta-stable honeycomb to the superdense OH-H_2O structure effectively prohibits the conversion at low temperatures. Thus, once the less dense honeycomb structure is formed it is very difficult to convert this to the super-dense OH-H_2O structure both on bare Ir(111) and Pt(111) without desorbing water. As the Gr cover on Ir(111) prevents water desorption the temperature can be increased to room temperature without losing water and it becomes possible to overcome the conversion barrier. Therefore, it is likely that similar water structures can be formed under the Gr cover on other metal surfaces such as Pt(111).

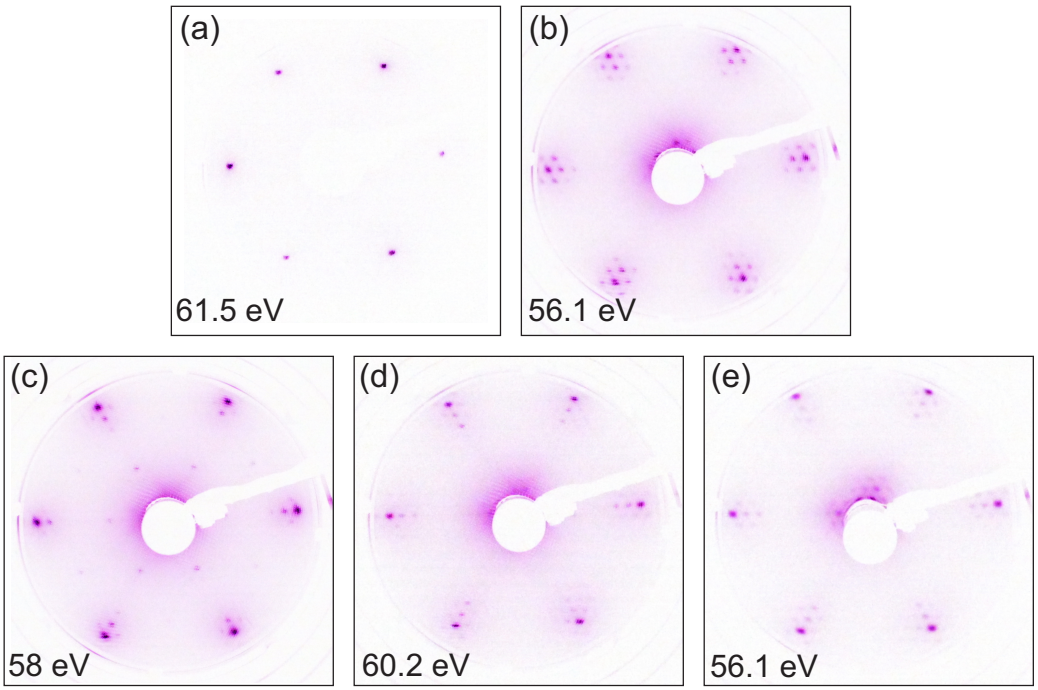

Figure 6.6: LEED images of (a) bare Ir(111), (b) 0.8 ML Gr, (c) 0.8 ML Gr intercalated by 750 L O_2 at 520 K, (d) Gr after 4 cycles of (O_2 + H_2) (see Section 6.4), (e) as (d) but imaged at 100 K. (a-d) were imaged at room temperature. Electron energies were chosen to obtain the best contrast and are indicated in the images.

6.4 Cycles of O_2-H_2-dosing

We have now found that one cycle of O-intercalation and subsequent H_2 exposure leads to the formation of a super-dense OH-H_2O structure consisting of rows of H_2O and OH molecules under Gr. Next we will demonstrate that it is possible to dissolve atomic oxygen into this structure, already at room temperature, leading to a less dense mixed structure. In Figure 6.7(a) we compare O 1s and C 1s spectra of Gr partly intercalated by the superdense OH-H_2O structure before and after an additional room temperature oxygen exposure cycle. Focusing first on the C 1s spectra it is clear that the C_2 component assigned to the super-dense OH-H_2O structure is removed upon the oxygen dosing and replaced by a broad C_3 component located at 283.95 eV and thus shifted 0.14 eV. In contrast to the significant changes in the C 1s spectra, the OH and H_2O components in the O 1s spectra are essentially unaffected by the oxygen dosing as demonstrated by Figure 6.7(a) and in the in-situ experiments shown in Figure 6.4. The simplest scenario to reconcile these observations is that O dissolves into the OH-H_2O structure, whereby the Gr becomes slightly more p-doped, turning C_2 into C_3 [compare Figure 6.7(a)], while the amount of OH-H_2O is unchanged. Comparison of the intensity of the O_{at}-component of p(2 × 1)-O (corresponding to step (1) in Figure 6.2) and the O_{at}-component in step (3) in Figure 6.7(a) reveals that the O_{at}-intensity in step (3) is reduced to half of the intensity of the p(2 × 1)-O structure (see also Figure 6.4). This observation suggests that the majority of the oxygen adsorbs on bare Ir(111) patches and only a smaller fraction is dissolved into the OH-H_2O structure. Since the super-dense OH-H_2O structure intercalated under Gr initially covers locally all Ir-sites we expect the less dense intercalated O-H_2O-OH structure to expand causing more intercalation and less non-intercalated Gr. Both our XPS and STM data agree with this picture. When the super-dense OH-H_2O structure is saturated with oxygen at room temperature our XPS experiments reveal a reduction of the C_0 component intensity by 23% [compare (2) and (3) in Figure 6.7(a)], while our STM images show an area reduction of the non-intercalated Gr by ≈ 27% [marked C_0 in Figure 6.7(b)], in good agreement with the XPS data. When the intercalated O-H_2O-OH structure is exposed to H_2 again we find that the dissolved oxygen can be fully converted to OH and H_2O causing the C_2 component to reappear with increased intensity. In more detail we observe that the C_3 component, signaling the mixed O-OH-H_2O phase, disappears upon H_2 dosing while the C_2 component, signaling the super-dense OH-H_2O phase, reappears with a 10 % increase in relative intensity [Figure 6.7(a)+(c)]. Upon continued cycles of subsequent O_2 and H_2 dosing at room temperature the relative intensity of the C_2 component increases more and more for each cy-

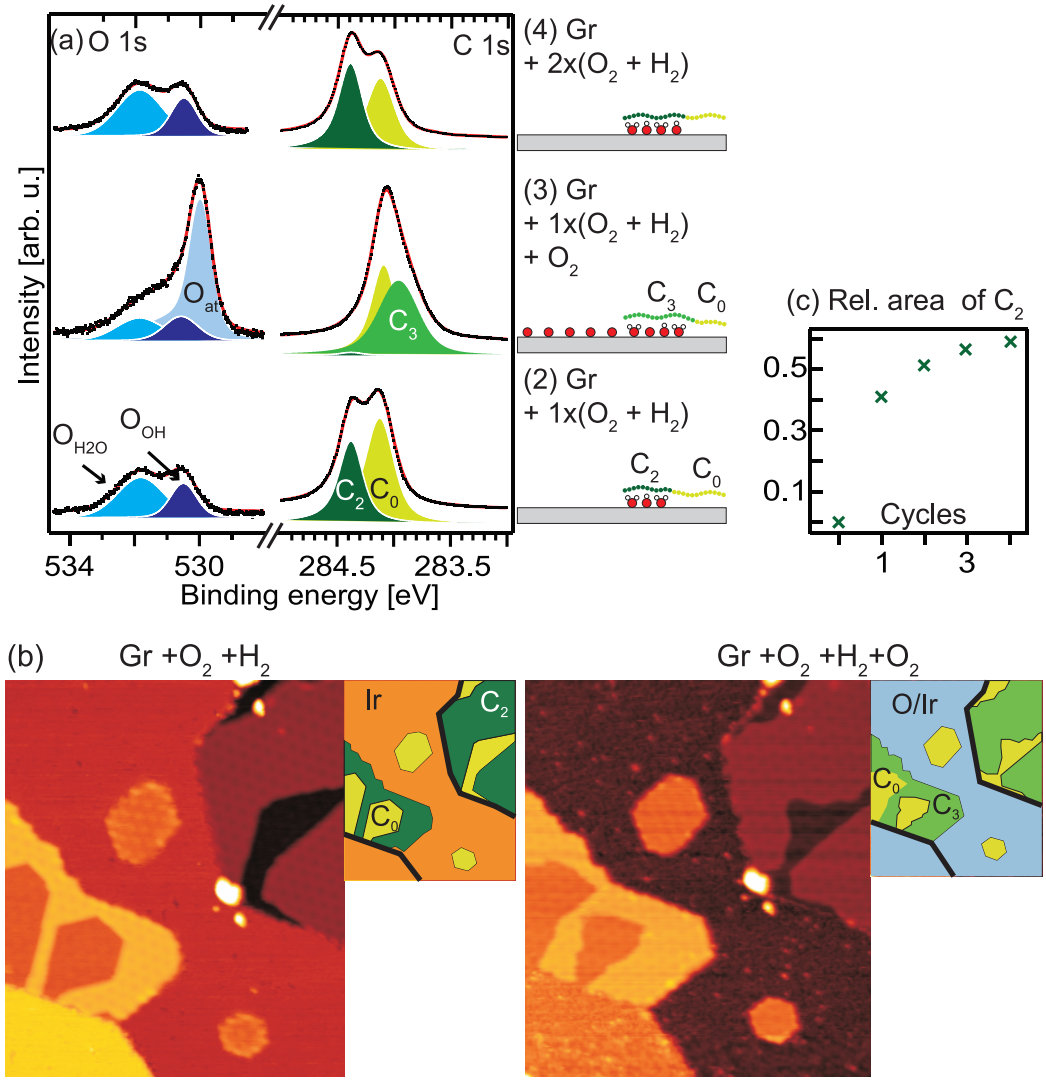

Figure 6.7: O-uptake in the super-dense OH-H_2O phase studied with XPS and STM. (a) O 1s and C 1s spectra of Gr exposed to: (2) one cycle of (O_2 + H_2) , (3) after an additional O_2 exposure, and (4) after two cycles of (O_2 + H_2). The experimental spectra are shown as black dots, the fits as red lines and the filled curves represent the components of the fit. (b) Left STM image: UHV, after 4 cycles of (O_2+H_2). Right STM image: During additional exposure to $1 \cdot 10^{-7}$ mbar of O_2 after approximately 30 min (265 L). Image size 60 nm × 70 nm, $U = -1$ V, $I = 1$ nA. Schematic representations of the STM images are shown in between. Colors analog to the colors used for the XPS components, orange is bare Ir, and black lines show Ir step edges. (c) The relative area of the C_2 component versus the number of (O_2 + H_2) cycles obtained from XPS experiments. From [213].

cle. The increase for each cycle is moderate, in agreement with our previous conclusion that only a smaller amount of oxygen atoms is dissolved into the OH-H_2O phase upon room temperature oxygen dosing.

O 1s and C 1s spectra acquired after each cycle are shown in Figure 6.8(a). The lowest spectra show the pristine 0.5 ML Gr, the second spectra are taken after exposure to 200 L O_2 at 450 K and 100 L H_2 at 300 K. Thereafter, the spectra in each row were taken after exposure to an additional cycle of 200 L O_2 and 100 L H_2 at 300 K. The areas in Figure 6.7 were calculated from the spectra shown here. Also present in the C 1s spectra after H_2 exposure is a component corresponding to adsorbed CO, located at 286.2 eV, and an unidentified carbon component located at 283.3 eV, as can be seen in Figure 6.8(b). The CO adsorbs from the background and the component increases with time. The area of the CO component relative to the total graphene area is always less than 0.5%. The component at 283.2 eV we tentatively assign to a CH species adsorbed on Ir(111) [231], forming either through reactions between the H_2 and CO on the surface or through a beam induced reaction. The area of this carbon component is always less than 1% of the total graphene area.

6.5 Summary

To summarize, we showed that a super-dense OH-H_2O phase forms exclusively beneath Gr-flakes. We assign this finding to the role of the Gr cover to block water desorption from less dense OH-H_2O phases that may initially form. We have thus shown for the first time that Gr enables new reaction paths that would not be possible without Gr. The superdense phase is characterized by an OH-to-H_2O ratio of roughly 1:2, hence an H:O ratio of roughly 5:3 and a suprisingly high local coverage of 0.79 molecules (OH or H_2O) per Ir surface atom. This is different from the known honeycomb OH-H_2O phase on Pt(111) [230]. The superdense phase is mobile at room temperature, as evidenced by our live STM measurements. Also at low temperatures, LEED does not reveal an ordered structure.

We have also shown that O-atoms can be dissolved into the super-dense OH-H_2O phase at room temperature once it is formed beneath the Gr-flakes, and we expect that many other molecules also will be able to do so. This finding paves the way for studying room temperature reactions within trapped OH-H_2O films under Gr at UHV conditions, which is extremely relevant for understanding reactions taking place on metal surfaces in humid environments.

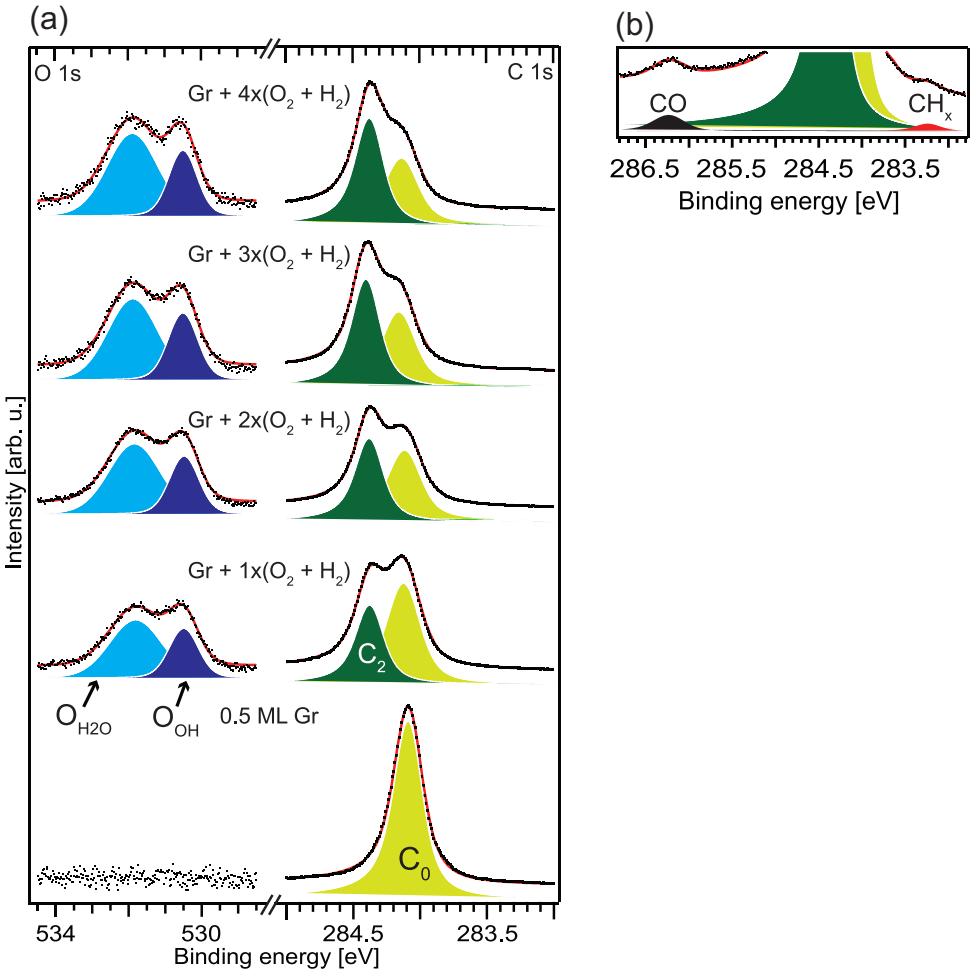

Figure 6.8: (a) O 1s (left) and C 1s (right) spectra corresponding to pristine 0.5 ML Gr (bottom), and after exposure to an additional cycle of 200 L O_2 and 100 L H_2 for each pair of O 1s and C 1s spectra. The experimental spectra are shown as black dots, the fits as red lines and the filled curves represent the components of the fit. (b) The same spectrum as the top one in (a), with an exteneded binding energy region and adjusted intensity scale to show the low intensity peaks. From [213].

Chapter 7

Deuteration of graphene on Ir(111)

Sections 7.1 - 7.5 are based on the master thesis of C. Murray [124] and contain contributions from: C. Murray and T. Michely. I was involved in the planning of the experiments, the measurements and analyses were carried out under my supervision. I performed additional STM analyses. Section 7.6 contains contributions from: T. Michely, E. Grånas, J. Knudsen, A. J. Martínez-Galera, and M. A. Arman. For this part, I was involved in the XPS measurements, performed the TPD measurements, and analyzed all data.

Due to the bandgap that can be bestowed in deuterated or hydrogenated Gr, this system, and specifically Gr/Ir(111), has been studied with XPS, STM, DFT, HREELS and SFG [6, 16–18, 105–107]. Here, we present for the first time TPD measurements of Gr/Ir(111). With complementary STM measurements and comparison with other Gr systems we suggest an interpretation for the two distinct binding states observed in TPD. Further, the role of intercalation of D is studied, and we show that it is not possible to form graphane by deuterating an D-intercalated Gr film.

7.1 Deuterated Gr/Ir: TPD and STM

The desorption behavior of D from Gr/Ir(111) is shown in Figure 7.1 for 15 L D dosed on 1 ML Gr, in one case at 100 K and the other at 300 K sample

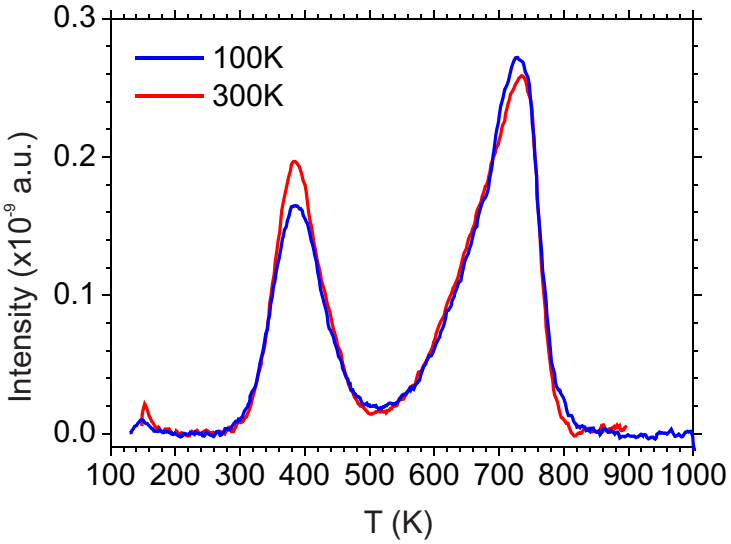

Figure 7.1: TPD spectra (mass 4 u) of 15 L D adsorbed on 1 ML Gr/Ir(111) at 100 K (blue) and 300 K (red). Heating rate 5 K/s. Adapted from [124].

temperature. The two spectra are largely the same, with two main peaks and little activity below room temperature. The heights of the peaks differ slightly but this is well within the typical deviations experienced in the system. The two main peaks, lying at ≈ 380 K and ≈ 730 K, suggest that there are two distinct binding states for D on Gr/Ir(111). We henceforth refer to them respectively as the *weakly* and *strongly* bound states of deuterium. They will be discussed in greater detail in Sections 7.2 and 7.3 with the help of STM measurements. Small signals are additionally seen at ≈ 150 K. However, these were not observed in every spectrum and they have occurred shortly after the TPD heating process has begun, when the heating rate may not yet be linear. Therefore we dismiss these as an experimental artifact. That aside, there is no significant activity seen below room temperature and no strong dependence on whether dosing was performed at 100 K or 300 K. Thus we hereafter operate at room temperature, to avoid the slow cool-down process. No desorption activity was seen above 900 K up to 1100 K (consistent with the observation of other groups [18]).

Figure 7.2 shows TPD for different doses of D at 300 K on 1 ML Gr, performed sequentially. The desorption spectra show the same shape as in Figure 7.1. One exception is the double-peak structure seen around 400 K at low doses. The inset shows the integrated areas under each spectrum, that is, the relative amount of D desorbing in each case. A limit is approached representing saturation. Increasing the dosage from 15 L (4 min) to 36 L (10 min)

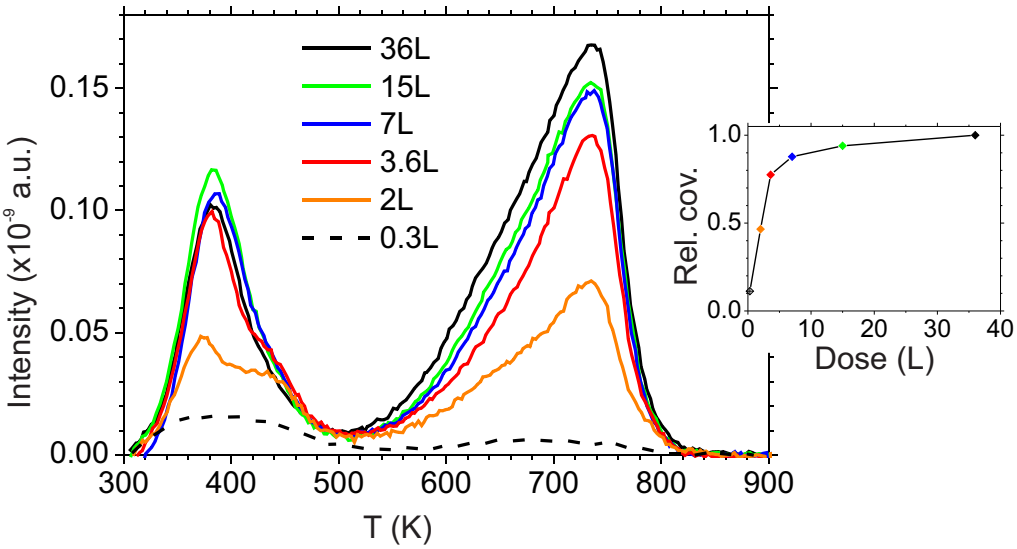

Figure 7.2: TPD spectra (mass 4 u) of various doses of D on 1 ML Gr/Ir(111), each dosed at 300 K. D pressure ($8 \cdot 10^{-8}$ mbar) and cracking power (65 W) were the same for each spectrum; only the exposure time was varied, ranging from 5 to 600 s (0.3 L to 36 L, respectively). Heating rate 5 K/s. The inset shows the integrated area under the curves, normalized to the area under the black curve. Adapted from [124].

results in only 6% more D adsorbed on the sample. Possibly, a higher coverage could be reached by increasing the dose another order of magnitude, this was not feasible due to experimental restrictions[1]. Thus we take 15 L as our standard dose. As pointed out in Section 3.7, the true pressure at the sample and hence the true dose that the sample sees is unknown, however, as shown below in Figure 7.14, dosing 15 L of molecular D_2 through the cracker is enough to saturate the Ir surface and could thus represent a true dose of ≈ 1000 L (compare to Figure 2.16).

The peak temperatures, T_P , are independent of initial coverage. Constant T_P and the asymmetric peak shapes both indicate first-order desorption kinetics [30]. Such kinetics are typically associated with single atoms desorbing independently. This is in contrast to second-order kinetics, which are distinguished by T_P shifting to lower temperatures as coverage increases. Such a shift would be expected if single D atoms would 'randomly walk' until they meet one another, recombine, and desorb as a molecule. The higher the coverage, the shorter the average walk, and thus the more likely for radicals to meet at a given temperature. Apparantly, this is not the case here.

Our next observation is that both peaks appear approximately at the same dose. The weakly bound peak saturates already at 3.6 L, while the strongly bound peak continues to grow in intensity.

Estimates of the two states' desorption activation energies E can be obtained by using a basic Redhead analysis [122, 232]. Based on our $\beta = 5\,\mathrm{K/s}$ heating rate, first-order desorption and assuming a standard $10^{-13}\,\mathrm{s}^{-1}$ frequency factor, values of $E \approx 1.0$ eV and ≈ 2.1 eV for the weakly and strongly bound states were found, respectively [124].

Together with TPD, we employ STM to elucidate the nature of D-Gr binding. In Figure 7.3(a,b) we see the standard 15 L D dose on 1 ML Gr, imaged at room temperature. Immediately apparent is that the D adatoms adsorb in a periodic manner. We observe regular 'spots' - roughly circular in most cases and appearing 1.7 ± 0.3 nm in diameter. They appear approximately 0.8 to 1 Å high. We term these spots deuterium islands (D-islands). They are seen to follow a hexagonal lattice symmetry. Through line-profiling and calibrating against clean Gr/Ir(111) imaged with the same system, we calculate their hexagonal lattice constant to be 2.54 ± 0.17 nm. This is very close to the known 2.53 nm periodicity of the Gr/Ir(111) moiré [23], illustrating that the D-islands are following its registry. Some areas of coalesced D-islands are visible, as indicated by the black arrows. The close-up shown in Figure 7.3(b) reveals that the D-islands are not flat but possess an often ring-

[1] These were twofold: Arcing of the cracker prevented us from going to higher pressures, and the piezo leak valve proved to be too unstable to increase the time by a factor of 10.

like structure. Also noted are the many smaller spot-like features in between the islands. It was rather difficult to image D adsorbed at 300 K, probably due to the weakly bound species interacting with the tip. Other than that we did not detect any mobility in the adsorbed features. LEED images of the sample did not reveal any additional spots, only the moiré spots appeared weakened (not shown).

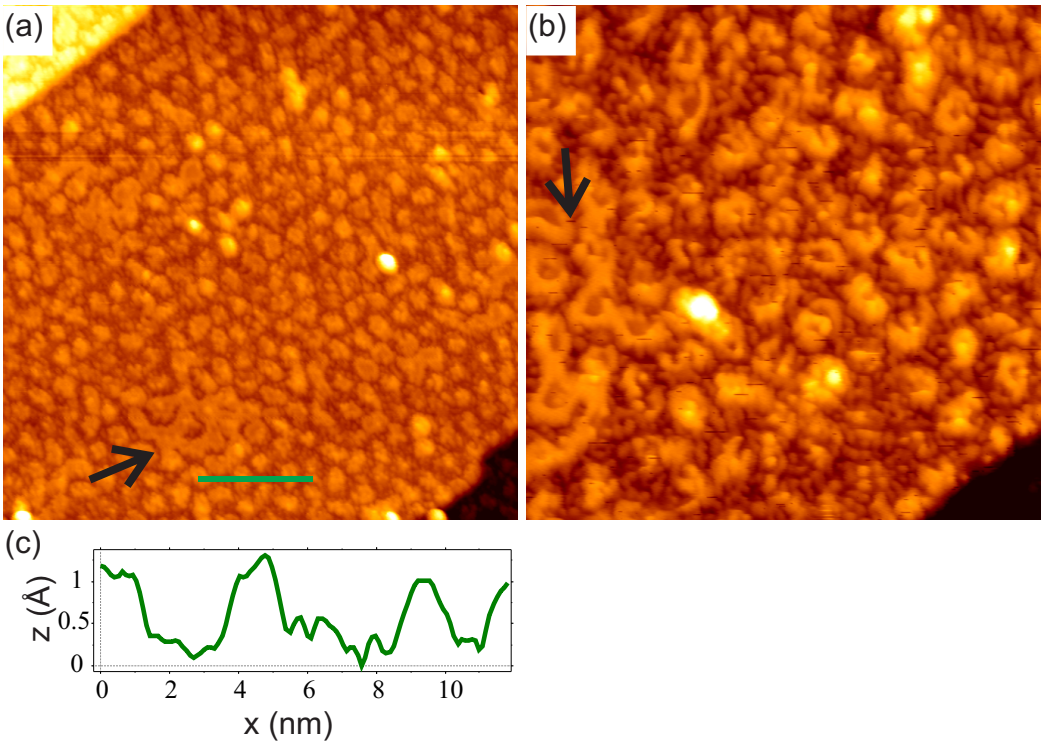

Figure 7.3: STM topographs of 15 L D on 1 ML Gr/Ir at 300 K. Black arrows point to coalesced areas of adsorbed D. Image size (a) 53 nm × 53 nm; (b) 26.5 nm × 26.5 nm. Tunneling parameters (a) $I = 0.13$ nA, $U = -1.03$ V; (b) $I = 0.13$ nA, $U = -0.91$ V. (c) Height profile along the green line in (a).

Deuterium coverage calibration

To calibrate the amount of D adsorbed on 1 ML Gr, we compare it to the desorption spectra of 3600 L D dosed onto Ir(111), shown in purple in Figure 7.4. The shape of this desorption spectrum closely resembles those found in the literature, described in Section 2.6. We find the peaks β_1 and β_2 at $\approx$ 155 K and $\approx$ 250 K respectively. A shoulder is seen towards higher temperatures, just as in Figure 2.16(b). We found near identical spectra for 1100 L

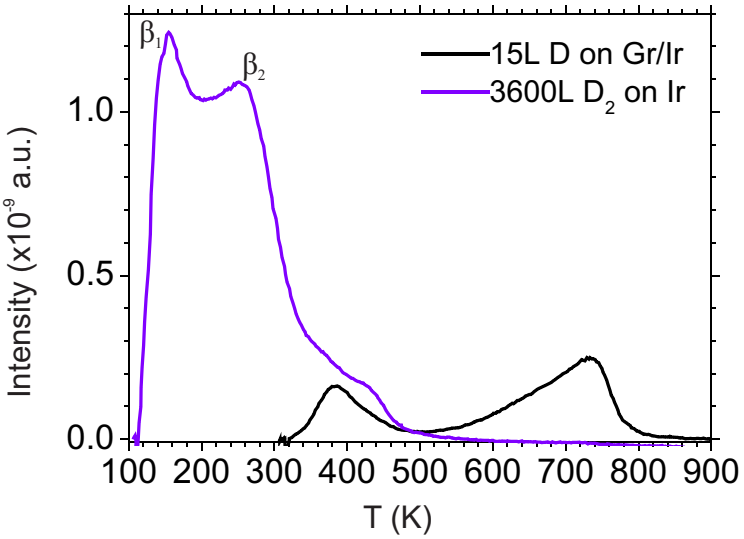

Figure 7.4: TPD spectra (mass 4 u) of 3600 L D_2 on bare Ir (purple) and 15 L D on 1 ML Gr/Ir (black). The two desorption peaks of D on Ir(111) are labelled β_1 and β_2. Heating rate 5 K/s. Adapted from [124].

doses of D_2, indicating that saturation occurs already at that dose or lower. Integrating under the curves in Figure 7.4, we find an area $0.480 \cdot 10^{-7}$ (in arbitrary units) for 15 L D on Gr/Ir and $2.285 \cdot 10^{-7}$ for bare Ir. We therefore calculate a coverage of (0.21 ± 0.06) ML (where 1 ML corresponds to D adsorbing on Ir in a (1×1) structure [90]). A conservative 20% error was assumed for both area values, based on potential discrepancies in background fitting and mass spectrometer sensitivity (Section 3.2), though the two experiments were performed within days of each other to minimize this effect. An additional source of error is that we assumed complete 1-to-1 saturation of D on Ir atoms, though in reality it may be slightly less than this [90]. The average moiré unit cell contains 86.8 Ir atoms and 213.0 C atoms. Assuming 1-to-1 coverage, there is thus a factor 2.45 ± 0.10 more Gr adsorption sites than on the bare Ir, and the fraction of Gr adsorption sites being occupied by D is 0.086 ± 0.024. Thus, 8.6% of C atoms are bound to a D or, in other words, 18.3 ± 5.2 D adatoms are found per moiré cell. Further to this, we may estimate the number of adatoms which contribute to each of the two peaks. Taking 500 K as the dividing line, we find 5.1 ± 1.5 D atoms in the weakly bound state and 13.1 ± 3.7 in the strongly bound state, per moiré unit cell.

Hydrogen-1 on Gr/Ir(111): The isotope effect

TPD of atomic H on 1 ML Gr is shown in Figure 7.5 for three different doses. Because H is naturally much more abundant in UHV systems than D, TPD of it shows much more background and noise. As such, we do not scrutinize the shape of the desorption spectra or the coverage. Nonetheless, the peak desorption temperatures are reliable; they do not depend on coverage and the same heating rate was used in all experiments.

In Figure 7.5 the weakly and strongly bound peaks are clearly visible, despite the increased background. They lie at $\approx 360\,\mathrm{K}$ and $\approx 705\,\mathrm{K}$, respectively. This represents shifts of approximately 20 K and 25 K from the respective peaks for D. This shift in desorption temperature between H and D on Gr/Ir(111) is due to the isotope effect. We can compare it to the isotopic shift seen on HOPG(0001) which is found to range between 20 K and 45 K [95,97,99], similar to what we observe. It has been suggested in the literature [99] that the isotopic shift is due to D having a smaller preexponential factor in the Arrhenius equation [233].

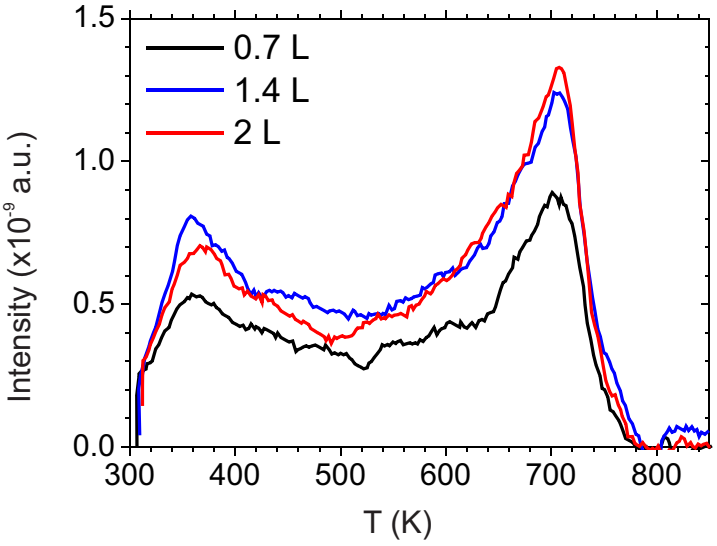

Figure 7.5: TPD spectra (mass 2 u) of H on 1 ML Gr/Ir(111). H was dosed at $3.1 \cdot 10^{-8}$ mbar at 75 W. Heating rate 5 K/s.

7.2 Strongly bound D state

Having observed the two binding states in TPD, the immediate questions are: what is the physical difference between them, and how do they correspond

to what is imaged in STM? We consider each state in turn, beginning with strongly bound D. Investigating it is more straightforward - by simply flash annealing the sample to 550 K, we desorb the weakly bound D away, leaving only the stronger bound adatoms (≈ 730 K).

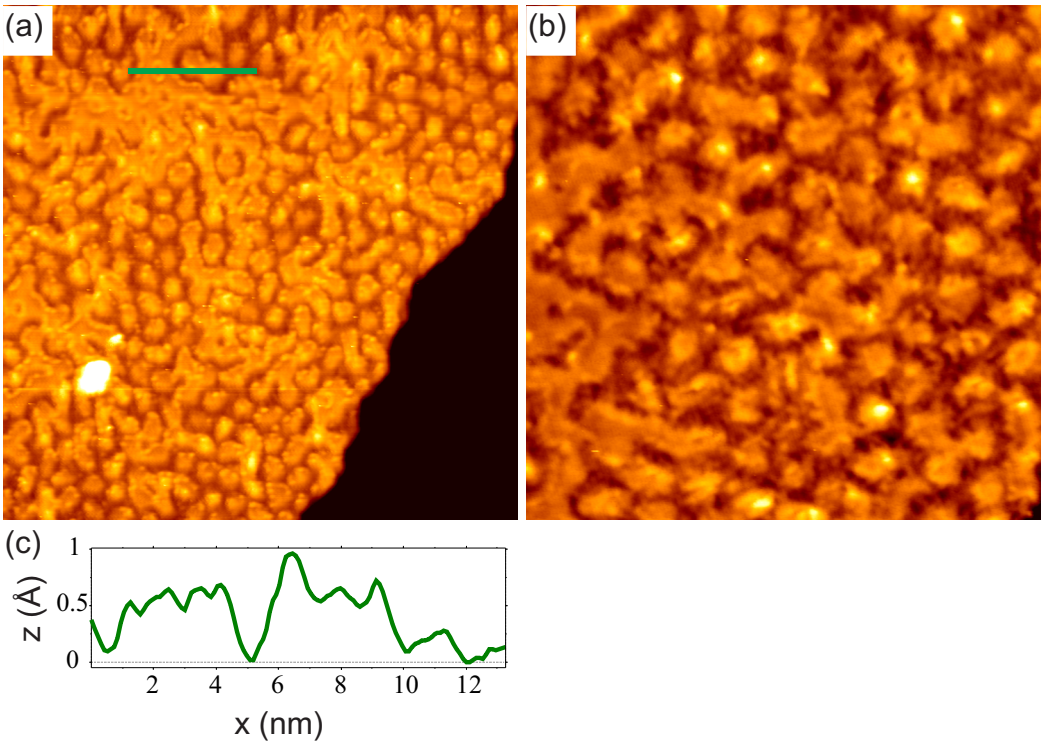

Figure 7.6: STM topographs of 15 L D dosed on 1 ML Gr/Ir at 300 K and subsequent flash annealing to 550 K. Imaged at room temperature. The lower terrace in (a) appears black due to contrast adjustment. Image size (a) 53 nm $\times$ 53 nm; (b) 26.5 nm $\times$ 26.5 nm. Tunneling parameters (a) $I = 0.11$ nA, $U = -1.08$ V; (b) $I = 0.24$ nA, $U = -1.08$ V. (c) Height profile along the green line in (a).

Figure 7.6 shows 15 L D dosed on 1 ML Gr, flash annealed to 550 K, and imaged at room temperature. Rather surprisingly, the image is very similar to the situation before the flash (Figure 7.3), although we have desorbed almost one third of the deuterium. The islands exhibiting the hexagonal moiré periodicity are still present, they appear somewhat flatter and more rounded than before. As seen in the height profile of Figure 7.6(c), they also appear lower than before, approximately 0.6 Å higher than their surroundings. Also the space in between the islands has become more homogeneous, less features can be distinguished there. More of the islands are coalesced, and if anything,

it looks like as if there is more D on the sample than before.

First, we take a look at the periodicity of the islands - D adatoms favour particular areas of the Gr. This can only be due to its interaction with the Ir substrate underneath. We draw parallels with metal cluster superlattices grown on Gr/Ir(111), which are described in Section 2.2. The appearance of such metal clusters in STM (Figure 2.4) has obvious similarity with our D-islands. It is conceivable that D adatoms would form islands on Gr/Ir(111) in a similar way, and indeed this has previously been proposed by Balog et al. [6, 105]. We designed an experiment to confirm this explicitly: block the hcp-sites with Pt clusters, dose D as normal and then observe in TPD if the strongly bound peak is attenuated. Specifically, we evaporated approximately 0.45 ML of Pt onto clean Gr at room temperature. STM [Figure 7.7(a)] showed an ordered Pt-cluster superlattice as desired. 2 L of D was then dosed onto the sample, with STM being performed again afterwards to confirm that the Pt-cluster superlattice had survived deuteration [Figure 7.7(b)]. Finally, TPD was performed and compared to a control run of 2 L on clean Gr. Seen in Figure 7.7(c), the strongly bound peak is attenuated by the presence of Pt clusters while the weakly bound peak is increased in intensity. The simplest conclusion is that the clusters have blocked the hcp-regions, thereby confirming them as the preferential binding sites for D radicals on Gr/Ir(111). The lower temperature peak is higher compared to the control experiment without Pt clusters. This could be due to D being adsorbed on the Pt clusters [234]. An easy experiment to exclude that the low temperature peak is exclusively due to desorption from Pt is recording a TPD spectrum after dosing molecular D_2 on ≈ 0.45 ML Pt clusters.

The high desorption temperature of the D is then explained by the sp^3-rehybridization of the C atoms in these areas. This tetrahedral hybridization, like that of C in diamond-form, gives rise to a strong bonding. To summarize: the registry of the Gr/Ir(111) moiré in hcp-sites facilitates the C atoms binding alternately to Ir substrate atoms below and D adatoms above in a 'graphanelike' fashion. This sp^3-rehybridization results in relatively strong binding and explains the 730 K peak desorption temperature (Figure 7.2). Furthermore, as there is one hcp-site per moiré unit cell, the D-islands exhibit this periodicity in STM. We propose that, although hcp-sites are preferred slightly, it is very possible for islands to form in neighbouring fcc-sites also, these neighbouring islands then coalescing. When this occurs, instead of islands punctuating the moiré periodicity, it is deuterium-less atop-regions which appear as 'holes'. This can be seen inside of the gray rectangle in Figure 7.8(a). Our hypothesis is in fitting with previous observations and calculations by Balog et al. [6, 105], who claim that H occupies both fcc and hcp areas, but do not differentiate between the two. As demonstrated by

Murray [124], their data also show that one particular moiré site is initially preferred for H- or D-island formation.

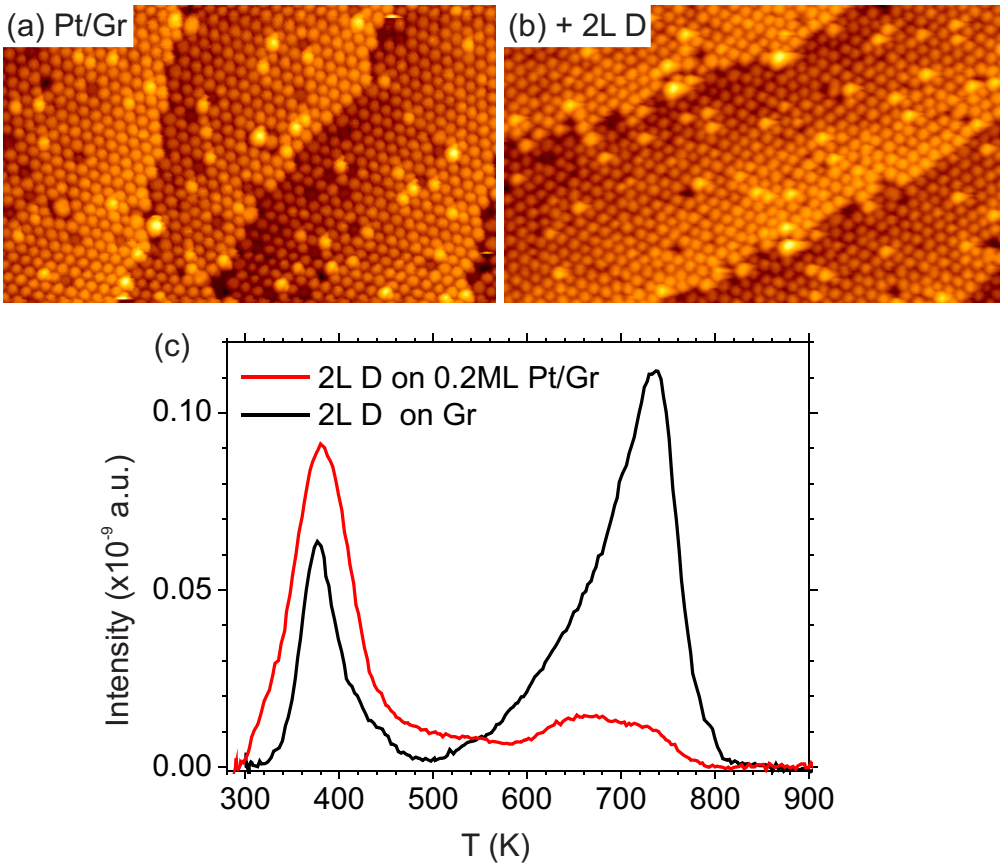

Figure 7.7: STM topographs of ≈ 0.45 ML Pt on 1 ML Gr/Ir (a) before and (b) after dosing 2 L D ($5{\cdot}10^{-9}$ mbar, 8 min, 63 W) at room temperature. Image size 107 nm × 64 nm. Tunneling parameters (a) $I = 0.17$ nA, $U = 1.59$ V; (b) $I = 0.18$ nA, $U = 1.77$ V. (c) TPD spectra (mass 4 u) of the sample shown in (b) in red; for comparison 2 L D on 1 ML Gr is shown in black. Heating rate 5 K/s. (c) adapted from [124].

In the STM topograph of Figure 7.6 some coalesced islands are seen, more than what was observed when D was dosed at 300 K (Figure 7.3). Another good example is provided in Figure 7.8(a), in which D was dosed onto 1 ML Gr at 450 K (to reduce the quantity of weakly bound D adsorbates). Many coalesced islands are seen there, e.g., inside the gray rectangle in Figure 7.8(a). Figure 7.8(b,c) show a close-up, some D-islands in a cat-like shape are marked as a reference point in all three STM images. Here, we see that

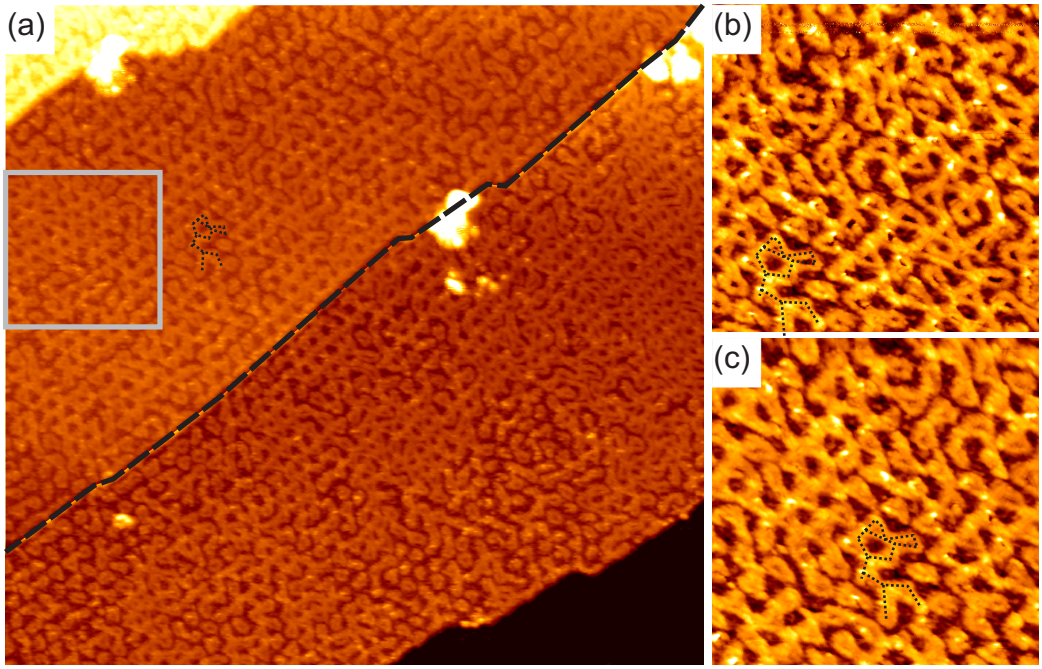

Figure 7.8: STM topographs of 15 L D dosed on 1 ML Gr at 450K. Imaged at room temperature. The gray rectangle in (a) marks coalesced regions (see text). The contrast on each side of the Ir step edge indicated by dashed black line was adjusted separately so that features on both terraces are well visible. (b,c) close-up of the region marked by a cat-like shape, as indicated by a dotted line in (a,b,c). Image size (a) 106 nm × 100 nm; (b,c) 26.5 nm × 26.5 nm. Tunneling parameters (a) $I = 0.12\,\mathrm{nA}$, $U = -0.98\,\mathrm{V}$; (b,c) $I = 0.12\,\mathrm{nA}$, $U = -0.98\,\mathrm{V}$.

the D-islands are now closed, irregular rings. These structures appear more perfect than those observed when D is dosed at 300 K [Figure 7.3(b)]. We also demonstrate that rings are only imaged with a good tip, in Figure 7.8(b) the holes inside the rings are hardly resolved, due to a more blunt tip. We thus attribute the observation that the coverage seems to increase after flash annealing to a blunt tip.

From the increase in coalesced islands and the more homogeneous appearance of adsorption structures, we tentatively conclude that there is deuterium diffusion present when heating up the sample. As shown for H on Gr/Ni(111), diffusion of isolated H atoms into *meta* positions is favored compared to direct desorption. Additionally, local *para* and *ortho* dimers diffuse into *meta* configurations, here diffusion is favored by roughly 0.3–0.4 eV over direct desorption. As Gr grows commensurately on Ni(111), the situation is comparable to our hcp and fcc regions, and the coalesced regions could form due to diffusion of single H atoms or local diffusion of *ortho* and *para* states into *meta* arrangements. The closed-ring-like structures, sometimes coalesced, are the most stable states of D, which only desorb at high temperatures of ≈ 730 K.

7.3 Weakly bound D state

We now seek to explain the weaker binding (≈ 380 K) state of D on Gr/Ir(111). It is difficult to link the STM to the TPD data, because we do not know which changes in the STM images are due to diffusion into the strongly bound state and which are due to desorption. We unambiguously attributed the strongly bound peak to adsorbates in hcp and fcc regions of the moiré lattice of the Gr. It is plausible that D can also adsorb in other regions, and so we tentatively attribute the weakly bound peak to D adsorbed in the sp^2 regions of the Gr.

Evidence for this conjecture comes from the comparison with an sp^2-hybridized system, namely, D adsorbed on the HOPG(0001) surface (see Section 2.7). The respective TPD spectra are displayed in Figure 7.9. For comparison TPD spectra with similar heating rate and resolution as our spectra were chosen from the literature. From HOPG [Figure 7.9(b)] a main desorption peak is found at 490 K, accompanied by a shoulder at 580 K [99]. In comparison our weakly bound state from Gr/Ir(111) [Figure 7.9(a)] shows peak desorption at ≈ 380 K. It also shows a shoulder at approximately 450 K in some spectra of lower coverages - 2 L and 3.6 L for example. The shape of our desorption peak closely resembles that from HOPG - they both have a common leading edge, a distinct peak and a broader trailing edge. The obvious difference is that the desorption from Gr/Ir(111) is shifted ≈ 110 K

lower in temperature. On HOPG, D adsorbs in a dimer configuration, i.e., pairs of D adatoms bound to the same C-ring [97]. Due to the similarity in TPD spectra of the two systems, we suggest dimer configurations of D in sp^2-hybridized regions of Gr/Ir(111) as well. Assuming our $\approx 380\,K$ does correspond to D-dimers, this temperature shift shows that their binding to sp^2-hybridized areas of Gr/Ir(111) is weaker than to the topmost Gr layer of HOPG. There are many differences between the systems - for example coupling, doping and Gr curvature - and so speculation on the main cause for this shift is beyond the scope of this work. Nonetheless, the resemblance of the D-dimer desorption from HOPG to our weakly bound peak is noticeable. Our $\approx 730\,K$ peak is conspicuous by its absence from the HOPG spectra. The strengthening sp^3-rehybridization cannot occur in graphite, and so these well-bound islands cannot possibly form.

In all STM images where the weakly bound state is present, we observe features between the D-islands (Figure 7.3). We tentatively attribute these features to D-dimers. Line-profiling was performed on Figure 7.3 and found the proposed dimers to measure approximately 9 Å−13 Å across. Considering the C-ring geometry, the D atoms should lie 1.42 Å or 2.84 Å apart (for *ortho* and *para* dimers respectively). It is not surprising that they appear larger than this however, as STM tends to broaden small features. A similar ≈ 10 Å diameter was seen for D-dimers on HOPG in the literature [97] (Figure 2.18). Ideally we would image the dimers with atomic resolution, thereby confirming the individual D atoms' positions on the C-ring. Unfortunately, this level of detail was not attained. In general, imaging the D/Gr/Ir sample was difficult with the $\approx 380\,K$ state present; possibly the weak binding of these D atoms allowed them to interfere with the STM tip. Previously H- or D-dimers have been atomically resolved on Gr/SiC(0001) [235–237], on Gr/Pt(100) [238] and on HOPG [97], for example. However, to the best of our knowledge they have not been imaged on Gr/Ir(111) until now.

Dimers on Gr/Ir(111) have not been detected irrefutably in the literature, their existence has only been inferred. In experiments with XPS [105], HREELS [18], and SFG spectroscopy [107] a certain state of H (or D) on Gr/Ir(111) is observed, and each of the respective authors attributes it to dimers. This consensus is mostly based on DFT calculations [105] and the fact that dimers were observed on HOPG(0001) (see Section 2.7). We can compare these proposed dimers with our own observations, to a certain extent. Temperature-dependent XPS analysis of hydrogenated Gr/Ir(111) shows a component which vanishes gradually between ≈ 300 and $\approx 630\,K$, [105]. Similarly in HREELS, a vibrational feature 'strongly decreases' after flashing to $650\,K$ [18]. Both of the observations are attributed to dimers, and corroborated by DFT. Inspection of our TPD results (Figure 7.2) suggests

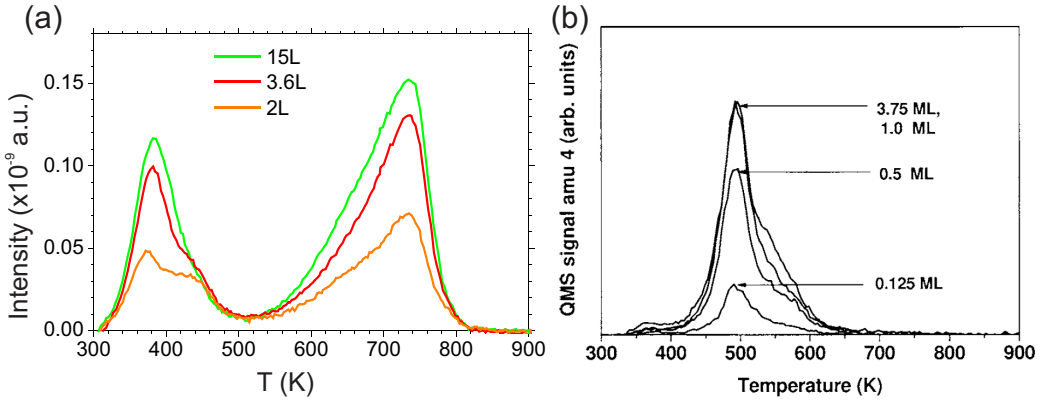

Figure 7.9: TPD spectra (mass 4 u) of (a) three different doses, as indicated in the figure, of D on 1 ML Gr/Ir(111) at room temperature (from Figure 7.2). Heating rate 5 K/s. Adapted from [124]. (b) Four given doses of atomic D dosed on HOPG at room temperature. Heating rate 1-3 K/s. Reprinted from [99], with the permission of AIP Publishing.

dimer desorption by ≈ 550 K, and so there is some discrepancy in temperature. However, it seems possible that not all dimers are desorbed by 550 K, as we still see small features present between islands even after flashing to this temperature (Figure 7.6). Kim et al. [107] have purportedly detected the dimers in SFG spectroscopy, and in fact claim to distinguish the *ortho* and *para* configurations from one another. However, these results have been disputed [18] and will be discussed in Section 7.4. They do not investigate the temperature-dependence of the state, and so direct comparison with our results is difficult anyway.

Summary

We wish to briefly summarize the main arguments for D-dimer existence on Gr/Ir(111):
(i) They are present on HOPG [97, 100], which is sp^2-hybridized like certain areas of our Gr. They show similar desorption behavior, albeit shifted in temperature as one would expect. They are also known to exist on Gr on other substrates [235–238].
(ii) In STM imaging we observe features in the sp^2-hybridized areas of Gr. However, detailed resolution was not achieved.
(iii) Their existence on Gr/Ir(111) has been suggested by DFT calculations, XPS [105], HREELS [18] and SFG spectroscopy [107]. The desorption tem-

peratures suggested by XPS and HREELS are in reasonable congruence with our results.

On the other hand, it is not clear that the features observed in the sp^2-hybridized areas of the Gr moiré are precisely dimers, they could also consist of more than two D atoms. Especially at high coverages, 'dimer' might not be the precise term anymore. However, from our observations it is likely that the low temperature peak in TPD is due to desorption from the sp^2-hybridized areas. Low coverage D adsorption STM experiments with high resolution, possibly at low temperatures, could elucidate the nature of the proposed dimers.

Alternative origins of the weakly bound D/Gr/Ir(111) peak

While STM measurements clearly show that the strongly bound peak is linked to the features in hcp and fcc sites of the moiré, a clear connection between the weakly bound peak and structures visible in STM is somewhat difficult. Three alternative sources for the 380 K peak seen in TPD spectra of atomic deuterium on graphene where proposed, namely that it could be due to (i) contributions from the sample holder, (ii) coadsorption, or (iii) intercalation of D. In the following, we will rule out these possibilities.

Firstly, it was considered that D or D_2 could be coming from the sample holder. Two equivalent experiments were performed; with the Feulner cup of the mass spectrometer in its normal position over the sample, and with it directly over the sample holder (8 mm to the side of its normal position). If deuterium were coming from the sample holder we would expect an increased signal at 380 K, but instead it is decreased. This can be seen in Figure 7.10. Thus we dismiss the sample holder as a possible source of the weakly bound deuterium.

Secondly, it was suggested that this peak could be due to co-adsorption - that the deuterium atoms stable binding is dependent on the presence of a foreign atom or molecule, perhaps in a similar fashion to the two atoms of a dimer existing in codependent equilibrium. Then, the desorption of this foreign species would cause the deuterium to desorb also. This was tested by performing TPD as normal but concurrently detecting levels of H_2, H_2O, D_2O, CO and CO_2 - all of which are known to exist in small quantities in the chamber or can appear as products of thermal cracking. This is shown in Figure 7.11. Nothing was detected in considerable quantity except for mass 2 u. It could represent either molecular hydrogen or be an artifact of molecular deuterium due to dissociation occurring on the filament of the

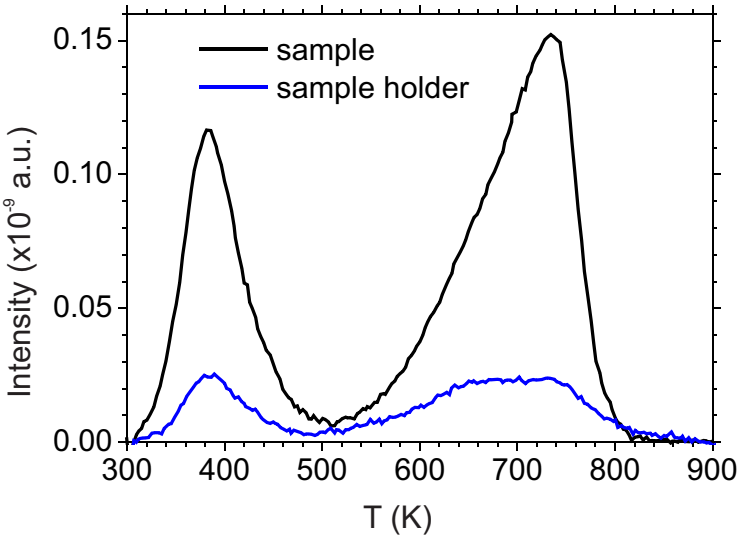

Figure 7.10: TPD spectra (mass 4 u) of 15 L D adsorbed on Gr/Ir at 300 K recorded with the Feulner cup over the sample as usual (black), and with the Feulner cup over the sample holder (blue). Heating rate 5 K/s. Adapted from [124].

mass spectrometer. It is known to dissociate 3% of collected H_2 [239], and we assume a similar factor for D_2-to-D. In Figure 7.11 the integrated intensity of mass 2 u particles detected is $\approx 6\%$ that of mass 4 u. We can attribute half of this to dissociated D_2. The other half could be due to molecular hydrogen. An approximate 3 : 100 ratio of H_2 to D_2 does not suggest strong interplay. Thus, we find it unlikely that co-adsorption is responsible for the weakly bound deuterium state.

Thirdly, it was suggested that intercalated D could be causing the low temperature peak in our TPD spectra, based on the observation that saturated D/Ir(111) still shows desorption around 400 K (see Figure 7.4). Intercalation can be envisioned to happen by two mechanisms, (i) via Gr edges or (ii) via tunneling through the Gr layer. We disregard intercalation via defects because at room temperature no diffusion of D on Gr/Ir(111) is observed in STM.

The red curve in Figure 7.12 shows 15 L D dosed on 0.5 ML Gr at room temperature, displaying the two peaks. If D were to intercalate via the edges, i.e., process (i), we would expect the low temperature peak to considerably drop when dosing atomic D on Gr with significantly less edges (that is, 1 ML Gr) [32]. However, the opposite is the case, the black curve in Figure 7.12 represents 15 L D dosed on 1 ML Gr at room temperature. The high temper-

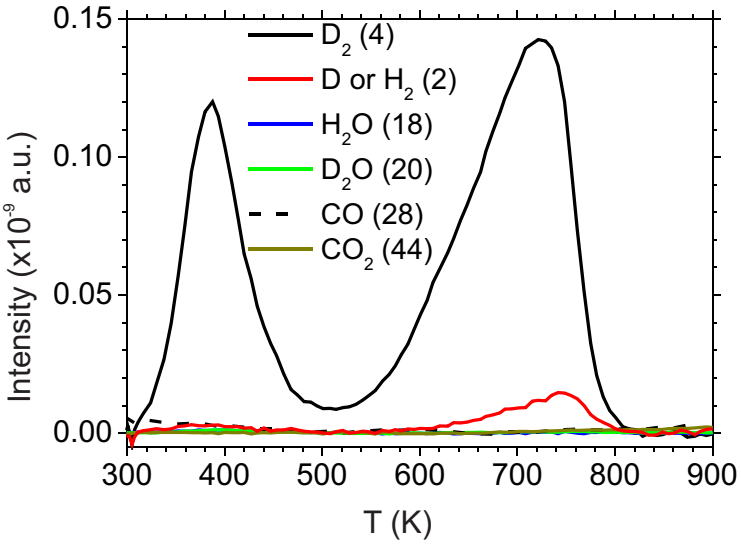

Figure 7.11: TPD of 15 L D adsorbed on Gr/Ir at 300 K. Simultaneously detecting for suspected co-adsorbates, the respective masses of which are given in parentheses, in u. Heating rate 5 K/s. Adapted from [124].

ature peak due to D-islands roughly doubles, as it should because we double the Gr coverage. The low temperature peak also increases in intensity. This lets us conclude that the peaks are in fact related to the Gr coverage. We observe that the ratio of the two peaks changes with Gr coverage, in the case of 0.5 ML Gr the lower peak appears roughly at the same height as the high temperature peak. We attribute this to desorption of D bound to the bare Ir surface, contributing to the low temperature peak in the 0.5 ML case but not in the 1 ML Gr case.

If the H or D were to tunnel through the Gr layer to become intercalated, i.e., process (ii), the intensity of the low temperature peak should differ significantly, as the tunneling probability depends exponentially on the square root of the mass ($\propto e^{-A\sqrt{m}}$). Comparing Figures 7.1 and 7.5, it is clear that the low temperature peak is present regardless whether H or D is dosed. We therefore rule out tunneling of D or H to play a significant role.

7.4 Intercalation and graphane: An alternative hypothesis

The group of Hasselbrink *et al.* [16, 17, 107] gives an interpretation of D adsorption on Gr/Ir(111) somewhat contrary to ours. They epitaxially grow Gr

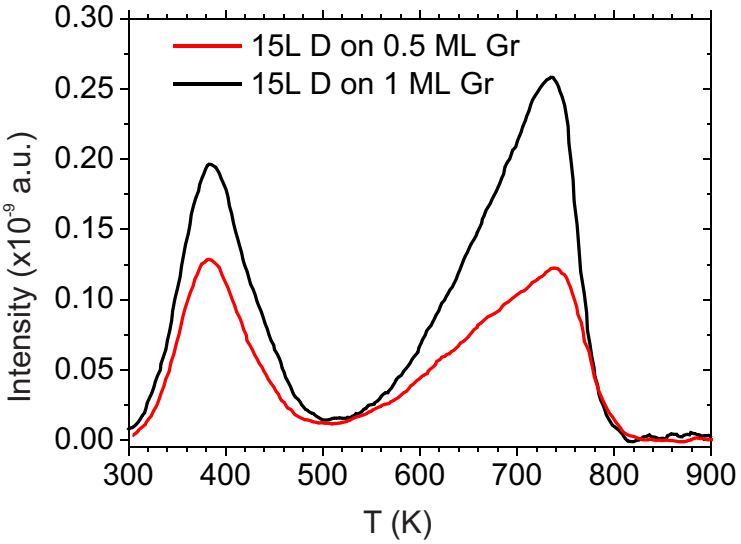

Figure 7.12: TPD spectra (mass 4 u) of 15 L D dosed on 1 ML Gr (black), 0.5 ML Gr (red). Heating rate 5 K/s.

flakes of average diameter > 100 nm which, based on LEED, are believed to "nearly completely" cover the Ir sample [17]. They dose molecular H_2 (or D_2) to intercalate the Gr, and then saturate with atomic D (or H), all at room temperature. This supposedly yields graphane, with H on the underside and D on the vacuum-side of Gr (or vice versa). This switching of isotopes is done to satisfy IR selection rules for SFG spectroscopy; having the same isotope on both sides of Gr would yield symmetric stretching modes, which are undetectable [16]. In SFG spectroscopy they observe three peaks, at 2563, 2716 and 2847 cm^{-1}, which they attribute to H *para* dimers, *ortho* dimers and graphane clusters respectively. Similarly for D they measure 1881, 2027 and 2130 cm^{-1}, respectively. These wavenumbers are compared to literature values for equivalent H-C stretching modes: for dimers they compare to dimers on HOPG [240], for clusters to H on the diamond C(111) surface [241]. The values are found to match closely.

Thus they agree D-dimers exist on Gr/Ir(111). They claim to have identified *para* and *ortho* dimers separately, which would make them the only ones to have done so concretely.

However, while we agree on dimers, their understanding of the strongly bound state is different. Instead of D-islands where Gr binds to Ir in hcp-areas, they instead claim to create graphane. A schematic illustrating these conflicting interpretations is seen in Figure 7.13. Their explanation for the sample maintaining the moiré periodicity is that H atoms mobile on the Ir

surface are most likely to 'jump up' and bind to Gr in hcp- or fcc-areas, because there the Ir and C atoms are closest [17].

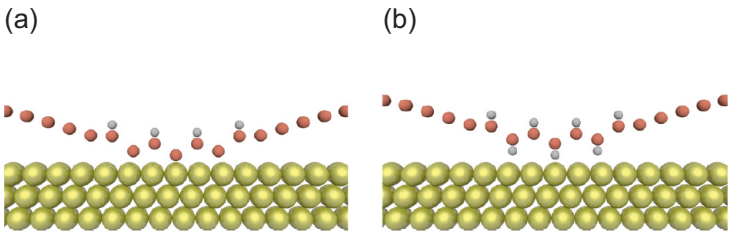

Figure 7.13: Schematics of H (gray) adsorbed on Gr (red) on Ir (yellow) in hcp or fcc areas, reprinted figure with permission from [18], ©2016 American Physical Society. (a) is the interpretation of the Hornekaer group [18] and our work. (b) of the Hasselbrink group [16,17]. Note that (b) is misleading because it suggests that the graphane is binding down to the substrate although this is not suggested in refs [16,17] nor would it be expected to do so.

Their results have recently been disputed by Kyhl *et al.* [18]. Performing HREELS, they attribute the first peak to dimers (without specifying configurations), the second peak to D-islands like ours, and the third to Gr defects. They cast aspersions on the quality of Gr grown by Hasselbrink *et al.*, as the green laser they used for SFG admittedly deteriorated the Gr [16]. We do not find any indications in support of Hasselbrink *et al.*, and rule out the formation of graphane under the experimental conditions used here.

7.5 Molecular and atomic deuterium on partial Gr layers

In the previous sections we have studied complete, 1 ML Gr films. It is also interesting to look at D dosed on partial Gr layers, i.e., 0.5 ML Gr grown by three TPG steps.

Molecular deuterium on partial Gr layers

The cracking efficiency of our cracker is only roughly 50%, so a certain amount of molecular D_2 will always be present when dosing atomic D. Thus, we first study the case of dosing molecular D_2 on 0.5 ML Gr. D_2 is only capable of weakly binding to Gr by physisorption [242], with a calculated lifetime in the order of picoseconds [243] in our temperature regime - D_2 impinging on the

Gr will quickly be desorbed again and lost to the vacuum. Indeed, recent XPS experiments show no adsorption of D_2 on Gr/Ir(111) at 140 K [32]. Thus we can imagine that half of the Ir is covered with a shield which D_2 will bounce off of.

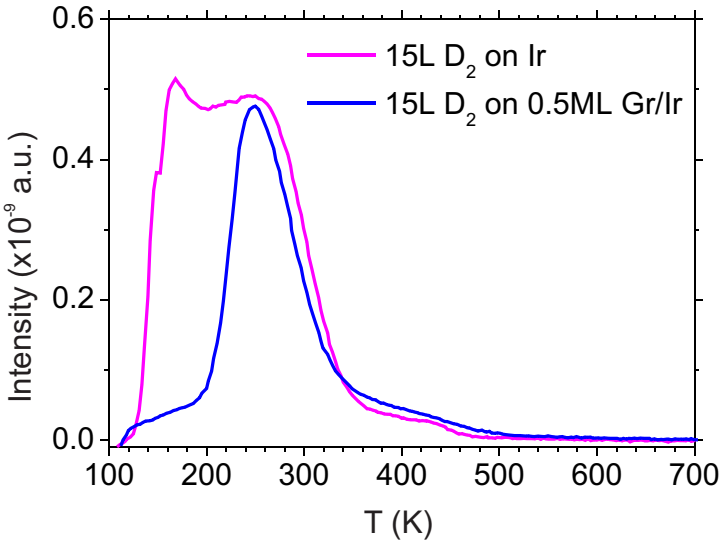

Figure 7.14: TPD spectra (mass 4 u) of 15 L D_2 dosed at 100 K on bare Ir (pink) and on 0.5 ML Gr/Ir (blue). Heating rate 5 K/s. Adapted from [124].

We dosed 15 L of D_2 onto a 0.5 ML Gr-covered sample and onto a bare Ir sample for comparison. The resulting TPD spectra are shown in Figure 7.14. The 15 L D on Ir spectrum has the saturated form, with both β_1- and β_2-peaks apparent. We see that the desorption from D_2 on 0.5 ML Gr/Ir resembles that of D_2 on Ir, but with the β_1-peak missing. Integrating the area under each curve, we find the half-ML sample to have ≈ 0.57 D_2 coverage compared to bare Ir. This is not surprising, as roughly half the dosed D_2 will have 'bounced off' of the Gr. However, if the available Ir surface area was simply halved, we would expect the spectra to have the same shape but with the half-ML intensities also simply halved. Instead, it resembles the (c) or (d) spectra in Figure 2.16 in which mostly β_2-sites are occupied. We offer a physical explanation for this, using the schematics in Figure 7.15 for illustrative purposes. Dosed D_2 adsorbs to bare Ir but not to Gr [Figure 7.15 (a,e)]. On Ir it dissociates and occupies all available sites until saturation or close thereto (b,f). It has been shown that H can intercalate Gr flakes on Ir at 100 K, but due to the activation energy required only a certain percentage of flakes will be intercalated at this temperature [32]. Thus we expect that while our sample sits at 100 K, some D adatoms will find their way under

the Gr (f). This will create space on the bare Ir for new D_2 during dosing, but the remaining D_2 dose might not be enough to fully populate the β_2 states, as evidenced in Figure 2.16. Once we begin the linear heating process of TPD, more D atoms can overcome the activation barrier and intercalate the flakes. Their mobility is not believed to be restricted once under the Gr [32], and thus they can find and occupy the preferred β_2-sites all over the sample (g). For temperatures up to $\approx 160\,\mathrm{K}$, adatoms occupying β_1-sites will desorb from the saturated bare Ir areas (c,d). If Gr is present, however, the rate of intercalation in this temperature range is higher than the desorption rate from the β_1-sites (g,h). This explains the vanishing β_1-peak in Figure 7.14. This line of reasoning is quite complicated, and so we wish to reiterate some of it for clarity. The shielding effect of the Gr half-ML reduced the effective D_2 dose by half. If the Ir surface area was also halved, the resultant desorption spectrum would simply be half as tall. Instead its shape suggests D intercalated the Gr to selectively occupy β_2-sites. If all intercalation occurred already at 100 K this would free up adsorption sites on the bare Ir, and a considerably higher relative coverage than 50% would be seen. Instead, our coverage of 57% suggests some intercalation occurs at 100 K but the majority is thermally activated, as shown in the literature [32].

Atomic deuterium on partial Gr layers

It is also instructive to dose atomic D on partial Gr layers. At 100 K, we dose 15 L of D on a 0.5 ML Gr-covered sample and on a bare Ir sample for comparison. Resulting TPD spectra are shown in Figure 7.16. Also shown are 15 L D_2 on 0.5 ML Gr and 15 L D on 1 ML Gr for reference. D on 0.5 ML/Gr (solid black) shows various features. There is broad desorption activity between $\approx 100\,\mathrm{K}$ and $\approx 500\,\mathrm{K}$, within which we identify three elements: (i) a large shoulder at $\approx 170\,\mathrm{K}$, (ii) a peak at $\approx 260\,\mathrm{K}$ and (iii) another distinct shoulder at $\approx 400\,\mathrm{K}$. Separately (iv) a clear desorption peak is seen also at $\approx 740\,\mathrm{K}$. These features are easily identifiable based on the desorption behaviors we have characterized already. The peak (iv) clearly corresponds to D-islands on Gr. The shoulder (iii) represents D-dimers on Gr, supplemented by the high-temperature shoulder from bare Ir. The largest signal, occurring between $\approx 100\,\mathrm{K}$ and $\approx 300\,\mathrm{K}$, also matches up with the desorption of D from Ir. The dominant element of this (ii) coincides with the aforementioned β_2-peak, also seen in the D_2 on 0.5 ML/Gr spectrum (blue). However, the β_1-peak is also contributing strongly. Thus D on 0.5 ML/Gr (solid black) can be seen approximately as a combination of the D_2 on 0.5 ML/Gr (blue) and D on 1 ML/Gr (dashed black), but with β_1 also present. What is the physical explanation for this?

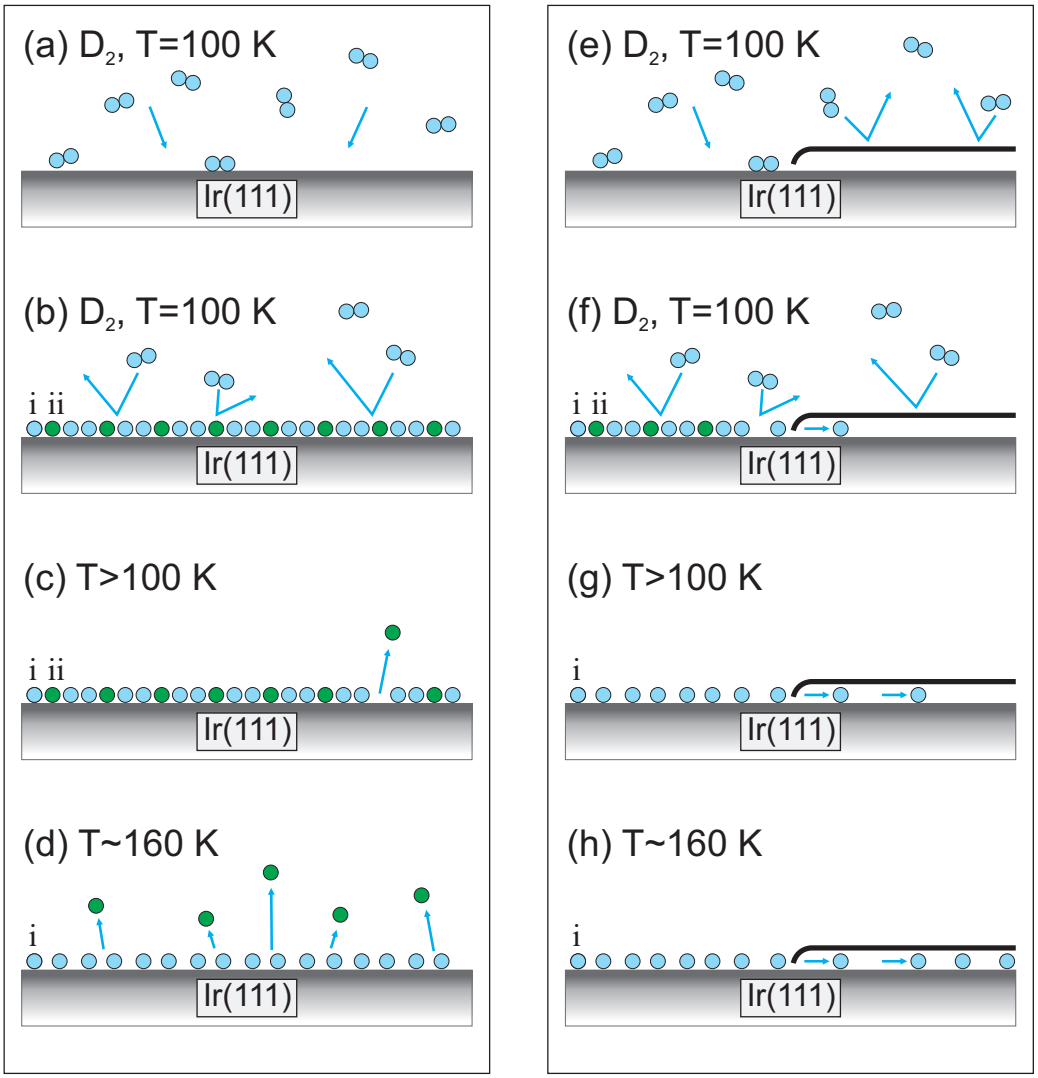

Figure 7.15: Simplified schematics (not to scale) of D_2 adsorption on (a-d) bare Ir and on (e-g) 0.5 ML Gr/Ir, as per the spectra in Figure 7.14. The Ir substrate is shown in gray, Gr in black, D atoms in the β_1 site (i) in blue and D atoms in the β_2 site (ii) in green. (a,e) represent the start of dosing; (b,f) represent saturation being reached during dosing; (c,g) represent the beginning of TPD heating; and (d,h) represent the situation at ≈ 160 K.

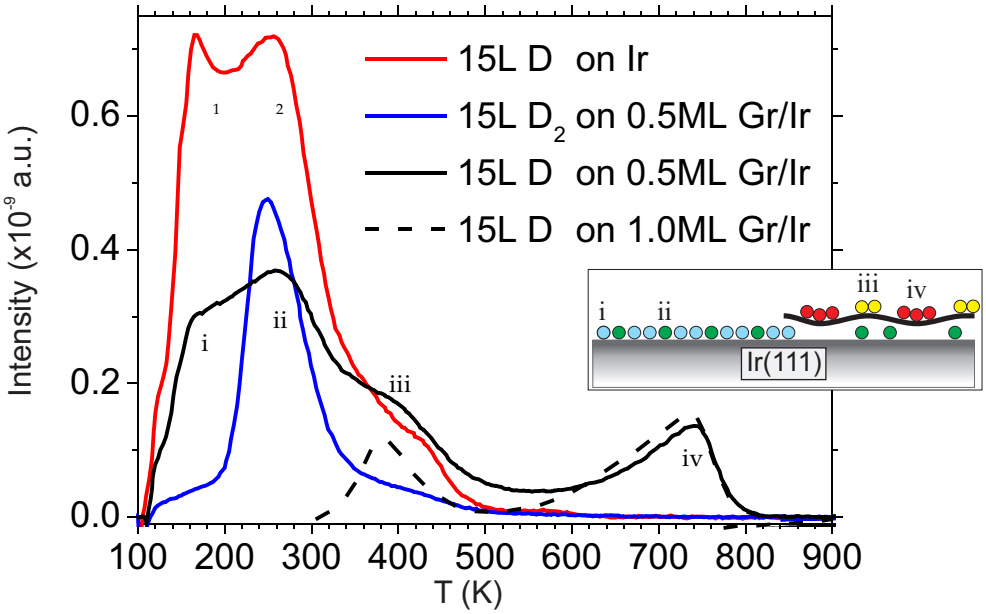

Figure 7.16: TPD spectra (mass 4 u) of 15 L D on Ir (red) and on 0.5 ML Gr/Ir (black). Shown for comparison are also 15 L D_2 on 0.5 ML GR/Ir (blue, from Figure 7.14) and 15 L D on 1 ML Gr/Ir (dashed black). The two adsorption states of D/Ir, β_1, β_2 are marked, as well as four features (i-iv) in the 15 L D on 0.5 ML Gr/Ir spectrum (see text). Heating rate 5 K/s. The inset shows schematically (not to scale) the four different adsorption sites marked (i-iv) and colored for clarity: (i, light blue) D atoms on Ir(111) in β_1-sites; (ii, green) D atoms on Ir(111) in β_2-sites; (iii, yellow) D-dimers on Gr; (iv, red) D-islands on Gr. Adapted from [124].

Half of the atomic D lands on Gr and - unlike D_2 - will bind, forming dimers and islands as usual. The other half of the D lands on exposed Ir and - based on Section 4.1 - we expect this to intercalate during heating. It appears that some of it does, based on the reduced intensity of the β_1-peak compared to the D/Ir case. However, though reduced, the β_1-peak is present, implying that not all D atoms could intercalate and find β_2-sites. This could be due to the pinning effect of D-islands restricting the general movement of intercalated D under the Gr. Additionally it may be due to β_2-sites in hcp-regions now being unavailable. A simplified schematic of this arrangement is provided in the inset of Figure 7.16, with the different adsorption states numbered according to the corresponding features in the desorption spectrum.

7.6 Deuteration of D-intercalated Gr: A graphane attempt

The works of the Hasselbrink group [16, 17, 244] prompted us to perform the following experiments with the goal of forming graphane: 0.5 ML Gr layers were intercalated by cooling down from elevated temperatures to 100 K in a D_2 or H_2 atmosphere. For TPD measurements, the sample was flash annealed and cooled down from 1000–400 K in a D_2 pressure of $1 \cdot 10^{-5}$ mbar ($\approx$ 1300 L), from 400–100 K the pressure was increased to $5 \cdot 10^{-5}$ mbar ($\approx$ 45000 L). For the XPS measurements, the sample was cooled down in a D_2 pressure of $1 \cdot 10^{-6}$ mbar. Between 125 and 100 K, the H_2 pressure was increased to $5 \cdot 10^{-6}$ mbar. Atomic H or D was then dosed with the sample temperature at 100 K to prevent deintercalation. The reason for the inconsistent pressures used during hydrogen intercalation is that with XPS the crucial intercalation step can be easily verified by a CLS of 0.18 eV of the C 1s peak [32], and repeated if found unsuccessful. Using the same parameters in Cologne (no XPS available), we could not reliably produce intercalated Gr. We tested this by evaporating Pt on the intercalated islands, using the absence of well-ordered cluster growth as an indicator for intercalation, and found that with the XPS parameters the majority of Gr flakes were not intercalated. Thus, the intercalation pressures were increased.

Figure 7.17 shows the TPD results. The red curve in Figure 7.17(a) serves as a reference experiment and shows the desorption behavior of D-intercalated 0.5 ML Gr. We observe the maximum desorption peak at $\approx$ 220 K, with three shoulders to lower temperatures ($\approx$ 140, 160, 189 K) and one shoulder to higher temperature. Desorption ceases around 350 K. Ad-

ditional dosing of 15 L atomic D on intercalated Gr flakes yields the blue desorption spectrum. Maximum desorption occurs at ≈ 189 K, a temperature that coincides with a shoulder in the purely intercalated sample. The shoulder to higher temperature is visibly reduced. While most of the D desorbs below 350 K as before, some desorption is visible at higher temperature at ≈ 390 K and ≈ 740 K, better visible in the zoom in Figure 7.17(b). Irrespective of the slight variation in peak shape, the striking finding is that in both cases the vast majority of D has desorbed below 350 K, and we conclude that we have not succeeded in forming a significant amount of graphane, as this should be much more stable than D adsorbed to Ir. The small peaks at higher temperature coincide with the peaks observed for deuterated unintercalated Gr/Ir(111) and thus can very well be explained by D adsorbing to some unintercalated Gr flakes that are always present [32].

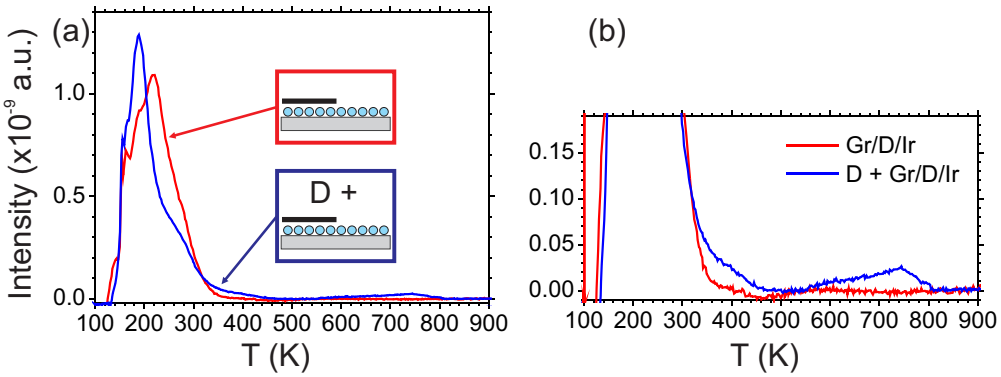

Figure 7.17: TPD spectra (mass 4 u) of (a) 0.5 ML Gr intercalated by deuterium (red) and D-intercalated 0.5 ML Gr exposed to 15 L atomic D at 100 K (blue). (b) is a zoom of (a) showing the small desorption features at higher temperatures. Heating rate 5 K/s.

Figure 7.18(a,b) show the C 1s and Ir $4f_{7/2}$ core levels, respectively, of the analog XPS experiments. The bottom spectra display pristine 0.5 ML Gr on Ir(111), with the C 1s peak situated at 284.1 eV, and the Ir $4f_{7/2}$ displaying two peaks, the contribution from the bulk at 60.8 eV and the contribution from surface atoms at 60.3 eV. Hydrogen was then intercalated by cooling down in a hydrogen atmosphere and the resulting spectra are shown in the middle in red. The C 1s peak is shifted to lower BE by 0.18 eV with respect to the pristine Gr peak (displayed as a dotted black line for comparison), indicating successful hydrogen intercalation. This is supported by the Ir $4f_{7/2}$ surface peak vanishing and a new component which is shifted by approximately 0.3 eV, in line with Ir surface atoms binding to H atoms [32].

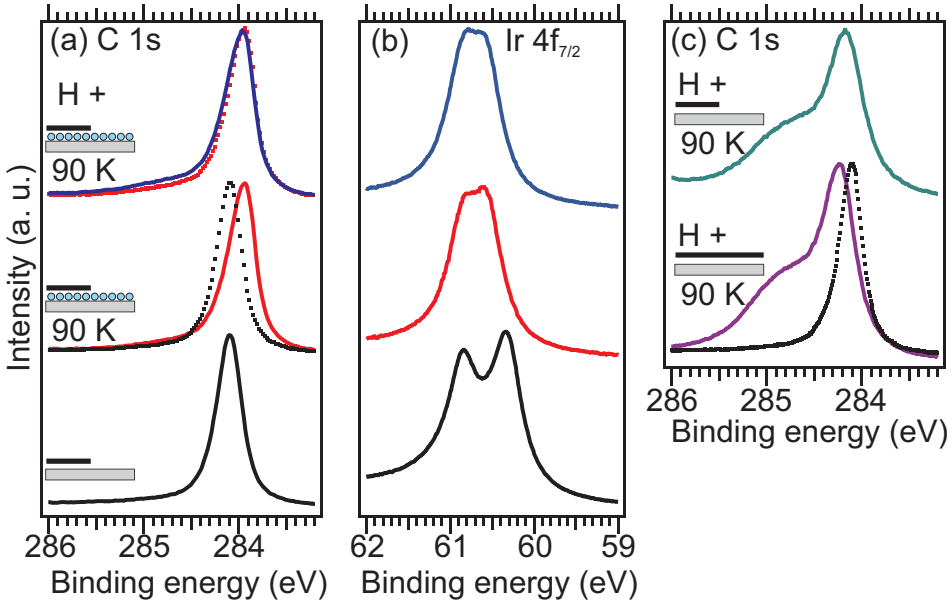

Figure 7.18: XP spectra of (a) the C 1s, and (b) the Ir $4f_{7/2}$ region, from bottom to top of pristine 0.5 ML Gr (black), 0.5 ML Gr intercalated by H_2 exposure (red), and atomic H dosed onto H-intercalated Gr (blue). Dotted spectra in (a) are for comparison. (c) Upper spectrum: 0.5 ML Gr exposed to atomic H at 90 K. In the lower part 1 ML Gr exposed to atomic H at 90 K (purple) and for comparison 1 ML pristine Gr (dotted black) are shown.

The top spectra (blue) show the situation after a saturation amount of atomic H was dosed. Compared to the intercalated case, displayed in dotted red, a very slight shift back to higher energies and the appearance of a weak high BE shoulder are the only differences visible. In the Ir $4f_{7/2}$ spectrum, a slight reduction of the Ir-H peak is visible.

For comparison, Figure 7.18(c) shows unintercalated 0.5 ML Gr/Ir(111) exposed to a somewhat lower amount of atomic H at 90 K (upper spectrum). Below, the spectra for pristine Gr, and for 1 ML Gr exposed to the same amount of atomic H at 90 K are shown. The shoulder to higher BE is not as pronounced as for the saturation case (Figure 2.20(b)), but the shape of the spectra is the same regardless of whether the Gr is completely or only partially covering the sample when exposed to atomic H. Note that the spectral shapes in Figure 7.18(a) and (c), however, are quite different.

The simplest explanation of the above observations is that we have not formed graphane, but that the blue curve in Figure 7.18(a) is simply H-intercalated Gr. The small high BE shoulder can be explained by hydrogenation of some pristine Gr/Ir flakes, and the slight shift to higher BE can be attributed to a small amount of deintercalation, possibly due to CO contamination from the cracker.

Water adsorption

We want to point out that in the above experiments there is also a significant amount of water present on the sample after D intercalation. Figure 7.19 shows the TPD of another D-intercalated 0.5 ML Gr sample, this time masses 18 u (H_2O) and 28 u (CO) were measured simultaneously. A large, sharp H_2O desorption peak is visible at 145 K. Additionally, a $(\sqrt{3} \times \sqrt{3})R30°$ superstructure was visible in LEED (not shown), into which water structures transform upon prolonged electron exposure [245, 246]. The water probably comes from the unbaked gas lines during the long D_2 exposure.

For completeness, we note that we observe the same desorption peak and $(\sqrt{3} \times \sqrt{3})R°30$ in LEED when we expose a clean Ir(111) surface to D_2 following the same procedure as for intercalation. This is shown in Figure 7.20. Compared to the saturation spectra measured before, e.g., in Figure 7.4, a large peak at ≈ 135 K is present that was not observed before. This atypical feature could be caused by the significant amount of water coadsorbed on the sample.

Some contamination upon H intercalation was also observed in the XPS experiments. Figure 7.21(a) shows the O 1s region normalized to the Ir $4p_{3/2}$ peak visible at 495 eV. A peak at approximately 530 eV is visible after intercalation and it grows in intensity after dosing atomic H. This could be due to

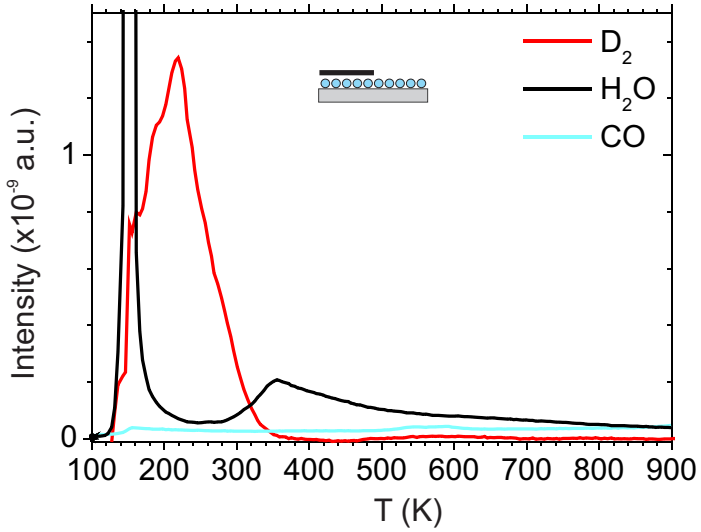

Figure 7.19: TPD spectra of D-intercalated Gr with masses 4 u (D_2, red), 18 u (H_2O, black), and 28 u (CO, light blue) recorded. Heating rate 5 K/s.

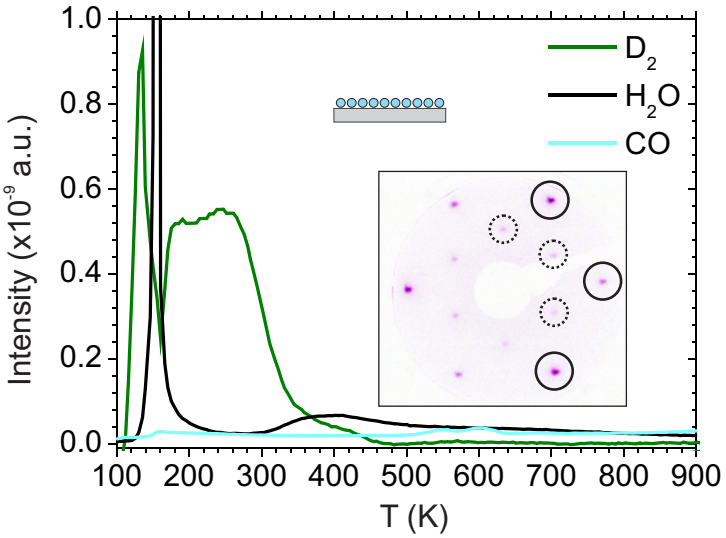

Figure 7.20: TPD spectra of clean Ir(111) cooled down in D_2 as detailed in the text. Masses 4 u (D_2, green), 18 u (H_2O, black), and 28 u (CO, light blue) were recorded. Heating rate 5 K/s. The inset shows a LEED image of the sample taken at 52.3 eV below 220 K, consisting of the Ir(111) spots (solid circles) and $(\sqrt{3} \times \sqrt{3})$R30° spots.

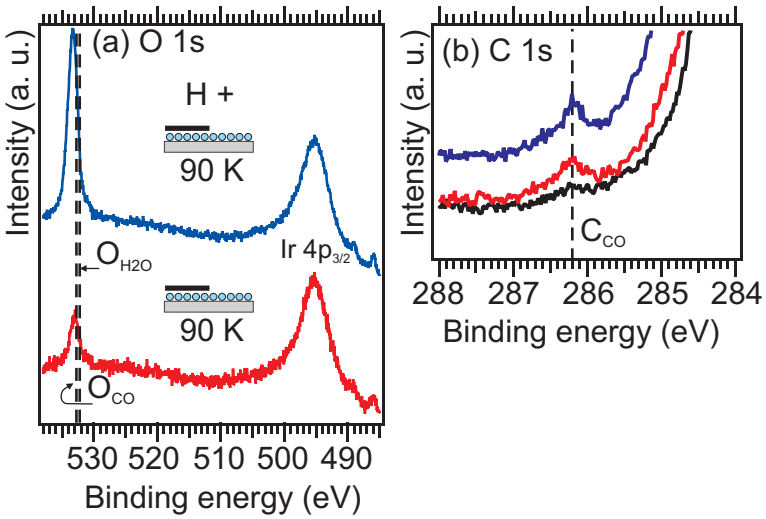

Figure 7.21: XP spectra of (a) the O 1s region of 0.5 ML Gr intercalated by hydrogen (red), and atomic H dosed onto H-intercalated Gr (blue). The O 1s spectra were normalized to the Ir $4p_{3/2}$ peak height. The left dashed lines indicate the O 1s peak positions of CO and H_2O adsorbed on Ir(111). (b) displays the corresponding C 1s region characteristic for CO adsorption. Red and blue spectra correspond to (a) [compare also to Figure 7.18(a)]. The black curve is of pristine 0.5 ML Gr. The dashed line indicates the C 1s peak position of CO adsorbed on Ir(111). The C 1s spectra were normalized to the peak height. All spectra were recorded at 90 K.

H_2O, CO or both, as the oxygen signals of those molecules are very close in energy, as indicated by the dashed lines. The small peak situated at 286.2 eV in the C 1s region, shown in Figure 7.21(b) characteristic for CO suggests that least part of the signal in (a) is due to CO on the sample. However, the large increase of the signal after atomic H exposure is not equaled by a similar increase in the C 1s CO peak, so we conclude this increase to be due to water. The large increase of the O 1s signal after atomic H exposure (instead already after intercalation) is attributed to different experimental conditions (lower H_2 intercalation pressure, but a higher H_2 background pressure during cracking due to a different cracker design).

Preventing water contamination

Turning back to our failed graphane attempt, one could argue that an ice film effectively inhibits D adsorption and thus graphane formation. We therefore repeated the XPS experiments but dosed the atomic H at slightly increased sample temperatures to reduce water contamination.

The results are displayed in Figure 7.22. The black and red spectra in the lowest and second-lowest row are, for reference, the same as in Figure 7.18, namely, pristine Gr in black, and H-intercalated Gr at 90 K in red.

Prior to dosing atomic H the temperature was increased to 145 K (green spectra, second row). Indeed, a reduction of the O 1s peak in Figure 7.22(c) is visible. Also after dosing atomic H, there is no increase in the O 1s signal (blue spectrum), while the C_{CO} component does not decrease much. Together with the TPD results, we conclude that we have significantly reduced the amount of water adsorbed. The remaining O 1s peak and the shoulder in C 1s is due to CO coming from the residual gas or the cracker. Thus, we can now examine the C 1s region in Figure 7.22(a) more closely for signs of graphane formation. We are confident that increasing the temperature to 145 K has only led to little deintercalation, indicated by the slight shift back to higher BE of the C 1s peak in the green spectrum, so that most of the Gr is still intercalated. Dosing atomic H (top-most spectrum, blue) shows another slight shift to higher BE and the sp^3-shoulder a bit more pronounced than before. Again, the simplest explanation is, no graphane has been formed, and the small differences between the green and the blue spectrum can be accounted for by deintercalation and hydrogenation of unintercalated Gr. We are thus confident that water is not accountable for blocking atomic D adsorption, and that it is not possible to form graphane from Gr/Ir(111) under these experimental conditions, if at all.

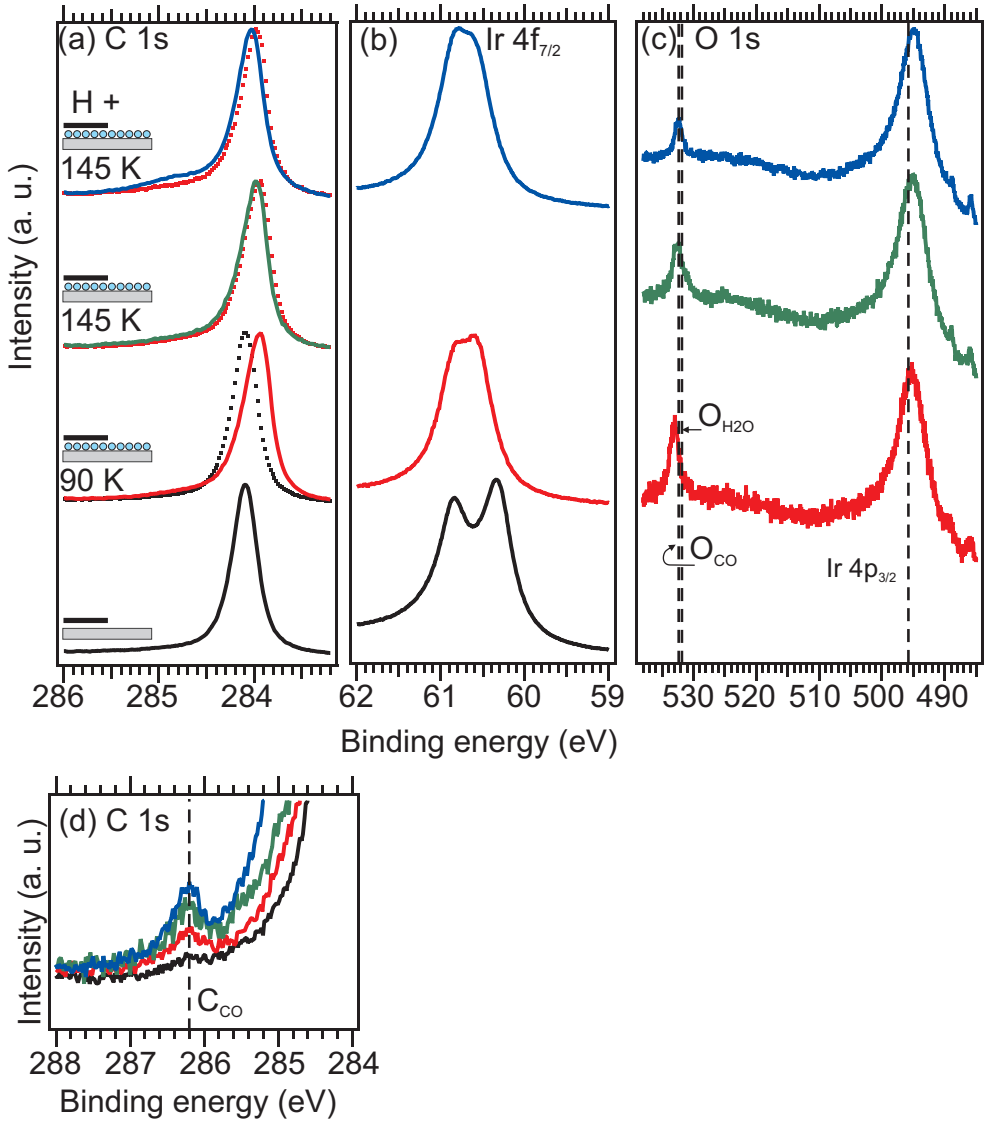

Figure 7.22: XP spectra of (a) the C 1s, (b) the Ir $4f_{7/2}$, and (c) the O 1s region, from bottom to top of 0.5 ML Gr (black), 0.5 ML Gr intercalated by hydrogen (red), the same sample heated to 145 K (green), and atomic H dosed onto H-intercalated Gr at 145 K (blue). Dotted spectra in (a) are replotted for comparison. (d) shows a zoom of the C 1s region, the dashed line indicates the C 1s peak position of CO adsorbed on Ir(111). The O 1s spectra were normalized to the Ir $4p_{3/2}$ peak (right dashed line). The left dashed lines in (c) indicate the O 1s peak positions of CO and H_2O adsorbed on Ir(111).

Intercalating deuterated Gr

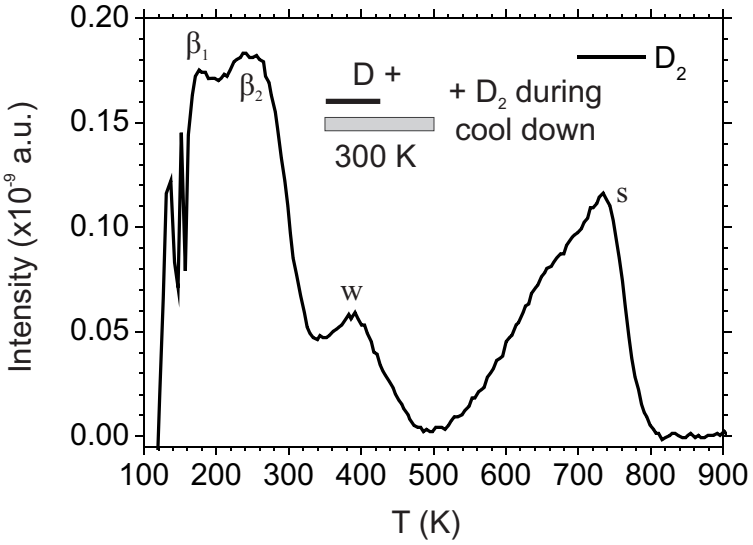

Figure 7.23: TPD spectra (mass 4 u) of 0.5 ML Gr exposed to 15 L atomic D at room temperature, and subsequently to 45000 L D_2 while ramping down the temperature (see text). β_1 and β_2 denote the desorption peaks of D on Ir(111), w and s the weakly and strongly bound peak of D on Gr/Ir(111), respectively. Heating rate 5 K/s.

The last section in this chapter deals with what happens if we *first* dose atomic D on the Gr, and then try to intercalate the deuterated sample. Similar experiments with Pt clusters binding to Gr show that the clusters become unstable when oxygen is intercalated [33]. Figure 7.23 shows the TPD spectrum of 0.5 ML Gr exposed to 15 L D at room temperature which was then cooled down in a deuterium atmosphere as using the same pressures as described before. We observe four peaks that we can identify based on Section 7.1. The β_1 and β_2 peaks are characteristic for D/Ir(111), the peaks (w,s) correspond to weakly and strongly bound D/Gr. From the peaks (w,s) it is apparent that the atomic D dosed in the first step is still in place.

7.7 Summary

We characterized D adsorption on and desorption from a complete layer Gr/Ir(111) with TPD and STM. Two distinct binding states are observed in TPD, at $\approx$ 380 K and $\approx$ 730 K. Calibration to an Ir(111) surface saturated with deuterium yields a D coverage on 1 ML Gr of $\approx (0.21 \pm 0.06)$ ML,

corresponding to $\approx 18.3 \pm 5.2$ atoms per moiré cell. TPD of H adsorbed to Gr/Ir(111) reveals an isotopic shift of $\approx 20\,\mathrm{K}$ and $\approx 25\,\mathrm{K}$ for the weakly and strongly bound peak, respectively. The stronger bound state is due to D atoms adsorbed in ring-like structures in the hcp and sometimes fcc site of the moiré unit cell, as STM measurements unambiguously show. Upon annealing, or dosing at elevated temperatures (450 K), also fcc sites become more and more occupied and the observed structures become more regular in STM, hinting that diffusion sets in somewhere below 450 K. We tentatively attribute the weaker bound state to adsorption of D, possibly in dimer configuration, in the sp^2-hybridized areas of the moiré cell. We have excluded coadsorption, contributions from the sample holder, and intercalated D as sources for the weakly bound state. Upon deuteration of 0.5 ML Gr at 100 K, we find evidence for some intercalation. Deuterated Gr is stable against intercalation of deuterium, and significantly less intercalation is possible if Gr is previously deuterated, which we attribute to the pinning of Gr to the Ir substrate via D adsorption. We show that it is not possible to form graphane by deuterating D- or H-intercalated Gr flakes, a process suggested by the group of Hasselbrink [16, 17]. In fact, we show that hydrogen intercalated Gr inhibits formation of hydrogen-Gr bonds that are stable above $\approx 300\,\mathrm{K}$. The different experimental conditions and the corresponding outcomes are summarized schematically in Figure 7.24.

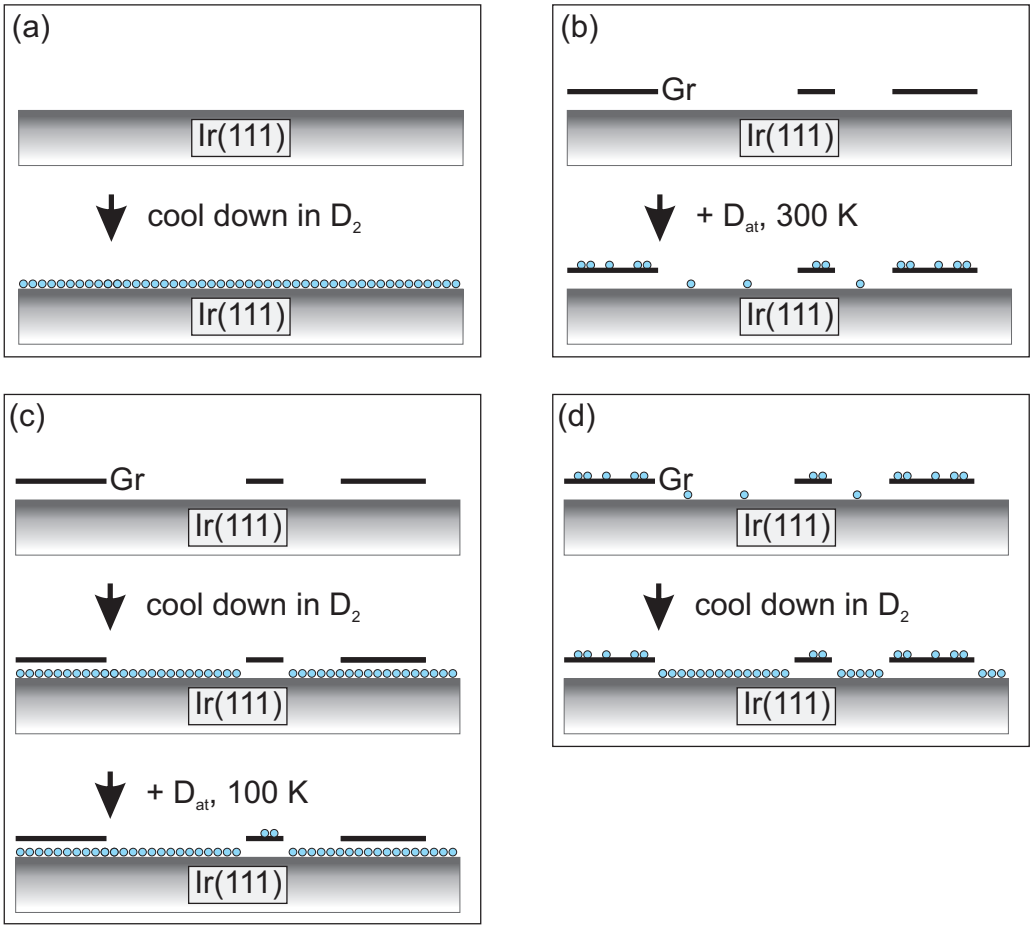

Figure 7.24: Schematic visualization of the interpretation of the experiments presented in this section. (a) clean Ir(111) cooled down in D_2 atmosphere, leading to dissociative adsorption of deuterium (blue circles). (b) Ir(111) partially covered by Gr, exposed to atomic D at 300 K, leading to deuterated Gr islands. (c) Ir(111) partially covered by Gr, cooled down in D_2 atmosphere, leading to intercalation of most Gr islands, subsequently exposed to atomic D at 100 K leading to deuteration of the few unintercalated Gr islands. (d) Ir(111) partially covered by deuterated Gr, cooled down in D_2 atmosphere, leading to dissociative adsorption of deuterium on the bare Ir(111) patches but no intercalation under the Gr.

Chapter 8

Gold-intercalated graphene and deuteration of Gr/Au/Ir

This chapter contains contributions from: C. Murray and T. Michely. I designed and carried out the experiments and analyses.

In this chapter, we wish to study the interaction of D with Gr/Au. Compared to Ir(111) as a substrate for Gr, as presented in the previous chapter, Au(111) interacts only very weakly with Gr. With this system, we can explore to what extent the substrate influences the adsorption of D. We first consider briefly the growth of Au on Ir(111), then turn to the Au-intercalation of Gr which has been successfully employed for Gr/Ni(111) [63,64], Gr/SiC [48,65] and underneath Gr nanoflakes on Ir(111) [67]. Then, we study the interaction of atomic D with Gr/Au/Ir(111).

8.1 Gold on Ir(111): Strain relief patterns

The growth of Au on Ir(111) has been studied with STM by Ogura *et al.* [247]. At 300 K deposition temperature and below 1 ML Au coverage, Au forms two-dimensional dendritic islands with their branches growing into three $\langle\overline{1}\overline{1}2\rangle$ directions rotated by 120° with respect to each other, reflecting the three-fold symmetry of the Ir(111) substrate. With increasing coverage, the first layer becomes more compact, with triangular indentations pointing to $\langle 11\overline{2}\rangle$ directions (rotated by 60° with respect to the $\langle\overline{1}\overline{1}2\rangle$ directions), remnant of the dendritic structure. Second layer islands have a compact triangular

shape. Third and higher layers show a partly hexagonal, partly irregular compact shape. Multilayer growth starts once the first layer is almost closed, due to the lower step-down diffusion barrier on the first Au layer, compared to higher layers [247].

This situation is depicted in the STM topograph of Figure 8.1(a) where approximately 1.44 ML Au were deposited onto Ir(111) at room temperature. Three Ir step edges, indicated by dashed lines, run from the top to the bottom of the image; a fourth is visible in the lower right corner of the image. Their path is better discernible in Figure 8.1(b), the differentiated STM image. The lowest level on each terrace appears flat with the exception of the triangular shaped indentations, two of which are marked by black arrows. Inside those triangles, bright protrusions are visible. This flat level is attributed to the first monolayer of Au, in line with the observations of Ogura *et al.* [247]. At the bottom of the triangular holes is thus the Ir(111) substrate. The clusters in the holes are attributed to Au nucleating on contaminants - the latter preferentially adsorbing to Ir instead of Au and thus being concentrated in the holes. A similar high contaminant concentration acting as nucleation sites for metal adsorbates was observed in Figure 6.5(b) for etch holes in a Gr layer.

The second layer of Au consists of partly coalesced islands, for most of which a triangular shape can still be discerned. Almost all Ir steps are, on their lower side, decorated by second layer islands. Third layer flakes, of a more compact and almost hexagonal form, visibly nucleate in the middle of all but the smallest second layer islands.

From the flat appearance of the first Au layer we can deduce that this layer grows pseudomorphic with the Ir substrate, as pointed out by e.g. Parschau *et al.* [79]. While the first Au layer appears flat, the second and third layers display a faint, wavy, trigonal pattern that is most clearly visible in the differentiated image in Figure 8.1(b). Similar pattern formation is known as a strain relief mechanism from metal-on-metal epitaxy for hexagonally close-packed metals, described in Section 2.5. For Au/Ir(111), to the best of our knowledge, these patterns have not been observed up to now, so in the following they will be explored in some detail.

Upon annealing the sample to 780 K, only two levels are observed on each terrace, as shown in the STM topograph of Figure 8.2(a,b), in which the height profile runs along the green line. Substrate step edges are indicated by dashed lines. The situation is visualized in the side-view schematics in Figure 8.2(c) along the green line. The lowest level, again corresponding to 1 ML Au, appears flat and without the triangular holes of before. The second layer Au forms compact islands attached to step edges. Islands attached to the upper side of a step edge are of an almost perfect hexagonal shape, while those on

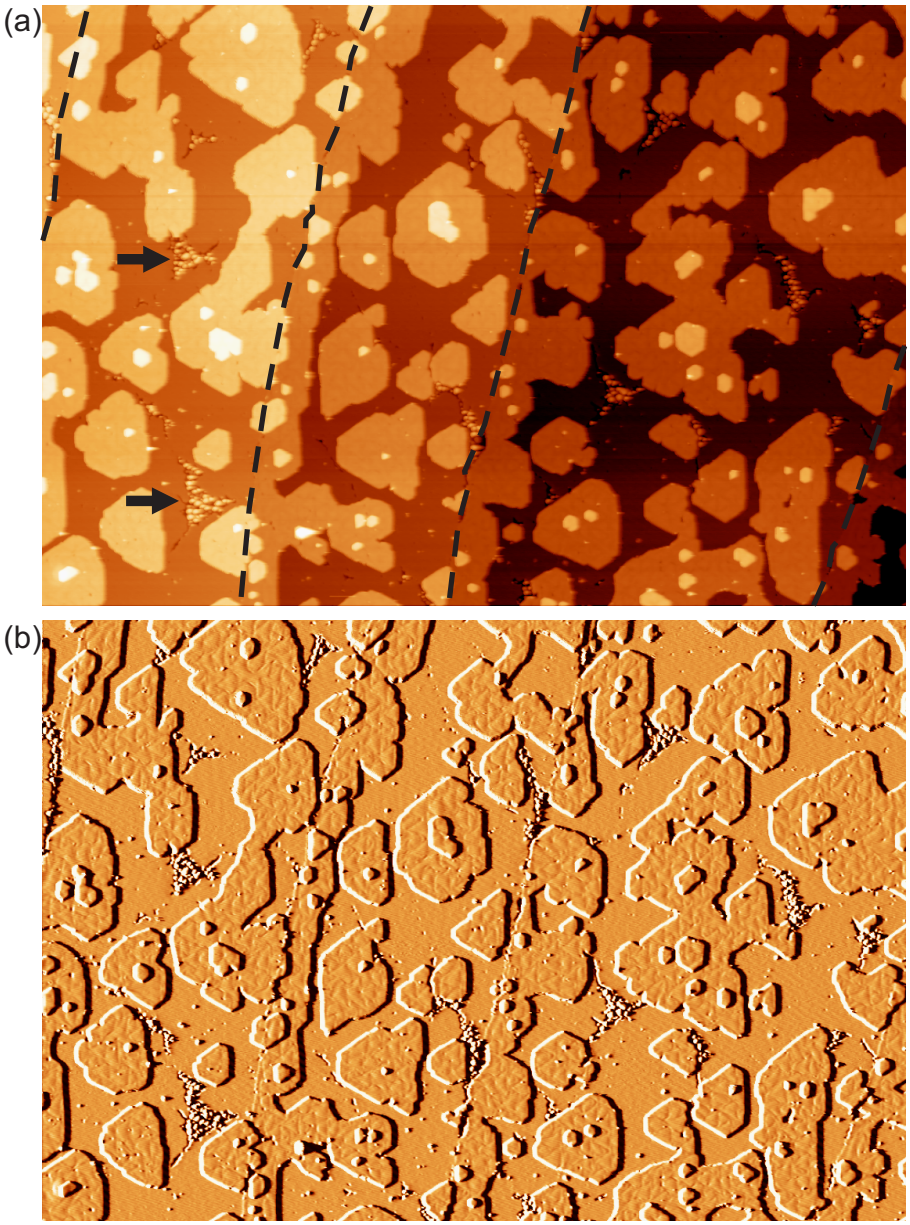

Figure 8.1: (a) STM topograph of approximately 1.44 ML Au deposited on Ir(111) at 300 K. Dashed black lines indicate Ir substrate step edges. Two triangular indentations are marked with black arrows. (b) is a differentiated version of (a). Image size 425 nm × 295 nm. Tunneling parameters $I = 0.19$ nA, $U = -1.3$ V.

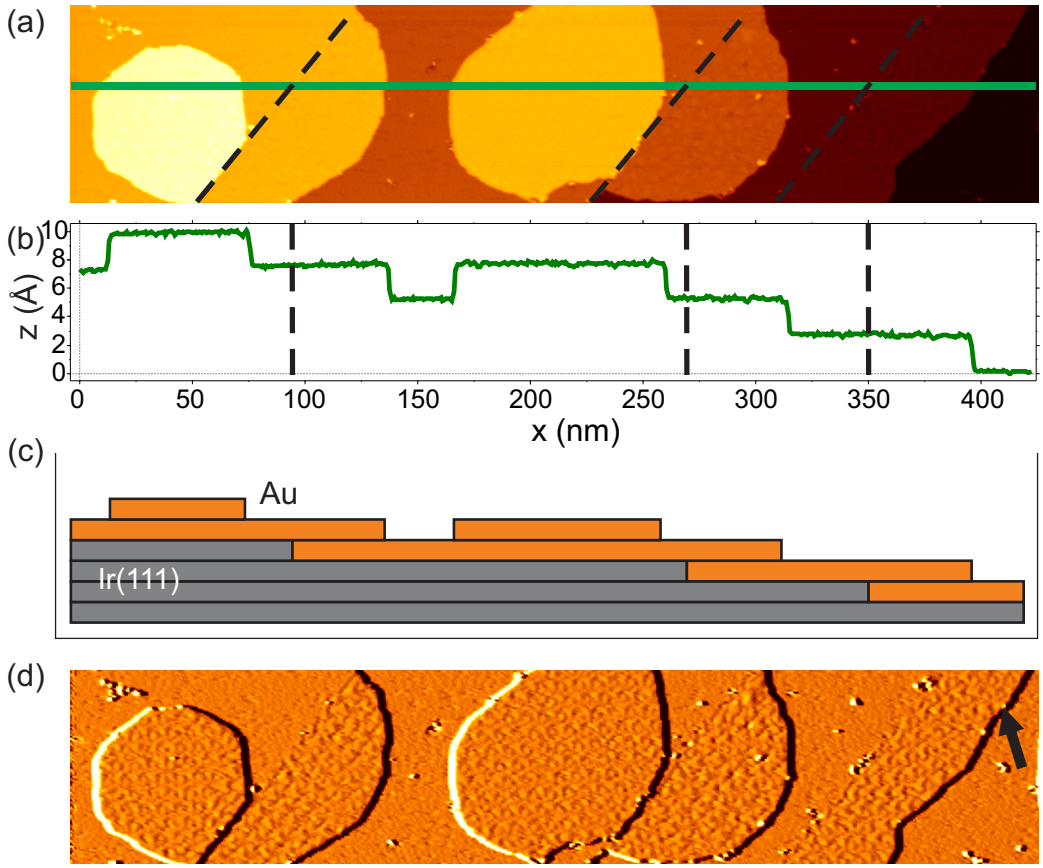

Figure 8.2: Approximately 1.44 ML Au deposited at 300 K on Ir(111) and subsequently annealed to 780 K. (a) STM topograph. Dashed black lines indicate Ir step edges. (b) Height profile along the green line in (a), dashed black lines indicate Ir step edges. (c) Schematic side-view of a cut along the green line, dark gray rectangles are Ir layers, orange rectangles are Au layers. (d) Differentiated image of (a). The black arrow indicates a region of hexagonal strain relief patterns on the lower side of a step edge (see text). Image size 425 nm × 86 nm. Tunneling parameters $I = 0.7$ nA, $U = -1.5$ V.

the lower terrace are elongated and wet the step edge, at the expense of a more compact shape. Interestingly, after annealing, the strain relief patterns become better defined, best seen in the differentiated STM image in Figure 8.2(d) such that a distinction can be made. On the compact islands, mostly a hexagonal arrangement of 'inverted donuts', i.e., protrusions surrounded by hexagonal or triangular depressions, can be seen with a lattice constant of approximately 8 nm. On the elongated islands, connected to ascending steps, mostly a trigonal-wavy patterns is observed, although in some regions it turns into the 'inverted donut' pattern [indicated by the black arrow in Figure 8.2(b)].

A compact shape of second layer Au islands appears reasonable, in order to minimize the number of under-coordinated edge atoms as well as the strain due to the difference in lattice constants between Au and Ir. Au islands wet ascending steps because this also allows to reduce the amount of edge atoms. The higher residual strain present in the more elongated islands attached to ascending steps might explain the trigonal, wavy shaped strain relief patterns, in contrast to the inverted donuts on compact islands.

Up to now, we established that both before and after annealing to 780 K 1 ML Au appears flat, the second layer displays a trigonal or hexagonal strain relief pattern and also the third layer, at least at low third layer coverage, still shows a similar pattern. In the following, we will refer to Au exhibiting the trigonal or hexagonal strain relief patterns as 'few-layered Au', in contrast to 'many-layered Au' displaying the typical herringbone reconstruction.

8.2 Gold intercalation and the role of Gr's morphology

Intercalation attempt of 1 ML Gr

For TPD studies, homogeneous samples are preferred so as not to have signals from different sample morphologies. A completely closed Gr film, intercalated homogeneously by a certain number of Au layers is desirable. However, this proved to be rather difficult. We were not successful in intercalating a complete Gr layer. As Gr flakes can easily be intercalated [67], it can be assumed that Au intercalates at the edges of Gr flakes. Thus, we turned to intercalating partial Gr layers.

Intercalation of TPG-Gr

In a first step, we used 0.5 ML Gr grown by three TPG cycles ($T_{\mathrm{TPG}} = 1450\,\mathrm{K}$), in the following referred to as TPG-Gr. Growing Gr by TPG cycles (as opposed to using TPG + CVD) is an easy way to control the Gr coverage with relative precision [26], ensuring that there is still bare Ir and hence Gr edges present, enabling intercalation.

Intercalation was carried out at 780 K. This temperature is known to produce compact Au islands (Figure 8.2) when the sample is annealed after room temperature deposition of Au, and thus we expect step-flow or layer-by-layer growth [30], in contrast to room temperature Au growth. Note that for intercalation of small Gr flakes on Ir(111), also room temperature Au deposition and subsequent annealing give good results for many-layered Au intercalation [67].

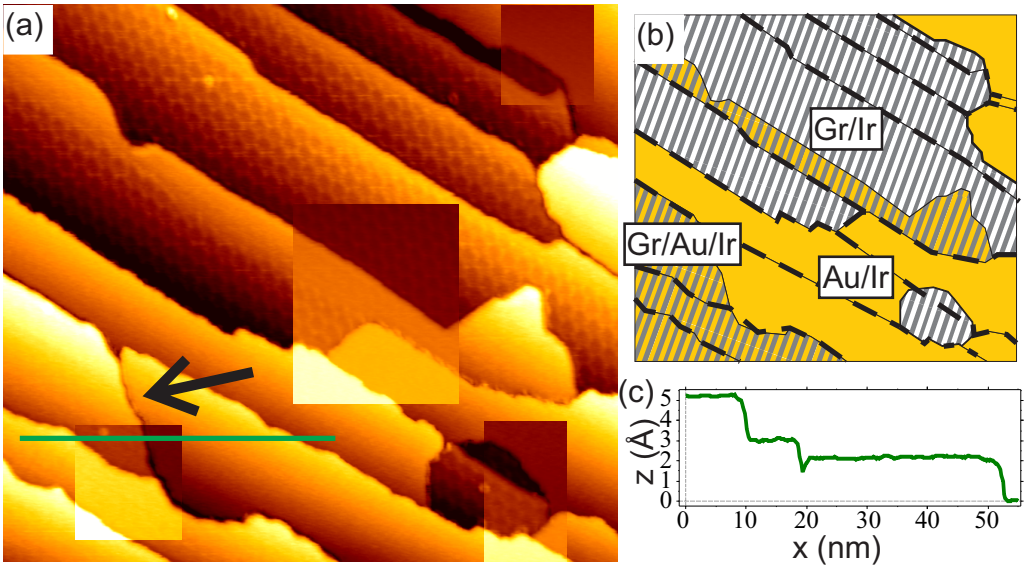

Figure 8.3: (a) STM topograph of 1.2 ML Au deposited onto 0.5 ML TPG-Gr/Ir(111) at 780 K. The black arrow indicates a border between Au on Ir and Au-intercalated Gr. In some areas, a local plane was subtracted and the contrast was adjusted for better visibility of height levels. (b) Schematics indicating 1 ML Au on Ir(111) (orange), Gr/Ir(111) (black and white stripes), and Gr on 1 ML Au (black and orange stripes). (c) Height profile along the green line in (a). Image size 110 nm × 100 nm. Tunneling parameters $I = 3\,\mathrm{A}$, $U = -1.54\,\mathrm{V}$.

Figure 8.3(a) shows a representative STM image of 1.2 ML Au deposited on TPG-Gr at 780 K. Several Ir step edges run across the image diagonally,

they are indicated by dashed lines in the schematic in Figure 8.3(b). In four rectangular areas, a local plane was subtracted and the contrast was adjusted, so as to clarify the different height levels in those areas. The surface consists of flat areas and areas displaying a moiré of roughly 2.5 nm lattice constant. As established in Section 8.1, the flat areas are attributed to 1 ML Au on Ir. The moiré areas, clearly, are covered by Gr.

In the lower right corner of Figure 8.3(a) a small Gr flake, displaying a moiré, grows over an Ir step. The surrounding 1 ML Au/Ir area is approximately 1.4 Å higher. This leads to the following interpretation: the Gr flake itself is not intercalated by Au, but surrounded by 1 ML Au/Ir.

In the upper part of the image, a large Gr flake grows over several terraces. A moiré superstructure is visible in most parts, except for stripes parallel to step edges on the lower terraces that display no corrugation and appear approximately 2.3 Å higher than the moiré. We attribute these areas to Gr intercalated by a single Au layer.

In the lower left corner, a trench is visible, indicated by a black arrow. As shown in the profile taken along the green line, displayed in Figure 8.3(c), the area to the left of the trench appears approximately 0.9 Å higher than that to the right. This height difference is too small to be an Ir or Au step edge (both of which appear approximately 2.2 Å high). We therefore attribute the region to the left and below the trench to a Gr flake intercalated by 1 ML of Au. The trench indicates that the edge of the Gr flakes still binds down to the Ir substrate.

It is noteworthy that the amount of Au we actually observe on the sample is less than the deposited 1.2 ML according to our calibration. Regions of 1 ML Au/Ir, unintercalated Gr/Ir, and Gr/1 ML Au/Ir are almost exclusively present. Very rarely do we observe small patches of second layer Au growth (not shown), identifiable by the trigonal strain relief pattern. Thus, we conclude that the Au, at least partly, re-evaporates from the Gr at 780 K. Re-evaporation from Au or Ir is excluded, for the following reason: The vapor pressure of Au at 780 K is below $1 \cdot 10^{-11}$ mbar [248] and, as indicated by the wetting behavior of the first Au layer on Ir, Au adheres more strongly to Ir than to itself. In the following, the coverages given for Au intercalation are based on the calibration on clean Ir(111), i.e., they do not represent the true Au coverage.

Some Gr flakes are only partly intercalated. This can be understood because delaminating the Gr makes intercalation less favorable than adsorption on bare Ir. However, intercalation, and thus covering more Ir, is apparently more favorable than second layer formation. The intercalated Au prefers to adsorb to ascending step edges, as was already observed for growth of Au on Ir without the presence of Gr (Section 8.1).

Gr/Ir displays a clear moiré, whereas Gr/1 ML Au/Ir does not. Although the first Au layer grows pseudomorphic and thus possesses the same lattice constant as Ir, decisive here is the much weakened interaction between Gr and Au [67, 249]. We will see later on, that sometimes it is possible to image a weak moiré on Gr intercalated by two or more Au layers.

To achieve complete intercalation, the amount of Au deposited onto 0.5 ML TPG-Gr was increased to 3.7 ML, again with the sample at 780 K. The resulting sample is shown in Figure 8.4. The differentiated STM image in Figure 8.4(a) shows three different patterns: flat areas, areas with trigonal patterns, and three distinct flakes with a pronounced moiré. The assignment of the observed areas is summarized in the schematic of Figure 8.4(b), and is rationalized in the following. Analog to what was observed for Au grown on Ir without Gr, flat areas again are attributed to 1 ML Au (yellow), and trigonal-patterned areas to 2 ML Au on Ir (orange) that may or may not be covered by Gr. In the middle of the image three Gr flakes with a pronounced moiré are visible (white circles). They are attributed to non-intercalated Gr/Ir. The apparent height difference between 1 ML Au/Ir and Gr/Ir measured in this image amounts to only 0.4 Å, less than the 1.4 Å measured in Figure 8.3. A flat flake, elevated by 1.9 Å, is visible in the middle of the image (yellow triangle). Due to the typical hexagonal shape, a small wrinkle at the edge of the flake (indicated by the white arrow), and its elevation, this flake is attributed to Gr intercalated by 1 ML Au. This height difference is 1 Å more than that measured in Figure 8.3. Note that the height difference between Gr/Ir and Gr/Au/Ir amounts again to approximately 2.2 Å, as before. We thus attribute the different apparent heights of the Gr with respect to Au to tip effects. Also for Gr on Ir the Gr apparent height may vary depending on the tip.

There is a sharp transition visible between the flat Gr/Au/Ir area (yellow triangle) and the trigonal pattern marked by a black circle. Both appear at the same height and there is no trench separating the two regions. As the trigonal pattern is typical for 2 ML Au/Ir, we conclude that there is an Ir step edge situated at the sharp transition, and on the lower terrace a second Au layer is present that is also covered by Gr. The Gr flake extends also over the next Ir step edge, where a wrinkle is visible (black arrow).

Another Gr flake showing almost no corrugation is visible at the left border of the image, marked by a blue square. It is attributed to Gr intercalated by 1 ML Au, but lies one Ir step edge below the extended 1 ML Au/Ir resulting in an apparent height difference of 0.2 Å. The height difference to the other Gr/1 ML Au/Ir flake (yellow triangle) is 2.2 Å, in line with the presence of a step edge. The blue-square Gr/Au/Ir flake is separated by a distinct trench from the adjacent trigonally patterned area marked by a gray cross.

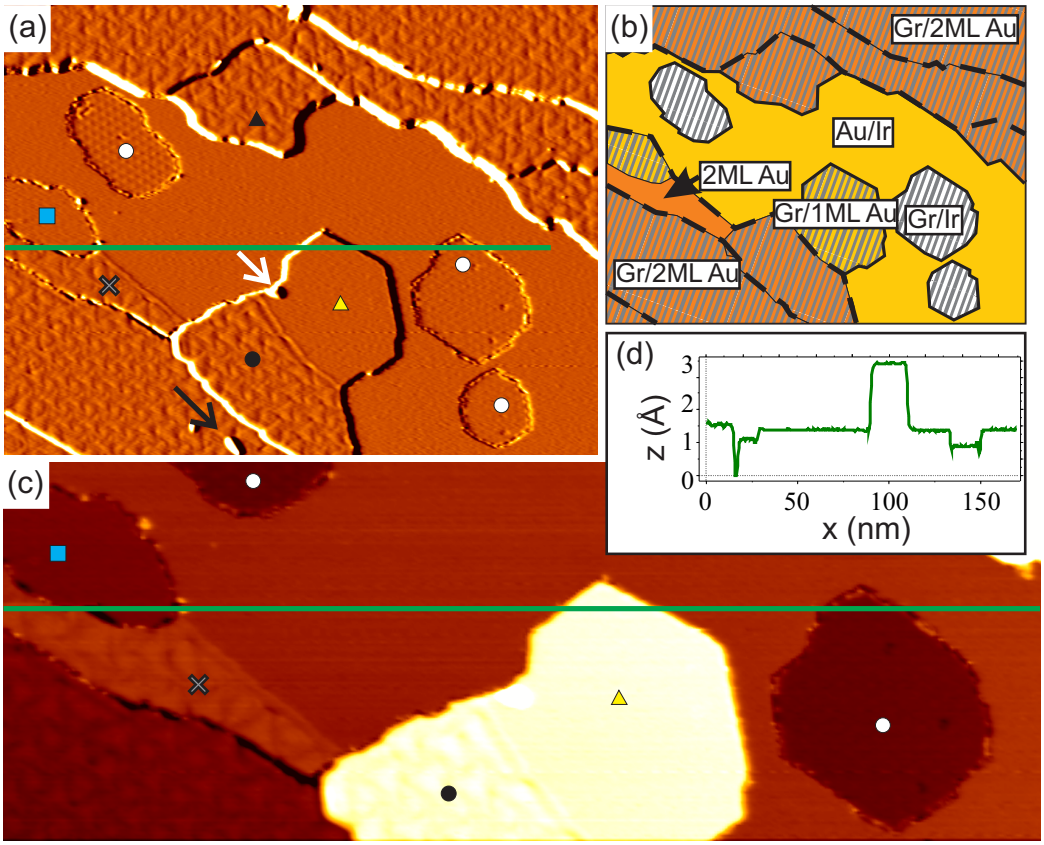

Figure 8.4: (a) Differentiated STM topograph of 3.7 ML Au deposited onto 0.5 ML Gr/Ir(111) at 780 K. The arrows point to wrinkles, the colored symbols are used to identify regions described in the text. (b) Schematic of (a) indicating 1 ML Au/Ir (yellow), 2 ML Au/Ir (orange), Gr/Ir(111) (black and white stripes), Gr on 1 ML Au/Ir (black and yellow stripes), and Gr on 2 ML Au/Ir (black and orange stripes). Ir step edges are indicated by dashed lines. (c) Non-differentiated zoom of the region around the green line in (a). (d) Height profile and schematic profile (not to scale) along the green line in (a, c). Image size (a) 184 nm × 139 nm; (c) 170 nm × 62 nm. Tunneling parameters $I = 3\,\mathrm{nA}$, $U = -1.88\,\mathrm{V}$.

The height difference between the two is 0.3 Å, similar to the unintercalated Gr flakes embedded in 1 ML Au (white circles).

The upper half of Figure 8.4(a) is dominated by the trigonal patterns. Two step edges are visible. The area marked by a black triangle is 3.9 Å high compared to the flat 1 ML Au/Ir; we attribute it to Gr/2 ML Au/Ir.

To summarize our observations from the 3.7 ML Au deposited on 0.5 ML TPG-Gr at 780 K, we see that the intercalation path is similar to the growth mode of Au without Gr. That is, Au preferably adsorbs at the downside of step edges, and starts growing from there. At 780 K, Au growth is layer-by-layer. This explains why the part of the Gr flake marked by a yellow triangle in Figure 8.4 is intercalated only by a single Au layer whereas the rest of the flake (black circle), situated below a substrate step edge, is already intercalated by 2 ML Au.

Furthermore, the border of second layer Au islands coincides with Gr flake edges, as visible in the upper half of Figure 8.4(a) (black triangle).

Small Gr flakes resist intercalation even at this higher Au exposure. This is more evident in Figure 8.5(a), where two compact Gr/Ir flakes embedded in 2 ML Au are visible, appearing at the lowest height level. A profile along the green line and a schematic side-view is displayed in Figure 8.5(b). The differentiated STM image in Figure 8.5(c) of the same two flakes reveals a moiré superstructure on the flakes and on the two higher levels on the left side as well, indicating that Gr is present there. The moiré periodicity on the low flakes is ≈ 2.5 nm, that of the left side ≈ 2 nm. The two compact flakes are thus Gr/Ir and the apparent height difference of 3.2 Å indicates that the surroundings must be 2 ML Au/Ir. The lower level of the left Gr flake is rougly 1.5 Å higher than the 2 ML Au/Ir. The higher level is due to an Ir step edge running along the dashed line in Figure 8.5(a) with an apparent height of 2.2 Å. The appearance of a moiré on Au-intercalated Gr depends on the specific tip and/or the tunneling parameters. Figure 8.5(d) is the differentiated version of Figure 8.5(a) and was taken with different tunneling parameters and possibly after a tip change. Now, only on the embedded Gr/Ir flakes a clear moiré is visible. Opposed to that, a trigonal strain relief pattern is visible on all areas with 2 ML Au present. The pattern is visible more clearly in Figure 8.6, of which Figure 8.5 is a detail (indicated by a black square).

The trigonal strain relief pattern typically is best visible on large terraces, but often appears distorted near step edges or Gr flakes, probably due to more strain present in those areas. This is well-evidenced in the large scale differentiated STM image of Figure 8.6. Also to be seen in this image are two regions where a third layer of Au grows, enclosed by the two dashed blue rectangles. The third layer can be recognized by a somewhat changed

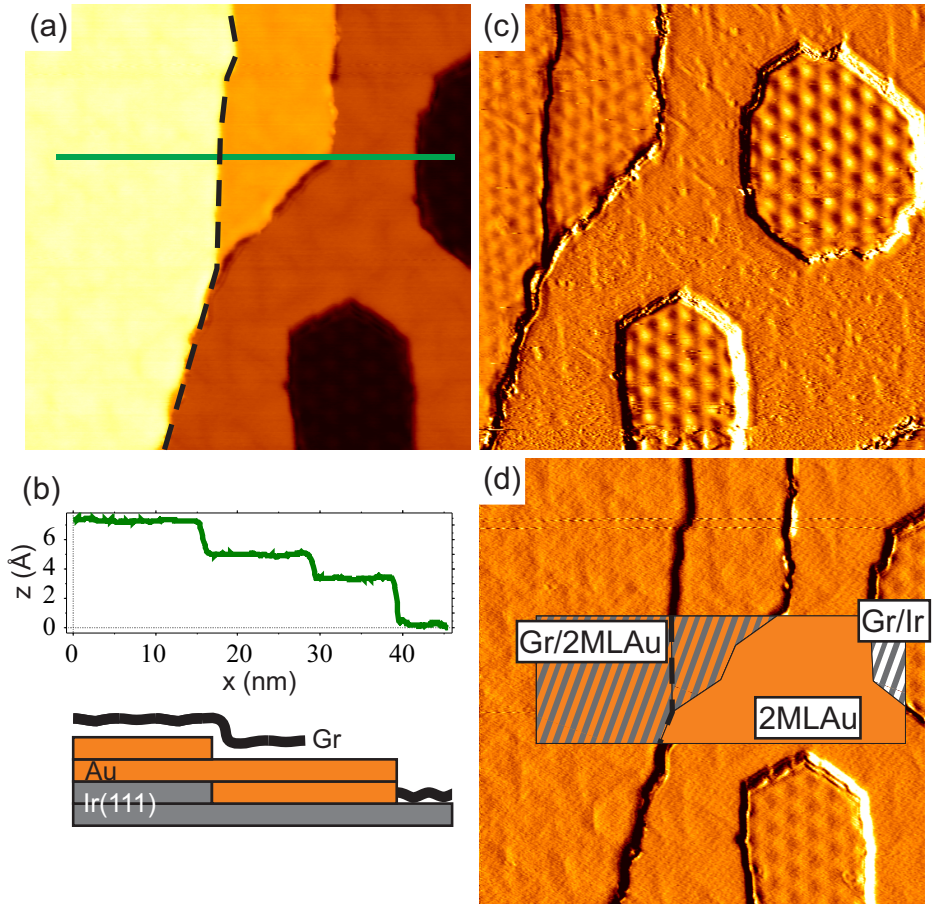

Figure 8.5: (a) STM image of TPG-Gr exposed to 3.7 ML Au at 780 K. The dashed line indicates an Ir step edge. (b) Height profile and schematic side-view along the green line in (a), dark gray rectangles are Ir layers, orange rectangles are Au layers, black lines are Gr. (c,d) Differentiated STM images of the same region as in (a). In (d), the inset shows the sample morphology with 2 ML Au/Ir in orange, Gr/Ir in gray-and-white stripes, and Gr/2 ML Au/Ir in gray-and-orange stripes. Image size 53 nm × 53 nm. Tunneling parameters (a,d) $I = 5.1\,\mathrm{nA}$, $U = -1.21\,\mathrm{V}$; (c) $I = 6.4\,\mathrm{nA}$, $U = 0.56\,\mathrm{V}$.

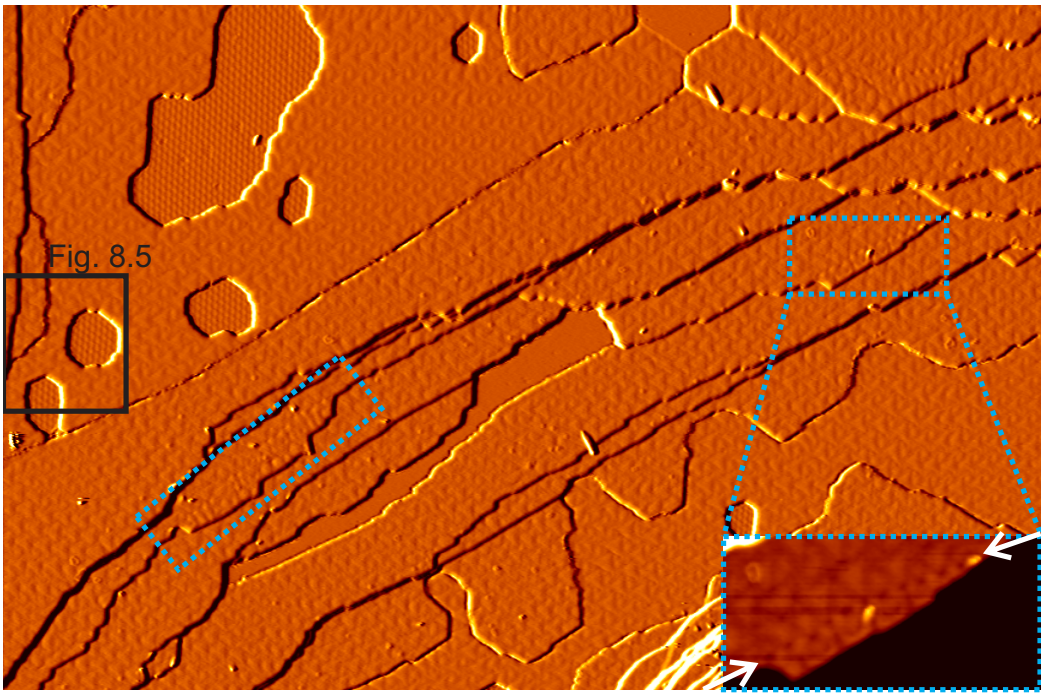

Figure 8.6: Differentiated STM overview of TPG-Gr with 3.7 ML Au deposited at 780 K. The black square indicates the region shown in Figure 8.5. The dotted blue rectangles mark regions where a third ML Au grows; one is shown undifferentiated and enlarged in the inset. The white arrows indicate the separation line between second (top) and 3rd (bottom) layer growth. Image size 425 nm × 280 nm, inset 67 nm × 32 nm. Tunneling parameters $I = 1.4\,\mathrm{nA}$, $U = -1.18\,\mathrm{V}$.

strain relief pattern, always appears downwards from step edges, and shows a periodically modulated separation line towards the 2 ML Au one Ir step higher. This separation line can be seen between the two white arrows in the inset of Figure 8.6. Third layer growth was only observed in regions with high step density. This can be explained by a Ehrlich-Schwoebel barrier [250, 251], making it more difficult for Au atoms to diffuse up or down step edges.

Several small and one rather large Gr flake are situated on a terrace in Figure 8.6 and do not cross a step edge. They are not intercalated. In fact, we never observed a flake not connected to or crossing a step edge to be Au-intercalated. We conjecture that it is not purely the small total edge length that makes intercalation more difficult, but that flakes crossing a step provide an easy entry point for Au atoms. A similar behavior was observed for O intercalation - for lower intercalation temperatures the first intercalated areas appear always at the downside of steps over which a Gr flake grows [33, 55]. Also for H intercalation we observed that small flakes resist intercalation and flakes crossing step edges are more likely to be intercalated, and speculated that the Gr edge crossing a step provides an easy entry point for H atoms [32].

Intercalation of CVD-Gr

The aforementioned difficulty of intercalating small flakes and flakes not crossing steps led to the approach to grow partial Gr flakes only by the CVD method. As shown by Coraux *et al.* [130], Gr grown by CVD leads to fewer flakes, exclusively nucleating at step edges, and frequently spanning both sides of a step edge, which is exactly what we require for Au intercalation. Gr flakes were grown by CVD ($t = 160\,\mathrm{s}$, $p_{\mathrm{CVD}} = 5 \cdot 10^{-10}\,\mathrm{mbar}$, $T_{\mathrm{CVD}} = 1120\,\mathrm{K}$, following the recipe of ref. [130]), in the following referred to as CVD-Gr. To test that the Gr film still exhibits some bare Ir on which the Au can adsorb, and subsequently intercalate, we exposed the sample to CO after Gr growth, and measured with TPD how much CO desorbs. This is shown in Figure 8.7. First, 10 L CO was dosed on bare Ir(111) (black desorption spectrum) which should result in a coverage of approximately 0.44 ML [90]. Although 10 L is not the saturation dose, an increase in dose by a factor 10 only results in an increase in coverage by a factor 1.3, thus 10 L is a sufficiently high dose for our needs. After Gr growth, the sample was exposed again to 10 L CO (red desorption spectrum). The LEED image in the inset of Figure 8.7 shows the typical $(\sqrt{3} \times \sqrt{3})\mathrm{R}30^\circ$ adsorption structure of CO/Ir(111). As CO neither sticks to Gr nor intercalates the Gr [219] under our experimental conditions, the area under the red curve corresponds to the amount of CO desorbing from Ir not covered by Gr. The shape of the two curves is similar, both show a maximum desorption temperature of $\approx 500\,\mathrm{K}$. The red curve is reduced

in intensity. Measuring the areas underneath the curves shows that the area under the red curve is ≈ 25% of the area under the black curve, indicating a Gr coverage of ≈ 75%.

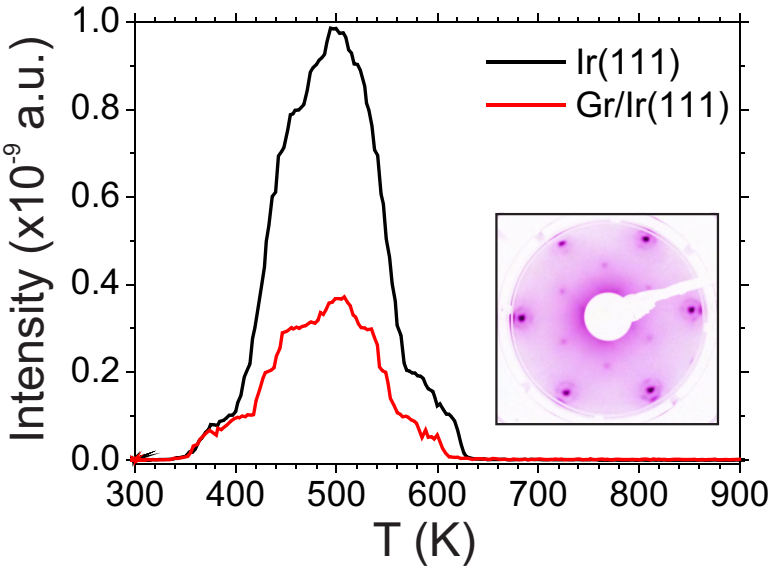

Figure 8.7: TPD spectra of mass 28 u (CO) of clean Ir(111) exposed to 10 L of CO at 300 K (black curve) and Ir partially covered with Gr exposed to the same dose CO (red curve). The inset displays a LEED image taken at an electron energy of 49.1 eV of the Gr covered sample after CO exposure.

Figure 8.8(a) shows a LEED image of CVD-Gr. The Gr spots are elongated because the Gr flakes are rotated slightly with respect to each other, typical for CVD growth. The rotational scatter lies below 10°. Figure 8.8(b) shows a LEED image after the sample was exposed to 11.1 ML Au at 780 K. The disappearance of the moiré and Ir spots indicate successful intercalation.

Confirmation of Au intercalation comes from STM images of the resulting sample, as displayed in Figure 8.9(a,b) - the latter being the derivative of the former. The images show two Gr flakes extending over two step edges on Au layers displaying the herringbone reconstruction, i.e., on many-layered Au. The Gr flake appears approximately 1.1 Å higher than the underlying Au. This is in line with previous observations [67]. DFT calculations [252] indicate that the geometrical height of Gr above Au is 3.23 Å, both in fcc and hcp positions. Two hexagonal superstructures can be observed. The larger superstructure is visible both on the Gr and on the uncovered Au. It is attributed to the herringbone reconstruction, since it appears whenever the herringbone stripes run almost parallel to the fast scanning direction, i.e.,

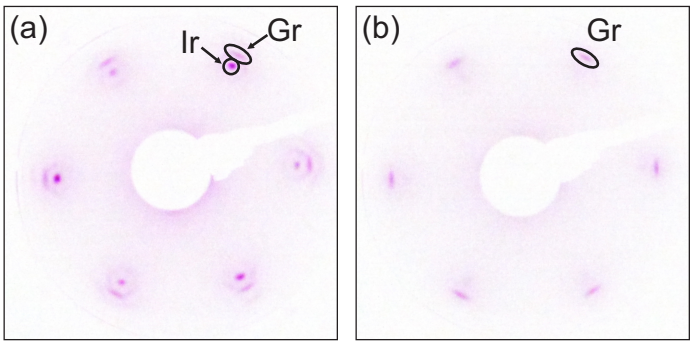

Figure 8.8: LEED images of (a) CVD-Gr on Ir(111) and (b) CVD-Gr exposed to 11.1 ML Au at 780 K, taken at an electron energy of 67.9 eV.

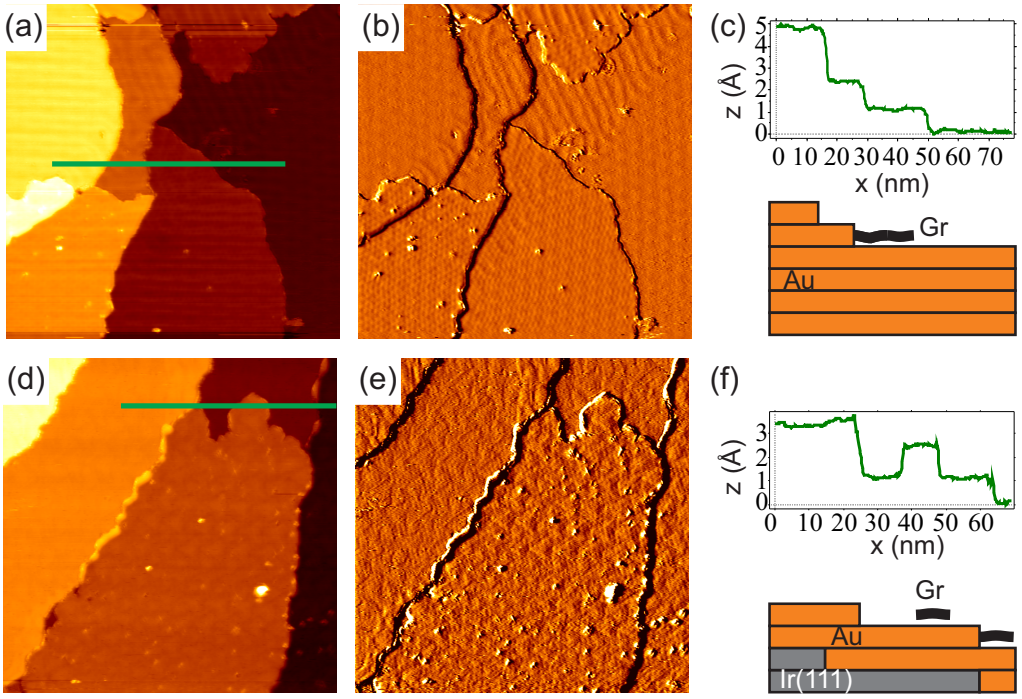

Figure 8.9: STM topograph of CVD-Gr intercalated by 11.1 ML Au at 780 K. Shown are Gr flakes on (a,b) herringbone-reconstructed Au layers, (d,e) trigonally reconstructed Au layers. (b) and (e) are differentiated. (c) and (f) show profiles and schematic side-views along the green lines in (a) and (d), respectively; dark gray rectangles are Ir layers, orange rectangles are Au layers, black lines are Gr. Image size 106 nm × 106 nm. Tunneling parameters (a,b) $I = 0.95\,\mathrm{nA}$, $U = +0.54\,\mathrm{V}$; (d,e) $I = 0.92\,\mathrm{nA}$, $U = -0.21\,\mathrm{V}$.

horizontally in our case. The smaller superstructure, e.g., on the lower flake results from the 14.7% lattice mismatch between Gr and Au [68, 249, 252].

On the same sample, also Gr intercalated by few-layered Au is observed; Figure 8.9(d,e) shows a Gr flake on Au layers displaying the trigonal reconstruction. The Gr flake appears 1.3 Å higher than the Au on the same terrace. A slight elevation can be seen near the upper edge of Figure 8.9(d,e). We take

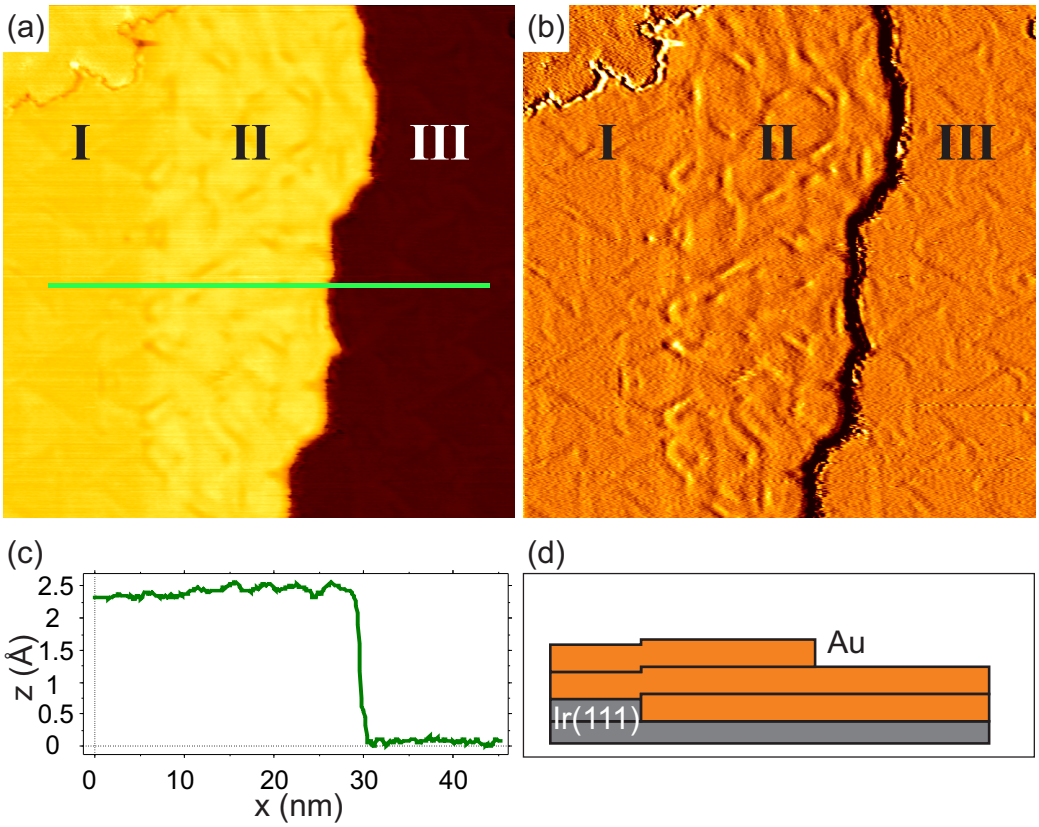

Figure 8.10: (a) STM topograph of few-layered Au/Ir(111). Three regions I, II, III of different heights are visible. (b) Differentiated STM image of the same region as (a). (c) shows the profile along the green line in (a). (d) Schematics of the situation in (a,b); dark gray rectangles are Ir layers, orange rectangles are Au layers. Image size 53 nm × 53 nm. Tunneling parameters $I = 0.9\,\mathrm{nA}$, $U = -0.21\,\mathrm{V}$.

a closer look at this feature in Figure 8.10. Three regions of different apparent heights are visible. Region I and III have a height difference of approximately a monatomic step of Ir. Region II appears 0.1 Å higher than region I and displays a larger corrugation. An Ir step edge separates regions I and II/III, and an additional Au layer grows at the step edge and leads to the elevation of

region II. The trigonal pattern, very similar to what was observed in Section 8.1, makes it plausible that regions I and III consist of 2 ML Au, and region II consequently of 3 ML, as shown in the schematic side-view of Figure 8.10(d), along the green line in Figure 8.10(a). However, we cannot exclude that the trigonal pattern continues also for a larger number of Au layers, as this was not studied further in this work.

8.3 Deuteration of Au/Ir(111)

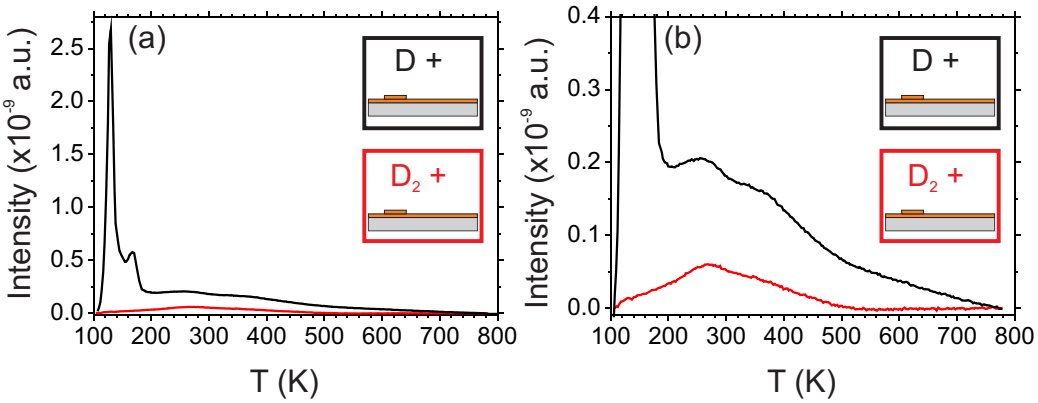

Figure 8.11: (a) TPD spectra (mass 4 u) of 1.2 ML Au/Ir(111) exposed to 15 L molecular D_2 (red curve) and 15 L atomic D (black curve) at 100 K. (b) Adjusted intensity scale to better show the weak features at higher temperatures. Heating rate 5 K/s. The insets schematically depict the sample morphology, with the Ir substrate in light gray and Au layers in orange.

We first characterize D and D_2 desorption from Au/Ir(111). 1.2 ML Au was evaporated onto Ir(111) at 780 K. 15 L D_2 was dosed through the thermal cracker (but with the cracking filament switched off) with the sample at 100 K, and then TPD was performed. This was then repeated but with the cracker on, i.e., dosing 15 L atomic D. The resulting TPD spectra are shown in Figure 8.11. D_2 on Au yields a broad, very weak desorption peak at ≈ 270 K. This can also be seen to contribute to the D on Au spectrum (as D_2 is first fed through the cracker before the filament is switched on). There is also now a shoulder at ≈ 370 K, which extends until ≈ 510 K. Above 510 K, the signal decreases linearly in the case of atomic D dosed, and drops to zero in the case of D_2. The linear decrease is attributed to the finite pumping speed in the system and is thus considered background. Additionally, atomic D shows a much larger desorption at ≈ 130 K, and at ≈ 167 K. In total, the amount

of D_2 desorbing after exposure with atomic D is almost a factor 10 higher compared to exposure with molecular D_2.

The failure of Au to dissociate hydrogen has been noted for the Au(110)-(1x2) surface [253], and a general explanation is given by Hammer *et al.* [254]. This has been challenged for thin Au layers on Ir(111) by Okada *et al.* [255, 256], who dose molecular D_2 onto 2 ML Au/Ir(111) and observe ≈ 0.5 ML D_2 (where 1 ML D_2 corresponds to a D-saturated Ir(111) surface) coming off in their TPD spectrum. This is in contradiction to our results. The amount of D_2 desorbing from our 1.2 ML Au/Ir(111) is around 10 times lower compared to dosing 15 L atomic D on the same surface. In addition, the TPD spectra of D_2 desorbing from Au and Ir differ in shape, which is not the case in the works of Okada *et al.*. Possibly, the D_2 desorption observed by Okada *et al.* stems from bare Ir patches and step edges, as they grow their Au at room temperature, leading to a more fractal and multilayer growth.

8.4 Deuteration of Gr/Au/Ir(111)

We can now examine D desorption behavior from CVD-Gr on Au on Ir(111). CVD-Gr intercalated by 11.1 ML Au at 780 K was exposed to various dosages of D, and each was studied with TPD. The sample was held at 180 K during dosing, to avoid the tall low-temperature peaks (Figure 8.11). It was confirmed that no further desorption occurs for temperatures higher than 780 K, and thus, TPD was typically performed up to 780 K only, so as not to alter the state of the sample. Of course some areas of Au will not be covered by Gr, but their contribution to the desorption spectra should be easily identifiable based on the previous section. Additionally, a D_2 dose (through the cracker) was performed for comparison. These TPD spectra are shown in Figure 8.12(a). The spectra display four main features. A small, broad peak (i) is seen around 260 K in all spectra, including the control ($t = 0$ s). A peak (ii) appears towards higher doses (> 5.4 L), first at 450 K and shifting towards 470 K upon dosage increase. A broad peak (iii) is apparent at 540 K already at the lowest dose. It develops a shoulder (iv) at 650 K. Towards higher doses this shoulder remains at this temperature, while peak (iii) shifts towards it until they merge. At the highest dose this results in a single peak (iv), still at 650 K.

Peak (i) clearly corresponds to desorption from bare Au, based on the previous section. The other peaks (ii-iv) cannot be explained based on this information alone.

Figure 8.12(b) displays the same sample, exposed to the same doses of atomic D as before, but at 330 K sample temperature. Except for peak (i)

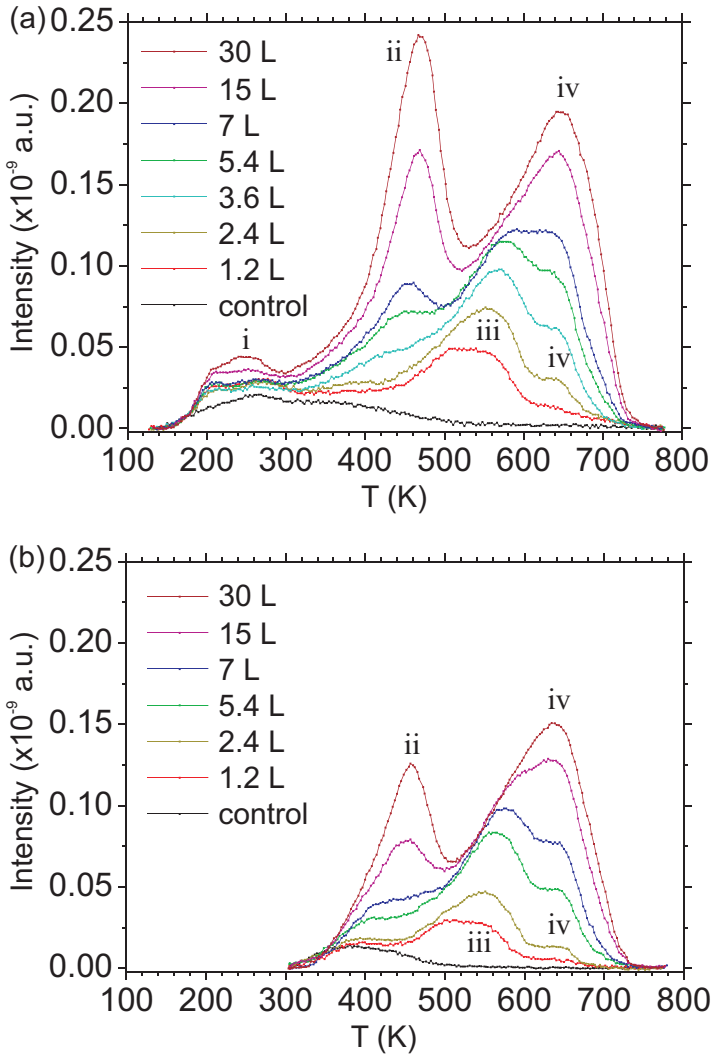

Figure 8.12: TPD spectra (mass 4 u) of different amounts of atomic D as indicated in the figure dosed onto Gr/many-layered Au/Ir. (a) D dosed at 180 K. (b) D dosed at 330 K. Heating rate 5 K/s. See text for an explanation of the peak labeling.

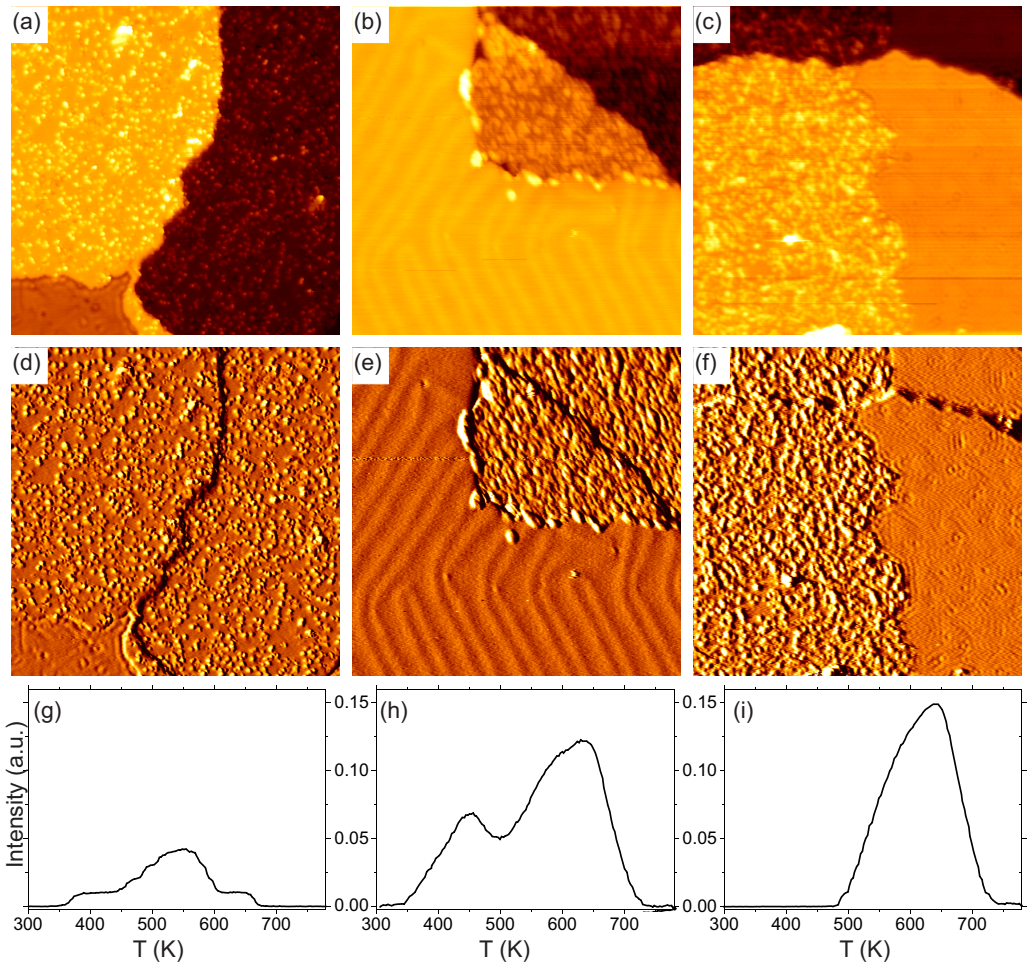

Figure 8.13: STM and TPD for atomic D dosed on Gr/Au/Ir(111). (a) STM topograph of 2.4 L D dosed on Gr/Au/Ir(111). (b) STM topograph of 15 L D dosed on Gr/Au/Ir(111). (c) STM topograph after the sample of (b) was annealed to 500 K. (d-f) are the differentiated versions of (a-c), respectively. (g,i) are TPD spectra (mass 4 u) of the samples in (a,c) taken subsequently, (h) is a TPD spectrum of a sample prepared in the same way as (b). Image size 53 nm × 53 nm. Tunneling parameters (a,d) $I = 0.48\,\mathrm{nA}$, $U = +0.57\,\mathrm{V}$, (b,e) $I = 0.17\,\mathrm{nA}$, $U = -0.69\,\mathrm{V}$, (c,f) $I = 0.33\,\mathrm{nA}$, $U = -1.51\,\mathrm{V}$. Heating rate in (g-i) 5 K/s.

which has its desorption maximum well below the exposure temperature, the same peaks as before are present. However, the amount of D that can be adsorbed is considerably less when dosing at 330 K. For peak (ii) this is understandable, as from Figure 8.12(a) we see that the desorption from this peak already starts around 300 K, so we will not be able to populate this state fully when dosing at 330 K.

For further insight into the nature of the TPD peaks we employ STM. D dosing was performed at 330 K, i.e., above the main desorption behavior of D from bare Au. The corresponding TPD spectra for D dosing at this temperature are shown in Figure 8.12(b). Figure 8.13 shows STM topographs (a-c) of the Gr/Au sample with different D coverages. Also shown are their respective differentiated images (d-f) and results from TPD (g-i), performed after imaging. Care was taken never to anneal the sample above 780 K, the temperature at which Au had been intercalated. Therefore, between topographs (a), (b) and (c) the only differences should be the quantity of D, and the section of the sample being imaged. Figure 8.13(a,d) shows the sample after a 2.4 L D dose. An Ir step edge runs down the center of the images. Small dots can be seen over most of the surface, except for a 'clean' patch in the lower left corner, displaying a trigonal strain relief pattern. Considering our chosen sample temperature of 330 K during dosing - at which D will not adsorb to Au - the conclusion is thus: most of the image shows D (appearing as dots) adsorbed on Gr/few-layered Au/Ir, while there is also a small section of bare few-layered Au/Ir. It is clear that the Gr has been successfully intercalated, because we do not observe the D-islands of Gr/Ir(111) (Chapter 7). Instead, the D adatoms appear to be distributed randomly. In TPD, Figure 8.13(g), the spectrum shows the peak (iii) and shoulder (iv) as before for this dose.

Figures 8.13(b,e) show the sample after a 15 L D dose. The majority of the topograph displays the Au(111) herringbone reconstruction. In the upper right quadrant, we see deuterated Gr on Au, passing over an Ir step edge. The D concentration is clearly higher than in Figure 8.13(a,d), not surprising as the dosage is sixfold. In TPD [Figure 8.13(h)] we observe two peaks (ii and iv), though in STM we cannot distinguish two distinct binding states for D. To try to explain these two peaks, we again dosed 15 L D and then flashed annealed to 500 K, thereby desorbing the first. The sample was then STM imaged at room temperature as before, shown in Figure 8.13(c,f). The right side of the images show bare Au, this time displaying the trigonal strain relief pattern. Thus, we believe the left side of (c,f) to show D adsorbed to Gr/few-layered Au/Ir. In STM we cannot discern a difference in the D adsorption structures between this and the D/Gr/many-layered Au/Ir case (b,e). TPD performed after imaging (i) confirmed that indeed only the highest temperature peak (iv) was present. Although we did not manage to image a herringbone Au area

in the (c,f) case, we believe it is unlikely that D adsorption to Gr in such an area appears differently with the (ii) peak absent, since the properties of Gr intercalated by few- or many-layered Au films should not differ significantly.

Deuteration of TPG-Gr/few-layered Au/Ir

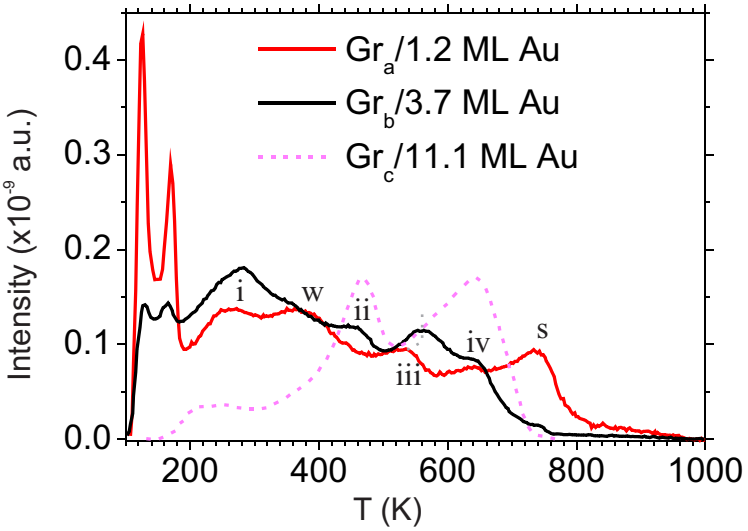

Figure 8.14: TPD spectra (mass 4 u) of 15 L D dosed at 100 K onto 0.5 ML TPG-Gr intercalated by 1.2 ML Au (red curve) and 3.7 ML Au (black curve) at 780 K. For comparison, the corresponding spectrum from Figure 8.12(a) (D exposure at 180 K on CVD-Gr, dashed pink curve) is shown. Note that for each curve a new sample was prepared. Gr_a corresponds to the TPG-Gr sample shown in Figure 8.3, Gr_b to TPG-Gr shown in Figures 8.4 - 8.6, while Gr_c is CVD-Gr. See text for an explanation of the peak labeling.

We also conducted TPD experiments of the TPG-Gr shown in Figures 8.3 and 8.4 exposed to 15 L D at 100 K. The results are displayed in Figure 8.14. Both samples exhibit a broad number of peaks in TPD. The sharp double-peak feature below 180 K is D desorbing from clean Au, as established in Section 8.3. It is strongly reduced in intensity for the case of Gr/3.7 ML Au/Ir [Figure 8.14(b)]. This might indicate that this double-peak is in fact typical for 1 ML Au/Ir. Two more features can be identified from Chapter 7, namely those labelled (w) and (s) at 365 K and 740 K, respectively. They can be attributed to D adsorbed on unintercalated Gr, resulting in a weakly (w) and strongly (s) bound peak. As would be expected, the (w) and (s) peak intensity drops significantly when going from 1.2 ML to 3.7 ML Au, as in the

latter case much less Gr is still unintercalated. Peaks (i,ii, iii, and iv) lie in a similar region as for the case of CVD-Gr (displayed in pink for comparison), however, an attribution of the peaks is difficult without further experiments.

8.5 Discussion

In the following, we want to make some comparison of D desorption from CVD-Gr/Au/Ir with D desorption from the unintercalated Gr/Ir(111) system and from other systems known from literature. The high-temperature desorption peak (iv) of D/Gr/Au/Ir(111) lies only $\approx 80\,\mathrm{K}$ below the desorption peak of D-islands, $\approx 730\,\mathrm{K}$. As explained in Chapter 7, the Gr undergoes sp^3-rehybridization and binds to the Ir substrate in these regions, and this gives the D-islands such stability. With multiple layers of Au intercalated, binding to the Ir is impossible. In STM [Figure 8.13(a-c)] we see nothing resembling regular structures like islands, but perhaps sp^3-rehybridization occurs nevertheless. For hydrogenation of Gr/1 ML Au/Ni(111), Haberer *et al.* [63] see signs of sp^3-hybridization in XPS. However, they attribute this only to those C atoms binding to an H atom on top. The C atoms neighboring a hydrogenated C are not thought to bind down to the substrate. Unfortunately, no Au-XPS-spectra are presented in their work. Of course, the Gr/1 ML Au/Ni(111) system differs from Gr/Au/Ir(111). For one, Au intercalation on Gr/Ni(111) seems to be limited to 1 ML [64]; secondly, complete dehydrogenation is observed after heating to $\approx 600\,\mathrm{K}$ [63], i.e., more than 100 K below what we observe. In STM measurements of deuterated Gr/Au/Ni(111), elongated shapes visible after low D doses were attributed to *meta* configurations - i.e., D adsorbed next-nearest neighbor C atoms - based on calculated charge density distributions [115]. *Meta* configurations have been shown to be unstable on HOPG [97] and are only believed to be stable on systems like Gr/Ir(111), Gr/Pt(111) or Gr/Ni(111) [6,105,106,113] where they are stabilized by C atoms binding down to the substrate. The finding of Scheffler *et al.* [115] could thus signify that C atoms bind down to the Au. However, it is not obvious whether this is true for their system only where the Ni substrate might still have some influence through 1 ML Au, or if this is generally the case for Gr/Au. However, it could explain why we observe a surprisingly high peak temperature for D on Gr/Au.

The 650 K desorption peak of Gr/Au/Ir is higher than for D-dimers on HOPG ($490-580\,\mathrm{K}$ [95–97,99]) and higher still than D-dimers on Gr/Ir(111) (380 K, Chapter 7). Thus this binding state of D on Gr/Au/Ir(111) is comparatively strong.

Hydrogenation of Gr/Ni(111) was studied by Zhao *et al.* (see also Chap-

ter 2.7), who performed extensive TPD measurements for doses ranging over several orders of magnitude [113]. Gr/Ni(111) grows commensurately [114], and the Gr interacts very strongly with its Ni substrate. At full H coverage, alternate C atoms bind upwards to an H and down to a Ni atom, similar to what we believe happens in the hcp and fcc regions for D/Gr/Ir. The authors see a strong dosage dependent peak behavior (see Figure 2.23), where the peak at $\approx 600\,\mathrm{K}$ is dominant at low doses and is due to diffusion of randomly adsorbed H into the *meta* state, from where desorption occurs. Direct desorption from the *meta* state is observed for high coverages at $\approx 370\,\mathrm{K}$. We do not observe this behavior for our systems. It would be interesting, though, to go to much higher D dosages, which was not done due to the limitations of the cracker used. It should be pointed out, however, that the maximum desorption temperature of H/Gr/Ni, a strongly interacting system, lies well below the maximum desorption peaks for Gr/Ir and Gr/Au, systems which are well decoupled compared to Gr/Ni.

A system closer to ours, H/Gr/Pt(111), was studied by Dinger *et al.* [112]. Atomic H dosed on Gr/Pt(111) results in a double-peak desorption between 500 and 700 K from H/Gr (although wrongly attributed to desorption exclusively from Gr edges by the authors). Rajasekaran *et al.* [109] observed with STM that, similar to D/Gr/Ir, hydrogen clusters in periodically arranged islands which follow the moiré.

There is a wealth of theory papers on hydrogenation of Gr, however, many of them do not include a substrate and hence neglect the physics induced by it. Andersen *et al.* [257] have compared H/Gr/Pt(111) and H/Gr/Ni(111) and found very stable graphane-like clusters in both systems. On Gr/Ni(111) the binding energies of the H clusters are almost independent of the cluster size, while for H/Gr/Pt(111), binding energies increase with cluster size. We did not observe a binding energy increase for D/Gr/Ir in the dosage range studied by us. In Gr/Au/Ir, however, such a behavior was observed for the desorption peak (ii) (between 450 and 470 K) and (iii) (between 540 and 650 K). We suggest that peaks (ii,iii) come from adsorption structures that become more stable the larger they become.

8.6 Summary

The first monolayer of Au/Ir(111) grows pseudomorphic, is almost completely closed before nucleation of the second layer [247] and appears flat in STM. Upon second and third layer deposition trigonal strain relief patterns appear. Although these kind of patterns are known from metal-on-metal epitaxy (see Section 2.5), to the best of our knowledge, they have not been observed for

Au/Ir(111) before. For many layers of Au, the known herringbone pattern of Au(111) is present.

Au-intercalation of a closed, 1 ML Gr film was found to be impossible, under the experimental conditions explored. Small Gr flakes that do not cross Ir step edges are also difficult to intercalate. This is attributed to intercalation proceeding via the Gr edges. Similar to oxygen and hydrogen intercalation, points where Gr edges and Ir step edges cross are likely entry points for Au intercalation. At 780 K, Au exhibits step-flow growth, and Gr intercalation proceeds from step edges downwards. At this temperature, at least part of the incoming Au is reflected by Gr. Interestingly, relatively deep trenches are sometimes observed at the Gr edges for the case of Gr/few-layered Au/Ir. It seems that the Gr edge binds down, possibly still to the Ir substrate. Gr interacts only very weakly with the underlying Au. Consequently, mostly the Au is imaged through the Gr, and the Au strain relief patterns remain unchanged. Sometimes, a weak moiré is visible, arising from the superposition of the Au and the Gr lattice.

Exposing 1.2 ML Au to molecular deuterium at 100 K results in only very little adsorption, with ≈ 270 K, evidencing the inability of Au to dissociate hydrogen or deuterium [253]. When adsorbing the same amount of atomic D, the amount of detected desorbing D_2 is by a factor of 10 higher. Now, deuterium can easily adsorb as the dissociation energy has already been paid by the cracker. Additionally to an increased broad peak at ≈ 270 K, a double peak structure at ≈ 130 K and ≈ 167 K appears. This double peak structure seems to decrease for more layers of Au, but more experiments are necessary to verify this observation.

TPD measurements of D dosed onto Gr/many-layered Au/Ir reveal three additional peaks, compared to D adsorption on Au. At low doses, a peak at ≈ 540 K develops. Next, a dosage-independent shoulder at ≈ 650 K develops. Increasing the dose leads to a shift to higher temperatures of the ≈ 540 K peak, which eventually merges with its shoulder. At slightly higher dosages than the aforementioned peaks, a peak at ≈ 450 K is visible, shifting up to ≈ 470 K for increased dosing. All peaks grow in intensity when more D is dosed. Further experimental and also theoretical input is necessary to explain the desorption peaks we observed. We find a surprisingly high maximum desorption temperature for D on Gr/Au/Ir, only ≈ 80 K lower than what was observed for D on Gr/Ir(111) and more than 100 K higher than for the strongly interacting Gr/Ni(111) system [113]. The amount of interaction between Gr and its substrate alone is obviously not a good indicator to predict the binding strength of D on Gr.

In STM, adsorption of atomic D on Gr/many-layered Au/Ir(111) leads to the appearance of randomly spaced, dot-like structures. Increasing the dosage

to 15 L increases the apparent coverage, but no ordered structures were observed at any coverage. Although annealing the sample to 550 K should result in about one third of the D to desorb, no clear difference can be seen in STM.

Dosing 15 L D results in an amount of adsorbed D of, very roughly, 0.2 ML (where 1 ML corresponds to the saturation coverage of D/Ir), similar to D on Gr/Ir(111). However, no calibration experiments were carried out close in time to the D/Gr/Au TPD experiments, so this coverage has a relatively big error.

Deuteration or hydrogenation of Gr seems to very sensitively depend on the underlying substrate. It would be worth to perform further investigations to elucidate the underlying physics. In the case of Gr/Au/Ir(111), low dosage, high resolution STM and STS experiments at low temperatures might lead to further insights concerning the nature of D adsorption on Gr/Au. At low coverage, one should be able to image the standing waves visible on the Au through the Gr and detect whether they are perturbed by adsorbing D atoms. If they are, this would point to an interaction of the Gr with the Au substrate. Also, XPS of Au core levels could be useful to determine the amount of interaction between Gr and Au. Systematic, dosage dependent TPD measurements, e.g., of a weakly interacting system such as Gr/Cu and differently intercalated systems as well as theory input such as DFT calculation including the specific substrate should be fruitful as well.

Chapter 9

Summary and Outlook

The stability of Gr at high temperatures and in the presence of O_2 is crucial for applications envisioned under these conditions. Furthermore, Gr represents an ideal model to learn more about carbon combustion and develop an understanding on the atomic scale. For perfectly closed Gr layers we found 5-7 defects to be the nucleation sites for hexagonal etch holes bound predominantly by zigzag edges. Once holes in the Gr layer are present, O_2 dissociatively adsorb on the bare Ir, diffuses to and attacks the edges of Gr as atomic O, and finally desorbs as CO or CO_2. While the onset temperature for a perfectly closed layer is approximately 700 K, the etching onset for Gr flakes is significantly reduced ($\approx$ 550 K) because in this case, bare Ir for dissociation and Gr edges as easy attack sites are already present. Furthermore, we found that the temperature necessary for etching decreases with decreasing Gr flake size, down to 410 K for nanoflakes. This effect is predominantly due to geometry, as Gr is etched only from the edges, and the edge concentration strongly depends on the flake size. We model the elementary etch process as a thermally activated process at the Gr edge and find an activation energy of the order of $E_a = 0.44\,\mathrm{eV}$, and a prefactor of $\nu_0 = 500\,\mathrm{s}^{-1}$, irrespective of flake size. Consistent with the relatively inefficent etching process, this unusually low prefactor indicates a complex transition state. Based on our results, we find that intercalation is not a necessary precondition for etching but is largely irrelevant to the etching process.

We believe that 5-7 defects could also act as nucleation sites for etching on complete Gr layers on other substrates, and also on graphite. Additional insight into the atomistic details of the oxygen attack could be provided by DFT calculations.

Intercalation of atoms and molecules underneath Gr is extremely useful for many reasons. From an application point of view, being able to precisely control intercalation of a variety of substances under Gr enormously increases

the flexibility in designing possible devices. Profound understanding of the fundamental mechanisms involved is indispensable. Also on the more fundamental side of research, intercalation provides flexibility as it is a simple means of changing the material with which Gr is in contact. Of specific interest are intercalants that decouple the Gr from its substrate and thus restore the free-standing properties of Gr. Intercalants are a convenient way to dope Gr without modifying the Gr layer itself. Moreover, subsequent chemical functionalization can be performed on the side of Gr not in contact with the intercalation layer, and can be influenced through the choice of intercalant.

Monitoring the XPS-BE of the C 1s core level electrons change upon intercalation is a quick way to control intercalation processes, so improving the understanding of the origins of these CLSs is a worthwhile endeavor. For the case of Gr weakly interacting with its substrate or the intercalation layer, we found that both the CLSs and the C 1s peak shape display a universal, non-monotonic dependence on the doping level in Gr. This was shown by comparing a number of different intercalating species measured by us or taken from literature. Additionally, to prove without doubt that the observed relationship is indeed solely dependent on the doping level, we continuously tuned the doping level via Li intercalation, and observed the same behavior of CLS and peak shape.

Doping is the result of charge transfer from the substrate into Gr, or vice-versa. The non-monotonic change in BE is due to a superposition of two effects: At low and moderate doping levels the CLS is dominated by a rigid shift of the Gr bandstructure. Due to the small density of states near the Dirac point, substantial rigid band shifts arise already for small amounts of transferred charge. The rigid band shift is counteracted by an effect proportional to the transferred charge per C atom, such that for n-doping levels beyond 1.2 eV the CLS decreases in magnitude. A simple explanation for a charge transfer effect is an electrostatic initial state effect, meaning that the transferred charge changes the electrostatic potential energy felt by the core level electron prior to ionization. This electrostatic initial state effect indeed is in the right order of magnitude. However, further thorough theoretical analyses are necessary, especially to elucidate the role of final state effects on the CLSs. Based on our simple model we predict the doping level of H-intercalated Gr/Ir(111) to be $E_D \approx 0.2\,\mathrm{eV}$.

The characteristic change in peak shape encompasses an asymmetric peak broadening towards higher BE, and the development of a broad shoulder to higher BEs. Similar observations have been made in the literature for a variety of n-doped Gr and graphite systems. The asymmetric broadening is typically attributed to the enhanced phase space for electron-hole pair excitations. The pronounced shoulder evolves at $E_D \approx 1.2\,\mathrm{eV}$, is shifted by

0.5-0.7 eV towards higher BE relative to the main component, and diminishes again upon continued doping ($E_D \approx 1.36\,\mathrm{eV}$). We rule out different chemical environments as the cause for the high BE shoulder, but attribute it, as others before us, to a loss process of the outgoing photo electron, possibly a 2D plasmon. To discern the exact nature of this loss feature, theoretical input such as DFT calculations is needed.

We studied the formation of a superdense OH-H_2O phase underneath Gr with XPS, TPD, LEED and live STM measurements. It is characterized by an OH-to-H_2O ratio of roughly 1:2, and hence an H:O ratio of roughly 5:3. The local coverage is suprisingly high with 0.79 molecules (OH or H_2O) per Ir surface atom. The superdense OH-H_2O phase has never been observed on the bare Ir(111) surface, and is also different to the honeycomb OH-H_2O structure observed on Pt(111) [230] which exhibits an H:O ratio of 3:2. The superdense phase would immediately desorb from Ir. Also at low temperatures it has not been observed on Ir which we attribute to an energy barrier involved when transforming the known honeycomb phase into the superdense phase. This barrier apparently can be only overcome at room temperature. The role of the Gr is simply that of a cover, confining the reaction products to the surface and thus inhibiting desorption. Although Gr being a protective cover is not a particularly new concept [41], with our work, for the first time, we have observed that Gr opens up a new reaction path. Not only does this lead to the possibility to study the behavior of metal surfaces in humid environments at room temperature and in UHV, but one might also speculate that it is possible to infuse other atoms and molecules into the OH-H_2O phase and to perform chemistry under the 2D nanoreactor Gr.

The interaction of hydrogen with Gr is of interest because it enables manipulation of Gr's electronic properties. This spans from introducing a bandgap of the order of 0.5 eV [6] to the formation of graphane [93], an insulating material which is interesting in itself. Although seemingly a simple system, the interaction of hydrogen with Gr/Ir(111) has not yet been understood.

In this work, for the first time we show TPD measurements of D adsorbed on Gr/Ir(111) and find a D coverage on 1 ML Gr of $\approx (0.21 \pm 0.06)$ ML where 1 ML corresponds to the Ir(111) surface saturated with D. We find two distinct binding states of D. We attempt to link this finding with the observations from STM experiments. The strongly bound state corresponds to D structures preferentially adsorbed on the hcp areas, but to some extent also on the fcc areas of the moiré lattice. The structures themselves have a ring-like appearance in STM but atomic resolution was not obtained. The state of the tip has a large influence on the sharpness of the features and thus on the apparent coverage.

Explaining the weakly bound state of D proved to be more challenging, as it is difficult to image with STM. Additionally, there is evidence for diffusion between room temperature and 450 K when heating up the deuterated Gr film. This makes the interpretation of room temperature STM images difficult. Comparison with literature, especially deuterated HOPG, suggests that D atoms adsorbed in the sp^2-hybridized areas of Gr in dimer structures – i.e., two D atoms sitting on the same C ring – might account for the weakly bound state. We have excluded alternative sources for the weakly bound peak, namely, coadsorption effects, contributions from the sample holder, and intercalated D.

Desorption of H from Gr/Ir(111) reveals an isotopic shift of ≈ 20 K and ≈ 25 K for the weakly and strongly bound peak, respectively.

In the literature there is dispute as to whether or not graphane formation is possible on Gr/Ir(111) [16–18]. Being able to form graphane from Gr/Ir(111), ideally in a locally controlled manner, would be an extremely useful tool. One could envision patterned samples where isolating graphane alternates with, if doped, conducting Gr areas. Our attempt to form graphane consisted of intercalating hydrogen underneath Gr and then dosing atomic hydrogen from atop, thus providing atomic hydrogen on both sides of the Gr [17]. However, we found no evidence for graphane formation. Instead, intercalated hydrogen effectively blocks the formation of stable H or D bonds to the Gr.

The ability of intercalated hydrogen to block formation of stable H or D bonds and also the regular adsorption pattern with moiré periodicity of D on Gr/Ir(111) suggests that the substrate underneath the Gr is what really governs the interaction of Gr with D. When comparing TPD measurements of D adsorption to Gr resting on different substrates [89,92,95,99,110,112,113], the complexity of and difference in the resulting TPD spectra is striking. This prompted us to study deuteration of Gr in contact with a very simple substrate: Au. Au is known to effectively decouple Gr. Our findings on deuterated Gr/Au/Ir(111) are quite surprising. Although there is very little interaction between Gr and Au, D is still remarkably stable, with a maximum desorption temperature of ≈ 650 K, only 80 K below what is observed for Gr/Ir(111). Apparently, the strength of interaction between Gr and its substrate is not a good indicator as to how stable D is on the respective system.

Additionally to the desorption at ≈ 650 K, we find peaks at ≈ 270 K, $\approx 540 - 650$ K, and $\approx 450 - 470$ K. Further experiments are necessary to determine the nature of these peaks.

No regular adsorption patterns are detected in STM, and it is an open question whether the Gr binds down to the Au upon D adsorption, as is

the case for, e.g., Gr/Ir(111). XPS of the Au 4f core levels [258] could show whether the surface peak vanishes upon exposure of Gr/Au to D. We also believe low coverage STM and STS experiments at low temperature to be worthwhile. As Au exhibits standing wave patterns, it should be straightforward to analyze whether these are influenced by D atoms. If they are, this would be a proof for bonding between Gr and Au. Further research is also needed to clarify the effect of the number of Au layers. We found that the desorption peaks in TPD change both in number and desorption temperature with the number of Au layers, especially in the regime 1-3 Au layers, however, this was not investigated further here.

Prior to studying the desorption behavior of D on Gr/Au/Ir, we had to develop an intercalation recipe. This is based on previous work [67], although we found an increased intercalation temperature of 780 K to yield very satisfying results in our case. A closed 1 ML Gr film could not be successfully intercalated, and small flakes which are always present after TPG Gr growth are also difficult to intercalate [67]. We thus used Gr flakes grown by just the CVD method which yields large flakes nucleating at the Ir step edges. While many layers of Au yield the herringbone reconstruction know from the Au(111) surface [72], we find that the first layer of Au on Ir(111) grows pseudomorphic, and appears flat in STM. The second and third layers display trigonal strain relief patterns. Further high-resolution STM studies of these regimes would be interesting.

To summarize, we have studied different tools and how they allow to change specific properties of Gr. Oxygen etching allows to pattern Gr and change its morphology. Intercalation is a powerful means as it changes the doping level and may decouple Gr, enables chemistry underneath Gr, and influences the interaction of Gr with material deposited on the other side, as shown for the case of atomic D. Deuteration itself is interesting due to its modification the electronic properties of Gr, and it is very much influenced by the substrate underneath the Gr.

Chapter 10

Appendix

Live oxygen etching of 1 ML Gr

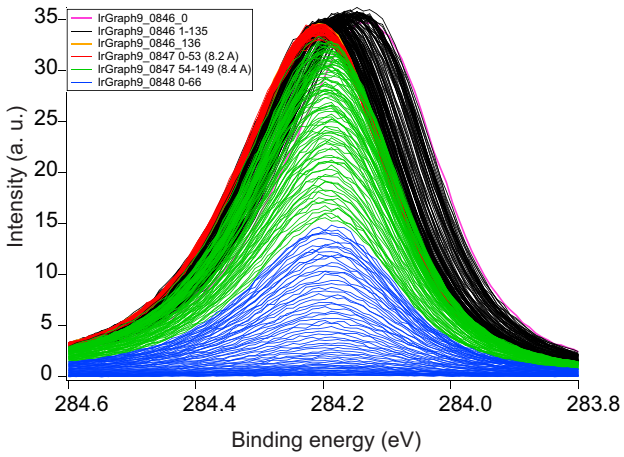

Figure 10.1: Live XP spectra of the C 1s region of oxygen etching of 1 ML Gr in front of the analyzer. The sample was kept between 750 K and 790 K, after five spectra O_2 was dosed with a pressure of $1 \cdot 10^{-7}$ mbar. Before turning on the O_2 pressure, the C 1s peak position is at $\approx$ 284.14 eV (red curve at the lowest BE), upon the start of O_2 dosing it experiences a shift of +0.01 eV (within the error margin of the experiment) and continues shifting until 284.21 eV (black curves). At this point, 97% of the Gr is still there. For the green and blue curves the heating current was increased, the slight peak shift to lower BE can be attributed to this. After this, the peak position stays roughly constant until the Gr is gone. Although we cannot explain the +0.06 eV CLS, note that it is not consistent with oxygen intercalation, as a dilute oxygen phase would exhibit a CLS of -0.17 eV.

Coadsorption spectra for D/Au/Ir(111)

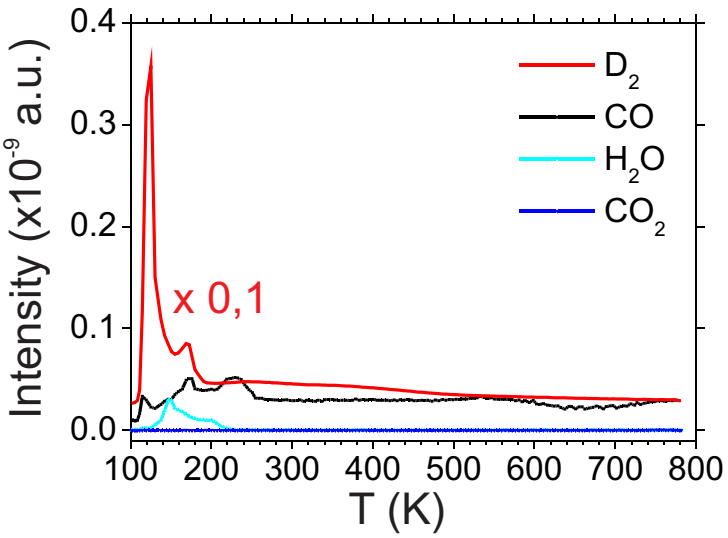

Figure 10.2: TPD spectra of masses of 4 (D_2), 18 (H_2O), 28 (CO), 44 (CO_2) of 1.2 ML Au/Ir(111) exposed to 15 L atomic D at 100 K.

D/Gr/11.1 ML Au/Ir reproducibility

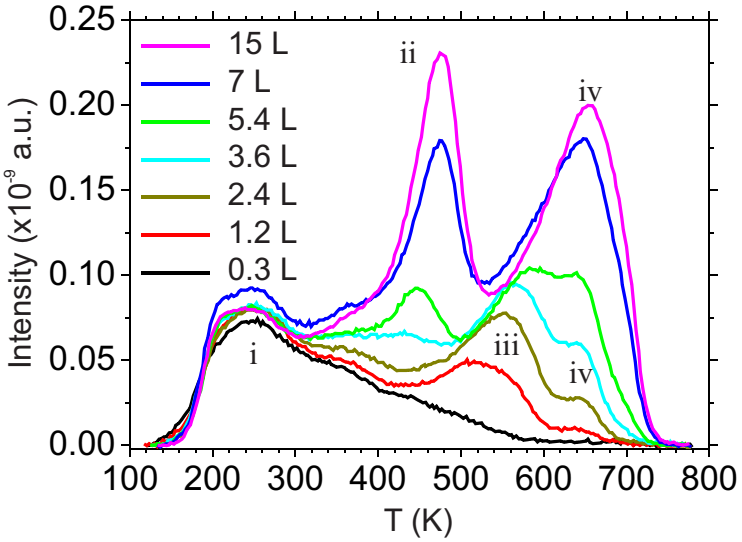

Figure 10.3: TPD spectra (mass 4 u) of different amounts of atomic deuterium as indicated in the figure dosed onto Gr/11.1 ML Au/Ir. Same sample preparation as in Figure 8.12(a). Heating rate 5 K/s.

Deuteration of Cs-Au-intercalated Gr

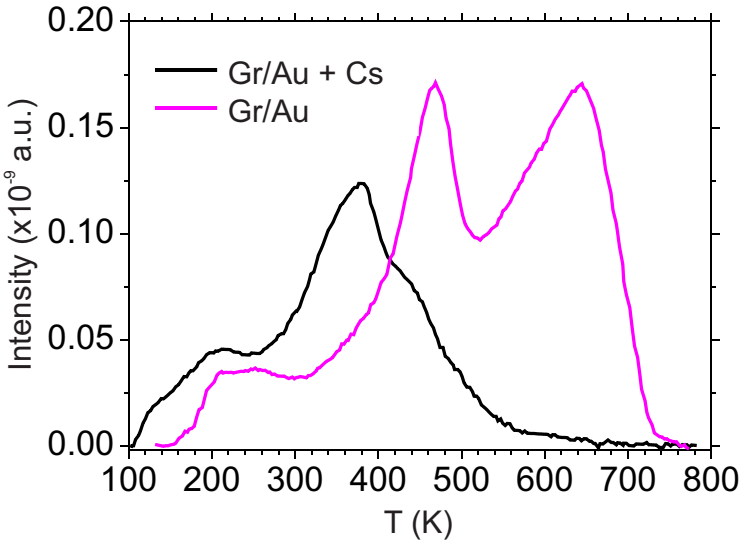

Figure 10.4: TPD spectra of Gr/many-layer Au/Ir(111) exposed to 15 min Cs (with a current of 6.1 A through the dispenser) and subsequently to 15 L D, both at room temperature (black curve). For comparison, Gr/many-layer Au/Ir(111) exposed to 15 L D without Cs is shown in pink. Heating rate 5 K/s.

Growth of Pd clusters on Gr/Ir(111)

Growth at 100 K and temperature stability

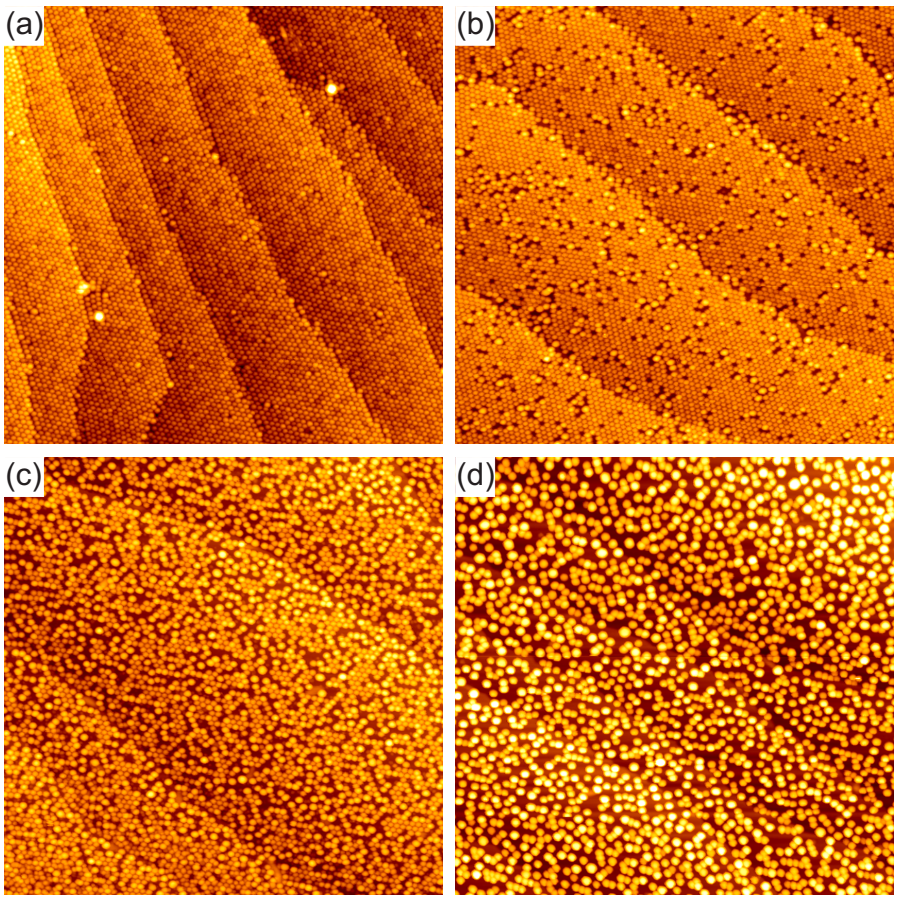

Figure 10.5: STM topographs of 0.4 ML Pd deposited on 1 ML Gr/Ir(111) at 100 K. (a) Imaged at 100 K, (b) imaged at 300 K. (c) annealed to 400 K, imaged at 300 K, (d) annealed to 500 K, imaged at 300 K. Image sizes 180 nm × 180 nm. Tunneling parameters: (a) $U_s = 1.06$ V and $I_t = 0.06$ nA, (b) $U_s = 2.5$ V and $I_t = 0.13$ nA, (c) $U_s = 2.16$ V and $I_t = 0.06$ nA, (d) $U_s = 2.16$ V and $I_t = 0.07$ nA.

Seeded growth at room temperature and temperature stability

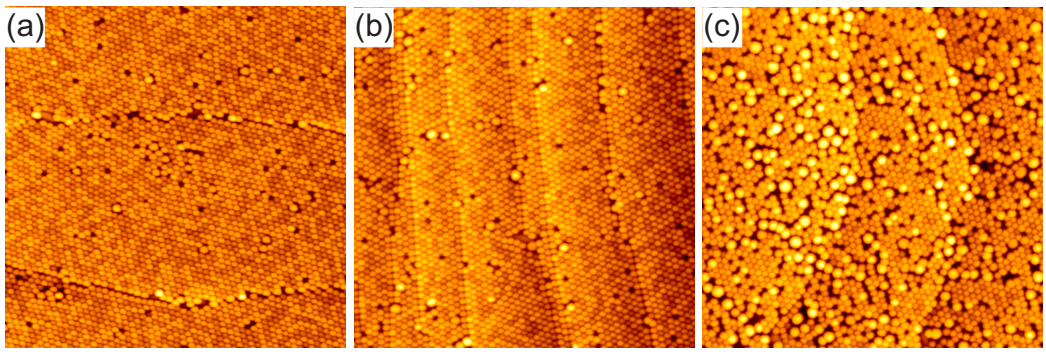

Figure 10.6: STM topographs of (a) 0.6 ML Pd deposited on 0.15 ML Ir clusters on 1 ML Gr/Ir(111) at room temperature. (b) After subsequent flash annealing to 400 K, (c) after subsequent flash annealing to 500 K. Image sizes 125.2 nm × 125.2 nm. Tunneling parameters: (a) $U_s = 2.05\,\mathrm{V}$ and $I_t = 0.06\,\mathrm{nA}$, (b) $U_s = -2.21\,\mathrm{V}$ and $I_t = 0.06\,\mathrm{nA}$, (c) $U_s = 2.05\,\mathrm{V}$ and $I_t = 0.03\,\mathrm{nA}$

H_2 exposure and temperature stability

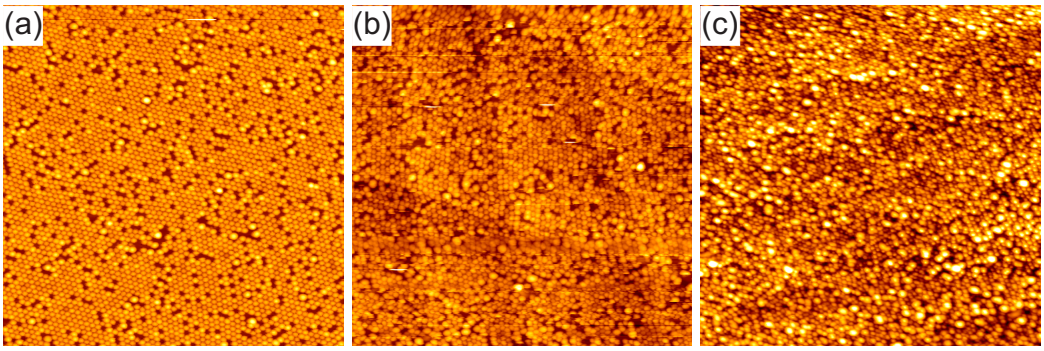

Figure 10.7: STM topographs of (a) 0.35 ML Pd deposited on 0.08 ML Ir clusters on 1 ML Gr/Ir(111) at room temperature, (b) after subsequent exposure to $\approx$ 960 L H_2 at room temperature, and (c) after subsequent flash annealing to 550 K. Image sizes 142 nm $\times$ 142 nm. Tunneling parameters: (a) $U_s = -0.55$ V and $I_t = 0.01$ nA, (b) $U_s = -2.1$ V and $I_t = 0.16$ nA, (c) $U_s = 3.05$ V and $I_t = 0.03$ nA

Al intercalation

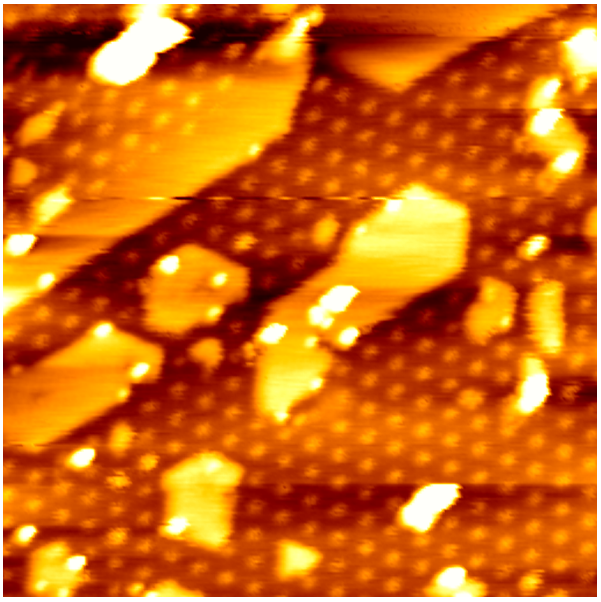

Figure 10.8: Intercalated Al under Gr/Ir(111). Evaporated at 31 W, 25 nA for 30 s at room temperature. Image size 53 nm × 53 nm. Tunneling parameters $U_s = 2.07\,\mathrm{V}$ and $I_t = 0.45\,\mathrm{nA}$.

Bibliography

[1] K. Novoselov, A. Geim, S. Morozov, D. Jiang, Y. Zhang, S. Dubonos, I. Grigorieva, and A. Firsov. *Electric field effect in atomically thin carbon films.* Science, 306, 5696, pp. 666–669, 2004. http://dx.doi.org/10.1126/Science.1102896.

[2] A. K. Geim and K. S. Novoselov. *The rise of graphene.* Nat. Mater., 6, 3, pp. 183–191, 2007. http://dx.doi.org/10.1038/nmat1849.

[3] A. A. Balandin, S. Ghosh, W. Bao, I. Calizo, D. Teweldebrhan, F. Miao, and C. N. Lau. *Superior thermal conductivity of single-layer graphene.* Nano Lett., 8, 3, pp. 902–907, 2008. http://dx.doi.org/10.1021/nl0731872.

[4] M. Y. Han, B. Zyilmaz, Y. Zhang, and P. Kim. *Energy band-gap engineering of graphene nanoribbons.* Phys. Rev. Lett., 98, 20, pp. 1–4, 2007. http://dx.doi.org/10.1103/PhysRevLett.98.206805.

[5] E. J. Duplock, M. Scheffler, and P. J. D. Lindan. *Hallmark of perfect graphene.* Phys. Rev. Lett., 92, 22, pp. 225502–1, 2004. http://dx.doi.org/10.1103/PhysRevLett.92.225502.

[6] R. Balog, B. Jørgensen, L. Nilsson, M. Andersen, E. Rienks, M. Bianchi, M. Fanetti, E. Lægsgaard, A. Baraldi, S. Lizzit, Ž. Šljivančanin, F. Besenbacher, B. Hammer, T. G. Pedersen, P. Hofmann, and L. Hornekær. *Bandgap opening in graphene induced by patterned hydrogen adsorption.* Nat. Mater., 9, 4, pp. 315–9, 2010. http://dx.doi.org/10.1038/nmat2710.

[7] S. Bae, H. Kim, Y. Lee, X. Xu, J.-S. Park, Y. Zheng, J. Balakrishnan, T. Lei, H. Ri Kim, Y. I. Song, Y.-J. Kim, K. S. Kim, B. Özyilmaz, J.-H. Ahn, B. H. Hong, and S. Iijima. *Roll-to-roll production of 30-inch graphene films for transparent electrodes.* Nat. Nanotechnol., 5, 8, pp. 574–578, 2010. http://dx.doi.org/10.1038/nnano.2010.132.

[8] I. Šrut Rakić, D. Čapeta, M. Plodinec, and M. Kralj. *Large-scale transfer and characterization of macroscopic periodically nano-rippled graphene.* Carbon, 96, pp. 243–249, 2015. http://dx.doi.org/10.1016/j.carbon.2015.09.046.

[9] R. Larciprete, S. Ulstrup, P. Lacovig, M. Dalmiglio, M. Bianchi, F. Mazzola, L. Hornekær, F. Orlando, A. Baraldi, P. Hofmann, and S. Lizzit. *Oxygen switching of the epitaxial graphene-metal interaction.* ACS Nano, 6, 11, pp. 9551–9558, 2012. http://dx.doi.org/10.1021/nn302729j.

[10] P. Pervan, P. Lazić, M. Petrović, I. Šrut Rakić, I. Pletikosić, M. Kralj, M. Milun, and T. Valla. *Li adsorption versus graphene intercalation on Ir(111): From quenching to restoration of the Ir surface state.* Phys. Rev. B, 92, 24, pp. 1–6, 2015. http://dx.doi.org/10.1103/PhysRevB.92.245415.

[11] M. I. Katsnelson, K. S. Novoselov, and A. K. Geim. *Chiral tunnelling and the Klein paradox in graphene.* Nat. Phys., 2, September, p. 1986, 2006. http://dx.doi.org/10.1038/nphys384.

[12] Y. Zhang, Y. Tan, H. Stormer, and P. Kim. *Experimental observation of the quantum Hall effect and Berry's phase in graphene.* Nature, 438, 7065, pp. 201–204, 2005. http://dx.doi.org/10.1038/Nature04235.

[13] K. Novoselov, A. Geim, S. Morozov, D. Jiang, M. Katsnelson, I. Grigorieva, S. Dubonos, and A. Firsov. *Two-dimensional gas of massless Dirac fermions in graphene.* Nature, 438, 7065, pp. 197–200, 2005. http://dx.doi.org/10.1038/Nature04233.

[14] G. Ruan, Z. Sun, Z. Peng, and J. M. Tour. *Growth of graphene from food, insects, and waste.* ACS Nano, 5, 9, pp. 7601–7607, 2011. http://dx.doi.org/10.1021/nn202625c.

[15] J. Brunner and H. Hammerschmid. *Zur Morphologie des Graphits.* Z. anorg. allg. Chem., 155, 1, pp. 255–256, 1926. http://dx.doi.org/10.1002/zaac.19261550125.

[16] H. Kim, T. Balgar, and E. Hasselbrink. *Is there sp3-bound H on epitaxial graphene? Evidence for adsorption on both sides of the sheet.* Chem. Phys. Lett., 546, pp. 12–17, 2012. http://dx.doi.org/10.1016/j.cplett.2012.07.049.

[17] T. Balgar, H. Kim, and E. Hasselbrink. *Preparation of graphene with graphane areas of controlled hydrogen isotope composition on opposite sides.* J. Phys. Chem. Lett., 4, 12, pp. 2094–2098, 2013. http://dx.doi.org/10.1021/jz400690w.

[18] L. Kyhl, R. Balog, T. Angot, L. Hornekær, and R. Bisson. *Hydrogenated graphene on Ir(111): A high-resolution electron energy loss spectroscopy study of the vibrational spectrum.* Phys. Rev. B, 93, 11, p. 115403, 2016. http://dx.doi.org/10.1103/PhysRevB.93.115403.

[19] *Graphen-Modell by AlexanderAlUS.* `https://de.wikipedia.org/wiki/Graphen#/media/File:Graphen.jpg`. Accessed: 28.06.2016. Published under `http://creativecommons.org/licenses/by-sa/3.0/`.

[20] C. Lee, X. Wei, J. W. Kysar, and J. Hone. *Measurement of the elastic properties and intrinsic strength of monolayer graphene.* Science, 321, pp. 385–388, 2008.

[21] `http://www.head.com/en/sports/tennis/technology/graphene-xt/?_ga=1.193847725.1086092799.1465132447`. Accessed: 28.06.2016.

[22] A. H. Castro Neto, F. Guinea, N. M. R. Peres, K. S. Novoselov, and A. K. Geim. *The electronic properties of graphene.* Rev. Mod. Phys., 81, pp. 109–162, 2009. http://dx.doi.org/10.1103/RevModPhys.81.109.

[23] A. T. N'Diaye, J. Coraux, T. N. Plasa, C. Busse, and T. Michely. *Structure of epitaxial graphene on Ir(111).* New J. Phys., 10, 4, p. 043033, 2008. http://dx.doi.org/10.1088/1367-2630/10/4/043033.

[24] C. Busse, P. Lazić, R. Djemour, J. Coraux, T. Gerber, N. Atodiresei, V. Caciuc, R. Brako, A. T. N'Diaye, S. Blügel, J. Zegenhagen, and T. Michely. *Graphene on Ir(111): Physisorption with chemical modulation.* Phys. Rev. Lett., 107, p. 036101, 2011. http://dx.doi.org/10.1103/PhysRevLett.107.036101.

[25] J. Coraux, A. T. N'Diaye, C. Busse, and T. Michely. *Structural coherency of graphene on Ir(111).* Nano Lett., 8, p. 565, 2008.

[26] M. Kralj, I. Pletikosić, M. Petrović, P. Pervan, M. Milun, A. T. N'Diaye, C. Busse, T. Michely, J. Fujii, and I. Vobornik. *Graphene on Ir(111) characterized by angle-resolved photoemission.* Phys. Rev. B, 84, 7, p. 075427, 2011. http://dx.doi.org/10.1103/PhysRevB.84.075427.

[27] A. T. N'Diaye, T. Gerber, C. Busse, J. Mysliveček, J. Coraux, and T. Michely. *A versatile fabrication method for cluster superlattices.* New J. Phys., 11, p. 103045, 2009. Published under https://creativecommons.org/licenses/by-nc-sa/3.0/. http://dx.doi.org/10.1088/1367-2630/11/10/103045.

[28] P. J. Feibelman. *Pinning of graphene to Ir(111) by flat Ir dots.* Phys. Rev. B, 77, 16, 165419, 2008. http://dx.doi.org/10.1103/PhysRevB.77.165419.

[29] J. Knudsen, P. J. Feibelman, T. Gerber, E. Grånäs, K. Schulte, P. Stratmann, J. N. Andersen, and T. Michely. *Clusters binding to the graphene moiré on Ir(111): X-ray photoemission compared to density functional calculations.* Phys. Rev. B, 85, p. 035407, 2012. http://dx.doi.org/10.1103/PhysRevB.85.035407.

[30] K. Oura. *Surface science - An introduction.* Springer Verlag, 2003.

[31] M. P. Seah and W. A. Dench. *Quantitative electron spectroscopy of surfaces: A standard data base for electron inelastic mean free paths in solids.* Surf. Interface Anal., 1, 1, pp. 2–11, 1979. http://dx.doi.org/10.1002/sia.740010103.

[32] E. Grånäs, T. Gerber, U. A. Schröder, K. Schulte, J. N. Andersen, T. Michely, and J. Knudsen. *Hydrogen intercalation under graphene on Ir(111).* Surf. Sci., pp. 1–5, 2016. http://dx.doi.org/10.1016/j.susc.2016.03.002.

[33] E. Grånäs, J. Knudsen, U. A. Schröder, T. Gerber, C. Busse, M. A. Arman, K. Schulte, J. N. Andersen, and T. Michely. *Oxygen intercalation under graphene on Ir(111): Energetics, kinetics, and the role of graphene edges.* ACS Nano, 6, 11, pp. 9951–9963, 2012. http://dx.doi.org/10.1021/nn303548z.

[34] J. Knudsen, P. J. Feibelman, T. Gerber, E. Grånäs, K. Schulte, P. Stratmann, J. N. Andersen, and T. Michely. *Clusters binding to the graphene moiré on Ir(111): X-ray photoemission compared to density functional calculations.* Phys. Rev. B, 85, 3, p. 035407, 2012. http://dx.doi.org/10.1103/PhysRevB.85.035407.

[35] W. F. Egelhoff. *Core-level binding-energy shifts at surfaces and in solids.* Surf. Sci. Rep., 6, 6-8, pp. 253 – 415, 1987. http://dx.doi.org/10.1016/0167-5729(87)90007-0.

[36] P. S. Bagus, F. Illas, G. Pacchioni, and F. Parmigiani. *Mechanisms responsible for chemical shifts of core-level binding energies and their relationship to chemical bonding.* J. Electron Spectros. Relat. Phenomena, 100, 1-3, pp. 215–236, 1999. http://dx.doi.org/10.1016/S0368-2048(99)00048-1.

[37] P. W. Atkins and J. de Paula. *Physikalische Chemie.* Wiley-VCH Verlag, Weinheim, 2013.

[38] C. Riedl, C. Coletti, T. Iwasaki, A. A. Zakharov, and U. Starke. *Quasi-free-standing epitaxial graphene on SiC obtained by hydrogen intercalation.* Phys. Rev. Lett., 103, p. 246804, 2009. http://dx.doi.org/10.1103/PhysRevLett.103.246804.

[39] J. A. Robinson, M. Hollander, M. LaBella, K. A. Trumbull, R. Cavalero, and D. W. Snyder. *Epitaxial graphene transistors: Enhancing performance via hydrogen intercalation.* Nano Lett., 11, 9, pp. 3875–3880, 2011. http://dx.doi.org/10.1021/nl2019855.

[40] S. Oida, F. R. McFeely, J. B. Hannon, R. M. Tromp, M. Copel, Z. Chen, Y. Sun, D. B. Farmer, and J. Yurkas. *Decoupling graphene from SiC(0001) via oxidation.* Phys. Rev. B, 82, p. 041411, 2010. http://dx.doi.org/10.1103/PhysRevB.82.041411.

[41] P. Sutter, J. T. Sadowski, and E. A. Sutter. *Chemistry under cover: Tuning metal-graphene interaction by reactive intercalation.* J. Am. Chem. Soc., 132, 23, pp. 8175–8179, 2010. http://dx.doi.org/10.1021/ja102398n.

[42] E. Starodub, N. C. Bartelt, and K. F. McCarty. *Oxidation of graphene on metals.* J. Phys. Chem. C, 114, 11, pp. 5134–5140, 2010. http://dx.doi.org/10.1021/jp912139e.

[43] C. Herbig, M. Kaiser, N. Bendiab, S. Schumacher, D. F. Förster, J. Coraux, K. Meerholz, T. Michely, and C. Busse. *Mechanical exfoliation of epitaxial graphene on Ir(111) enabled by Br_2 intercalation.* J. Phys. Condens. Matter, 24, 31, p. 314208, 2012.

[44] I. Pletikosić, M. Kralj, P. Pervan, R. Brako, J. Coraux, A. T. N'Diaye, C. Busse, and T. Michely. *Dirac cones and minigaps for graphene on Ir(111).* Phys. Rev. Lett., 102, p. 056808, 2009. http://dx.doi.org/10.1103/PhysRevLett.102.056808.

[45] L. Huang, Y. Pan, L. Pan, M. Gao, W. Xu, Y. Que, H. Zhou, Y. Wang, S. Du, and H. J. Gao. *Intercalation of metal islands and films at the interface of epitaxially grown graphene and Ru(0001) surfaces.* Appl. Phys. Lett., 99, 16, 2011. http://dx.doi.org/10.1063/1.3653241.

[46] A. Varykhalov, J. Sánchez-Barriga, A. M. Shikin, C. Biswas, E. Vescovo, A. Rybkin, D. Marchenko, and O. Rader. *Electronic and magnetic properties of quasifreestanding graphene on Ni.* Phys. Rev. Lett., 101, 15, p. 157601, 2008. http://dx.doi.org/10.1103/PhysRevLett.101.157601.

[47] Y. S. Dedkov, M. Fonin, U. Rüdiger, and C. Laubschat. *Graphene-protected iron layer on Ni(111).* Appl. Phys. Lett., 93, 2, p. 022509, 2008. http://dx.doi.org/10.1063/1.2953972.

[48] B. Premlal, M. Cranney, F. Vonau, D. Aubel, D. Casterman, M. M. De Souza, and L. Simon. *Surface intercalation of gold underneath a graphene monolayer on SiC(0001) studied by scanning tunneling microscopy and spectroscopy.* Appl. Phys. Lett., 94, 26, pp. 9–11, 2009. http://dx.doi.org/10.1063/1.3168502.

[49] L. Jin, Q. Fu, R. Mu, D. Tan, and X. Bao. *Pb intercalation underneath a graphene layer on Ru(0001) and its effect on graphene oxidation.* Phys. Chem. Chem. Phys., 13, 37, pp. 16655–16660, 2011. http://dx.doi.org/10.1039/c1cp21843c.

[50] A. L. Walter, K.-J. Jeon, A. Bostwick, F. Speck, M. Ostler, T. Seyller, L. Moreschini, Y. S. Kim, Y. J. Chang, K. Horn, and E. Rotenberg. *Highly p-doped epitaxial graphene obtained by fluorine intercalation.* Appl. Phys. Lett., 98, 18, 184102, 2011. http://dx.doi.org/10.1063/1.3586256.

[51] C. W. Tucker. *Low-energy electron diffraction studies of gas adsorption on platinum (100), (110), and (111) surfaces.* J. Appl. Phys., 35, 6, p. 1897, 1964. http://dx.doi.org/10.1063/1.1713766.

[52] P. Zhdan, G. Boreskov, W. Egelhoff, and W. Weinberg. *The application of XPS to the determination of the kinetics of the CO oxidation reaction over the Ir(111) surface.* Surf. Sci., 61, 2, pp. 377–390, 1976. http://dx.doi.org/10.1016/0039-6028(76)90052-2.

[53] A. J. Martínez-Galera, U. A. Schröder, F. Huttmann, W. Jolie, F. Craes, C. Busse, V. Caciuc, N. Atodiresei, S. Blügel, and

T. Michely. *Oxygen orders differently under graphene: New superstructures on Ir(111).* Nanoscale, 8, 4, pp. 1932–1943, 2016. http://dx.doi.org/10.1039/C5NR04976H.

[54] W. Jolie, F. Craes, M. Petrović, N. Atodiresei, V. Caciuc, S. Blügel, M. Kralj, T. Michely, and C. Busse. *Confinement of Dirac electrons in graphene quantum dots.* Phys. Rev. B, 89, 15, p. 155435, 2014. http://dx.doi.org/10.1103/PhysRevB.89.155435.

[55] U. A. Schröder. *Interaction of molecular oxygen with graphene on Ir(111): Intercalation and etching*, Master thesis, Universität zu Köln, 2012.

[56] S. Schumacher, T. O. Wehling, P. Lazić, S. Runte, D. F. Förster, C. Busse, M. Petrović, M. Kralj, S. Blügel, N. Atodiresei, V. Caciuc, and T. Michely. *The backside of graphene: Manipulating adsorption by intercalation.* Nano Lett., 13, 11, pp. 5013–5019, 2013. http://dx.doi.org/10.1021/nl402797j.

[57] S. Schumacher, F. Huttmann, M. Petrović, C. Witt, D. F. Förster, C. Vo-Van, J. Coraux, A. J. Martínez-Galera, V. Sessi, I. Vergara, R. Rückamp, M. Grüninger, N. Schleheck, F. Meyer zu Heringdorf, P. Ohresser, M. Kralj, T. O. Wehling, and T. Michely. *Europium underneath graphene on Ir(111): Intercalation mechanism, magnetism, and band structure.* Phys. Rev. B, 90, 23, p. 235437, 2014. http://dx.doi.org/10.1103/PhysRevB.90.235437.

[58] M. Petrović, I. Šrut Rakić, S. Runte, C. Busse, J. T. Sadowski, P. Lazić, I. Pletikosić, Z.-H. Pan, M. Milun, P. Pervan, N. Atodiresei, R. Brako, D. Šokčević, T. Valla, T. Michely, and M. Kralj. *The mechanism of caesium intercalation of graphene.* Nat. Commun., 4, p. 2772, 2013. http://dx.doi.org/10.1038/ncomms3772.

[59] S. Basu, C. Zeller, P. Flanders, C. Fuerst, W. Johnson, and J. Fischer. *Synthesis and properties of lithium-graphite intercalation compounds.* Mater. Sci. Eng., 38, 3, pp. 275–283, 1979. http://dx.doi.org/10.1016/0025-5416(79)90132-0.

[60] G. Wertheim, P. Van Attekum, and S. Basu. *Electronic structure of lithium graphite.* Solid State Commun., 33, 11, pp. 1127–1130, 1980. http://dx.doi.org/10.1016/0038-1098(80)91089-3.

[61] C. Virojanadara, S. Watcharinyanon, A. A. Zakharov, and L. I. Johansson. *Epitaxial graphene on 6H-SiC and Li intercalation.* Phys. Rev. B, 82, 20, pp. 1–6, 2010. http://dx.doi.org/10.1103/PhysRevB.82.205402.

[62] J. Halle, N. Néel, and J. Kröger. *Filling the gap: Li-intercalated graphene on Ir(111).* J. Phys. Chem. C, 120, 9, pp. 5067–5073, 2016. http://dx.doi.org/10.1021/acs.jpcc.6b00729.

[63] D. Haberer, D. V. Vyalikh, S. Taioli, B. Dora, M. Farjam, J. Fink, D. Marchenko, T. Pichler, K. Ziegler, S. Simonucci, M. S. Dresselhaus, M. Knupfer, B. Büchner, and A. Grüneis. *Tunable band gap in hydrogenated quasi-free-standing graphene.* Nano Lett., 10, 9, pp. 3360–3366, 2010. http://dx.doi.org/10.1021/nl101066m.

[64] A. M. Shikin, G. V. Prudnikova, V. K. Adamchuk, F. Moresco, and K.-H. Rieder. *Surface intercalation of gold underneath a graphite monolayer on Ni(111) studied by angle-resolved photoemission and high-resolution electron-energy-loss spectroscopy.* Phys. Rev. B, 62, 19, pp. 13202–13208, 2000. http://dx.doi.org/10.1103/PhysRevB.62.13202.

[65] I. Gierz, T. Suzuki, R. T. Weitz, D. S. Lee, B. Krauss, C. Riedl, U. Starke, H. Höchst, J. H. Smet, C. R. Ast, and K. Kern. *Electronic decoupling of an epitaxial graphene monolayer by gold intercalation.* Phys. Rev. B, 81, 23, p. 235408, 2010. http://dx.doi.org/10.1103/PhysRevB.81.235408.

[66] C. Enderlein, Y. S. Kim, A. Bostwick, E. Rotenberg, and K. Horn. *The formation of an energy gap in graphene on ruthenium by controlling the interface.* New J. Phys., 12, pp. 0–9, 2010. http://dx.doi.org/10.1088/1367-2630/12/3/033014.

[67] P. Leicht, L. Zielke, S. Bouvron, R. Moroni, E. Voloshina, L. Hammerschmidt, Y. S. Dedkov, and M. Fonin. *In situ fabrication of quasi-free-standing epitaxial graphene nanoflakes on gold.* ACS Nano, 8, 4, pp. 3735–3742, 2014. http://dx.doi.org/10.1021/nn500396c.

[68] J. M. Wofford, E. Starodub, A. L. Walter, S. Nie, A. Bostwick, N. C. Bartelt, K. Thürmer, E. Rotenberg, K. F. McCarty, and O. D. Dubon. *Extraordinary epitaxial alignment of graphene islands on Au(111).* New J. Phys., 14, 5, p. 053008, 2012. http://dx.doi.org/10.1088/1367-2630/14/5/053008.

[69] A. Varykhalov, M. R. Scholz, T. K. Kim, and O. Rader. *Effect of noble-metal contacts on doping and band gap of graphene.* Phys. Rev. B, 82, 12, p. 121101, 2010. http://dx.doi.org/10.1103/PhysRevB.82.121101.

[70] C. J. Murphy, X. Shi, A. D. Jewell, A. F. McGuire, D. O. Bellisario, A. E. Baber, H. L. Tierney, E. A. Lewis, D. S. Sholl, and E. C. H. Sykes. *Impact of branching on the supramolecular assembly of thioethers on Au(111).* J. Chem. Phys., 142, 10, 2015. http://dx.doi.org/10.1063/1.4907270.

[71] Z.-X. Xie, Z.-F. Huang, and X. Xu. *Influence of reconstruction on the structure of self-assembled normal-alkane monolayers on Au(111) surfaces.* Phys. Chem. Chem. Phys., 4, 8, pp. 1486–1489, 2002. http://dx.doi.org/10.1039/b109159j.

[72] C. Wöll, S. Chiang, R. J. Wilson, and P. H. Lippel. *Determination of atom positions at stacking-fault dislocations on Au(111) by scanning tunneling microscopy.* Phys. Rev. B, 39, 11, pp. 7988–7991, 1989.

[73] J. V. Barth, H. Brune, G. Ertl, and R. J. Behm. *Scanning tunneling microscopy observations on the reconstructed Au(111) surface: Atomic structure, long-range superstructure, rotational domains, and surface defects.* Phys. Rev. B, 42, 15, pp. 9307–9318, 1990. http://dx.doi.org/10.1103/PhysRevB.42.9307.

[74] H. Brune, H. Röder, C. Boragno, and K. Kern. *Strain relief at hexagonal-close-packed interfaces.* Phys. Rev. B, 49, 4, pp. 2997–3000, 1994. http://dx.doi.org/10.1103/PhysRevB.49.2997.

[75] C. B. Carter and R. Q. Hwang. *Dislocations and the reconstruction of (111) fcc metal surfaces.* Phys. Rev. B, 51, 7, pp. 4730–4733, 1995. http://dx.doi.org/10.1103/PhysRevB.51.4730.

[76] H. Brune and K. Kern. *Chapter 5 Heteroepitaxial metal growth: the effects of strain.* In D. King and D. Woodruff, eds., *Growth and Properties of Ultrathin Epitaxial Layers*, vol. 8 of *The Chemical Physics of Solid Surfaces*, pp. 149 – 206. Elsevier, 1997.

[77] G. O. Pötschke and R. J. Behm. *Interface structure and misfit dislocations in thin Cu films on Ru(0001).* Phys. Rev. B, 44, 3, pp. 1442–1445, 1991. http://dx.doi.org/10.1103/PhysRevB.44.1442.

[78] C. Günther, J. Vrijmoeth, R. Q. Hwang, and R. J. Behm. *Strain relaxation in hexagonally close-packed metal-metal*

interfaces. Phys. Rev. Lett., 74, 5, pp. 754–757, 1995. http://dx.doi.org/10.1103/PhysRevLett.74.754.

[79] M. Parschau, D. Schlatterbeck, and K. Christmann. *Nucleation and growth of silver films on a rhenium (0001) surface: A combined STM and LEED study.* Surf. Sci., 376, pp. 133–150, 1997. http://dx.doi.org/10.1016/S0039-6028(96)01303-9.

[80] S. Ouazi, T. Pohlmann, A. Kubetzka, K. Von Bergmann, and R. Wiesendanger. *Scanning tunneling microscopy study of Fe, Co and Cr growth on Re(0001).* Surf. Sci., 630, pp. 280–285, 2014. http://dx.doi.org/10.1016/j.susc.2014.08.026.

[81] R. Q. Hwang, J. C. Hamilton, J. L. Stevens, and S. M. Foiles. *Near-surface buckling in strained metal overlayer systems.* Phys. Rev. Lett., 75, 23, pp. 4242–4245, 1995. http://dx.doi.org/10.1103/PhysRevLett.75.4242.

[82] W. L. Ling, J. De La Figuera, N. C. Bartelt, R. Q. Hwang, A. K. Schmid, G. E. Thayer, and J. C. Hamilton. *Strain relief through heterophase interface reconstruction: Ag(111)/Ru(0001).* Phys. Rev. Lett., 92, 11, pp. 116102–1, 2004. http://dx.doi.org/10.1103/PhysRevLett.92.116102.

[83] W. L. Ling, J. C. Hamilton, K. Thürmer, G. E. Thayer, J. de la Figuera, R. Q. Hwang, C. B. Carter, N. C. Bartelt, and K. F. McCarty. *Herringbone and triangular patterns of dislocations in Ag, Au, and AgAu alloy films on Ru(0001).* Surf. Sci., 600, 9, pp. 1735–1757, 2006. http://dx.doi.org/10.1016/j.susc.2006.01.055.

[84] J. Hamilton, R. Stumpf, K. Bromann, M. Giovannini, K. Kern, and H. Brune. *Dislocation structures of submonolayer films near the commensurate-incommensurate phase transition: Ag on Pt(111).* Phys. Rev. Lett., 82, 22, pp. 4488–4491, 1999. http://dx.doi.org/10.1103/PhysRevLett.82.4488.

[85] V. Fournée, J. Ledieu, T. Cai, and P. Thiel. *Influence of strain in Ag on Al(111) and Al on Ag(100) thin film growth.* Phys. Rev. B, 67, 15, pp. 3–8, 2003. http://dx.doi.org/10.1103/PhysRevB.67.155401.

[86] J. de la Figuera, A. Schmid, N. Bartelt, K. Pohl, and R. Hwang. *Determination of buried dislocation structures by scanning tunneling microscopy.* Phys. Rev. B, 63, 16, p. 165431, 2001. http://dx.doi.org/10.1103/PhysRevB.63.165431.

[87] E. Lundgren, B. Stanka, M. Schmid, and P. Varga. *Thin films of Co on Pt(111): Strain relaxation and growth.* Phys. Rev. B, 62, 4, pp. 2843–2851, 2000. http://dx.doi.org/10.1103/PhysRevB.62.2843.

[88] M. Stindtmann, M. Farle, T. S. Rahman, L. Benabid, and K. Baberschke. *Growth and morphology of Ni(111)/Re(0001) ultrathin films: An in-situ study using scanning tunneling microscopy.* Surf. Sci., 381, 1, pp. 12–17, 1997. http://dx.doi.org/Doi 10.1016/S0039-6028(97)00067-8.

[89] C. Hagedorn, M. Weiss, and W. Weinberg. *Dissociative chemisorption of hydrogen on Ir(111): Evidence for terminal site adsorption.* Phys. Rev. B, 60, 20, pp. R14016–R14018, 1999. http://dx.doi.org/10.1103/PhysRevB.60.R14016.

[90] J. Lauterbach, M. Schick, and W. H. Weinberg. *Coadsorption of CO and hydrogen on the Ir(111) surface.* J. Vac. Sci. Technol. A, 14, 3, p. 1511, 1996. http://dx.doi.org/10.1116/1.579978.

[91] W. P. Krekelberg, J. Greeley, and M. Mavrikakis. *Atomic and molecular adsorption on Ir(111).* J. Phys. Chem. B, 108, 3, pp. 987–994, 2004. http://dx.doi.org/10.1021/jp035786c.

[92] K. Moritani, M. Okada, M. Nakamura, T. Kasai, and Y. Murata. *Hydrogen-exchange reactions via hot hydrogen atoms produced in the dissociation process of molecular hydrogen on Ir(111).* J. Chem. Phys., 115, 21, p. 9947, 2001. http://dx.doi.org/10.1063/1.1415494.

[93] D. C. Elias, R. R. Nair, T. M. G. Mohiuddin, S. V. Morozov, P. Blake, M. P. Halsall, A. C. Ferrari, D. W. Boukhvalov, M. I. Katsnelson, A. K. Geim, and K. S. Novoselov. *Control of graphene's properties by reversible hydrogenation: Evidence for graphane.* Science, 323, 5914, pp. 610–613, 2009. http://dx.doi.org/10.1126/science.1167130.

[94] A. Savchenko. *Transforming graphene.* Science, 323, 5914, pp. 589–590, 2009. http://dx.doi.org/10.1126/science.1169246.

[95] T. Zecho, A. Güttler, X. Sha, B. Jackson, and J. Küppers. *Adsorption of hydrogen and deuterium atoms on the (0001) graphite surface.* J. Chem. Phys., 117, 18, p. 8486, 2002. http://dx.doi.org/10.1063/1.1511729.

[96] T. Zecho, A. Güttler, and J. Küppers. *A TDS study of D adsorption on terraces and terrace edges of graphite (0001) surfaces.* Carbon, 42, 3, pp. 609–617, 2004. http://dx.doi.org/10.1016/j.carbon.2003.12.068.

[97] L. Hornekær, Ž. Šljivančanin, W. Xu, R. Otero, E. Rauls, I. Stensgaard, E. Lægsgaard, B. Hammer, and F. Besenbacher. *Metastable structures and recombination pathways for atomic hydrogen on the graphite (0001) surface.* Phys. Rev. Lett., 96, 15, p. 156104, 2006. http://dx.doi.org/10.1103/PhysRevLett.96.156104.

[98] L. Hornekær, E. Rauls, W. Xu, Ž. Šljivančanin, R. Otero, I. Stensgaard, E. Lægsgaard, B. Hammer, and F. Besenbacher. *Clustering of chemisorbed H(D) atoms on the graphite (0001) surface due to preferential sticking.* Phys. Rev. Lett., 97, 18, p. 186102, 2006. http://dx.doi.org/10.1103/PhysRevLett.97.186102.

[99] S. Baouche, G. Gamborg, V. V. Petrunin, A. C. Luntz, A. Baurichter, L. Hornekær, S. Baouche, G. Gamborg, V. V. Petrunin, A. C. Luntz, and A. Baurichter. *High translational energy release in H_2 (D_2) associative desorption from H (D) chemisorbed on C(0001).* J. Chem. Phys., 125, p. 084712, 2006. http://dx.doi.org/10.1063/1.2220565.

[100] A. Andree, M. L. Lay, T. Zecho, and J. Küpper. *Pair formation and clustering of D on the basal plane of graphite.* Chem. Phys. Lett., 425, 1-3, pp. 99–104, 2006. http://dx.doi.org/10.1016/j.cplett.2006.05.015.

[101] G. Vidali. *H_2 formation on interstellar grains.* Chem. Rev., 113, 12, pp. 8762–8782, 2013. http://dx.doi.org/10.1021/cr400156b.

[102] S. Cazaux and A. G. G. M. Tielens. *H_2 formation on grain surfaces.* Astrophys. J., 604, pp. 222–237, 2004.

[103] D. A. Williams and E. Herbst. *It's a dusty Universe: Surface science in space.* Surf. Sci., 500, 1-3, pp. 823–837, 2002. http://dx.doi.org/10.1016/S0039-6028(01)01538-2.

[104] S. Casolo, O. M. Løvvik, R. Martinazzo, and G. F. Tantardini. *Understanding adsorption of hydrogen atoms on graphene.* J. Chem. Phys., 130, 5, 2009. http://dx.doi.org/10.1063/1.3072333.

[105] R. Balog, M. Andersen, B. Jørgensen, Ž. Šljivančanin, B. Hammer, A. Baraldi, R. Larciprete, P. Hofmann, L. Hornekær, and S. Lizzit. *Controlling hydrogenation of graphene on Ir(111).* ACS Nano, 7, 5, pp. 3823–32, 2013. http://dx.doi.org/10.1021/nn400780x.

[106] M. L. Ng, R. Balog, L. Hornekær, A. B. Preobrajenski, N. A. Vinogradov, N. Mårtensson, and K. Schulte. *Controlling hydrogenation of*

graphene on transition metals. J. Phys. Chem. C, 114, 43, pp. 18559–18565, 2010. http://dx.doi.org/10.1021/jp106361y.

[107] H. Kim, T. Balgar, and E. Hasselbrink. *The stretching vibration of hydrogen adsorbed on epitaxial graphene studied by sum-frequency generation spectroscopy.* Chem. Phys. Lett., 508, 1-3, pp. 1–5, 2011. http://dx.doi.org/10.1016/j.cplett.2011.04.025.

[108] D. A. Abanin, A. V. Shytov, and L. S. Levitov. *Peierls-type instability and tunable band gap in functionalized graphene.* Phys. Rev. Lett., 105, 8, pp. 1–6, 2010. http://dx.doi.org/10.1103/PhysRevLett.105.086802.

[109] S. Rajasekaran, S. Kaya, F. Abild-Pedersen, T. Anniyev, F. Yang, D. Stacchiola, H. Ogasawara, and A. Nilsson. *Reversible graphene-metal contact through hydrogenation.* Phys. Rev. B, 86, 7, p. 075417, 2012. http://dx.doi.org/10.1103/PhysRevB.86.075417.

[110] S. Rajasekaran, F. Abild-Pedersen, H. Ogasawara, A. Nilsson, and S. Kaya. *Interlayer carbon bond formation induced by hydrogen adsorption in few-layer supported graphene.* Phys. Rev. Lett., 111, 8, p. 085503, 2013. http://dx.doi.org/10.1103/PhysRevLett.111.085503.

[111] M. Enachescu, D. Schleef, D. F. Ogletree, and M. Salmeron. *Integration of point-contact microscopy and atomic-force microscopy: Application to characterization of graphite/Pt(111).* Phys. Rev. B, 60, pp. 16913–16919, 1999.

[112] A. Dinger, C. Lutterloh, J. Biener, and J. Küppers. *Hydrogen atom reactions with graphite island edges on Pt(111) surfaces: hydrogenation through Eley-Rideal and hot-atom processes.* Surf. Sci., 421, 1-2, pp. 17–26, 1999. http://dx.doi.org/10.1016/S0039-6028(98)00799-7.

[113] W. Zhao, J. Gebhardt, F. Späth, K. Gotterbarm, C. Gleichweit, H. P. Steinrück, A. Görling, and C. Papp. *Reversible hydrogenation of graphene on Ni(111)-synthesis of graphone.* Chem. Eur. J., 21, 8, pp. 3347–3358, 2015. http://dx.doi.org/10.1002/chem.201404938.

[114] Y. Gamo, A. Nagashima, M. Wakabayashi, M. Terai, and C. Oshima. *Atomic structure of monolayer graphite formed on Ni(111).* Surf. Sci., 17, 12, pp. 745–749, 1997. http://dx.doi.org/10.1380/jsssj.17.745.

[115] M. Scheffler, D. Haberer, L. Petaccia, M. Farjam, R. Schlegel, D. Baumann, T. Hänke, A. Grüneis, M. Knupfer, C. Hess, and

B. Büchner. *Probing local hydrogen impurities in quasi-free-standing graphene.* ACS Nano, 6, 12, pp. 10590–10597, 2012. http://dx.doi.org/10.1021/nn303485c.

[116] A. Paris, N. Verbitskiy, A. Nefedov, Y. Wang, A. Fedorov, D. Haberer, M. Oehzelt, L. Petaccia, D. Usachov, D. Vyalikh, H. Sachdev, C. Wöll, M. Knupfer, B. Büchner, L. Calliari, L. Yashina, S. Irle, and A. Grüneis. *Kinetic Isotope Effect in the Hydrogenation and Deuteration of Graphene.* Adv. Funct. Mater., 23, 13, pp. 1628–1635, 2013. http://dx.doi.org/10.1002/adfm.201202355.

[117] R. Nyholm, J. N. Andersen, U. Johansson, B. N. Jensen, and I. Lindau. *Beamline I311 at MAX-LAB: A VUV/soft X-ray undulator beamline for high resolution electron spectroscopy.* Nucl. Instr. Meth. Phys. Res. A, 467-468, pp. 520–524, 2001. http://dx.doi.org/10.1016/S0168-9002(01)00399-0.

[118] G. Binnig, H. Rohrer, C. Gerber, and E. Weibel. *Tunneling through a controllable vacuum gap.* Appl. Phys. Lett., 40, 2, pp. 178–180, 1982. http://dx.doi.org/10.1063/1.92999.

[119] T. Michely, M. Kaiser, and M. J. Rost. *Plug "n" play scanning probe microscopy.* Rev. Sci. Instrum., 71, 12, pp. 4461–4467, 2000. http://dx.doi.org/10.1063/1.1322587.

[120] I. Horcas, R. Fernández, J. M. Gómez-Rodríguez, J. Colchero, J. Gómez-Herrero, and A. M. Baro. *WSxM: A software for scanning probe microscopy and a tool for nanotechnology.* Rev. Sci. Instrum., 78, 1, 013705, 2007. http://dx.doi.org/10.1063/1.2432410.

[121] S. Standop. *Water adsorption and ion induced defect formation: A comparative study of graphene and noble metal surfaces.* Ph.D. thesis, Universität zu Köln, 2013.

[122] D. A. King. *Thermal desorption from metal surfaces: A review.* Surf. Sci., 47, 1, pp. 384–402, 1975. http://dx.doi.org/10.1016/0039-6028(75)90302-7.

[123] P. Feulner and D. Menzel. *Simple ways to improve "flash desorption" measurements from single crystal surfaces.* J. Vac. Sci. Technol., 17, 2, p. 662, 1980. http://dx.doi.org/10.1116/1.570537.

[124] C. D. H. Murray. *Deuteration of graphene on Ir(111): Adsorption, desorption and the influence of intercalants*, Master thesis, Universität zu Köln, 2016.

[125] A. Petersen. *Diploma thesis*, 2002.

[126] http://www.maxlab.lu.se/beamlines/bli311/beamline.html.

[127] https://ulisse.elettra.trieste.it/services/elements/WebElements.html.

[128] N. Mårtensson, P. Baltzer, P. Brühwiler, J.-O. Forsell, A. Nilsson, A. Stenborg, and B. Wannberg. *A very high resolution electron spectrometer*. J. Electron. Spectrosc. Relat. Phenom., 70, 2, pp. 117 – 128, 1994. http://dx.doi.org/10.1016/0368-2048(94)02224-N.

[129] C. Herbig, E. H. Åhlgren, U. A. Schröder, A. J. Martínez-Galera, M. A. Arman, J. Kotakoski, J. Knudsen, A. V. Krasheninnikov, and T. Michely. *Xe irradiation of graphene on Ir(111): From trapping to blistering.* Phys. Rev. B, 92, 8, p. 085429, 2015. http://dx.doi.org/10.1103/PhysRevB.92.085429.

[130] J. Coraux, A. T. N'Diaye, M. Engler, C. Busse, D. Wall, N. Buckanie, F. J. Meyer Zu Heringdorf, R. Van Gastel, B. Poelsema, and T. Michely. *Growth of graphene on Ir(111).* New J. Phys., 11, 2, p. 023006, 2009. http://dx.doi.org/10.1088/1367-2630/11/2/023006.

[131] R. Van Gastel, a. T. N'Diaye, D. Wall, J. Coraux, C. Busse, N. M. Buckanie, F. J. Meyer Zu Heringdorf, M. Horn Von Hoegen, T. Michely, and B. Poelsema. *Selecting a single orientation for millimeter sized graphene sheets.* Appl. Phys. Lett., 95, 12, p. 121901, 2009. http://dx.doi.org/10.1063/1.3225554.

[132] C. Herbig, E. H. Åhlgren, W. Jolie, C. Busse, J. Kotakoski, A. V. Krasheninnikov, and T. Michely. *Interfacial carbon nanoplatelet formation by ion irradiation of graphene on iridium(111).* ACS Nano, 8, 12, pp. 12208–12218, 2014. http://dx.doi.org/10.1021/nn503874n.

[133] D. Hagen, B. Nieuwenhuys, G. Rovida, and G. Somorjai. *Low-energy electron diffraction, Auger electron spectroscopy, and thermal desorption studies of chemisorbed CO and O_2 on the (111) and stepped [6(111)x(100)] iridium surfaces.* Surf. Sci., 57, 2, pp. 632–650, 1976. http://dx.doi.org/10.1016/0039-6028(76)90352-6.

[134] M. Bianchi, D. Cassese, A. Cavallin, R. Comin, F. Orlando, L. Postregna, E. Golfetto, S. Lizzit, and A. Baraldi. *Surface core level shifts of clean and oxygen covered Ir(111).* New Journal of Physics, 11, 6, p. 063002, 2009.

[135] M. Shek, J. Hrbek, T. Sham, and G.-Q. Xu. *A soft X-ray study of the interaction of oxygen with Li.* Surf. Sci., 234, 3, pp. 324–334, 1990. http://dx.doi.org/10.1016/0039-6028(90)90564-O.

[136] U. A. Schröder, E. Gråsäs, T. Gerber, M. A. Arman, A. J. Martínez-Galera, K. Schulte, J. N. Andersen, J. Knudsen, and T. Michely. *Etching of graphene on Ir(111) with molecular oxygen.* Carbon, 96, pp. 320–331, 2016. http://dx.doi.org/10.1016/j.carbon.2015.09.063.

[137] Y. W. Yang and J. Hrbek. *Oxidation of cesium-modified graphite supported on a Ru(001) surface.* J. Phys. Chem., 99, 10, pp. 3229–3234, 1995. http://dx.doi.org/10.1021/j100010a038.

[138] L. Liu, S. Ryu, M. R. Tomasik, E. Stolyarova, N. Jung, M. S. Hybertsen, M. L. Steigerwald, L. E. Brus, and G. W. Flynn. *Graphene oxidation: Thickness-dependent etching and strong chemical doping.* Nano Lett., 8, 7, pp. 1965–1970, 2008. http://dx.doi.org/10.1021/nl0808684.

[139] J. M. Carlsson, F. Hanke, S. Linic, and M. Scheffler. *Two-step mechanism for low-temperature oxidation of vacancies in graphene.* Phys. Rev. Lett., 102, 16, p. 166104, 2009. http://dx.doi.org/10.1103/PhysRevLett.102.166104.

[140] H. Zhang, Q. Fu, Y. Cui, D. Tan, and X. Bao. *Growth mechanism of graphene on Ru(0001) and O_2 adsorption on the graphene/Ru(0001) surface.* J. Phys. Chem. C, 113, 19, pp. 8296–8301, 2009. http://dx.doi.org/10.1021/jp810514u.

[141] Y. Cui, Q. Fu, H. Zhang, D. Tan, and X. Bao. *Dynamic characterization of graphene growth and etching by oxygen on Ru(0001) by photoemission electron microscopy.* J. Phys. Chem. C, 113, 47, pp. 20365–20370, 2009. http://dx.doi.org/10.1021/jp907949a.

[142] E. Starodub, N. C. Bartelt, and K. F. McCarty. *Oxidation of graphene on metals.* J. Phys. Chem. C, 114, 11, pp. 5134–5140, 2010. http://dx.doi.org/10.1021/jp912139e.

[143] D. L. Duong, G. H. Han, S. M. Lee, F. Gunes, E. S. Kim, S. T. Kim, H. Kim, Q. H. Ta, K. P. So, S. J. Yoon, S. J. Chae, Y. W. Jo, M. H.

Park, S. H. Chae, S. C. Lim, J. Y. Choi, and Y. H. Lee. *Probing graphene grain boundaries with optical microscopy.* Nature, 490, 7419, pp. 235–239, 2012. http://dx.doi.org/10.1038/nature11562.

[144] K. Gotterbarm, W. Zhao, O. Höfert, C. Gleichweit, C. Papp, and H.-P. Steinrück. *Growth and oxidation of graphene on Rh(111).* Phys. Chem. Chem. Phys., 15, 45, pp. 19625–31, 2013. http://dx.doi.org/10.1039/c3cp53802h.

[145] Y. Zhang, Q. Fu, Y. Cui, R. Mu, L. Jin, and X. Bao. *Enhanced reactivity of graphene wrinkles and their function as nanosized gas inlets for reactions under graphene.* Phys. Chem. Chem. Phys., 15, 43, pp. 19042–8, 2013. http://dx.doi.org/10.1039/c3cp52115j.

[146] I. Vlassiouk, P. Fulvio, H. Meyer, N. Lavrik, S. Dai, P. Datskos, and S. Smirnov. *Large scale atmospheric pressure chemical vapor deposition of graphene.* Carbon, 54, pp. 58–67, 2013. http://dx.doi.org/10.1016/j.carbon.2012.11.003.

[147] R. Blume, P. R. Kidambi, B. C. Bayer, R. S. Weatherup, Z.-J. Wang, G. Weinberg, M.-G. Willinger, M. Greiner, S. Hofmann, A. Knop-Gericke, and R. Schlogl. *The influence of intercalated oxygen on the properties of graphene on polycrystalline Cu under various environmental conditions.* Phys. Chem. Chem. Phys., 16, pp. 25989–26003, 2014. http://dx.doi.org/10.1039/C4CP04025B.

[148] N. Severin, S. Kirstein, I. M. Sokolov, and J. P. Rabe. *Rapid trench channeling of graphenes with catalytic silver nanoparticles.* Nano Lett., 9, 1, pp. 457–461, 2009. http://dx.doi.org/10.1021/nl8034509.

[149] P. Nemes-Incze, G. Magda, K. Kamarás, and L. P. Biró. *Crystallographically selective nanopatterning of graphene on SiO2.* Nano Res., 3, 2, pp. 110–116, 2010. http://dx.doi.org/10.1007/s12274-010-1015-3.

[150] N. A. Vinogradov, K. Schulte, M. L. Ng, A. Mikkelsen, E. Lundgren, N. Mårtensson, and A. B. Preobrajenski. *Impact of atomic oxygen on the structure of graphene formed on Ir(111) and Pt(111).* J. Phys. Chem. C, 115, 19, pp. 9568–9577, 2011. http://dx.doi.org/10.1021/jp111962k.

[151] T. J. Booth, F. Pizzocchero, H. Andersen, T. W. Hansen, J. B. Wagner, J. R. Jinschek, R. E. Dunin-Borkowski, O. Hansen, and P. Bøggild. *Discrete dynamics of nanoparticle channelling in*

suspended graphene. Nano Lett., 11, 7, pp. 2689–2692, 2011. http://dx.doi.org/10.1021/nl200928k.

[152] Q. M. Ramasse, R. Zan, U. Bangert, D. W. Boukhvalov, Y. W. Son, and K. S. Novoselov. *Direct experimental evidence of metal-mediated etching of suspended graphene.* ACS Nano, 6, 5, pp. 4063–4071, 2012. http://dx.doi.org/10.1021/nn300452y.

[153] S. Chen, L. Brown, M. Levendorf, W. Cai, S. Y. Ju, J. Edgeworth, X. Li, C. W. Magnuson, A. Velamakanni, R. D. Piner, J. Kang, J. Park, and R. S. Ruoff. *Oxidation resistance of graphene-coated Cu and Cu/Ni alloy.* ACS Nano, 5, 2, pp. 1321–1327, 2011. http://dx.doi.org/10.1021/nn103028d.

[154] M. Topsakal, H. Aahin, and S. Ciraci. *Graphene coatings: An efficient protection from oxidation.* Phys. Rev. B, 85, 15, p. 155445, 2012. http://dx.doi.org/10.1103/PhysRevB.85.155445.

[155] M. Schriver, W. Regan, W. J. Gannett, A. M. Zaniewski, M. F. Crommie, and A. Zettl. *Graphene as a long-term metal oxidation barrier: Worse than nothing.* ACS Nano, 7, 7, pp. 5763–5768, 2013. http://dx.doi.org/10.1021/nn4014356.

[156] Y. P. Hsieh, M. Hofmann, K. W. Chang, J. G. Jhu, Y. Y. Li, K. Y. Chen, C. C. Yang, W. S. Chang, and L. C. Chen. *Complete corrosion inhibition through graphene defect passivation.* ACS Nano, 8, 1, pp. 443–448, 2014. http://dx.doi.org/10.1021/nn404756q.

[157] R. Larciprete, S. Fabris, T. Sun, P. Lacovig, A. Baraldi, and S. Lizzit. *Dual path mechanism in the thermal reduction of graphene oxide.* J. Am. Chem. Soc., 133, 43, pp. 17315–17321, 2011. http://dx.doi.org/10.1021/ja205168x.

[158] S. Ulstrup, M. Andersen, M. Bianchi, L. Barreto, B. Hammer, L. Hornekær, and P. Hofmann. *Sequential oxygen and alkali intercalation of epitaxial graphene on Ir(111): Enhanced many-body effects and formation of pn-interfaces.* 2D Mater., 1, 2, p. 025002, 2014. http://dx.doi.org/10.1088/2053-1583/1/2/025002.

[159] E. E. G. Hughes, B. R. Williams, and J. M. Thomas. *Etching of graphite surfaces with oxygen.* Trans. Faraday Soc., 1962. http://dx.doi.org/10.1039/tf9625802011.

[160] J. R. Hahn. *Kinetic study of graphite oxidation along two lattice directions.* Carbon, 43, 7, pp. 1506–1511, 2005. http://dx.doi.org/10.1016/j.carbon.2005.01.032.

[161] J. Lu, A. H. Castro Neto, and K. P. Loh. *Transforming moiré blisters into geometric graphene nano-bubbles.* Nat. Commun., 3, p. 823, 2012. http://dx.doi.org/10.1038/ncomms1818.

[162] J. R. Hahn, H. Kang, S. M. Lee, and Y. H. Lee. *Mechanistic study of defect-induced oxidation of graphite.* J. Phys. Chem. B, 103, 45, pp. 9944–9951, 1999. http://dx.doi.org/10.1021/jp9920895.

[163] T. Gerber. *Interaction of graphene and templated cluster arrays with CO, H_2, and O_2.* Ph.D. thesis, Universität zu Köln, 2013.

[164] P. Feibelman. *Pinning of graphene to Ir(111) by flat Ir dots.* Phys. Rev. B, 77, 16, p. 165419, 2008. http://dx.doi.org/10.1103/PhysRevB.77.165419.

[165] T. Michely and J. Krug. *Islands, mounds and atoms*, vol. 42 of *Springer Series in Surface Sciences.* Springer Berlin Heidelberg, Berlin, Heidelberg, 1 ed., 2004.

[166] G. Dobrik, L. Tapasztó, and L. P. Biró. *Selective etching of armchair edges in graphite.* Carbon, 56, pp. 332–338, 2013. http://dx.doi.org/10.1016/j.carbon.2013.01.018.

[167] P. Lacovig, M. Pozzo, D. Alfè, P. Vilmercati, A. Baraldi, and S. Lizzit. *Growth of dome-shaped carbon nanoislands on Ir(111): The intermediate between carbidic clusters and quasi-free-standing graphene.* Phys. Rev. Lett., 103, 16, p. 166101, 2009. http://dx.doi.org/10.1103/PhysRevLett.103.166101.

[168] S. Standop, O. Lehtinen, C. Herbig, G. Lewes-Malandrakis, F. Craes, J. Kotakoski, T. Michely, A. V. Krasheninnikov, and C. Busse. *Ion impacts on graphene/Ir(111): Interface channeling, vacancy funnels, and a nanomesh.* Nano Lett., 13, 5, pp. 1948–1955, 2013. http://dx.doi.org/10.1021/nl304659n.

[169] Y. Li, D. Subramaniam, N. Atodiresei, P. Lazić, V. Caciuc, C. Pauly, A. Georgi, C. Busse, M. Liebmann, S. Blügel, M. Pratzer, M. Morgenstern, and R. Mazzarello. *Absence of edge states in covalently bonded zigzag edges of graphene on Ir(111).* Adv. Mater., 25, 14, pp. 1967–1972, 2013. http://dx.doi.org/10.1002/adma.201204539.

[170] D. A. Cosma, J. R. Wallbank, V. Cheianov, and V. I. Fal'ko. *Moiré pattern as a magnifying glass for strain and dislocations in van der Waals heterostructures.* Faraday Discuss., 173, pp. 137–143, 2014. http://dx.doi.org/10.1039/C4FD00146J.

[171] O. V. Yazyev and S. G. Louie. *Topological defects in graphene: Dislocations and grain boundaries.* Phys. Rev. B, 81, 19, p. 195420, 2010. http://dx.doi.org/10.1103/PhysRevB.81.195420.

[172] O. Lehtinen, S. Kurasch, A. V. Krasheninnikov, and U. Kaiser. *Atomic scale study of the life cycle of a dislocation in graphene from birth to annihilation.* Nat. Commun., 4, p. 2098, 2013. http://dx.doi.org/10.1038/ncomms3098.

[173] O. V. Yazyev and Y. P. Chen. *Polycrystalline graphene and other two-dimensional materials.* Nat. Nanotechnol., 9, August, pp. 1–13, 2014. http://dx.doi.org/10.1038/nnano.2014.166.

[174] N. A. Vinogradov, K. A. Simonov, A. A. Zakharov, J. W. Wells, A. V. Generalov, A. S. Vinogradov, N. Mårtensson, and A. B. Preobrajenski. *Hole doping of graphene supported on Ir(111) by $AlBr_3$.* Appl. Phys. Lett., 102, p. 061601, 2013.

[175] N. A. Vinogradov, K. A. Simonov, A. V. Generalov, A. S. Vinogradov, D. V. Vyalikh, C. Laubschat, N. Mårtensson, and A. B. Preobrajenski. *Controllable p-doping of graphene on Ir(111) by chlorination with $FeCl_3$.* J. Phys. Condens. Matter, 24, p. 314202, 2012.

[176] E. N. Voloshina, A. Generalov, M. Weser, S. Böttcher, K. Horn, and Y. S. Dedkov. *Structural and electronic properties of the graphene/Al/Ni(111) intercalation system.* New J. Phys., 13, 11, p. 113028, 2011.

[177] M. Papagno, S. Rusponi, P. M. Sheverdyaeva, S. Vlaic, M. Etzkorn, D. Pacilé, P. Moras, C. Carbone, and H. Brune. *Large band gap opening between graphene dirac cones induced by Na adsorption onto an Ir superlattice.* ACS Nano, 6, 1, p. 199, 2012. http://dx.doi.org/10.1021/nn203841q.

[178] R. J. Koch, M. Weser, W. Zhao, F. Vines, K. Gotterbarm, S. M. Kozlov, O. Höfert, M. Ostler, C. Papp, J. Gebhardt, H.-P. Steinrück, A. Görling, and T. Seyller. *Growth and electronic structure of nitrogen-doped graphene on Ni(111).* Phys. Rev. B, 86, p. 075401, 2012. http://dx.doi.org/10.1103/PhysRevB.86.075401.

[179] A. B. Preobrajenski, M. L. Ng, A. S. Vinogradov, and N. Mårtensson. *Controlling graphene corrugation on lattice-mismatched substrates.* Phys. Rev. B, 78, p. 073401, 2008. http://dx.doi.org/10.1103/PhysRevB.78.073401.

[180] K. V. Emtsev, F. Speck, T. Seyller, L. Ley, and J. Riley. *Interaction, growth, and ordering of epitaxial graphene on SiC0001 surfaces: A comparative photoelectron spectroscopy study.* Phys. Rev. B, 77, p. 155303, 2008. http://dx.doi.org/10.1103/PhysRevB.77.155303.

[181] S. Watcharinyanon, C. Virojanadara, and L. I. Johansson. *Rb and Cs deposition on epitaxial graphene grown on 6H-SiC(0001).* Surf. Sci., 605, p. 1918, 2011. http://dx.doi.org/10.1016/j.susc.2011.07.007.

[182] S. Watcharinyanon, L. I. Johansson, C. Xia, and C. Virojanadara. *Changes in structural and electronic properties of graphene grown on 6HSiC(0001) induced by Na deposition.* J. Appl. Phys., 111, p. 083711, 2012. http://dx.doi.org/10.1063/1.4704396.

[183] S. Watcharinyanon, L. I. Johansson, A. A. Zakharov, and C. Virojanadara. *Studies of Li intercalation of hydrogenated graphene on SiC(0001).* Surf. Sci., 606, p. 401, 2012. http://dx.doi.org/10.1016/j.susc.2011.10.023.

[184] M. Andersen, L. Hornekær, and B. Hammer. *Understanding intercalation structures formed under graphene on Ir(111).* Phys. Rev. B, 90, 15, p. 155428, 2014. http://dx.doi.org/10.1103/PhysRevB.90.155428.

[185] A. V. Fedorov, N. I. Verbitskiy, D. Haberer, C. Struzzi, L. Petaccia, D. Usachov, O. Y. Vilkov, D. V. Vyalikh, J. Fink, M. Knupfer, B. Büchner, and A. Grüneis. *Observation of a universal donor-dependent vibrational mode in graphene.* Nature Comm., 5, p. 3257, 2014. http://dx.doi.org/10.1038/ncomms4257.

[186] S. Lizzit, R. Larciprete, P. Lacovig, M. Dalmiglio, F. Orlando, A. Baraldi, L. Gammelgaard, L. Barreto, M. Bianchi, E. Perkins, and P. Hofmann. *Transfer-free electrical insulation of epitaxial graphene from its metal substrate.* Nano Lett., 12, p. 4503, 2012. http://dx.doi.org/10.1021/nl301614j.

[187] R. Mu, Q. Fu, L. Jin, L. Yu, G. Fang, D. Tan, and X. Bao. *Visualizing chemical reactions confined under graphene.* Angew. Chem. Int. Ed., 51, p. 4856, 2012. http://dx.doi.org/10.1002/anie.201200413.

[188] Y. Yao, Q. Fu, Y. Y. Zhang, X. Weng, H. Li, M. Chen, L. Jin, A. Dong, R. Mu, P. Jiang, L. Liu, H. Bluhm, Z. Liu, S. B. Zhang, and X. Bao. *Graphene cover-promoted metal-catalyzed reactions.* Proc. Natl. Acad. Sci. USA, 111, 48, pp. 17023–17028, 2014. http://dx.doi.org/10.1073/Proc. Natl. Acad. Sci. USA.1416368111.

[189] E. Grånäs, U. Schröder, M. A. Arman, M. Andersen, T. Gerber, A. J. Martinez-Galera, K. Schulte, J. N. Andersen, T. Michely, B. Hammer, and J. Knudsen. *Water chemistry beneath graphene: Formation and breathing of super-dense OH-H_2O phase under graphene.* (in preparation).

[190] S. B. DiCenzo, G. K. Wertheim, S. Basu, and J. E. Fischer. *Charge distribution in potassium graphite.* Phys. Rev. B., 24, p. 2270, 1981.

[191] P. Bennich, C. Puglia, P. Brühwiler, A. Nilsson, A. Maxwell, A. Sandell, N. Mårtensson, and P. Rudolf. *Photoemission study of K on graphite.* Phys. Rev. B, 59, 12, pp. 8292–8304, 1999. http://dx.doi.org/10.1103/PhysRevB.59.8292.

[192] T. Kilgren, T. Balasubramanian, L. Waldén, and R. Yakimova. *K/graphite: Uniform energy shifts of graphite valence states.* Surf. Sci., 600, p. 1160195425, 2006. http://dx.doi.org/10.1016/j.susc.2006.01.011.

[193] M. Montalti, K. S., Y. Chao, Y. V. Butenko, V. L. Kuznetsov, V. R. Dhanak, M. R. C. Hunt, and L. Siller. *Photoemission spectroscopy of clean and potassium-intercalated carbon atoms.* Phys. Rev. B, 67, p. 113401, 2003.

[194] J. Schiessling, L. Kjeldgaard, T. Käämbre, I. Marenne, J. N. O'Shea, J. Schnadt, C. J. Glover, M. Nagasano, D. Nordlund, M. G. Garnier, L. Qian, J.-E. Rubensson, P. Rudolf, P. Martensson, J. Nordgren, and P. A. Brühwiler. *Bulk and surface charge states of K_3C_{60}.* Phys. Rev. B, 71, p. 165420, 2005. http://dx.doi.org/10.1103/PhysRevB.71.165420.

[195] A. Dahal, R. Addou, H. Coy-Diaz, J. Lallo, and M. Batzill. *Charge doping of graphene in metal/graphene/dielectric sandwich structures evaluated by C-1s core level photoemission spectroscopy.* Appl. Phys. Lett. Mater., 1, p. 042107, 2013. http://dx.doi.org/10.1063/1.4284038.

[196] L. I. Johansson, C. Xia, and C. Virojanadara. *Li induced effects in the core level and π-band electronic structure of graphene grown*

on C-face SiC. J. Vac. Sci. Technol. A, 33, 6, p. 061405, 2015. http://dx.doi.org/10.1116/1.4927856.

[197] A. Nagashima, N. Tejima, and C. Oshima. *Electronic states of the pristine and alkali-metal-intercalated monolayer graphite/Ni(111) systems.* Phys. Rev. B, 50, 23, pp. 17487–17495, 1994. http://dx.doi.org/10.1103/PhysRevB.50.17487.

[198] F. Bisti, G. Profeta, H. Vita, M. Donarelli, F. Perrozzi, P. M. Sheverdyaeva, P. Moras, K. Horn, and L. Ottaviano. *Electronic and geometric structure of graphene/SiC(0001) decoupled by lithium intercalation.* Phys. Rev. B, 91, 24, pp. 1–7, 2015. http://dx.doi.org/10.1103/PhysRevB.91.245411.

[199] B. E. Sernelius. *Core-level spectra from graphene.* Phys. Rev. B, 91, 4, p. 045402, 2015. http://dx.doi.org/10.1103/PhysRevB.91.045402.

[200] S. Schumacher, D. Förster, M. Rösner, T. O. Wehling, and T. Michely. *Strain in epitaxial graphene visualized by intercalation.* Phys. Rev. Lett., 110, p. 086111, 2013.

[201] S. Ulstrup, J. C. Johannsen, A. Crepaldi, F. Cilento, M. Zacchigna, C. Cacho, R. T. Chapman, E. Springate, F. Fromm, C. Raidel, T. Seyller, F. Parmigiani, M. Grioni, and P. Hofmann. *Ultrafast electron dynamics in epitaxial graphene investigated with time- and angle-resolved photoemission spectroscopy.* J. Phys. Condens. Matter, 27, 16, p. 164206, 2015. http://dx.doi.org/10.1088/0953-8984/27/16/164206.

[202] P. Sutter, J. T. Sadowski, and E. Sutter. *Graphene on Pt(111): Growth and substrate interaction.* Phys. Rev. B, 80, p. 245411, 2009. http://dx.doi.org/10.1103/PhysRevB.80.245411.

[203] M. Petrović. *Synthesis and intercalation of epitaxial graphene on iridium.* Ph.D. thesis, University of Zagreb, 2014.

[204] S. Reich, J. Maultzsch, C. Thomsen, and P. Ordejón. *Tight-binding description of graphene.* Phys. Rev. B., 66, p. 035412, 2002. http://dx.doi.org/10.1103/PhysRevB.66.035412.

[205] V. Z. Mordkovich. *Synthesis and XPS investigation of superdense lithium-graphite intercalation compound, LiC2.* Synth. Met., 80, 3, pp. 243–247, 1996. http://dx.doi.org/10.1016/0379-6779(96)80209-8.

[206] S. L. Qiu, C. L. Lin, J. Chen, and M. Strongin. *Photoemission studies of the interaction of Li and solid molecular oxygen.* Phys. Rev. B, 39, 9, pp. 6194–6197, 1989. http://dx.doi.org/10.1103/PhysRevB.39.6194.

[207] Q. H. Wu, A. Thissen, and W. Jaegermann. *Photoelectron spectroscopic study of Li oxides on Li over-deposited V_2O_5 thin film surfaces.* Appl. Surf. Sci., 250, 1-4, pp. 57–62, 2005. http://dx.doi.org/10.1016/j.apsusc.2004.12.023.

[208] L. Zhang, Y. Ye, D. Cheng, H. Pan, and J. Zhu. *Intercalation of Li at the graphene/Cu interface.* J. Phys. Chem. C, 117, 18, pp. 9259–9265, 2013. http://dx.doi.org/10.1021/jp401290f.

[209] J. L. McChesney, A. Bostwick, T. Ohta, T. Seyller, K. Horn, J. González, and E. Rotenberg. *Extended van Hove singularity and superconducting instability in doped graphene.* Phys. Rev. Lett., 104, 13, p. 136803, 2010. http://dx.doi.org/10.1103/PhysRevLett.104.136803.

[210] P. M. T. M. Van Attekum and G. K. Wertheim. *Excitonic effects in core-hole screening.* Phys. Rev. Lett., 43, 25, pp. 1896–1898, 1979. http://dx.doi.org/10.1103/PhysRevLett.43.1896.

[211] Z. Y. Li, K. M. Hock, and R. E. Palmer. *Phase transitions and excitation spectrum of submonolayer potassium on graphite.* Phys. Rev. Lett., 67, p. 1562, 1991.

[212] K. M. Hock and R. E. Palmer. *Temperature dependent behaviour in the adsorption of submonolayer potassium on graphite.* Surf. Sci., 284, p. 349, 1993.

[213] E. Grånäs. *Above and below graphene: Nanoparticle chemistry and interface reactions.* Ph.D. thesis, Lund University, 2014.

[214] K. Xu, P. Cao, and J. R. Heath. *Graphene visualizes the first water adlayers on mica at ambient conditions.* Science, 329, 5996, pp. 1188–1191, 2010. http://dx.doi.org/10.1126/science.1192907.

[215] D. Lee, G. Ahn, and S. Ryu. *Two-dimensional water diffusion at a graphene-silica interface.* J. Am. Chem. Soc., 136, 18, pp. 6634–6642, 2014. http://dx.doi.org/10.1021/ja4121988.

[216] S. Lizzit, R. Larciprete, P. Lacovig, M. Dalmiglio, F. Orlando, A. Baraldi, L. Gammelgaard, L. Barreto, M. Bianchi, E. Perkins, and P. Hofmann. *Transfer-free electrical insulation of epitaxial graphene*

from its metal substrate. Nano Lett., 12, 9, pp. 4503–4507, 2012. http://dx.doi.org/10.1021/nl301614j.

[217] R. Mu, Q. Fu, L. Jin, L. Yu, G. Fang, D. Tan, and X. Bao. *Visualizing chemical reactions confined under graphene.* Angew. Chem. Int. Ed., 51, 20, pp. 4856–4859, 2012. http://dx.doi.org/10.1002/anie.201200413.

[218] L. Jin, Q. Fu, A. Dong, Y. Ning, Z. Wang, H. Bluhm, and X. Bao. *Surface chemistry of CO on Ru(0001) under the confinement of graphene cover.* J. Phys. Chem. C, 118, 23, pp. 12391–12398, 2014. http://dx.doi.org/10.1021/jp5034855.

[219] E. Gråsäs, M. Andersen, M. A. Arman, T. Gerber, B. Hammer, J. Schnadt, J. N. Andersen, T. Michely, and J. Knudsen. *CO intercalation of graphene on Ir(111) in the millibar regime.* J. Phys. Chem. C, , 32, pp. 16438–16447. http://dx.doi.org/10.1021/jp4043045.

[220] L. Nilsson, M. Andersen, B. Hammer, I. Stensgaard, and L. Hornekær. *Breakdown of the graphene coating effect under sequential exposure to O_2 and H_2S.* J. Phys. Chem. Letters, 4, 21, pp. 3770–3774, 2013. http://dx.doi.org/10.1021/jz402054e.

[221] G. Tocci, L. Joly, and A. Michaelides. *Friction of water on graphene and hexagonal boron nitride from ab initio methods: Very different slippage despite very similar interface structures.* Nano Lett., 14, 12, p. 6872, 2014. http://dx.doi.org/10.1021/nl502837d.

[222] H. Ma, Y. Ding, M. Iannuzzi, T. Brugger, S. Berner, J. Hutter, J. Osterwalder, and T. Greber. *Chiral distortion of confined ice oligomers (n = 5,6).* Langmuir, 28, 43, pp. 15246–15250, 2012. http://dx.doi.org/10.1021/la302561r.

[223] G. A. Kimmel, J. Matthiesen, M. Baer, C. J. Mundy, N. G. Petrik, R. S. Smith, Z. Dohnálek, and B. D. Kay. *No confinement needed: Observation of a metastable hydrophobic wetting two-layer ice on graphene.* J. Am. Chem. Soc., 131, 35, pp. 12838–12844, 2009. http://dx.doi.org/10.1021/ja904708f.

[224] J. Rafiee, X. Mi, H. Gullapalli, A. V. Thomas, F. Yavari, Y. Shi, P. M. Ajayan, and N. A. Koratkar. *Wetting transparency of graphene.* Nat. Mater., 11, 3, pp. 217–222, 2012. http://dx.doi.org/10.1038/nmat3228.

[225] X. Feng, S. Maier, and M. Salmeron. *Water splits epitaxial graphene and intercalates.* J. Am. Chem. Soc., 134, 12, pp. 5662–5668, 2012. http://dx.doi.org/10.1021/ja3003809.

[226] K. T. He, J. D. Wood, G. P. Doidge, E. Pop, and J. W. Lyding. *Scanning tunneling microscopy study and nanomanipulation of graphene-coated water on mica.* Nano Lett., 12, 6, pp. 2665–2672, 2012. http://dx.doi.org/10.1021/nl202613t.

[227] N. Severin, P. Lange, I. M. Sokolov, and J. P. Rabe. *Reversible dewetting of a molecularly thin fluid water film in a soft graphene-mica slit pore.* Nano Lett., 12, 2, pp. 774–779, 2012. http://dx.doi.org/10.1021/nl2037358.

[228] A. Shavorskiy, M. J. Gladys, and G. Held. *Chemical composition and reactivity of water on hexagonal Pt-group metal surfaces.* Phys. Chem. Chem. Phys., 10, pp. 6150–6159, 2008. http://dx.doi.org/10.1039/B808235A.

[229] M. Pan, S. Hoang, and C. B. Mullins. *Interaction of water with the clean and oxygen pre-covered Ir(111) surface.* Catal. Today, 160, 1, pp. 198 – 203, 2011. http://dx.doi.org/http://dx.doi.org/10.1016/j.cattod.2010.05.008.

[230] T. Schiros, L.-A. Näslund, K. Andersson, J. Gyllenpalm, G. S. Karlberg, M. Odelius, H. Ogasawara, L. G. M. Pettersson, and A. Nilsson. *Structure and bonding of the water-hydroxyl mixed phase on Pt(111).* J. Phys. Chem. C, 111, 41, pp. 15003–15012, 2007. http://dx.doi.org/10.1021/jp073405f.

[231] C. J. Weststrate, W. Ludwig, J. W. Bakker, A. C. Gluhoi, and B. E. Nieuwenhuys. *Ethanol adsorption, decomposition and oxidation on Ir(111): A high resolution XPS study.* ChemPhysChem, 8, 6, pp. 932–937, 2007.

[232] P. Redhead. *Thermal desorption of gases.* Vacuum, 12, 4, p. 203, 1962. http://dx.doi.org/10.1016/0042-207X(62)90978-8.

[233] K. J. Laidler. *The development of the Arrhenius equation.* J. Chem. Educ., 61, 6, p. 494, 1984. http://dx.doi.org/10.1021/ed061p494.

[234] K. Christmann, G. Ertl, and T. Pignet. *Adsorption of hydrogen on a Pt(111) surface.* Surf. Sci., 54, 2, pp. 365–392, 1976. http://dx.doi.org/10.1016/0039-6028(76)90232-6.

[235] N. P. Guisinger, G. M. Rutter, J. N. Crain, P. N. First, and J. A. Stroscio. *Exposure of epitaxial graphene on SiC(0001) to atomic hydrogen.* Nano Lett., 9, 4, pp. 1462–1466, 2009. http://dx.doi.org/10.1021/nl803331q.

[236] R. Balog, B. Jørgensen, J. Wells, E. Lægsgaard, P. Hofmann, F. Besenbacher, and L. Hornekær. *Atomic hydrogen adsorbate structures on graphene.* J. Am. Chem. Soc., 131, 25, pp. 8744–5, 2009. http://dx.doi.org/10.1021/ja902714h.

[237] P. Merino, M. Švec, J. I. Martínez, P. Mutombo, C. Gonzalez, J. A. Martín-Gago, P. L. de Andres, and P. Jelinek. *Ortho and para hydrogen dimers on G/SiC(0001): Combined STM and DFT study.* Langmuir, 31, 1, pp. 233–239, 2015. http://dx.doi.org/10.1021/la504021x.

[238] S. Ulstrup, L. Nilsson, J. A. Miwa, R. Balog, M. Bianchi, L. Hornekær, and P. Hofmann. *Electronic structure of graphene on a reconstructed Pt(100) surface: Hydrogen adsorption, doping, and band gaps.* Phys. Rev. B, 88, p. 125425, 2013. http://dx.doi.org/10.1103/PhysRevB.88.125425.

[239] *Partialdruckmessung in der Vakuumtechnik.* Balzers Aktiengesellschaft.

[240] A. Allouche, Y. Ferro, T. Angot, C. Thomas, and J. M. Layet. *Hydrogen adsorption on graphite (0001) surface: A combined spectroscopy-density-functional-theory study.* J. Chem. Phys., 123, 12, 2005. http://dx.doi.org/10.1063/1.2043008.

[241] R. P. Chin, J. Y. Huang, Y. R. Shen, T. J. Chuang, and H. Seki. *Interaction of atomic hydrogen with the diamond C(111) surface studied by infrared-visible sum-frequency-generation spectroscopy.* Phys. Rev. B, 52, 8, pp. 5985–5995, 1995. http://dx.doi.org/10.1103/PhysRevB.52.5985.

[242] D. Henwood and J. D. Carey. *Ab initio investigation of molecular hydrogen physisorption on graphene and carbon nanotubes.* Phys. Rev. B, 75, p. 245413, 2007. http://dx.doi.org/10.1103/PhysRevB.75.245413.

[243] J. Petucci, C. LeBlond, M. Karimi, and G. Vidali. *Diffusion, adsorption, and desorption of molecular hydrogen on graphene and in graphite.* J. Chem. Phys., 139, 4, p. 044706, 2013. http://dx.doi.org/10.1063/1.4813919.

[244] H. Kim. *Das Schwingungsverhalten von Wasserstoff auf epitaktisch gewachsenen Graphen.* Ph.D. thesis, Universität Duisburg-Essen, 2013.

[245] S. Haq, J. Harnett, and A. Hodgson. *Growth of thin crystalline ice films on Pt(111).* Surf. Sci., 505, pp. 171–182, 2002. http://dx.doi.org/10.1016/S0039-6028(02)01152-4.

[246] J. Harnett, S. Haq, and A. Hodgson. *Electron induced restructuring of crystalline ice adsorbed on Pt(111).* Surf. Sci., 528, 1-3, pp. 15–19, 2003. http://dx.doi.org/10.1016/S0039-6028(02)02604-3.

[247] S. Ogura, K. Fukutani, and M. Okada. *Structure of gold thin films grown on Ir(111).* Top. Catal., 44, 1-2, pp. 65–71, 2007. http://dx.doi.org/10.1007/s11244-007-0279-7.

[248] L. I. Maissel and R. Glang. In *Handbook of Thin Film Technology.* McGraw-Hill, 1970.

[249] S. Nie, N. C. Bartelt, J. M. Wofford, O. D. Dubon, K. F. McCarty, and K. Thürmer. *Scanning tunneling microscopy study of graphene on Au(111): Growth mechanisms and substrate interactions.* Phys. Rev. B, 85, 20, pp. 1–6, 2012. http://dx.doi.org/10.1103/PhysRevB.85.205406.

[250] G. Ehrlich and F. G. Hudda. *Atomic view of surface self-diffusion: Tungsten on tungsten.* J. Chem. Phys., 44, 3, pp. 1039–1049, 1966. http://dx.doi.org/10.1063/1.1726787.

[251] R. L. Schwoebel and E. J. Shipsey. *Step motion on crystal surfaces.* J. Appl. Phys., 37, 10, pp. 3682–3686, 1966. http://dx.doi.org/10.1063/1.1707904.

[252] J. Tesch, P. Leicht, F. Blumenschein, L. Gragnaniello, M. Fonin, L. E. Marsoner Steinkasserer, B. Paulus, E. Voloshina, and Y. Dedkov. *Structural and electronic properties of graphene nanoflakes on Au(111) and Ag(111).* Sci. Rep., 6, November 2015, p. 23439, 2016. http://dx.doi.org/10.1038/srep23439.

[253] A. G. Sault, R. J. Madix, and C. T. Campbell. *Adsorption of oxygen and hydrogen on Au(110)-(1x2).* Surf. Sci., 169, 2-3, pp. 347–356, 1986. http://dx.doi.org/10.1016/0039-6028(86)90616-3.

[254] B. Hammer and J. K. Norskov. *Why gold is the noblest of all the metals.* Nature, 376, 6537, pp. 238–240, 1995. http://dx.doi.org/10.1038/376238a0.

[255] M. Okada, M. Nakamura, K. Moritani, and T. Kasai. *Dissociative adsorption of hydrogen on thin Au films grown on Ir.* Surf. Sci., 523, 3, pp. 218–230, 2003. http://dx.doi.org/10.1016/S0039-6028(02)02408-1.

[256] M. Okada, S. Ogura, W. A. Diño, M. Wilde, K. Fukutani, and T. Kasai. *Reactive gold thin films grown on iridium.* Appl. Surf. Sci., 246, 1-3, pp. 68–71, 2005. http://dx.doi.org/10.1016/j.apsusc.2004.10.051.

[257] M. Andersen, L. Hornekær, and B. Hammer. *Graphene on metal surfaces and its hydrogen adsorption: A meta-GGA functional study.* Phys. Rev. B, 86, p. 085405, 2012. http://dx.doi.org/10.1103/PhysRevB.86.085405.

[258] P. Heimann, J. F. van der Veen, and D. E. Eastman. *Structure-dependent surface core level shifts for the Au(111), (100), and (110) surfaces.* Solid State Commun., 38, 7, pp. 595–598, 1981. http://dx.doi.org/10.1016/0038-1098(81)90947-9.

Acknowledgements

Ich möchte mich zunächst bei Prof. Dr. Thomas Michely bedanken, für die Möglichkeit sowohl meine Masterarbeit als auch meine Doktorarbeit in seiner Gruppe durchzuführen, für seine hervorragende Betreuung, die konstruktive Kritik, seine weisen Worte und für die Möglichkeit meine Arbeit auf Konferenzen zu präsentieren, was einen enormen Motivationsfaktor für mich dargestellt hat.

Vielen Dank ebenfalls an Prof. Dr. Joachim Krug für die Übernahme der Zweitkorrektur trotz des fremden Fachgebiets.

I would like to thank my colleagues from Lund for the friendly atmosphere during beamtimes, the analysis of XPS data, and the help when I started out analyzing XPS data by myself. Thanks to Jan Knudsen for knowing an answer to almost everything related to XPS or the beamline and for pushing every beamtime to be a full success. Thanks to Alif Arman for his help, advice, and company during beamtimes. A special thank you goes to Elin Grånäs for making night shifts actually fun, always and quickly answering my numerous questions about XPS, for providing the fun lab stories, and the great atmosphere when working together. I also gratefully acknowledge the MAX-Lab staff for their valuable support and friendliness during beamtimes (even on early Sunday mornings).

I am grateful to Marin Petrović for providing the tight-binding calculations for Chapter 5, his work on the figures, as well as his always quick and highly valuable advice and comments.

Für das Korrekturlesen möchte ich mich bei Charlotte Herbig, Clifford Murray, Felix Huttmann, Janina Krieg, Joshua Hall, Wouter Jolie sowie bei Max Schröder und Tim Steinbach bedanken. Inbesondere bei den letzten beiden für die Übernahme der ein oder anderen Nachtschicht kurz vor Abgabeschluss sowie die Versorgung mit Essen und guter Laune.

Ich möchte mich ebenfalls bei "meinen" Bachelor-, Lehramts-, und Masterstudenten Benjamin Jost, Clifford Murray, Domenik Zimmermann und Mathias Pörtner für die gute Zusammenarbeit im Labor, ihre Hilfsbereitschaft und neue Denkanstöße bedanken. Vor allem möchte ich mich bei

(Calipso) Cliff bedanken, ohne dessen exzellente Arbeit das Kapitel 7 nicht existieren würde.

Ein ganz besonders großer Dank an Norbert Henn, der fröhlich und gut gelaunt stets zur Stelle war, wenn es irgendwo brannte und selbst kurz vor Weihnachten in Rekordzeit das neue STM startklar machte.

Auch der feinmechanischen und der elektronischen Werkstatt möchte ich für ihre Arbeit danken und für ihr Verständnis, wenn ein Auftrag, mal wieder, "diesmal ausnahmsweise wirklich, wirklich dringend" war. Ebenso gilt mein Dank unseren Sekretärinnen Carmen Handels und Britta Schulz, für den Durchblick in dem mir völlig unverständlichen Verwaltungsdschungel, und dem guten Geist des Instituts Ralph Müller für seine Hilfsbereitschaft und die guten Connections zur Chemie-Glasbläserei.

Ich möchte meinen tollen Bürokollegen danken, allen voran Charlotte Herbig, mit der irgendwie immer lustige Sachen passieren, Ferdinand Farwick zum Hagen, seines Zeichens Runkelrübenkönig, und Stefan Kraus, der mich die letzten Monate zuverlässig mit Schokolade versorgte. Ein großer Dank an Felix Huttmann, der zu jedem Thema etwas Cleveres zu sagen hat, sei es 5-7er Defekte oder Flüchtlingspolitik. Vielen Dank an Timm Gerber, der mir alles beigebracht hat, was man über TuMA III zu wissen hat, selbst über meine absurdesten Fragen nachgedacht hat (am Ende war es allerdings kein Drache, der TuMA III mitgenommen hat) und auch nach Verlassen der Arbeitsgruppe noch als Telefonsupport zur Verfügung stand. Thanks to Antonio Martínez-Galera for being an endless source of the friendly atmosphere in the lab, his willingness to help always and wherever possible, and for teaching me to always be on the lookout for the next joke.

Weiterhin danke ich allen jetzigen und ehemaligen Mitglieder der Arbeitsgruppe Caio Silva, Carsten Busse, Daniel Förster, Daniela Dombrowski, Fabian Craes, Georgia Lewes-Malandrakis, Jiaqi Cai, Jürgen Klinkhammer, Martin Engler, Moritz Will, Philipp Valerius, Sabina Simon, Sebastian Standop, Sven Macko, Sven Müller, Sven Runte und Timo Knispel für die gute Arbeitsatmosphäre, die Kickerduelle und die After-work Events.

Ein dicker Dank ans Cafe Duddel, wo große Teile dieser Arbeit entstanden sind, wenn mir im Büro oder zu Hause mal wieder die Decke auf den Kopf fiel. Ebenfalls danke ich Jogi Löw und der deutschen Nationalmannschaft für einen unvergesslichen Sommer in Köln. Danke an meine Freunde, die mich durchs Studium und die Promotion begleitet haben und diese Zeit zu einer besonderen gemachten haben. Danke auch an meine Mitbewohner Paul und seine Katze Lily, die mir, jeder auf seine eigene Art, mehr Gelassenheit sowie das Mäusefangen beigebracht haben.

Bei der Studienstiftung des deutschen Volkes möchte ich mich nicht nur für die Gewährung eines Promotionsstipendium bedanken, sondern inbeson-

dere auch für die Ermöglichung von interessanten Begegnungen und Erfahrungen auch außerhalb der Physik. Ebenfalls danke ich der Bonn-Cologne Graduate School für die Reisemittel und ideelle Förderung, und insbesondere Petra Neubauer-Günther für ihre völlig unkomplizierte, schnelle und nette Hilfe bei jedem Problem, von dem sie Wind bekam.

Knowing that I could have never been at this point without them, I am deeply thankful my teachers throughout school and university. I wish to representatively thank my highschool physics teacher Scott Wiley for his great way of teaching which encouraged my fascination for physics and continues to inspire me.

Das größte Dankeschön geht an meine Eltern und meine Familie. Die Tatsache, dass sie immer für mich da sind, mich motivieren und uneingeschränkt unterstützen, sehe ich nicht als selbstverständlich an und bedanke mich aus tiefstem Herzen dafür.

Publications

Parts of the results presented in this thesis can be found in the following publications:

1. Core Level Shifts of Intercalated Gr
   U. A. Schröder, M. Petrović, T. Gerber, E. Grånäs, A. J. Martínez-Galera, M. A. Arman, C. Herbig, J. Schnadt, M. Kralj, J. Knudsen, T. Michely *(2D Materials 4, 015013 (2017))*.

2. Etching of Graphene on Ir(111) with Molecular Oxygen
   U. A. Schröder, E. Grånäs, T. Gerber, M. A. Arman, B. Hammer, K. Schulte, J. N. Andersen, J. Knudsen, T. Michely
   Carbon 96, 320 (2016).

Further publications that are not part of this thesis:

3. Structure and Growth of Hexagonal Boron Nitride on Ir(111)
   F. Farwick zum Hagen, D. Zimmermann, C. Silva, C. Schlueter, N. Atodiresei, W. Jolie, A. J. Martínez-Galera, D. Dombrowski, U. A. Schröder, M. Will, P. Lazić, V. Caciuc, S. Blügel, T.-L. Lee, T. Michely, C. Busse
   ACS Nano 10, 11012 (2016) .

4. Stability and Reactivity of Graphene-Templated Nanoclusters
   T. Gerber, E. Grånäs, U. A. Schröder, P. Stratmann, K. Schulte, J. N. Andersen, J. Knudsen, T. Michely
   J. Phys. Chem. C 120, 26290 (2016).

5. Oxygen Orders Differently under Graphene: New Superstructures on Ir(111)
   A. J. Martínez-Galera, U. A. Schröder, F. Huttmann, W. Jolie, F. Craes, C. Busse, V. Caciuc, N. Atodiresei, S. Blügel, T. Michely
   Nanoscale 8, 1932 (2016).

6. Hydrogen Intercalation under Graphene on Ir(111)
   E. Grånäs, T. Gerber, U. A. Schröder, K. Schulte, J. N. Andersen, Thomas Michely, J. Knudsen
   Surface Science 651, 57 (2016).

7. Xe Irradiation of Graphene on Ir(111): From Trapping to Blistering
   C. Herbig, E. H. Åhlgren, U. A. Schröder, A. J. Martínez-Galera, M. A. Arman, J. Kotakoski, J. Knudsen, A. V. Krasheninnikov, T. Michely.
   Physical Review B 92, 085429 (2015).

8. Comment on "Interfacial Carbon Nanoplatelet Formation by Ion Irradiation of Graphene on Iridium(111)"
   C. Herbig, E. H. Åhlgren, U. A. Schröder, A. J. Martínez-Galera, M. A. Arman, W. Jolie, C. Busse, J. Kotakoski, J. Knudsen, A. V. Krasheninnikov, T. Michely.
   ACS Nano 9, 4664 (2015).

9. Oxygen Intercalation under Graphene on Ir(111): Energetics, Kinetics, and the Role of Graphene Edges
   E. Grånäs, J. Knudsen, U. A. Schröder, T. Gerber, C. Busse, M. A. Arman, K. Schulte, J. N. Andersen, and T. Michely
   ACS Nano 6, 9951 (2012).

10. Adsorption Dynamics of Water on the Surface of TiO2 (110)
    N. Bundaleski, A. G. Silva, U. Schröder, A. M. C. Moutinho and O. M. N. D. Teodoro
    25th Summer School and International Symposium on the Physics of Ionized Gases, Journal of Physics: Conference Series (2010).

11. Customizable Gas-Gap Heat Switch
    D. Martins, I. Catarino, U. Schröder, J. Ricardo, R. Patricio, L. Duband, G. Bonfait
    AIP Conf. Proc. 1218, 1652 (2010).

Erklärung

Ich versichere, dass ich die von mir vorgelegte Dissertation selbständig angefertigt, die benutzten Quellen und Hilfsmittel vollständig angegeben und die Stellen der Arbeit – einschließlich Tabellen, Karten und Abbildungen –, die anderen Werken im Wortlaut oder dem Sinn nach entnommen sind, in jedem Einzelfall als Entlehnung kenntlich gemacht habe; dass diese Dissertation noch keiner anderen Fakultät oder Universität zur Prüfung vorgelegen hat; dass sie – abgesehen von den angegebenen Teilpublikationen – noch nicht veröffentlicht worden ist, sowie, dass ich eine solche Veröffentlichung vor Abschluss des Promotionsverfahrens nicht vornehmen werde. Die Bestimmungen der Promotionsordnung sind mir bekannt. Die von mir vorgelegte Dissertation ist von Prof. Dr. Thomas Michely betreut worden.

Köln, den 5. Juli 2016

Ulrike Schröder